Metal-Organic Frameworks for Selective Gas Separation

A thesis presented in partial fulfilment of the requirements of the degree of

Doctor of Philosophy

in

Chemistry

at Massey University, Manawatū, New Zealand

Omid Taheri Qazvini

2019

For my family

Abstract

With an ever increasing need for a more energy-efficient and environmentally benign procedure for gas separation, adsorbents with tailored structures and tunable surface properties are in high demand. Metal–organic frameworks (MOFs), constructed from metal-containing nodes connected by organic bridges, are such a new type of porous materials. They are promising candidates as adsorbents for gas separations due to their large surface areas, adjustable pore sizes and controllable properties, as well as acceptable thermal stability. However, the bottleneck in this context is that MOFs are expensive to be fabricated and majority of them are not stable in harsh environments, which are often required by industrial processes. In this thesis, we introduce three families of metal-organic frameworks with exceptional gas separation performance for a variety of different gas mixtures separation. Their unique separation performances are well supported by isotherm measurement, X-ray crystallography, DFT calculations, and breakthrough test. These MOFs are all readily synthesizable by inexpensive precursor and highly stable at extreme conditions.

Contributions

All the work in this thesis was completed by Omid Taheri Qazvini

Except:

- All elemental analyses were performed by the Campbell Microanalytical Laboratory at the University of Otago, New Zealand.
- High pressure adsorption isotherms in Chapter 2 were measured by Dr. Yuebiao Zhang at Shanghai Tech University, China.
- All DFT calculations were performed by Dr. Ravichandar Babarao at RMIT University, Australia.
- X-ray crystallographic data of MUF-18 and MUF-22 were collected by Dr. Lauren Macreadie at the Australian synchrotron.

Acknowledgements

I would like to take the opportunity to thank the large number of people who have contributed to my PhD research and thesis. First, I would like to thank my supervisor Professor Shane Telfer for providing me this wonderful PhD opportunity and scholarship to carry out research in MOF chemistry. Thanks for his enthusiastic, encouraging and patient guidance to my research from the big picture all the way to technical details. Thanks for providing funding for me to attend conferences and visit Dr. Ravichandar Babarao's group in RMIT University and Mathew Hill's group in CSIRO.

I would also like to thank my co-supervisor, Professor Richard Haverkamp, for his much-valued guidance. I also thank Dr. Pat Edwards for assisting in NMR experiments, and David Lun for his technical assistance, Dr. Daniel Zhou for sharing his useful knowledge regarding Material Studio, Subo Lee, David Perl and Adil Alkas for their appreciable help regarding crystallography, and all other current and past Telfer group members for scientific discussions and technical assistance.

I thank Associate Professor Mathew Hill and Dr. Ravichandar Babarao for hosting my visit and all their group members.

I thank NeSI for providing computational resources, staff from Campbell Microanalytical Laboratory at the University of Otago for elemental analyses, Dr. Yuebiao Zhang for measuring high pressure isotherms, Steve Denby and Olaf Griewaldt for constructing the breakthrough apparatus. I also would like to thank Mahmood Ghorbani and Streat Control Ltd. for help and support to install the equipment for breakthrough test.

I would like to acknowledge the financial support from RSNZ Marsden Fund for a Doctoral scholarship and the SFS postgraduate travel fund for supporting me to visit Dr. Ravichandar Babarao's group in RMIT University and Mathew Hill's group in CSIRO. I greatly thank the MacDiarmid Institute for organizing and supporting annual student and postdoc symposiums and financial support for purchasing breakthrough apparatus equipment.

I also thank IFS administration and technical staff for their great assistance during my PhD research and thesis writing. I would like to acknowledge Massey Ventures LTD for financial support to lodge a provisional patent and technical advice and support for commercializing MUF-16.

Finally, I must thank my family for their support and encouragement over the last few years. Especially I would like to thank my mother Massomeh Taherkhani and Akbar Taheri Qazvini for their great help, understanding and support.

Abbreviations

BET	Brunauer-Emmett-Teller
CNG	compressed natural gas
CSIRO	Commonwealth Scientific and Industrial Research Organization
DAC	direct air capture
DFT	density functional theory
DEF	*N*,*N*-diethylformamide
DMF	*N*,*N*-dimethylformamide
DOE	U.S. Department of Energy
DSLF	Dual-Site Langmuir Freundlich
GCMC	Grand Canonical Monte Carlo
GPU	gas permeation unit
HKUST	Hong Kong University of Science and Technology
HOF	hydrogen-bonded organic framework
IAST	Ideal Adsorption Selectivity Theory
IRMOF	isoreticular metal-organic framework
IUPAC	International Union of Pure and Applied Chemistry
LCD	largest cavity diameter
LDF	linear driving force
LNG	liquefied natural gas
MAF	metal azolate framework
MCP	microporous coordination polymer
MFM	Manchester framework materials
MIL	Matérial Institut Lavoisier
MOF	metal-organic framework
MUF	Massey University framework
NMR	nuclear magnetic resonance

PCN	porous coordination network
PCP	porous coordination polymer
PLD	pore limiting diameter
PSA	pressure swing adsorption
PSM	postsynthetic modification
PXRD	powder X-ray diffraction
RH	relative humidity
SBU	secondary building unit
SCXRD	single crystal x-ray diffraction
SEM	scanning electron microscopy
STP	standard temperature and pressure
SUMOF	Stockholm University metal-organic framework
TGA	Thermogravimetric analysis
TSA	temperature swing adsorption
UTSA	University of Texas at San Antonio
UiO	University of Oslo
VASP	Vienna Ab initio Simulation Package
VSA	vacuum swing adsorption
ZIF	zeolitic imidazolate framework
ZJU	Zhejiang University

Publications, patent and thesis structure

Publications and patent relevant to this thesis

1. **Qazvini, O. T.**; Babarao, R.; Shi, Z.-L.; Zhang, Y.-B.; Telfer, S. G., A Robust Ethane-Trapping Metal–Organic Framework with a High Capacity for Ethylene Purification. *J. Am. Chem. Soc.* **2019,** *141* (12), 5014-5020. DOI:10.1021/jacs.9b00913.

   I carried out the experimental (except high pressure isotherm measurements) and computational work (except DFT calculations), put together the electronic supporting information, and wrote the first draft of this paper.

2. **Qazvini, O. T.**; Babarao, R.; Telfer, S. G., Multipurpose Metal–Organic Framework for the Adsorption of Acetylene: Ethylene Purification and Carbon Dioxide Removal. *Chem. Mater.* **2019**, in press**.** DOI:10.1021/acs.chemmater.9b01691.

   I carried out the experimental and computational work (except DFT calculations), put together the electronic supporting information, and wrote the first draft of this paper.

3. Qazvini, O. T.; Shane, S. G., A Universal Porous Adsorbent for the Selective Capture of Carbon Dioxide. ChemRxiv 2019. doi.org/10.26434/chemrxiv.9729665.v2.

   I carried out the experimental and computational work, put together the electronic supporting information, and wrote the first draft of this paper.

4. Telfer, S. G.; **Qazvini, O. T.**, Metal-organic frameworks for gas adsorption, Australian Patent No. AU 2018904882, 2018. Retrieved from http://pericles.ipaustralia.gov.au/ols/auspat/quickSearch.do?queryString=2018904882+&resultsPerPage=.

   A provisional patent on MUF-16 has been filed with IP Australia (application no. 2018904882). I carried out the experimental and computational work and wrote the first draft of this patent.

Additional publications

5. Zhou, C.; Longley, L.; Krajnc, A.; Smales, G. J.; Qiao, A.; Erucar, I.; Doherty, C. M.; Thornton, A. W.; **Qazvini, O. T.**; Telfer, S. G.et al. Metal-organic framework glasses with permanent accessible porosity. *Nat. Commun.* **2018,** *9* (1), 5042.

6. Wilson, B. H.; Scott, H. S.; **Qazvini, O. T.**; Telfer, S. G.; Mathonière, C.; Clérac, R.; Kruger, P. E. A supramolecular porous material comprising Fe(II) mesocates. *Chem. Commun.* **2018,** *54* (95), 13391.
7. Patil, K. M.; Telfer, S. G.; Moratti, S. C.; **Qazvini, O. T.**; Hanton, L. R. Non-interpenetrated Cu-based MOF constructed from a rediscovered tetrahedral ligand. *CrystEngComm* **2017,** *19* (48), 7236.
8. Bryant, M. R.; Burrows, A. D.; Kepert, C. J.; Southon, P. D.; **Qazvini, O. T**.; Telfer, S. G.; Richardson, C. Mixed-Component Sulfone–Sulfoxide Tagged Zinc IRMOFs: In Situ Ligand Oxidation, Carbon Dioxide, and Water Sorption Studies. *Cryst. Growth Des.* **2017,** *17* (4), 2016.
9. Conte, L.; Zhou, T.; **Qazvini, O. T.**; Liu, L.; Turner, D. R.; Telfer, S. G. and Richardson, C., The elusive nitro-functionalised member of the IRMOF-9 family. *Aust. J. Chem.* **2019**, in press.

Table of Contents

Chapter 1

Introduction

1.1 General introduction to metal-organic frameworks

1.1.1 Definition, terminology and nomenclature

Metal-organic frameworks (MOFs) are a new class of hybrid materials, constructed from metal ions or metal-containing clusters and divergent organic linkers to form one-, two- or three dimensional network-like structures. These materials are composed of metal centres, which are represented by metal ions, or metal clusters and one or several organic ligands, which serve as linkers between these metal centres. The interest in MOFs was sparked in the 1990s, with hundreds of these materials now discovered.[1] Such interest in MOFs is related to their unique properties. MOFs are crystalline (i.e. the atoms are arranged in a regular, ordered and periodic manner) and porous materials with high accessible pore volume. With a great variety of metal clusters and organic linkers, there seems to be infinite number of possible combinations to make MOFs. The tuneable nature of MOFs have allowed the rational structural design of numerous MOFs and the incorporation of various functionalities via constituent building blocks.

These materials have emerged from an interdisciplinary field with an origin in inorganic and coordination chemistry, so there is a variety of terminological usages for these materials in the literature. Additionally, different individual research groups have used, or formerly used, various names for MOFs, such as porous coordination networks (PCNs, by Zhou's group), porous coordination polymers (PCPs, by Kitagawa's group), and microporous coordination polymers (MCPs, by Matzger's group), which causes more confusion and unnecessary misunderstanding. In 2013, the International Union of Pure and Applied Chemistry (IUPAC) published its recommendations to give some clarity to the definitions and terminologies used in the field of MOFs. According to IUPAC, *a metal-organic framework, abbreviated to MOF, is a coordination network with organic ligands containing potential voids*.[2] Here, a coordination network refers to *a coordination compound extending, through repeating coordination entities, in one dimension, but with cross-links between two or more individual chains, loops, or spiro-links, or a coordination compound extending through repeating coordination entities in two or three dimensions.* IUPAC also defines a

coordination polymer as *a coordination compound with repeating coordination entities extending in one, two, or three dimensions.* As can be seen from these definitions, MOFs are a subset of coordination networks which they are again a subset of coordination polymers (Figure 1.1).

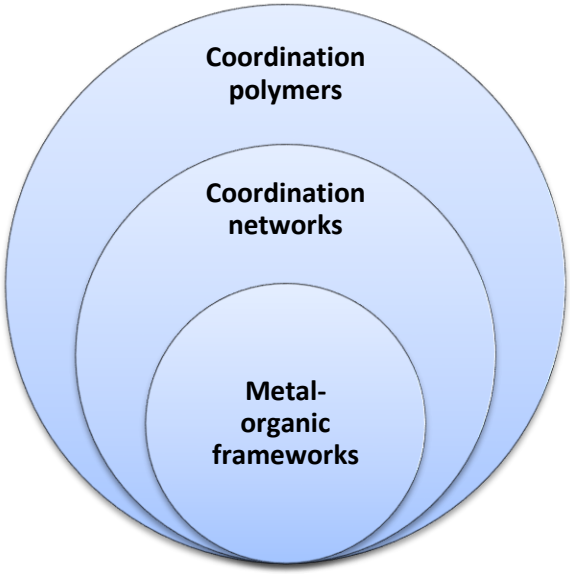

Figure 1.1 A diagram showing that MOFs are a subset of coordination networks, and that coordination networks are further subset of coordination polymers.

A task group from IUPAC has worked to revise the nomenclature of coordination and inorganic polymers.[2] In general, IUPAC agrees that the nickname of the MOFs (e.g. MOF-5[3]) or abbreviated formula [e.g. Mg_2(dobdc),[4-6] dobdc = 2,5-dioxido-1,4-benzenedicarboxylate], can be commonly used, when referring to a MOF. Another way of naming MOFs recognized by IUPAC is naming materials based on their place of origin followed by a number, such as MUF-15 (MUF = Massey University Frameworks),[7] MIL-101 (Matérial Institut Lavoisier),[8] and UiO-66 (UiO = University of Oslo).[9] In this thesis, the term MOF will be used based on IUPAC recommendations and all materials initially reported with alternative terms will be classified as MOFs.

1.1.2 A brief overview of the history of MOFs

As a subclass of coordination networks, the historical development of MOFs is closely related to that of coordination networks. Prussian blue, $Fe_4[Fe(CN)_6]_3 \cdot xH_2O$, might be the first coordination network which was first deliberately synthesized in 1706 as a pigment and its crystal structure was solved not earlier than 1977.[10] In spite of some different opinions, it is mostly agreed that the work of Hoskins and Robson proposed in 1989-1990 lead to a new

chapter in the study of MOFs. They presented a "design" flavour to the assembly of 3D frameworks by the combinations of organic building blocks (ligands) and metal ions.[11-12] Ten years after Hoskins and Robson's work, two outstanding MOFs, MOF-5 ($Zn_4O(bdc)_3$, bdc = 1,4-benzenedicarboxylate)[13] and HKUST-1 ($Cu_3(btc)_2$, btc = 1,3,5-benzenetricarboxylate)[14] were introduced, and greatly helped to advance this field, mainly because of their permanent porosity towards incoming gases which was verified experimentally (Figure 1.2). MIL-101 ($Cr_3OF(bdc)_3$), another milestone representative of MOFs, was introduced shortly thereafter showing not only permanent porosity but also high stability.[15]

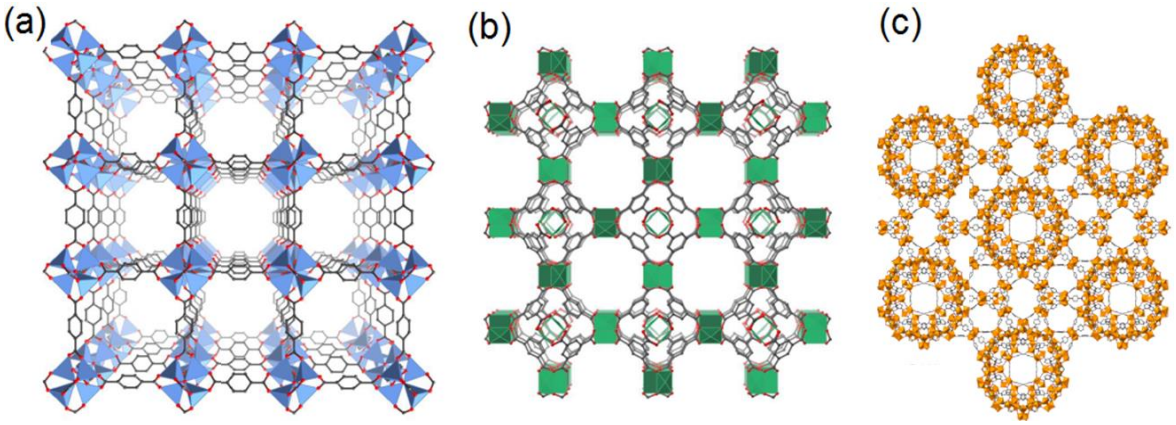

Figure 1.2 Crystal structure of (a) MOF-5, (b) HKUST-1 and (c) MIL-101 constructed from linking metal clusters and organic linkers. Colour code: orange: chromium; green: copper; blue: zinc; grey: carbon; red: oxygen.

Rapid development of MOF field can be clearly related to the observations of a variety of exciting properties and the great potential of these materials in the near future. Moreover, flexible behaviour of dynamic MOFs as well as other alluring properties of MOFs has added to the attraction of this field, and has discriminated them from traditional porous materials.[16] It should also be highlighted that among porous materials, MOFs exhibit the highest surface areas per gram by far reported to date.[17] Such high surface areas of MOFs has led to their enormous use in gas storage systems, where only 1 g of MOF can accommodate a football field in its pores.[18] As a developing field, the complication in properties and structures of MOFs is constantly increasing, and novel applications are being discovered.[19]

1.1.3 From traditional porous solid materials to MOFs

There were only two types of porous materials, inorganic and carbon-based materials that were being applied in industry by the mid-1990s.[20] Nowadays, porous materials are a broad family, ranging from organic to inorganic, from synthetic to natural, and from

crystalline to amorphous. A classic example of inorganic porous materials is zeolites, which are crystalline aluminosilicates with pores with a dimeter of 3-13 Å interconnected to each other.[21] A big portion of industrial processes, particularly separation processes, are performed using zeolites, which reflects the importance of these materials in our daily life. Compared to zeolites, activated carbons are amorphous materials and does not have uniform structures, but they possess higher specific surface area and porosity and hold a great share of the market.[22]

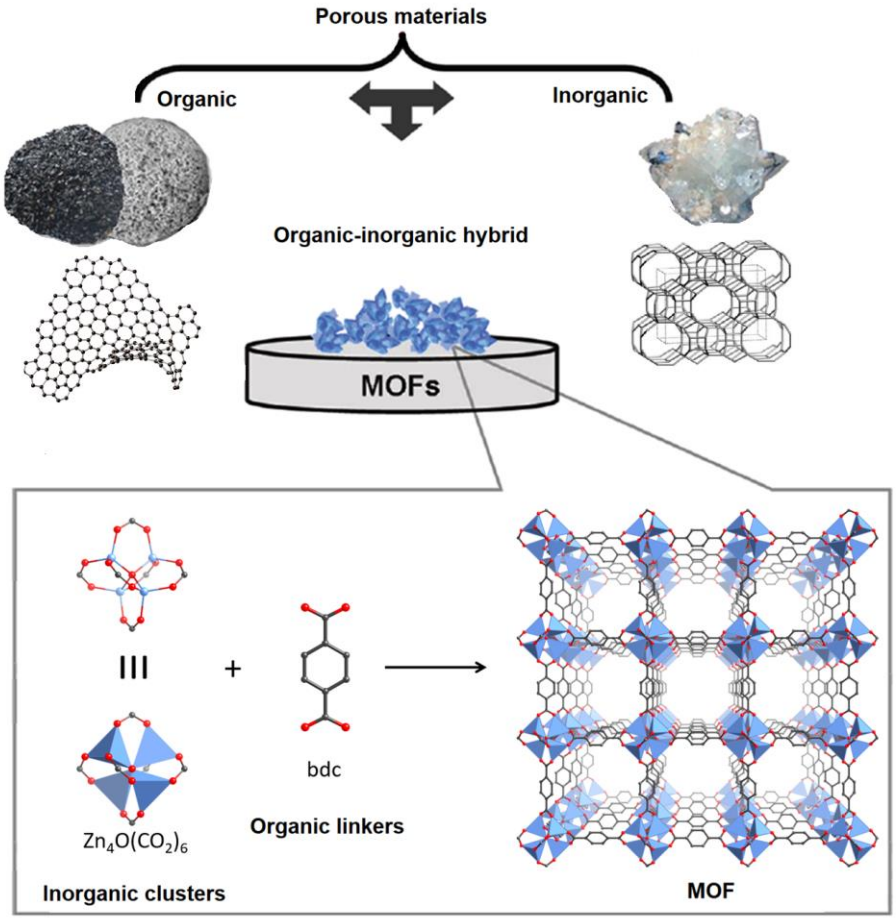

Figure 1.3 Schematic of porous solid classification emphasizing MOFs as hybrid porous materials. Three types of porous solids with polymers, zeolites and MOFs as an example porous organic solids, porous inorganic solids, and porous organic-inorganic hybrid solids, respectively, as well as a general construction procedure for a MOF.

The classification of porous materials is shown in Figure 1.3 presenting MOFs as a type of new hybrid materials, consisting of organic and inorganic compounds, as well as a typical procedure for the construction of MOFs. MOFs are regarded as one of the most advanced porous materials because of their crystallinity, regular pore size, diversity, flexibility, and designability in both structure and properties, which enable them to reach or outperform current adsorption technologies. In comparison to traditional inorganic porous solids and

activated carbons, the number of newly synthesized MOFs are drastically increasing due the vast library of inorganic and organic compounds. It can indeed be seen from the growing number of papers published on these materials in the last 20 years. In addition to adsorptive characteristic[23-24], because of the hybrid nature of MOFs takes advantage of the properties of both inorganic and organic moieties, and hence they can also be utilized in a number of other exciting applications including magnetism[25-26] and luminescence[27-28]. Because of their crystalline nature, the structure of MOFs can be determined by single-crystal X-ray diffraction. MOFs also possess uniform pore structure which aims in the easy exploration of them and properties-structure relationships understanding. It leads to further design and synthesis of new and improved MOFs. Actually, this regular pore size distribution has helped to determine a number of adsorption phenomena in MOFs directly.[29] Such a uniform pore space can be used as a molecular reactor for stabilizing reactants and conduct reactions more systematically.[30-31] Compared to other porous solid materials such as zeolites and activated carbons, MOFs possess a higher degree of designability and their functionality can be tuned by introducing different functional groups. The tunable nature of MOFs can be attributed to at least one of these concepts, (a) MOF are generally synthesized in mild conditions which allows for controlling the reactions easily; (b) by the virtue of organic chemistry, ligands can be readily designed or functionalized; (c) organic ligands and metal clusters have fixed coordination numbers which means a specific framework can be generated by combining rigid organic and inorganic building units; (d) MOFs sometimes obey isoreticular approach, i.e., their structure and functionality can be tuned while the topology and connectivity between nodes remains unchanged;[32] and (e) metal nodes or the organic linker in the framework can be post-synthetically modified.[33-34] As an example of one of these characteristics, isoreticular approach has led to the synthesis of the most fascinating families of MOFs whose physical structure and chemical affinity can be fine-tuned, whilst keeping the basic topology of the framework unchanged. For instance, isoreticular chemistry enables design of MOFs with tailored porosity and high surface areas that can lead to the development of highly efficient MOFs for storage applications. As an example, Schröder and co-workers developed a series of isoreticular MOFs through elongation of some octacarboxylate ligands where they have significantly improved the surface areas and deliverable CH_4 capacity.[35] As can be seen from Figure 1.4, substitution of extended octacarboxylate ligands in the MFM-180 (MFM: Manchester Framework Materials) structure has led to the development of MOFs with larger cages with improved surface areas, while the topology and structure of these MOFs remain intact. The surface area of the MOF with the most elongated ligand (MFM-185) has nearly doubled and the CH_4 deliverable capacity increased to 0.24 g g^{-1} and 163 vol/vol (298 K, 5–65 bar).

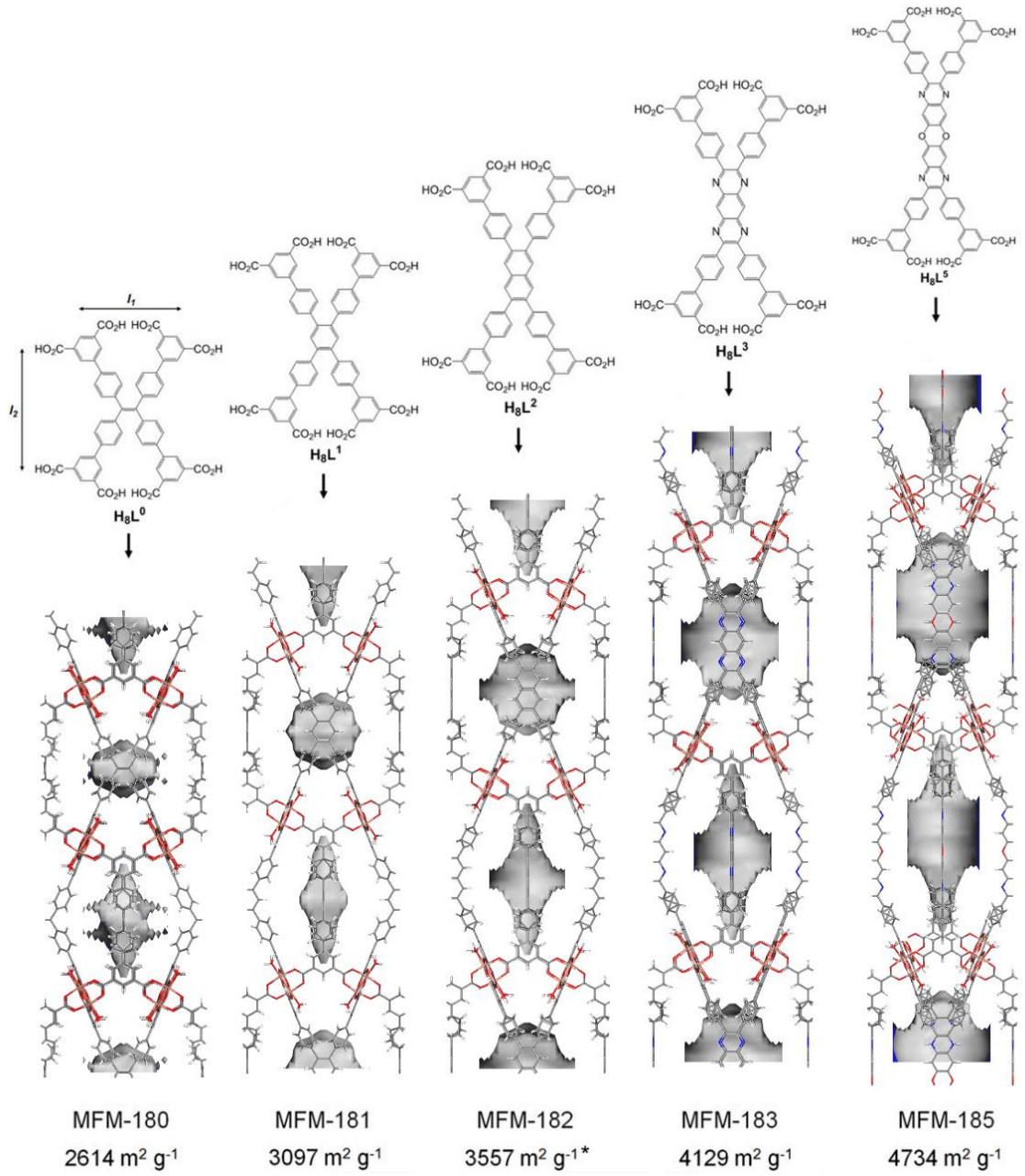

Figure 1.4 A series of isoreticular MOFs sharing the same topology and structures but different surface area and pore volumes.

Additionally, isoreticular approach allows for the design of MOFs with precise pore dimensions and favourable affinities by the right selection of organic linkers and metal ions so that they selectively adsorb specific guest molecules, while excluding other gases.[36-41] This unique ability also has led to significant improvements in design and development of MOFs with high thermal and physical stability compared to that of their parent MOF.[42-45]

By exposure to some certain stimuli, the structure of some MOFs can change. These frameworks that are referred to as flexible/dynamic MOFs are a unique subclass of these materials while other solid porous materials such as zeolites have a rigid frameworks. Mostly,

MOFs also have rigid frameworks and a similar properties to that of traditional inorganic porous solids, such as activated carbons and zeolites. Nonetheless, flexible/dynamic structures are specific to MOFs and they show interesting behaviour, especially during adsorption and adsorptive separations.[46-47] These structural transformations in flexible MOFs are generally seen during adsorption or desorption of guest molecules.

1.1.4 Design, synthesis, and potential applications of MOFs

The "design" of MOFs is somehow controversial, and it is hard to say a MOF has been rationally designed.[48] Conceptually speaking, MOFs are formed based on the direct connection of organic linker and inorganic nodes with specific coordination states and shapes.[49] This concept was applied in the early stages of this research area by Robson and others where they presented the "node and spacer" theory to form coordination polymers. Based on this approach, metal ions with a fixed coordination number and ligands with a certain coordination bond and connectivity, can enable synthesis of a coordination polymer with fixed shapes and linkage geometries.[50] This approach seems to be applicable for construction of a simple MOF to a certain extent (e.g., reaction of a tetrahedral node and a linear bridging linker offers a diamondoid shape coordination polymer), but when it comes to reality, it is more difficult to obtain the on-paper designed material, particularly when designing more complicated cases (for example, MOFs containing multiple ligands). The discussion of whether it is possible to rationally design a porous material is an ongoing question, and it even becomes more complicated when it comes to MOFs.[51] For example to synthesize a MOF under solvothermal conditions (the most common method of MOF synthesis), it may not be easy to control the formation of expected metal clusters or retain the single metal ion. Even in a simpler case where a single metal ion acts as node, it is quite possible that the metal forms various coordination geometries or different connectivities, which makes the prediction of the final product very difficult. The effects of solvent molecules and reaction temperature are other factors that need to be considered as they participate in the process of forming crystals.[52-53] Currently, MOFs are defined as materials that can be constructed by strong covalent bonds between metal-containing clusters (while assuming their formation can be controlled during MOF synthesis) which act as secondary building units (SBUs), and rigid organic moieties. Design seems to be absolutely practical in this sense.[54] Based on this approach, a MOF can be reproduced using an SBU with known coordination geometry and similar but new linkers. This "design" based on reticular approach, has assisted the evolution of the MOF field and led to a systematic design of the frameworks with the same topology and structure, and have enabled scientists to systematically explore the effects of various structural modification on a variety of MOFs

properties.[32] In another sense, "Design" can also be regarded as the ability of scientist to design an experiment to target a MOF that its topologies and pore characteristics are already anticipated,[54] or by designing organic linkers with the same linkage geometry to obtain a predetermined MOF.[55]

MOFs are commonly synthesized through self-assembly reaction of metal salts and organic ligands in a solution of one or more solvents at a temperature from room temperature to 300 °C in one pot. The desired products are crystalline solids precipitated (preferably large crystals for better X-ray diffraction) at the end of reactions. At near room temperatures, due to the slow diffusion of reactants in the solution and gradual evaporation of solvents, crystals can grow slowly and larger crystals might be obtained. At elevated temperatures and pressures, which is generally referred to as solvothermal synthesis, reaction times are normally less than room temperature reactions, but single crystals are still formed. Compared to reactions in room temperatures, the resultant products might be more complex and diverse at high temperatures. Another important factor that can control the reaction rate and purity of crystalline product is the pH value of the reaction solution. Also efforts have been made to drive the formation of the products kinetically rather than thermodynamically, even though this area has not studied largely. As a quick way of synthesizing a MOF, microwave-assisted techniques have been developed and has certainly offered several advantages in comparison to other MOF synthesis methods.[56] Other than using solvents, ionic liquids also have been used for the synthesis of MOFs. This method is termed as ionothermal synthesis and the ionic liquid serves both as a solvent and template during the formation of crystals.[57] Moreover, solvent-free synthesis has been developed and used for the synthesis of MOFs.[58] These methods are more convenient than former methods and largely cut down the environmental contamination. Apart from one-pot reactions, methods with a high degree of control but synthetically more complicated has been exploited through a stepwise method and using metal organic polyhedra acting as supramolecular building blocks.[59-60] MOFs also have been synthesized in nanoscale which have exhibited some outstanding characteristics.[61-62] Another notable concern in the synthesis of MOFs is formation of pure phase, as existence of other phases limits the determination of structure and full characterization. This might not be very simple in some cases; for instance, frameworks with various levels of interpenetration are usually difficult to be separated from each other. Moreover, to achieve the entire potential of MOFs full activation of samples are required to obtain empty and uniform pores which might sometimes be quite challenging, particularly for unstable or highly porous MOFs with strong guest-framework interactions. MOFs are generally activated by solvent exchange (washing with volatile solvents) followed by removing solvents and other guest molecules from pores by evacuation at elevated

temperatures. Besides this general methods, some advanced methods such as "density separation" for the purification and "supercritical CO_2 flowing" for activation of MOFs have been presented and performed.[63]

The scope of applications of MOFs is very broad. Due to their permanent porosity, diversity and tunable nature they have been exploited in a variety of different applications, such as catalysis,[64-66] magnetic materials,[67-68] luminescence,[69-70] wastewater treatments,[71-73] sensing,[74-75] biological systems,[76] non-linear optics,[77] electron[78-82] and proton[83-85] conduction, battery cathode materials,[86] photovoltaics,[87] semiconductors,[79, 87] guest inclusion,[8, 88-89] biomedical imaging,[62] drug delivery,[90-91] cancer therapy,[92] just to name a few areas. Gas separation is only a small portion of current research on MOFs. As the content of this thesis is about the ability of MOFs for gas separation, we further review this application in detail and readers are encouraged to go through the several reviews and monographs in the literatures for further information.

1.1.5 Method of characterizations

The direct determination of MOF structure is often performed by single-crystal X-ray diffraction, or in some cases by powder X-ray diffraction (PXRD). The latter also is employed to investigate the phase purity of the final product. Furthermore, gas adsorption experiments are used to establish the pore characteristics and guest-framework interactions of MOFs. Other tools such as nuclear magnetic resonance (NMR) of either acid-digested materials or in-tact solids, thermogravimetric analyses (TGA), infrared spectroscopy, and elemental analysis, also are frequently employed to characterize the structure of MOFs. Here, two methods of crystallography and gas adsorption are discussed in more detail.

1.1.5.1 Crystallography

Crystallographic structural data is perhaps the most utilized and powerful tool for characterizing MOFs. X-ray crystallography is the most common technique exploited for determination of the position of atoms and molecular structure of a crystal, where a beam of X-rays is diffracted to different specific direction after exposure to the crystalline structure. A 3D picture of the density of electrons within the crystal can be then obtained by measuring the angles and intensities of these diffracted beams. From this electron density, the mean positions of the atoms in the crystal can be determined, as well as their chemical bonds, their crystallographic disorder, and various other information. Another technique that has been used is neutron diffraction or elastic neutron scattering which is the application

of neutron scattering to the determination of the atomic and/or magnetic structure of a material.

A sample to be examined is placed in a beam of thermal or cold neutrons to obtain a diffraction pattern that provides information of the structure of the material. The technique is similar to X-ray diffraction but due to their different scattering properties, neutrons and X-rays provide complementary information: X-Rays are suited for superficial analysis, strong X-rays from synchrotron radiation are suited for shallow depths or thin specimens, while neutrons having high penetration depth are suited for bulk samples. From structural data, many properties, such as surface functionality, density, and surface area can be determined. Without these results, drawing conclusions about the origin of material behaviour towards guest molecules is challenging. Due to the modular nature of metal-organic frameworks, often powder diffraction patterns are sufficient to confirm that a new material is isostructural to a previously documented structure. Figure 1.5 indicates the structure of some well-known MOFs determined by single-crystal X-ray diffraction.

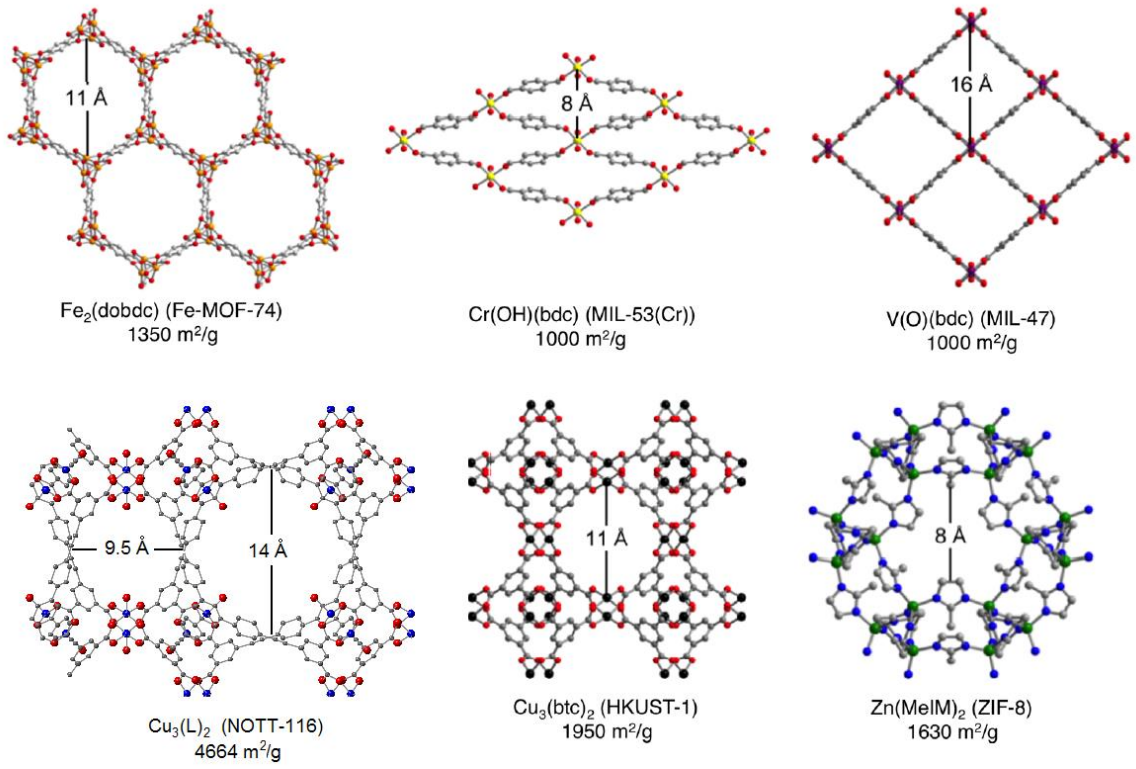

Figure 1.5 Crystallographic structure, molecular formula, common name, BET surface area, and centroid-centroid pore diameters for some well-known MOFs determined from single-crystal X-ray diffraction technique. Color code: Green, red, gray, yellow, purple, orange, dark red, and blue correspond to Zn, O, C, Cr, V, Fe, Cu, and N, respectively.

1.1.5.2 Gas adsorption

Gas sorption measurement has been employed to characterize MOFs in two senses: calculation of the surface area and pore volume, and the adsorption capacity and adsorption strength of different guest molecules. Usually, a N_2 adsorption isotherm at 77 K is used to measure surface area and pore volume using different methods such as Brunauer-Emmett-Teller (BET) and Langmuir method.[93-94] For example, the BET theory applies to systems of multilayer adsorption and usually utilizes probing gases that do not chemically react with material surfaces as adsorbates to quantify specific surface area. Based on this theory, adsorption occurs in a flat surface, while there is no interaction between adsorbate molecules in adjacent sites and they only interact with adjacent layers. These monolayers are covered by gas molecules until there is no space for incoming gas molecules.[93] A schematic of adsorption based on BET model is presented in Figure 1.6. A functional description of this method is presented in the BET section of this chapter.

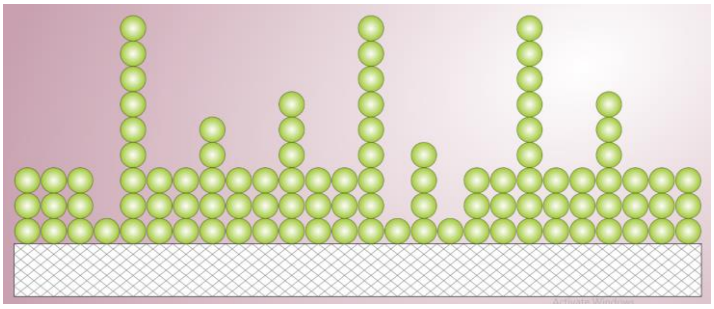

Figure 1.6 BET model of multilayer adsorption, that is, a random distribution of sites covered by one, two, three, etc., adsorbate molecules.

In the case of a MOF with smaller pore diameter than kinetic diameter of N_2, an argon isotherm at 87 K or CO_2 isotherm at 195 K can be alternatively used. In particular, surface area measurements are quite useful to establish the phase purity of a MOF. PXRD only can confirm the presence of an anticipated phase, and the existence of amorphous dense phases or other unwanted phases which are formed during MOF synthesis is not confirmed or denied. Elemental analyses and thermogravimetry are other methods that can be used to check the phase purity of a MOF, but they are also usually difficult to be interpreted in MOFs because of the existence of solvent molecules within the pores. Phase purity of a MOF can often be confirmed by matching the value of measured surface area and the surface area predicted from the crystallographic structural data (or the same samples that their surface area is previously determined). Storage and gas separation is one of the most promising applications of MOFs.[95] Hydrogen[93] and methane[96] storage by MOFs has direct impact on to emissions of less CO_2 to the environment, while separation of CO_2 from N_2 by MOFs

lead to the development of materials that can simply be placed to the exhaust streams of power plants to reduce the emissions of CO_2 into the environment.[97] Adsorption of these gases can be measured volumetrically, resulting in a further evaluation of MOFs for any gas separation application. Besides, adsorption isotherms at different temperatures can be used to determine the adsorption strength by fitting them to the Clausius-Clapeyron equation.[98]

1.2 Adsorptive gas separations

1.2.1 Essentials of adsorption phenomena

Generally, the surface of any solid is not smooth, and the forces acting in the surface are not saturated. Thus, upon exposure to a gas, a bond between surface and gas molecules are formed. This phenomenon is called *adsorption*. Based on the nature of interaction between the adsorbate molecules and solid surface, adsorption can be classified as physical adsorption or chemical adsorption (also called as chemisorption). Chemical adsorption involves electron transfer between the atoms of adsorbate and adsorbent, and is basically a two-dimensional chemical reaction (referred as covalent bonds). Chemical adsorption is not reversible, thus it is not often encountered largely in gas separation processes.[99] Therefore, this type of adsorption is not focused here.

In contrast to chemical adsorption, the bonds in physical adsorptions are held by electrostatic interactions including dipolar and Coulombic forces, and these forces are much weaker compared to chemical adsorptions (30-50 kJ/mol).[99] Coulombic forces are repulsive or attractive interactions between two ions (partial charges) because of their electric charges. In the context of MOF-guest system, this interaction only exists between highly polar molecules and highly polar surfaces, such as MOFs with open metal sites. These are the strongest intermolecular forces defined based on Coulomb's law. Polar covalent atoms/molecules are sometimes described as "dipoles", meaning that the molecule has two "poles". One end (pole) of the molecule has a partial positive charge while the other end has a partial negative charge. These molecules can orientate themselves so that they interact with the polar surface of the adsorbent favourably and create attractive force called dipolar interactions. These interactions can be categorized into dipole-dipole, induce dipole- dipole, and dispersive (London) interactions.[21, 100] The latter largely exist in MOF adsorption systems and arise from the rapid fluctuation of electron density in each atom of adsorbate molecules, which induce an electrical moment in neighbouring atoms on the surface of adsorbent, and thus generate an attractive or repulsive force between them.[99] A schematic of dispersive interactions between hydrogen atoms of ethane molecules and the rhombic cavity of aromatic rings in MOF $Cu(Qc)_2$ are presented in Figure 1.7.[37]

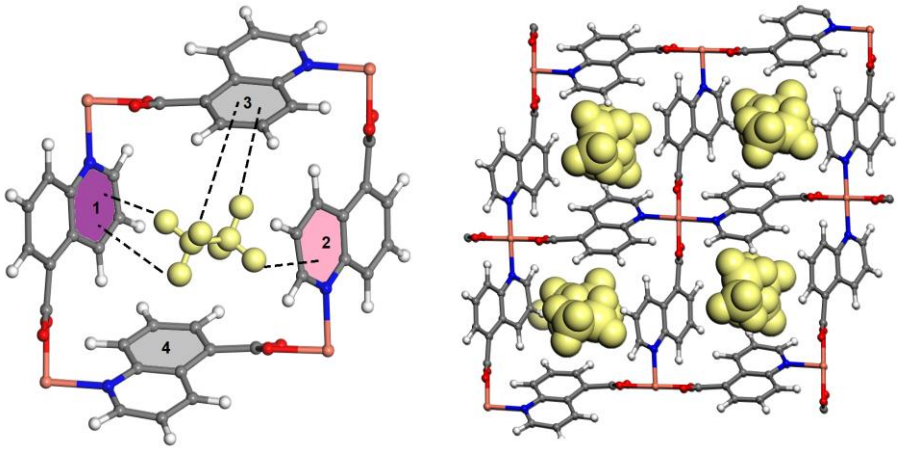

Figure 1.7 (a) Dispersive interaction between hydrogen atoms of ethane molecules and the rhombic cavity of aromatic rings in $Cu(Qc)_2$. (b) The highly packed accommodation of ethane molecules in the pores of $Cu(Qc)_2$ held by dispersive forces.

For a given solid-gas system, the amount of gas adsorbed at equilibrium is described as a function of pressure at a constant temperature, which is called an *adsorption isotherm*. The great majority of the isotherms observed to date, can be classified into six types, as demonstrated in Figure 1.8.[99, 101] Types I and II are the most frequently observed isotherms in separation processes. In the context of MOFs, Type IV is also encountered frequently in flexible MOFs.

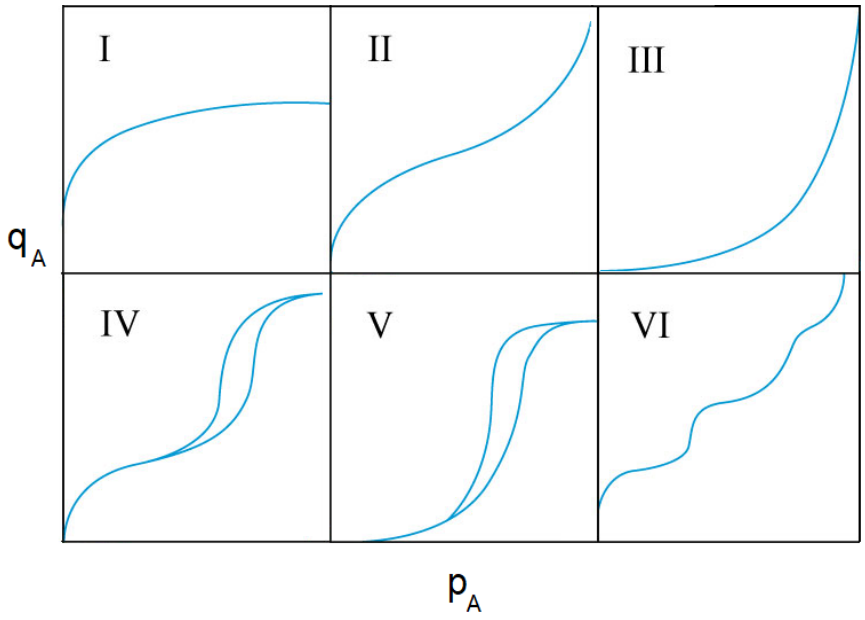

Figure 1.8 The five types of adsorption isotherms according to the BDDT classification.[101] q_A and p_A are the concentration of adsorbate in solid phase (adsorption uptake) and partial pressure of adsorbate in gas phase, respectively.

Numerous theories have been developed to interpret these different types of isotherms, of which three of them have been widely employed in adsorption systems: The Langmuir approach, the Gibbs approach and the potential theory. These approaches have presented various model to define these isotherms, such as Langmuir, Freundlich, combination of Langmuir and Freundlich, BET, Temkin and so on.[99]

1.2.2 Adsorptive gas separation technology

Gas separation techniques include a broad area ranging from membrane-based, absorption-based and adsorption-based technologies to cryogenic distillation.[20, 102-103] Shortly after the evolution of synthetically-prepared zeolites in the 1940s followed by the emergence of a number of different adsorbents and the progress in adsorption-based separation technologies, adsorptive separation has become one of the leading technologies for separating gases.[21, 99, 104] With the development of a significant number of new adsorbents with various functionalities, tailored porosity and exceptional properties and the increasing demand for environmental-friendly separation processes, adsorption-based separation has gained great attention in the gas separation industry. Hence, adsorption-based separation will likely play an important role in the future of energy and green technologies.[20, 99, 105] Among numerous gas separation application performed by adsorption-based processes, noticeable examples are purification of H_2 and CH_4, CO_2 capture, natural gas and biofuel upgrading, sulfur removal from transportation fuels, CO removal in fuel cell industry and other technologies that can greatly help to having a clean and energy efficient environment. Numerous monographs and reviews on adsorptive separation for these gas systems have been published.[99, 104-110]

In concept, adsorption-based gas separations can be classified into two types: purification and bulk separation. Purification implies the adsorption of an small quantity of impurities from a gas stream (generally less than 2 wt%), while the latter involves the adsorption of a notable amount of gas stream (usually 10 wt%).[20] In a typival adsorptive gas separation process, a gas mixture passes through a column filled with sorbents to produce a stream which is rich in weakly-adsorbed compound. As an example, a MOF with a highly polar pore surface can be packed into an adsorption column to produce pure N_2 from a mixture of CO_2/N_2 by adsorbing highly polar CO_2 molecules (Figure 1.9).

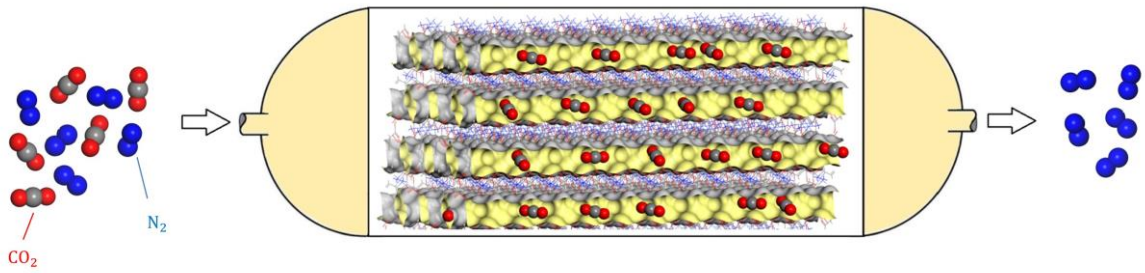

Figure 1.9 Schematic of an adsorption bed packed with MOF for separating CO_2 from N_2.

In adsorptive gas separation systems, the separation is usually achieved based on the ability of the adsorbent to recognize different species in the gas mixture. The performance of any adsorption-based separation is directly governed by the characteristics of both adsorbate and adsorbent. Based on these characteristics, separation can be achieved based on three mechanisms. Separation due to the difference in equilibrium capacity of species, difference in kinetics of adsorption, and difference in size of adsorbates (molecular sieving).[111-113] To better understand these mechanisms, schematic of the journey of a single CO_2 molecule from bulk gas to adsorption site in a MOF (Mg-MOF-74) is illustrated in Figure 1.10.

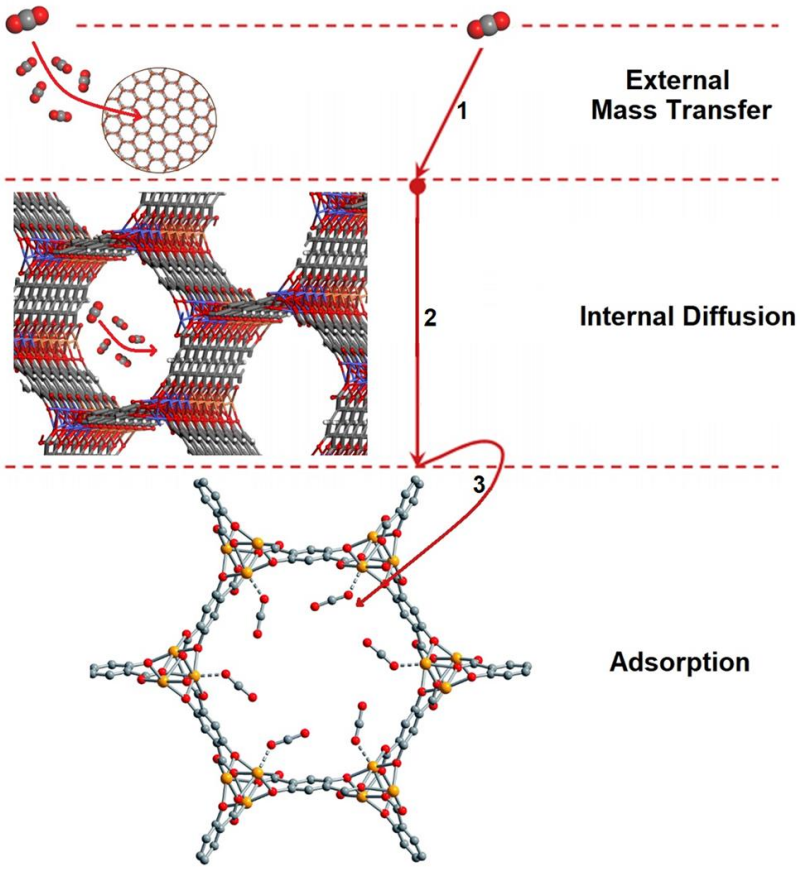

Figure 1.10 Typical steps of adsorption in a MOF (Mg-MOF-74): 1, diffusing through bulk gas to the external surface of MOF; 2, diffusing through the internal pores of the MOF to the adsorption site; 3, adsorption to the MOF.

Firstly, an adsorbate molecule in the bulk fluid phase diffuses through the bulk gas mixture to the external surfaces of the MOF (1), then it diffuses through the internal pores of the MOF, to the adsorption site (2), being adsorbed to the adsorption site (3). Now, in adsorptive gas separation based on the difference in equilibrium adsorption capacity, step 3 is the governing step. Both gases are given enough time to reach the adsorption site, but only one of them adsorbed strongly. In kinetic separation, step 1 and 2 controls the separation. Adsorption takes place as one of the species reach the adsorption site faster than the other one. And finally in size-based separation, step 2 dictate the efficiency of adsorption. Generally the pores are small enough that the larger molecule cannot get into the pores.

Because of the reversible nature of physical adsorption, adsorption processes can be designed in continuous cycles, in which the adsorbents are regenerated by desorbing the strongly-adsorbed component and reusing for the next cycle.[20] A number of different cyclic adsorption processes are developed based on the way of regenerating the adsorbent, such as pressure swing adsorption (PSA) processes, thermal swing adsorption (TSA) processes, vacuum swing adsorption (VSA) processes, inert purge cycles, and so on. Among these methods, PSA and TSA have been widely used in adsorptive gas separation processes. In a conventional PSA, desorption is performed by reducing the partial pressures of the strongly-adsorbed compound in the gas phase. It is usually carried out by either decreasing the total pressure of adsorption column or by recycling a portion of the product stream to the adsorption column around room temperatures, while in a TSA cycle, desorption is achieved by heating the adsorption column with either a portion of the feed stream or gas product at around atmospheric pressure. TSA cycles are often employed for gas purification purposes, whereas bulk separation is achieved by PSA.[99] Figure 1.11 shows a simplified and idealized schematic of PSA, TSA and VSA processes for CO_2 removal from natural gas (CH_4).

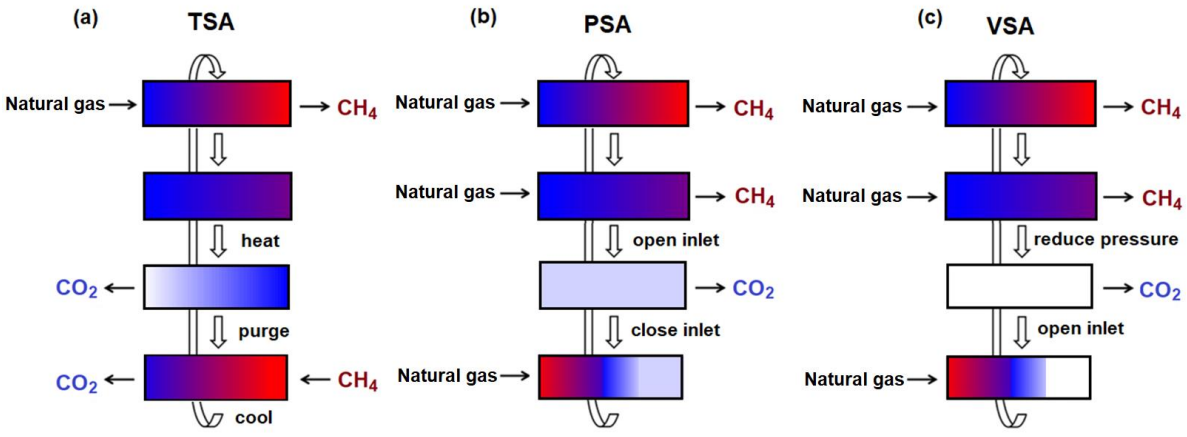

Figure 1.11 Schematic illustrations of simplified and idealized (a) TSA, (b) PSA, and (c) VSA cycles employed for the removal of CO_2 from natural gas.

In the first two stages of all of these three processes, a mixture of CH_4 and CO_2 passes through an adsorption column and CO_2 is captured by the bed, producing pure methane in the effluent. The captured CO_2 is then removed from the bed by heating and purging (usually with CH_4), pressure reduction and leaving the bed under vacuum in a TSA, PSA and VSA process, respectively. The bed will be cooled in TSA or pressurized in PSA/VSA processes to get ready for the next adsorption cycle.

Together with an acceptable mechanical strength and high adsorption capacity and selectivity, a promising adsorbent must be regenerable at reasonably mild operational conditions and have a favourable adsorption kinetics. To satisfy these requirements, firstly an adsorbent should possesses a relatively high surface area as well as a favourable pore characteristics to recognize different gases in the mixtures. As a good examples of these adsorbents, zeolites with their stable structures and uniform and somewhat tunable pores, have played important roles in the progress of adsorption-based processes and have been vastly exploited in industrial separation.[114-115] Notably, in practical adsorption-based separation, adsorbents are often pelletized into different shapes using a binder (usually a polymer) which not only improve the mechanical strength of adsorbents, but also reduce the pressure drop in adsorption columns. These polymeric diluents also facilitate the transfer of guest molecules from the gas stream to the adsorption sites by generating mesoporous or macroporous structures.[116]

1.2.3 Metrics for MOF evaluation

Different metrics are defined to evaluate separation performance of adsorbent (here MOFs), including adsorption isotherm, working capacity, recovery, adsorption kinetics, recovery, productivity, purity and breakthrough curves, which are discussed briefly here.

1.2.3.1 Adsorption isotherm

Adsorption isotherm is probably the most basic metric that provides information about the separation performance of a MOF. These information are mainly adsorption capacity, shape of isotherm, and steepness of isotherm. Adsorption capacity is the amount of gas, an adsorbent can take up before it become saturated. MOFs with high capacity are favourable in adsorption-based separations, as less amount of MOFs are required to produce a certain amount of a purified gas. Shape of isotherm also provides useful information about the mechanism of adsorption and thus the separation medium of any MOFs. For example flexible MOFs can be recognized based on the shape of their isotherms and they have been

vastly served for gas separation applications. Long and co-workers reported a series of MOFs with "phase changing" behaviour.[117] This behaviour was first recognized based on the unusual shape of their CO_2 isotherms (Figure 1.12)

These MOFs were then exploited for TSA processes, as they possess high working capacity and the temperature gap for adsorption and desorption are small so that the energy penalty for sorbent regeneration is low. The other precious information that can be obtained from isotherms is the adsorption strength of a particular adsorbate-MOF system. The steepness of an adsorption isotherm (Langmuir shape) is direct evidence of how strongly an adsorbate is adsorbed on the surface of a MOF. Isotherms with a steep shape at low pressure imply a strong interaction between adsorbate and MOF, while Henry (linear) isotherms typically indicate weak interactions.

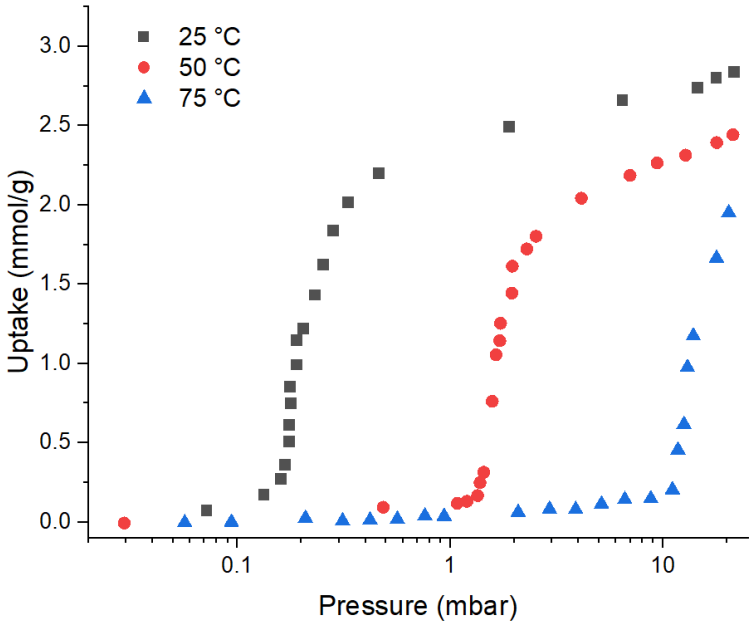

Figure 1.12 Adsorption isotherm of CO_2 on mmen-MOF-74 at different temperatures, showing a phase change at low pressures. The adsorbent shows negligible amount of adsorption at low pressure, followed by a steep jump showing the adsorption of CO_2 molecules by adsorbent. Data are extracted using a digitizer software from[117].

1.2.3.2 Selectivity

Selectivity is another crucial metric for determining the separation performance of a MOF. It is defined as the ability of a MOF to selectively adsorb one component over other components in a gas mixture. Different methods have been developed to obtain the selectivity of an adsorbent for different components in a gas mixture, but they mainly use single gas adsorption isotherms to predict the mixture adsorption isotherms, i.e, the adsorption uptake of one component in the presence of other components in the mixture.

There are two commonly used methods for determining selectivity in MOFs field. Selectivity defined as the ratio of Henry constants: In this method, Henry constants for different components can be simply obtained from the slope of their single adsorption isotherms at low pressure region and selectivity is calculated by dividing the Henry constant of strongly adsorbed component to weakly adsorbed one. Selectivity based on Ideal Adsorbed Solution Theory (IAST) proposed by Myers and Prausnitz:[99, 118]

The equation used to determine selectivity of component 1 over component 2 is:

$$S_{1,2} = \frac{q_1/p_1}{q_2/p_2} \quad (1)$$

Where, q is the adsorption uptake in the mixture and p is the partial pressure. q_1 and q_2 are obtained from IAST theory (see the last section of this chapter for further details of this method). A functional description of this method along with an example are presented in IAST section of this chapter.

There is frequently a trade-off between selectivity and adsorption capacity in adsorbent materials. Usually, high adsorption capacities arise from large pores which cannot discriminate between molecules of similar sizes, thus leading to a substantial decrease of selectivity. On the other hand, to boost the selectivity, pores are designed to only allow the passage of small guest molecules and block the larger ones, which in turn lead to low pore volumes and thus low uptake capacities. So design of adsorbent, which can accommodate large amount of guest molecules, while at the same time exhibiting good selectivity is one of the greatest challenge in the development of adsorbents.

1.2.3.3 Working capacity

Working capacity is another metric that can determine the performance of a MOF for adsorption-based separations. It mainly plays a key role in the design of cyclic adsorption processes. In PSA processes it is defined as the difference between the adsorption uptake of an adsorbent at adsorption stage pressure (high pressures) and adsorption uptakes at desorption stage (low pressures). On the other hand, in TSA processes, it is defined as the adsorption uptake of an adsorbent at adsorption stage temperature (low temperatures) and adsorption uptakes at desorption stage (high temperatures). The higher working capacity guarantees the efficiency of a cyclic adsorption processes, as the temperature/pressure swing are quite small so the required energy for regeneration is low for a certain amount of purified product.

1.2.3.4 Productivity

Productivity is a criterion for estimating the total amount of purified product by certain amount of adsorbent during a certain duration. For example, for a PSA unit, which produces component *i* and a portion of product *i* is used for purging, it can be defined as the sum of the amount of produced product during adsorption and blowdown stage minus the amount of product used for purging, per amount of adsorbent and duration of processes.

$$Productivity_i = \frac{\int_0^{t_{AD}} F_{i,out}\, dt + \int_0^{t_{BD}} F_{i,out}\, dt - \int_0^{t_{PU}} F_{i,in}\, dt}{Mass\ of\ adsorbent \times t_{AD+BD+PU}} \quad (2)$$

Where, AD, BD and PU are indicator of adsorption, blowdown and purging stage in PSA processes and F_i is the flowrate of component *i*. Productivity is an important criterion especially for the design of adsorption units, as it gives information about how fast a product can be produced and how much adsorbent is required.

In the context of MOF, another simplified definition has been used for the productivity based on a single adsorption stage as below:[37, 119-120]

$$Productivity = \frac{\int_{t_1}^{t_2} F_{product,out}\, dt}{m_{MOF}} \quad (3)$$

Here, productivity is simply the amount of produced product per amount of adsorbent during adsorption stage. It should be noted that the time required for producing a certain amount of product is not considered in this definition.

1.2.3.5 Heat of adsorption

The heat of adsorption is an indicator of the strength of the interaction between an adsorbate and a solid adsorbent. This parameter can be determined from the heat released in calorimetric experiments or from the analysis of adsorption isotherms at different temperatures. The latter, called isosteric heats of adsorption, are commonly used in the characterization of materials for gas-phase adsorption.[121]

The isosteric heats of adsorption of the components of a gas mixture are key thermodynamic variables for design of practical gas separation processes such as pressure

swing and thermal swing adsorption. They determine the extents of adsorbent temperature changes within the adsorber during the adsorption (exothermic) and desorption (endothermic) steps of the processes. The adsorbent temperature is a key variable in determining the local adsorption equilibria and kinetics on the adsorbent, which ultimately govern the separation performance of the processes.[99]

To calculate isosteric heat of adsorption, isotherm data are collected at very low pressure to follow the adsorption mechanism. Analyses are performed at different temperatures, thus, different adsorption isotherms are obtained, from which adsorption isobars are plotted. Then the Clausius-Clapeyron equation is applied to obtain the Isosteric heat of adsorption as a function of the degree of coverage.[122] These equations and a brief instruction for calculation of heat of adsorption is presented in Section 1.4.

1.2.3.6 Breakthrough curves

Adsorption is a transient process. The amount of material adsorbed within a bed depends both on position and time. Considering time dependence, as fluid enters the bed, it comes in contact with the first few layers of absorbent. Adsorbates are adsorbed, filling up some of the available sites. Soon, the adsorbent near the entrance is saturated and the fluid penetrates farther into the bed before all adsorbates are adsorbed. Thus the active region shifts down through the bed as time goes on until bed is fully saturated and the concentration of the adsorbed gas starts to breakthrough into the effluent. This concentration variation versus time in the effluent is called a breakthrough curve and is one of the most important results of a dynamic experiment under forced flow conditions on a fixed bed. For a gas mixture passing through an adsorption column, this curve indicates the period in which adsorption column can efficiently produce the desired product with acceptable purity (mainly the weakly adsorbed component) and often is the main metric for the design of adsorption columns. A schematic of a breakthrough curves are presented in Figure 1.13.

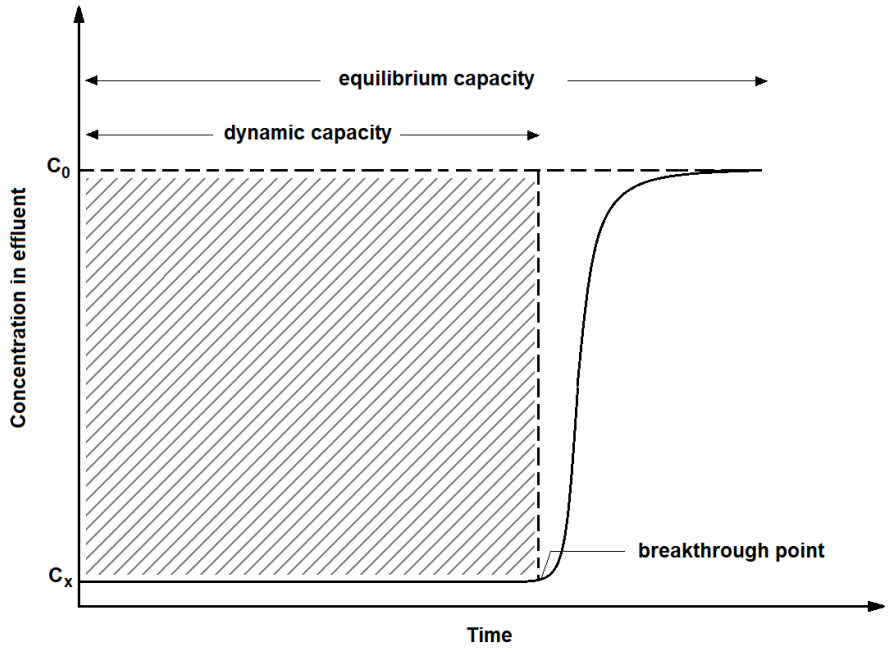

Figure 1.13 Schematic representation of breakthrough curve.

Integration of the area above the entire breakthrough curve gives the maximum capacity of the adsorptive material which is equal to equilibrium capacity. Additionally, the duration of the breakthrough experiment until a certain threshold of the adsorptive concentration at the outlet can be measured (breakthrough point), which enables the calculation of a technically usable sorption capacity (often called dynamic capacity). Up to this time, the quality of the product stream can be maintained. Considering the position dependence, in any particular time during the breakthrough test, three zones in the adsorption bed can be observed: Saturated zone, mass transfer zone and unused length of the bed.[99] A schematic of an adsorption column with three distinct zone is presented in Figure 1.14.

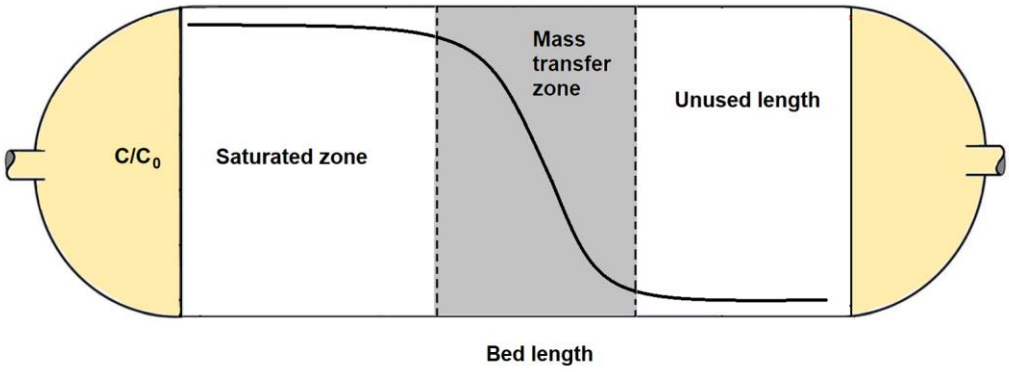

Figure 1.14 Schematic of an adsorption column with three zones.

The saturated zone is the area that is already has been saturated with adsorbates and no more adsorption takes place. Mass transfer zone is the active area in the adsorption column where adsorbates are being adsorbed. The wave front may change shape as it moves through the bed, and the mass transfer zone may broaden or diminish. Unfavourable and linear isotherms tend to broaden while favourable Langmuir and Freundlich isotherms may broaden at first, but quickly achieve a *constant pattern front.*[99] This means that the mass transfer zone is constant with respect to both position and time. The shape of the mass transfer zone depends on the adsorption isotherm (equilibrium expression), flow rate, and the diffusion characteristics. Usually, the shape must be determined experimentally. The last zone in the adsorption column is the unused part of the bed, where it does not go under adsorption. Before the wave front reaches this zone, the adsorption process is switched to the next stage. This parameter is often calculated and added to the effective length of the bed during adsorption bed design calculations.[99]

Since almost all adsorptive separation processes are dynamic, i.e., they are running under flow, testing porous materials for those applications for their separation performance has to be tested under flow as well. Hence, the most realistic metric to evaluate the separation performance of an adsorbent is breakthrough test. Apart from its dynamic nature, a breakthrough curve is an interplay of different kinetic and thermodynamic effects. The sorption capacity, selectivity, release and transfer of heat as well as the sorption rate, inlet concentration and gas velocity play a key role during the dynamic sorption process and influence the position and shape of the breakthrough curve considerably.[99]

The adsorption capacity has a big impact on the position of the breakthrough curve. By increasing the sorption capacity, the breakthrough curve will be shifted to longer breakthrough times (to the right), because more adsorbate molecules will be held back by the adsorbent. This is not the case if the sorption kinetics on the sample is too slow and a spontaneous breakthrough occurs.[99] In contrast to the sorption capacity, the sorption kinetics affect the shape of the breakthrough curve. For faster kinetics the breakthrough curve becomes steeper (sharper) and the mass transfer zone will be smaller. A fast mass transfer from the gas phase to the adsorption sites leads to short local equilibrium times and therefore for a smaller enlargement of the concentration front.[99] In some cases this relationship will be compensated by other phenomena, i.e. the release of heat by adsorption. An increasing sample temperature leads to a flatter, more asymmetric breakthrough curve. This effect can be a major factor in the expansion of the mass transfer zone.[99]

A fourth parameter is the axial dispersion, which is responsible for the broadening of the mass transfer zone. This parameter is also responsible for an increasing asymmetric character of the breakthrough curves.[99] Contrary to this effect, the curvature of the corresponding

isotherm can have effects on the shape of breakthrough curves as well. A type I isotherm leads to smaller mass transfer zones during adsorption. The desorption curve is broadened in such cases. The opposite can be observed for type III and type V isotherms.

It is clear that a simple distinction between the individual influences is hard to observe. Here simulations with mass and energy balances may help for a better understanding of the whole dynamic process. (see breakthrough curves simulation section in this chapter for further details).

To measure a breakthrough curve, a fixed bed of porous materials is pressurized and purged with a carrier gas. After becoming stationary, one or more adsorptives are added to the carrier gas, resulting in a step-wise change of the inlet concentration. The effluent concentration can be read over time by gas chromatography or mass spectrometry to obtain breakthrough curves. A schematic of breakthrough apparatus is provided in breakthrough section of this chapter. In the case of a gas mixture with two adsorptives, passing through an adsorption column, the area between the breakthrough point of the weakly adsorbed and highly adsorbed adsorptive is the amount of purified product (Figure 1.15).

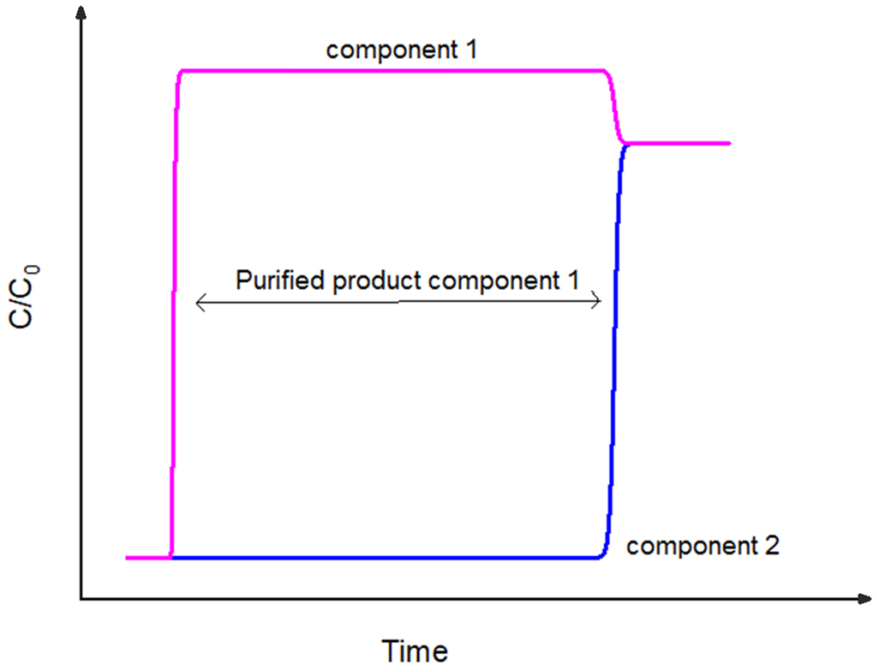

Figure 1.15 Schematic of a separation of a mixture of two gases shown by breakthrough curves. The area between the breakthrough point of the weakly adsorbed and highly adsorbed adsorptive is the amount of purified product

1.2.4 Metal-organic frameworks for adsorptive gas separations

Separation and purification processes account for almost half of energy consumption in industrial processes, which highlight the critical role of separation processes in modern

chemical industry for producing pure compounds from chemical mixtures.[123] Industrial gas separations, including natural gas processing and hydrocarbon separations, are vastly demanding in the production of bulk chemical products for manufacturing fuels, plastics and polymers[124-126]. Traditional gas separation techniques such as distillation or absorption are highly energy demanding and require huge capital cost. During distillation, gas mixture goes under repetitive evaporation-condensation cycle under harsh conditions, while the regeneration of liquid absorbent requires substantial amount of heat and energy.[127] Conversely, non-thermal separation alternatives, including adsorption-based and membrane technologies, taking the advantage of different chemical affinity and molecular size of species in the gas mixture, have been developed and employed as more energy efficient technologies.[99, 116, 128] For instance, energy consumption of membrane-based separation technologies is about 10% of that of distillation processes.[129] However, the efficiency of these developing technologies is highly dependent on the internal porosity and pore characteristic of porous solids because of their significant role in gas adsorption. In comparison to traditional porous solids like zeolites and carbon-based materials, MOFs are a new class of porous materials with customizable pore structure and functionality. MOFs can be synthesized straightforwardly through a self-assembly reaction between organic ligands and metal ions/clusters.[130-133] In contrast to zeolite which are mainly formed by tetrahedra SiO_4 connecting to each other by O_2/OH linkages, the countless combinations of numerous metal clusters and organic linkers for construction of MOFs have resulted in a vast library of these materials with different structures, porosity and functionalities. MOFs are unique in terms of their tunable pore size, uniform pore architecture, high porosity, high crystallinity, and customized/designable structures. More interestingly, the dimension and functionality of the pores within MOFs can be systematically tuned by proper selection and functionalization of organic ligands of different lengths and chemistry.[134-137] A selection of some important gas separation applications of MOFs that are within the scope of this thesis will be briefly introduced here.

1.3 Selected gas separation applications using metal-organic frameworks

MOFs have been extensively exploited for a variety of different gas mixture separations. Readers are referred to different reviews and monographs in the literatures for further information. In this thesis, the application of MOFs for C_2H_6/C_2H_4, C_2H_2/C_2H_4, C_2H_2/CO_2, CO_2/CH_4 and CO_2/N_2 separations will be discussed in details in the following chapters. Here as an example, the recent advances on the application of MOFs for carbon captures processes will be discussed briefly.

1.3.1 Carbon capture

Combustion of fossil fuels to generate electricity and power has undoubtedly emitted large amounts of CO_2 into the atmosphere which underlies the greenhouse effect and subsequent temperature increases.[138] Current technology for CO_2 capture involves absorption of CO_2 using wet amine chemisorptions such as primary and secondary alkyl because of their large capacity and high selectivity for acidic gas.[139-140] However, employments of these technologies is associated with several drawbacks including high energy consumption during the regeneration, solvent loss due to the degradation and evaporation, and corrosive nature of amines.[138, 141] Amongst alternative techniques that have lower energy requirements and operating costs, the adsorption of carbon dioxide into porous materials is very attractive. MOFs are porous, crystalline materials built up using metal ions and organic ligands. They can be systematically designed with desired pore metrics, which in turn leads to tailored host−guest interactions. Carbon capture processes using MOFs are generally categorized into four types: post-combustion capture, pre-combustion capture, oxy-fuel combustion, and direct capture from air.

1.3.1.1 Post-combustion CO_2 capture

The flue gas exhausting from current power plants is mostly composed of N_2 (72–78%) and CO_2 (14–15%), at atmospheric total pressure. After removing SOx, the temperature of flue gas is increased to 40-60 °C because of exposure to CO_2 scrubber which is operated at these temperatures.[138] Hence, post-combustion carbon capture is performed at 40 °C or higher for separating CO_2 from a N_2-rich stream containing ~15% CO_2. In the context of adsorption-based separation using MOFs, Mg-MOF-74 is remarkable because of its high CO_2 uptakes due to the pores decorated with a high density of open metal sites (5.28 mmol/g at 40 °C and 0.15 bar).[4, 142] However, it loses its CO_2 capacity in the presence of water molecules as water molecules largely occupy the open sites. As there is a considerable amount of water vapour (5– 7%) in flue gas, it is essential to develop MOFs with appreciable CO_2 adsorption in the presence of water. Different attempts were made to overcome this issue, including introduction of alkylamines into MOFs structure to mimic CO_2 absorption behaviour in alkanoamine solvents.[143-145] Long and co-workers developed a functionalized Mg-MOF-74 by incorporating N,N'-dimethylethylenediamine (mmen) into the open metal sites.[144] Mmen molecules coordinate to open metal sites from one end and the other end interacts with CO_2 molecules (Figure 1.16a).

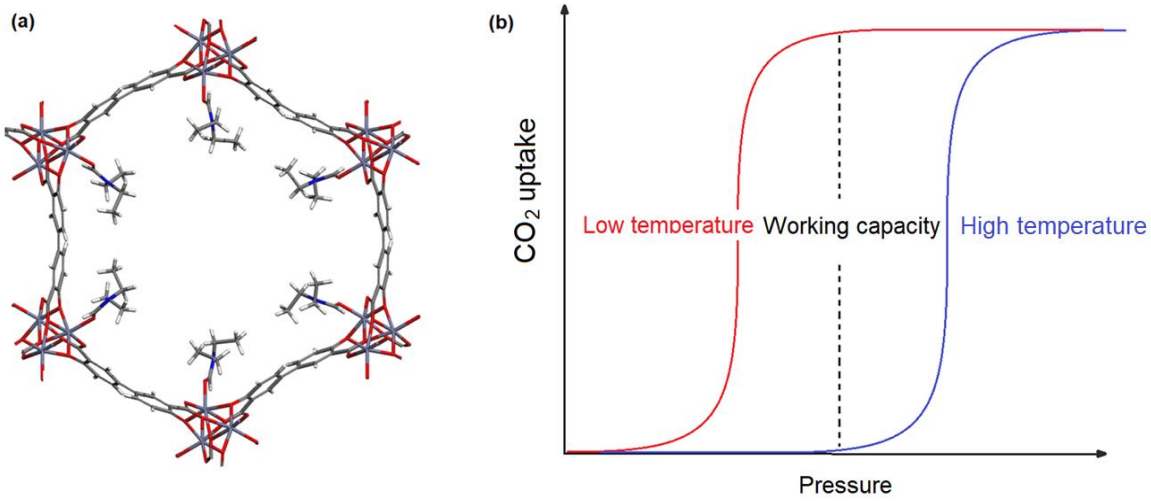

Figure 1.16 (a) Structure of the Mg-MOF-74 appended with mmen molecules. Color code: gray (carbon), red (oxygen), and green (magnesium). (b) Idealized adsorption isotherms of CO_2 at different temperatures in phase-change adsorbent.

Mmen-Mg-MOF-74 shows a high selectivity for CO_2 even in the presence of water, which stems from high density of amine groups within the pores. Besides, this functionalized MOFs show a unique CO_2 adsorption behaviour by a near zero adsorption of CO_2 at low pressure regions followed by a steep step at elevated pressure. Diffraction and spectroscopic studies revealed that this abrupt jump in adsorption capacity of CO_2 is attributed to a cooperative CO_2 insertion mechanism that involves a chemical reaction of the adsorbed CO_2. More interestingly, this phase-change pressure can be tuned by varying temperature and type of metals in the cluster, resulting in an unprecedented CO_2 working capacity with a relatively slight temperature swing (Figure 1.16b).[117]

Works on development of other alkylamines into structure of Mg-MOF-74 were also presented subsequently.[146-150] Besides MOFs with incorporated amine groups in open metal sites, different works have been done to functionalize MOFs with other functional groups. For instance, it was revealed that monodentate hydroxide can react strongly and reversibly with CO_2 molecules in a MOF called MAF-X27 ($[Co^{II}Co^{III}(OH)Cl_2(bbta)]$, H_2bbta = 1H, 5H-benzo (1,2-d:4,5-d′) bistriazole, MAF = metal azolate framework) through formation and decomposition of bicarbonate, enabling selective adsorption of CO_2 even in presence of water.[151] Another group of MOFs, SIFSIX-3-M (M = Cu, Zn, Ni), were also developed with optimal pore sizes and suitable decoration of inorganic anions to enhance the affinity of framework with CO_2. Although these MOFs adsorb CO_2 through physical interactions, still a good selectivity for CO_2 at humid conditions was achieved.[40, 152-153]

1.3.1.2 Pre-combustion CO_2 capture

CO_2 can be alternatively removed before fuel combustion. In pre-combustion CO_2 capture processes, fuel is firstly decarbonized through gasification processes and then resultant clean fuel is combusted, which results in near zero carbon dioxide emission during the combustion. As a result of coal gasification, a gas mixture, containing H_2, CO, CO_2, and water vapour is produced at high pressures and temperatures.[154] This gas mixture is then passed through the water–gas shift reaction to yield a stream of H_2 and CO_2 at a pressure of 5-40 bar and temperature of around 40 °C, depending on the plant.[155-157] Thus, pre-combustion CO_2 capture is referred as a processes, in which CO_2 is removed from H_2. Produced H_2 can be subsequently burned in power plants to generate CO_2-free energy.

In the context of MOFs for pre-combustion capture processes, adsorption-based processes (particularly PSA processes) and membrane-based technology using MOFs has been intensively studied.[138, 158-167] Herein, we present one work for each systems in detail. H_2 and CO_2 has an evident difference in their molecular size (2.89 and 3.30 Å for H_2 and CO_2, respectively). So it is quite favourable to separate them based on sieving H_2 from CO_2 through membrane-based processes. In a breakthrough in development of MOF membranes, Yang and co-workers successfully prepared molecular sieve nanosheets from a layered MOF, $Zn_2(bIm)_4$ (bIm^- = benzimidazolate). A single layer possess a aperture diameter of ~ 2.9 Å, which is perfectly suitable for the passage of H_2 molecules, while blocking the larger CO_2 molecules. As apertures were constructed from four flat bIm molecules, this membrane features uniform and straightforward pore windows, enabling easy and fast passage of H_2, which results in an unprecedented permeability for H_2.[167] Later, the separation performance of this MOF membrane was improved by fine tuning the fabrication temperature, upon which $Zn_2(bIm)_4$ nanosheets were coated onto α-Al_2O_3 support. This optimal temperature significantly increased the permeability of H_2 molecules by minimizing the existing restacking between the nanosheets which could block the passage of H_2 molecules. As a result, this MOF membrane obtains a simultaneous high H_2/CO_2 selectivity (291) and H_2 permeability (2700 GPU), which successfully places the performance of this membrane above the Robeson's upper limit.

In another work, Vaidhyanathan and co-workers proposed a 4-pyridylcarboxylate–based ultra-microporous MOF [Ni-4PyC, $Ni_9(m\text{-}H_2O)_4(H_2O)_2(C_6NH_4O_2)_{18}$], with an extraordinarily high CO_2 saturation capacity of ~8 mmol/g and appreciable CO_2/H_2 selectivity at high pressures, making this MOF a suitable candidate for H_2 purification by PSA processes.[160] A high pore space along with strong guest-guest interaction and multiple adsorption sites was found to be the main reason for high saturation capacity of this MOF.

The material also exhibits high water stability and favourable CO_2 diffusion coefficients as well as a relatively low heat of adsorption. Notably, [Ni-4PyC, $Ni_9(m\text{-}H_2O)_4(H_2O)_2(C_6NH_4O_2)_{18}$] can be scaled-up and synthesized straightforwardly from readily available ligand and metal salts in a one-pot synthesis mode.

1.3.1.3 Oxy-fuel combustion

Another way of reducing CO_2 emission into atmosphere is burning fossil fuels in a nearly pure O_2 environment, which is referred to as oxy-fuel combustion. In this way, the generated flue gas is only CO_2 and water. The coexisting water can be easily separated, isolating CO_2 for further sequestration.[97] Here, the separation target is switched to producing pure O_2 from air. Classical cryogenic distillations are extremely energy-intensive, which makes them inviable solutions for CO_2 capture from oxy-fuel combustion.[97] Hence, alternative technologies with less energy consumption are highly sought after. Membrane-based separation would not be a realistic solution here due to extremely close kinetic diameters of N_2 (3.64 Å) and O_2.[97] As for adsorption-based separation, selective adsorption of one of these gases over the other one through physisorption mechanism does not seems to be feasible because of nearly identical physical properties of O_2 and N_2 (including boiling point, polarizability and quadrupole moment). Conversely, separation by chemisorption mechanism sounds to be an effective way of separating O_2 from N_2, as O_2 exhibits a high tendency to accept electrons from redox-active metal sites, whereas N_2 does not feature such behaviour.[97] Numerous studies have been done in this area. Cr^{2+} and Fe^{2+} are known as metal ions with relatively strong redox ability. Different MOFs incorporating these metal sites such as $Cr_3(\text{-btc})_2$ (H_3btc = 1,3,5-benzenetricarboxylic acid), Cr-BTT (H_3BTT = 1,3,5-Tris(2H-tetrazol-5-yl)benzene), and Fe-MOF-74 has been intensively investigated.[168-170] However, Cr^{II}- containing MOFs exhibits gradual loss of O_2 capacity upon multiple adsorption-desorption cycles,[170-171] while Fe-MOF-74 is not recyclable at temperatures above 222 K because of its non-reversible oxidation.[168] Subsequently, more efforts were made with Co^{II}-containing MOFs. In contrast to previously reported Co-MOFs constructed from weak carboxylate-metal bond, strong N-donor ligands were incorporated into the formation of two MOFs, Co-BTTri (H_3BTTri = 1,3,5-tri(1H-1,2,3-triazol-5-yl)benzene) and Co-BDTriP (H_3BDTriP = 5,50 -(5-(1H-pyrazol-4-yl)-1,3- phenylene)bis(1H-1,2,3-triazole)).[172] Metals in these MOFs display greater tendency to share their electrons with O_2 molecules because of their higher energy level in comparison to MOFs with weak ligand-metal interaction. As a result, it gives rise to an appreciable O_2 adsorption capacity of 3.3 mmol/g at 0.21 bar and 195 K, and a selectivity of 41 at the same temperature for Co-BTTri.[172] Additionally,

recyclability and stability towards water is improved significantly, which makes Co^{II}-MOFs a promising adsorbent for future O_2/N_2 separations.

1.3.1.4 Direct capture from air

Previously mentioned scenarios were all dealing with capturing CO_2 from stationary point sources to slow down the increasing rate of CO_2 level in the atmosphere. To remove the CO_2 that has already been released into atmosphere, efforts can be made to capture CO2 directly from air. This concept, which is called direct air capture (DAC), recently has been pushed forward to decrease the level of existing CO_2 in the air.[173] Additionally, DAC can also be applied to reduce CO_2 level in spacecraft and submarines, to maintain a habitable environment.[173] Currently, the level of CO_2 in atmosphere is 400 ppm, so the operational condition for direct air capture process is 0.0004 bar and room temperature.[173] The strategies to develop MOFs suitable for DAC are similar to those mentioned in post-combustion section, involving introduction of functional groups with strong yet reversible interaction with CO_2, and rational design of pore with precise aperture window and suitable interior shape to enhance physical interaction of MOFs with CO_2 at such low concentrations. The DAC using MOFs has been intensively studied recently and outstanding progress has been made.[144, 150, 152, 174-179]

1.4 Introduction to selected experimental and computational techniques

1.4.1 BET surface area calculations

The BET model is the most widely accepted model by the porous materials community to calculate a material's apparent surface area. Experiments are usually carried out by measuring a nitrogen isotherm at 77 K (Figure 1.17a as an example). It was found in the past that often the entire isotherm does not fit well with the model (Figure 1.18c is derived from experimental data and supposed to be linear according to the BET equation). In order to obtain a reportable value, researchers have chosen a region of the isotherms which appear to be linear when the BET equation is applied. The choice is often arbitrary and can cause large deviations in surface area depending on the pressure region selected.[180] To regulate this chaos, Walton and Snurr proposed a procedure for deciding on appropriate pressure ranges for calculating BET surface areas,[93] which were followed in this thesis:

1) The isotherm region where $v(1 - P/P_0)$ increases versus P/P_0, where v is the amount of N_2 adsorbed, was identified. Here, P/P_0 is the relative pressure, P being the pressure of the adsorbent in equilibrium with the porous material at each point of

measurement and P_0 is the condensation pressure of the adsorbent at the temperature of measurement.

2) Within this isotherm region, sequential data points that led to a positive intercept in the plot of $\frac{P/P_0}{v(1-P/P_0)}$ against P/P_0, were found. This plot yields a slope a, and a positive intercept b. The number of gas molecules adsorbed in the initial monolayer is $v_m = \frac{1}{a+b}$.

3) The BET surface area was then calculated according to the following equation:

$$A_{BET} = v_m(cm^3 g^{-1}) * \frac{1\ (mol)}{22400\ (cm^3)} * \sigma_0(\text{Å}^2) * N_A(mol^{-1}) * 10^{-20}\left(\frac{m^2}{\text{Å}^2}\right) \qquad (4)$$

Where N_A is Avogadro's constant, and σ_0 is the cross-sectional area of a N_2 molecule, which is 16.2 Å^2.

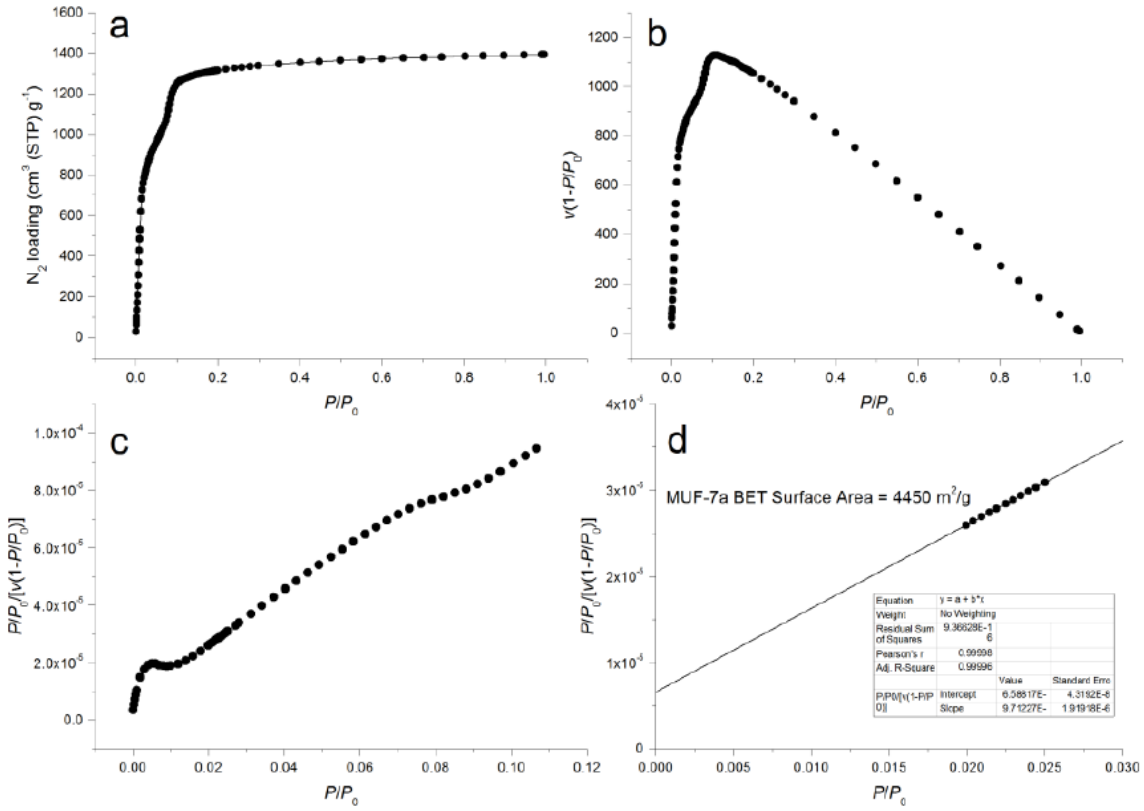

Figure 1.17 (a) An example N_2 adsorption isotherm measured at 77K for MUF-7a[181] (b) A plot to find the pressure region that meets the first consistency criterion for BET surface area calculation according to the method proposed by Walton and Snurr.[93] (c) A plot to find the pressure region that meets the second consistency criterion. (d) BET plot.

1.4.2 Pore volume calculations

When adsorption reaches saturation, the isotherm plateaus. At this point, the total pore volume of the material can be calculated by assuming that the adsorbed gas is in a condensed liquid-like phase (in case of N_2 isotherm, the liquid density of N_2 is 0.807 g/ml). Because

the amount of adsorbed gas is known, its corresponding volume is simply calculated based on the density of the liquid adsorbate. The total mass of the adsorbing material is always precisely measured prior to an isotherm measurement.

1.4.3 Isosteric heat of adsorption calculations

Heats of adsorption (Q_{st}) are quantitative enthalpic measures of the affinity of a porous material for a given guest molecule. These values are calculated according to the method described in the literature.[122] Briefly, two isotherms that are measured at two different temperatures are first fit to a virial equation:

$$\ln P = \ln N + \frac{1}{T}\sum_{i=0}^{m} a_i N^i + \sum_{i=0}^{n} b_i N^i \qquad (5)$$

where N is the amount of gas adsorbed at the pressure P.

Then, to calculate Q_{st}, the fitting parameters from the virial equation are used in the following equation:

$$Q_{st} = -R\sum_{i=0}^{m} a_i N^i \qquad (6)$$

where R is the universal gas constant.

1.4.4 Introduction to a gas adsorption analyser

Figure 1.18 illustrates the key components of a gas adsorption analyser.

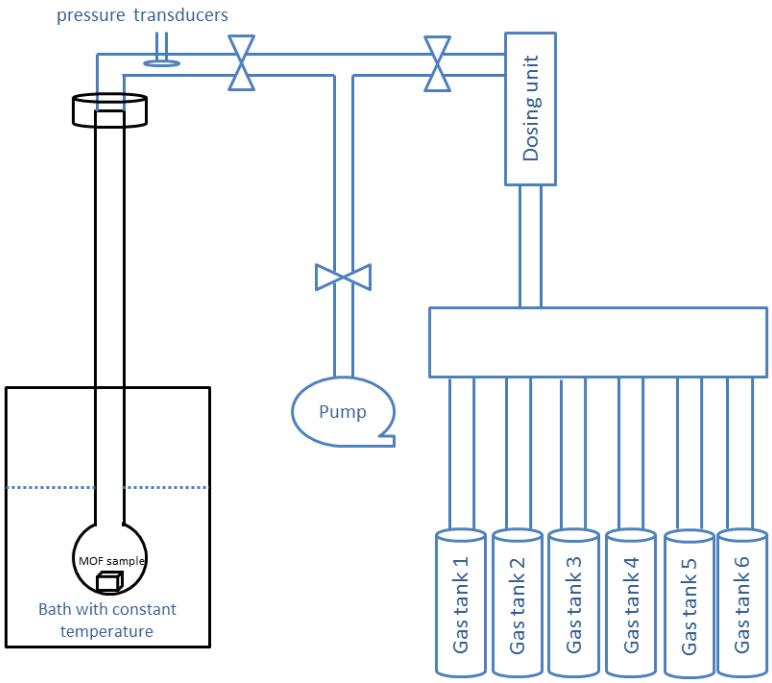

Figure 1.18 A cartoon showing the essential components of a gas adsorption analyser.

A sample tube containing MOF crystals is evacuated and immersed in to a bath with a constant temperature. The instrument then doses a known amount of gas into the sample tube and reads the pressure frequently. The equilibration of adsorbed and non-adsorbed gas is known to be reached when the pressure reaches a constant value. The amount of gas adsorbed in the MOF sample can be calculated by taking the difference of pressure expected from the real gas law and the equilibrated pressure. This process is repeated so a plot of amount adsorbed versus equilibration pressure is obtained as an adsorption isotherm.

1.4.5 IAST selectivity

The Ideal Adsorbed Solution Theory (IAST) starts by assuming that for a given adsorbent and at fixed temperature *T*, the pure-component isotherms $n_i(P)$ for each gas *i* of interest is known. Then, given a mixture of ideal gases adsorbing at total pressure P in an host framework and the composition of the gas phases (y_i)—such that the partial pressures are $P_i = y_i P$— the goal of the method is to predict the total adsorbed quantity n_{tot} and the molar fractions (x_i) in the adsorbed phase. In order to do so, Myers and Prausnitz[118] introduced a quantity homogeneous to a pressure, P_i^*, for each mixture component. The IAST method links this pressure to the compositions of the gas and adsorbed phases with two equations for each component:

$$Py_i = P_i^* x_i \tag{7}$$

for all *i* and *j*,

$$\int_0^{P_i^*} \frac{n_i(p)}{p}\,dp = \int_0^{P_j^*} \frac{n_j(p)}{p}\,dp \tag{8}$$

Equation 7 defines the link between P^*_i the total pressure P, the gas phase molar fraction y_i and the adsorbed phase molar fraction x_i. Equation 8 is an expression of the equality of chemical potentials at thermodynamic equilibrium. In the simpler case of two-component gas mixture (B, C), these two equations and the conservation of matter, can be rewritten to a set of four equations:

$$Py_A = P_B^* x_B \tag{9}$$

$$x_B = \frac{P_C^* - P}{P_C^* - P_B^*} \tag{10}$$

$$\frac{1}{n_{tot}} = \frac{x_B}{n_B P_B^*} + \frac{1 - x_B}{n_C P_C^*} \tag{11}$$

$$\int_0^{P_B^*} \frac{n_B(p)}{p}\,dp = \int_0^{P_C^*} \frac{n_C(p)}{p}\,dp \tag{12}$$

Solving these equations for P^*_B and P^*_C will give all the information on the system composition.[182] It can be done with either numerical integration of the isotherms, or by fitting the isotherms to a model, and then integrating the model analytically. The pyIAST package[182] was used to perform the IAST calculations. In order to predict the sorption performance of MOFs and their derivatives towards the separation of binary mixed gases, the single-component adsorption isotherms were first fit to an appropriate model (as an example, we have presented dual site Langmuir Freundlich model here (DSLF)):

$$y = \frac{q_1 b_1 P^{\frac{1}{t_1}}}{1 + b_1 P^{\frac{1}{t_1}}} + \frac{q_2 b_2 P^{\frac{1}{t_2}}}{1 + b_2 P^{\frac{1}{t_2}}} \tag{13}$$

Where q is the uptake of a gas; P is the equilibrium pressure and q_1, b_1, q_2, b_2, t_1 and t_2 are constants. These parameters were used subsequently to carry out the IAST calculations. As an example, the IAST selectivity calculation is presented for an equimolar mixture of CO_2 and CH_4 on MUF-7a at 298 K. Firstly, single gas adsorption isotherms were fitted with DSLF model as shown in Figure 1.19:

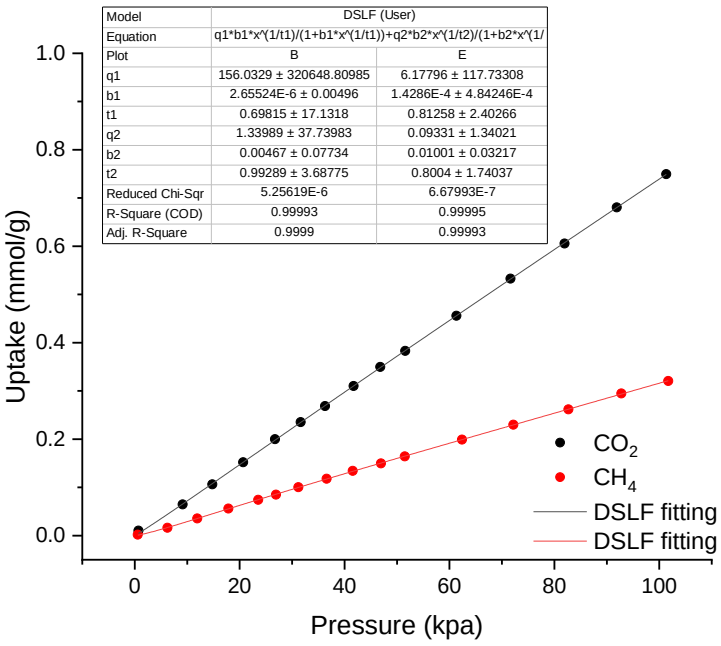

Figure 1.19 Single gas adsorption isotherms of CO_2 and CH_4 by MUF-7a at 298 K fitted by DSLF model.

The DSLF parameters were then used to predict the mixed gas isotherm by IAST method using the pyIAST software package. A selectivity of around 11 was found for CO_2 over CH_4 by MUF-7a. The mixed gas adsorption isotherms and selectivity are presented in Figure 1.20.

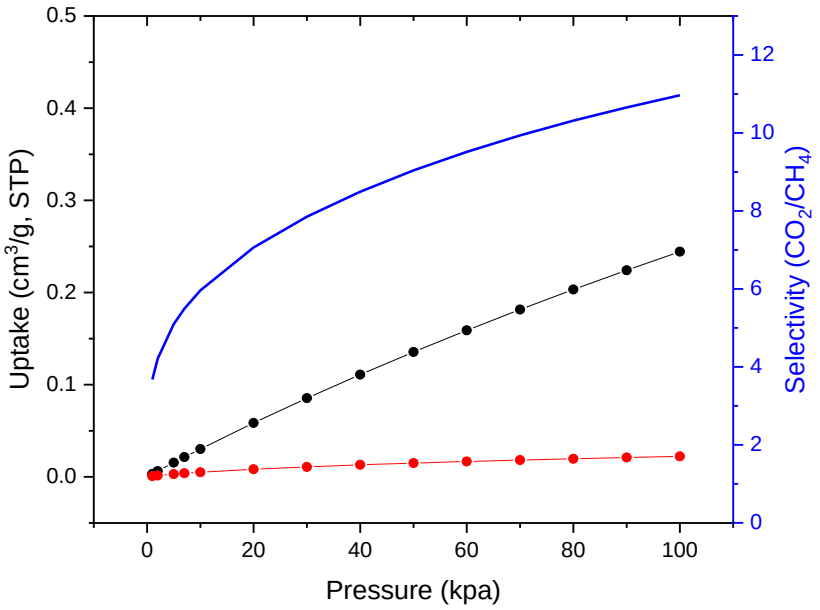

Figure 1.20 Mixed gas isotherms and IAST selectivity for an equimolar mixture of CO_2/CH_4 by MUF-7a at 298 K.

The IAST selectivity calculation shows the selectivity of CO_2 over CH_4 is low at low pressures and it increases at higher pressures. The reason behind such trend of selectivity is not fully understood and it is related to the shape of adsorption isotherms of CO_2 and CH_4 over the pressure ranges. The mixed gas adsorption capacity of both gases has been decreased due to the competitive adsorption of these two gases, where some portion of the void spaces have been filled with CO_2 molecules and some portion has been filled with CH_4 molecules.

1.4.6 Breakthrough curve simulation

1.4.6.1 Mathematical modelling

Considering a fixed bed adsorption column of length L filled with MOF, following assumptions were made to develop a mathematical model[183-185] that could be solved using proper numerical methods to calculate the concentration of gases at different elapsed times along the bed.

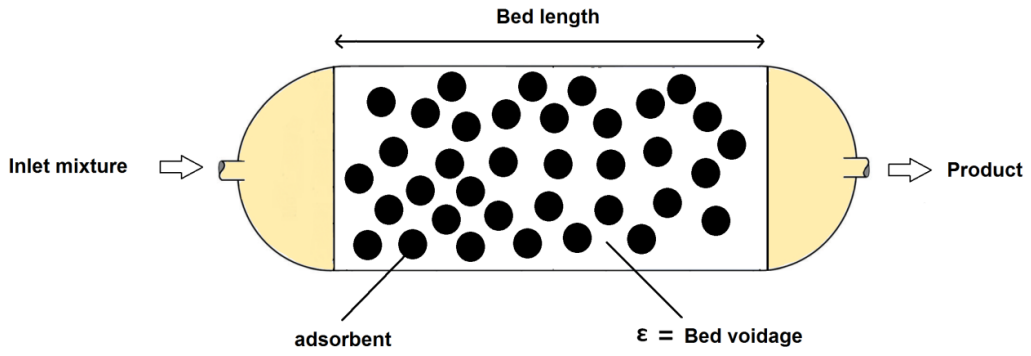

Figure 1.21 Schematic diagram of a fixed adsorption bed

The following assumptions were made:

- The dynamic behaviour of the fluid obeys an axial dispersion plug flow model in the bed.
- The gradient of the concentration along the radial and angular directions are neglected.
- The flow velocity is varied along the bed and it is calculated from the total mass balance equation.
- The gas property is described by the Peng-Robinson equation of state.
- Diffusion and adsorption into the particles is assumed as a lump kinetic transfer model.
- The mass transfer rate is represented by the linear driving force model.
- The pressure drop is considered along the bed using the Ergun equation.
- The adsorption columns operate under isothermal conditions.
- Mixed gas isotherms calculated by IAST method were fitted by single site Langmuir model and fitting parameters were used for breakthrough curves simulations.

Based on the preceding assumptions, the component and overall mass balances in the bulk phase of the adsorption column are written as follow:

$$\varepsilon \frac{\partial C_i}{\partial t} = -\frac{\partial (uC_i)}{\partial z} + \varepsilon D_{ax,i} \frac{\partial^2 C_i}{\partial z^2} - (1-\varepsilon)\rho_s \frac{\partial q_i}{\partial t} \quad (14)$$

$$\varepsilon \frac{\partial C}{\partial t} = -\frac{\partial (uC)}{\partial z} - (1-\varepsilon)\rho_s \sum_{1}^{n_c} \left(\frac{\partial q_i}{\partial t}\right) \quad (15)$$

Where C_i and q_i are, respectively, concentration of components in the gas phase and in the adsorbed phase, z is the axial coordinate in the bed, D_{ax} is the effective axial dispersion coefficient, u is the superficial gas velocity, ρ_s is the adsorbent density, n_c is the number of the adsorbed components in the mixture and ε is the bed voidage. The value of D_{ax} was calculated through the following equation[186]:

$$\frac{\varepsilon D_{ax,i}}{D_{m,i}} = 20 + 0.5\, Sc_i\, Re \tag{16}$$

Where *Re* is the Reynolds number and Sc is the Schmidt number and $D_{m,i}$ is the molecular diffusivity of component *i* in the mixture which was calculated by following equation:

$$D_{m,i} = \frac{1 - y_i}{\sum_{x=j}^{n} \frac{y_i}{D_{i,x}}} \tag{17}$$

Where y_i is the mole fraction of component I and $D_{i,x}$ is molecular diffusivity of component I in component x which was calculated by Wile-Lee equation[187]. Referring to the assumptions, the solid linear driving force (LDF) model is used to describe the mass transfer rate of the gas and solid phase[188]:

$$\frac{\partial q_i}{\partial t} = k_i(q_i^* - q_i) \tag{18}$$

Where k_i is the overall mass transfer coefficient, and a lumped parameter considering three different mass transfer resistances associated with film, macropore and micropore zone. As the overall mass transfer coefficient is in proportion to the steepness of breakthrough curves, the accurate value of it was obtained empirically by tuning its value until the steepness of the predicted and experimental breakthrough curves were the same. A schematic of tuning procedure is shown in Figure 1.22. The steepness of breakthrough curve increases by increasing the value of mass transfer coefficient.

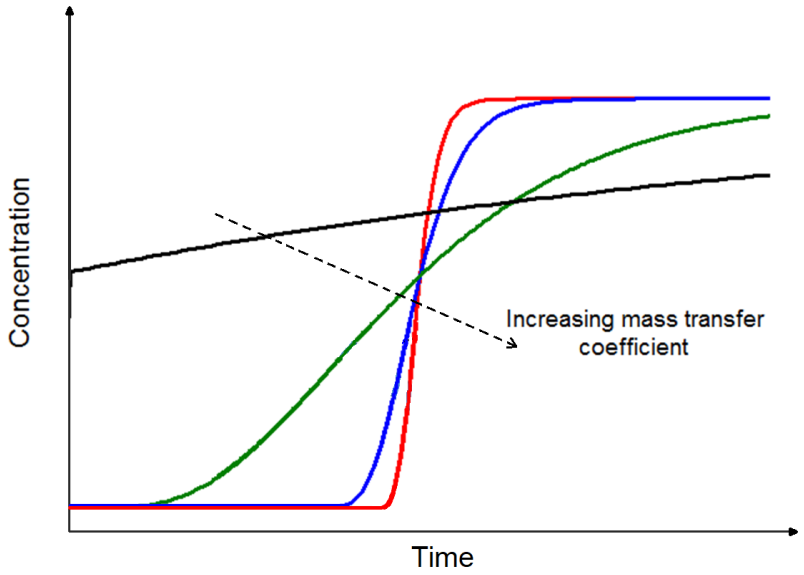

Figure 1.22 A schematic of breakthrough curve tuning procedure. The steepness of breakthrough curve increases by increasing the value of mass transfer coefficient.

This mass transfer coefficient tuned in this way was later used to predict breakthrough curves for other feed mixtures and operating pressures. q_i^* is the equilibrium concentration

of *i*th component in the adsorbed phase and is related to the concentration in the gas phase through isotherms. The IAST method was used to predict mixed gas isotherms and they were fitted by a Dual-Site Langmuir model. The pressure drop is defined by Ergun's equation as[99]:

$$\frac{\partial P}{\partial z} = -\left(\frac{37.5\,(1-\varepsilon)^2 \mu u}{\left(r_p \varphi\right)^2 \varepsilon^3} + 0.875\rho\,\frac{(1-\varepsilon)u^2}{r_p \varphi \varepsilon^3}\right)$$

Where P is the local pressure at the z axial coordinate, μ is the gas viscosity, φ is the shape factor and ρ is the gas density. Identical conditions to the experimental breakthrough measurement, including operating pressure, feed flowrate, temperature, bed size and amount of MOF, were used as input for simulations.

1.4.6.2 Numerical methods

Numerical solutions of the nonlinear parabolic PDEs derived from mass and momentum balance were conducted by an implicit method of lines using finite difference method for the spatial derivatives. Firstly, the second and first space derivatives were discreted by central and upwind- differential scheme (backward), respectively. In this way, the sets of partial equations were transformed to the sets of ODEs with respect to the time derivative terms. The length of the bed was divided into 50 increments and the set of equations were solved by the Implicit Euler method with a time step of one second.[189]

Chapter 2

An Ethane-Trapping Metal-Organic Framework with a High Capacity for Ethylene Purification

2.1 Introduction

Ethylene is one of the most important feedstocks for the production of polymers and high-value organic chemicals.[190] It is usually produced by the thermal cracking of hydrocarbons. The removal of ethane (C_2H_6) by-products that inevitably arise during these processes is one of the most challenging chemical separations due to the similarity of the physicochemical properties of ethane and ethylene.[110, 191-192] At present, cryogenic distillation is the main technology used to separate these compounds. This process is expensive and comes with a high energy penalty because of the requirement for high pressures and low temperatures (typically at 5–28 bar and 180–258 K using over 100 trays).[193-194] To avoid such a high consumption of energy, more efficient separation technologies at ambient conditions are highly sought after.[195-197] Among techniques with lower energy requirements and operating costs, adsorptive separation processes using porous solid materials have risen to prominence.[100, 198-200] Although conventional porous materials such as zeolites and carbon-based materials have been applied for hydrocarbon separations, in general they are not satisfactory in separation processes due to poor adsorption selectivity and low capacity.[126, 201-202] Thanks to their high pore volumes, designable pore characteristics, and countless structural possibilities, novel metal-organic frameworks (MOFs) are prime adsorbents.[24, 132, 134, 203] MOFs are of increasing importance in the context of hydrocarbon separation, especially the separation of ethylene from ethane.[119, 204-207]

MOFs differ widely in their relative affinities for ethane and ethylene (C_2H_4).[119, 208-209] The design strategy for MOFs that prefer C_2H_4 is comparatively straightforward and relies on introducing open metal sites or highly polar groups into the framework.[204, 210-213] This approach takes advantage of the larger quadrupole moment of C_2H_4 and the presence of π electrons, which render it capable of coordinating to metals. In contrast, for ethane selective MOFs, the dominant interactions can be ascribed to dispersion and induction forces as ethane has a higher polarizability than ethylene. Therefore, a MOF with a pore structure enriched

with nonpolar surfaces and pore dimensions that match the size of C_2H_6 may favour the preferential adsorption of this adsorbate.

The implementation of C_2H_4-selective MOFs has two significant disadvantages. First, water vapour is liable to diminish the affinity of the adsorbent for C_2H_4 because it will compete for the same highly polar sites. Second, these adsorbents require an additional desorption step to yield the C_2H_4-rich product stream in a C_2H_6/C_2H_4 separation process, which typically involves a purge gas and high temperatures or the application of a vacuum. In addition, due to the contamination of eluent by adsorbed C_2H_6 during this desorption step, further purification is demanded to reach the >99.95% purity required by C_2H_4 polymerization reactors.[211, 214-215] On the other hand, the efficiency of C_2H_6-selective MOFs is significantly greater because high-purity C_2H_4 is afforded directly through a single adsorption step, simplifying the process and resulting in an increase in productivity.[119, 216] Such an efficient approach offers an energy saving of 40% in pressure/temperature swing adsorbent technologies for this separation.[217-218] Despite these advantages, only a few such C_2H_6-selective MOFs have been identified so far, and they either suffer from poor selectivity because of the difficulty indiscriminating C_2H_6 and C_2H_4,[216, 219-224] or low C_2H_6 uptake due to moderate pore volumes.[119, 225-227]

Low selectivities result in a reduced purification efficiency of C_2H_4 and reduced pore volumes are antagonistic to productivity. Thus, fabricating adsorbents that combine good selectivity with high uptake capacity is of special interest.[228] Recently, Chen *et al.* reported an impressive MOF showing strong affinity towards ethane within channels of $[Fe_2(O_2)(dobdc)]$.[229] Although $[Fe_2(O_2)(dobdc)]$ exhibits good selectivity and ethane capacity, it suffers from a high energy penalty of regeneration (Q_{st} = −66.8 kJ/mol). Moreover, this MOF is not stable in air and requires special handling under inert conditions.

2.2 Results and discussion

A mixture of $Co(OAc)_2.4H_2O$ (0.125 g, 0.5 mmol), isophthalic acid (H_2ipa, 0.166 g, 1.0 mmol), MeOH (6 mL), and H_2O (0.5 mL) were sonicated for 10 min and sealed in a 25 ml Teflon-lined autoclave and heated at 120 °C for two days. After cooling to room temperature, the resulting purple plate crystals were washed with methanol several times and dried under vacuum (Figure 2.1). It yields 81 mg of guest-free crystal of $[Co_3(\mu_3\text{-}OH)(ipa)_{2.5}(H2O)]$ with a reaction yield of 78% based on cobalt. We named this MOF, MUF-15 (MUF = Massey University Framework). MUF-15 was discovered during screening of experimental MOFs for ethane/ethylene separation. Around 5000 MOFs were investigated for their ability to separate ethane from ethylene at room temperature and 1 bar and one of these materials was

a MOF synthesized from cobalt acetate and isophthalic acid with slightly different structure compared to MUF-15 (ccdc number: 751783).

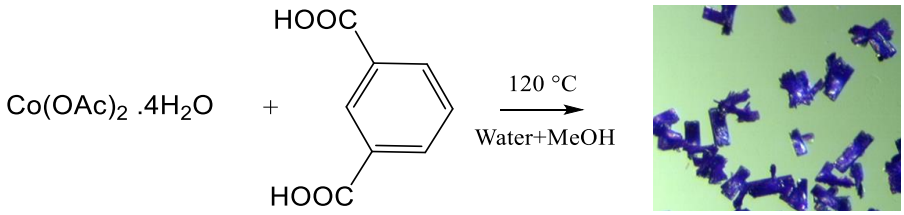

Figure 2.1 Synthetic route to MUF-15 with an optical microscopy image of single crystals.

MUF-15 can also be synthesized in a larger scale by mixing $Co(OAc)_2.4H_2O$ (0.75 g, 3.0 mmol) and H_2ipa (0.664 g, 4.0 mmol) in MeOH (40 mL) and H_2O (3 mL). After sonicating the mixture for 30 min, was sealed in a 100 mL Teflon-lined autoclave and heated at 120 °C for two days. After cooling to room temperature, the resulting purple plate crystals were washed with methanol several times and dried under vacuum (Yield *ca.* 0.42 g, 66% based on cobalt). MUF-15 is built up from inexpensive precursors and formed in a high yield. Based on commercial prices, we estimate the raw material cost of this material is less than $20 per kg. It should be noted that this price is only an estimated price of starting materials.

Single crystal X-ray diffraction revealed that MUF-15 crystallizes in the orthorhombic space group *Pnna* (Table 2.1).

Table 2.1 Crystal data and structure refinement for MUF-15.

Formula	$Co_3(\mu_3\text{-}OH)(ipa)_{2.5}(H_2O)$
CCDC deposition number	1892003
Empirical formula	$C_{20}H_{13}Co_3O_{12}$
Formula weight	622.09
Crystal system	orthorhombic
Space group	*P*nna
a/Å	28.714(2)
b/Å	21.1265(7)
c/Å	10.9460(3)
α/°	90
β/°	90
γ/°	90
Volume/Å^3	6640.1(5)
μ/mm^{-1}	12.006
F(000)	2480
2Θ range for data collection/°	12.044 to 70.24
Index ranges	$-21 \le h \le 21$, $-15 \le k \le 15$, $-8 \le l \le 8$
Reflections collected	16306
Independent reflections	1426 [R_{int} = 0.1075, R_{sigma} = 0.0582]

Data/restraints/parameters	1426/219/296
Goodness-of-fit on F^2	1.160
Final R indexes [I>=2σ (I)]	R_1 = 0.0878, wR_2 = 0.2481
Final R indexes [all data]	R_1 = 0.1056, wR_2 = 0.2680
Largest diff. peak/hole / e $Å^{-3}$	0.72/-0.42

As observed in a related Co^{II}-isophthalate material,[230] MUF-15 is assembled from a hexacobalt cluster connected by ten ipa linkers (Figure 2.2a). The cluster nodes are built up from two symmetry-related sets of three cobalt(II) ions. The ions within each set coordinate to a μ_3 bridging hydroxide ion, and the two sets are connected to each other through shared carboxylate groups. There is one terminal H_2O ligand per set of three cobalt ions, which is disordered over two sites. By considering the cobalt clusters as 10-connected nodes linked by ipa ligands (Figure 2.2c), MUF-15 can be depicted as a porous coordination polymer. The framework defines three narrow zigzag 1-dimensional pores that intersect each other, as highlighted in Figures 2.2d and e. These orthogonal channels run along the a, b and c axis with pore limiting windows of 8.5 × 3.5, 7 × 3.8 and 3.2 × 1.2 Å, respectively (Figure 2.3).

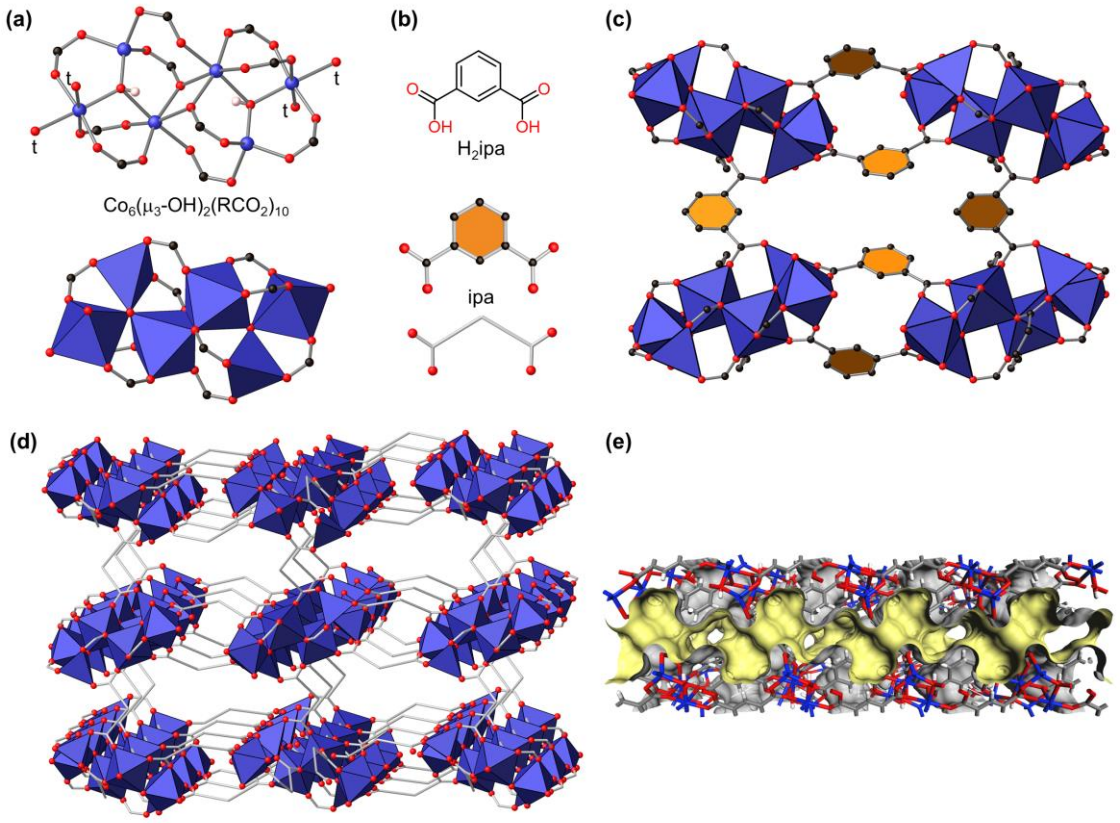

Figure 2.2 (a) The SCXRD structure of MUF-15 comprises of hexanuclear cobalt(II) clusters (cobalt = dark blue; oxygen = red; carbon = grey; hydrogen = pink (most omitted for clarity)). The sites occupied by terminal H_2O ligands are marked with a t. (b) The structure of H_2ipa linker and its stick representation. (c, d) The cobalt(II) clusters and ipa ligand assemble into network that defines a 3D array of channels. (e) The zig-zag channels of MUF-15 illustrated by the Connolly surface in yellow (probe of diameter 1.0 Å).

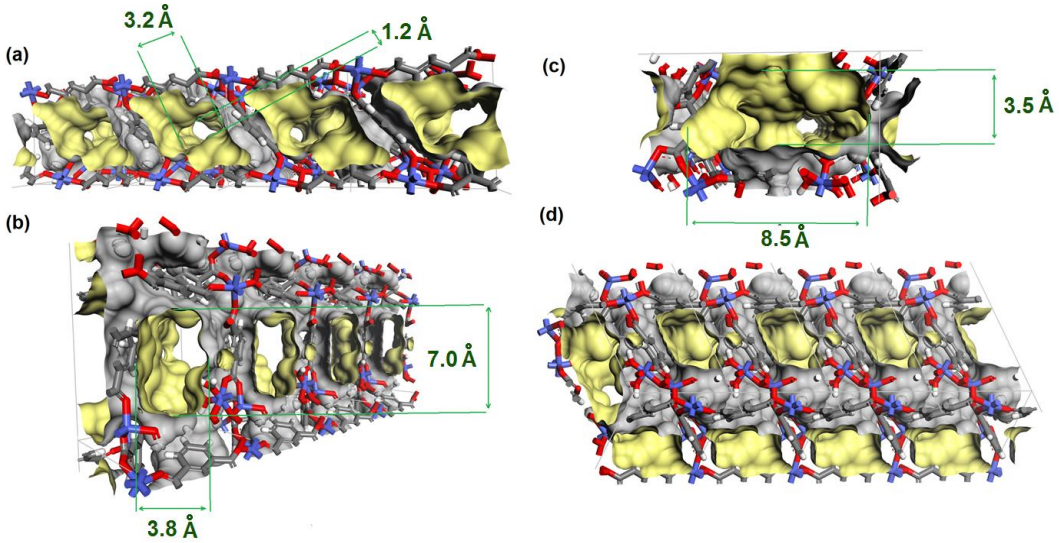

Figure 2.3 Pore structure and void space of MUF-15 illustrated by Connolly surface using a probe of diameter of 1 Å along the x (a), y (b), z (c) axes, and a top view showing the connectivity of the pores (d) (Co, blue; O, red; C, grey; and H, white).

Guest-free MUF-15 can be readily produced at 120 °C under vacuum, which preserves the coordinated water molecules. Since these water ligands are lost, together with the crystallinity and porosity, by heating above 200 °C such high temperatures were avoided. The phase purity of the material activated at 120 °C was confirmed by matching its powder X-ray diffraction pattern with that simulated from its SCXRD structure (Figure 2.4), analysis of the ^{1}H NMR spectrum of a digested sample (see Appendix A), and elemental analysis.

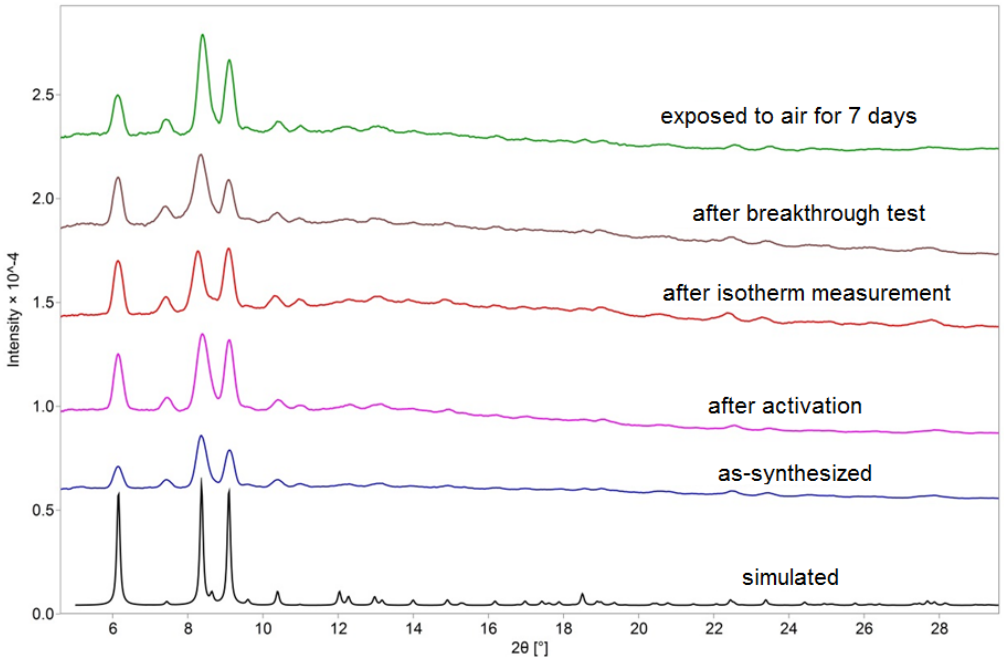

Figure 2.4 PXRD patterns of MUF-15 showing that its structure remains unchanged after activation at 120 °C under vacuum, after isotherm measurements, after breakthrough experiment and after exposure to an air with a relative humidity of 80% for one week.

The found values for carbon and hydrogen are 37.47 and 2.87, respectively, which are almost identical to their calculated ones of 37.53 and 2.36 obtained from the formula of MUF-15 with one water in its pore ($[C_{20}H_{13}Co_3O_{12}]\cdot H_2O$). Thermogravimetry and powder XRD demonstrated that MUF-15 decomposes above 400 °C under nitrogen (Figure 2.5), while it is stable when exposed to a laboratory atmosphere (~80% relative humidity) at ambient temperatures for at least one week (Figure 2.4), after activation, after isotherm measurements, and after breakthrough test.

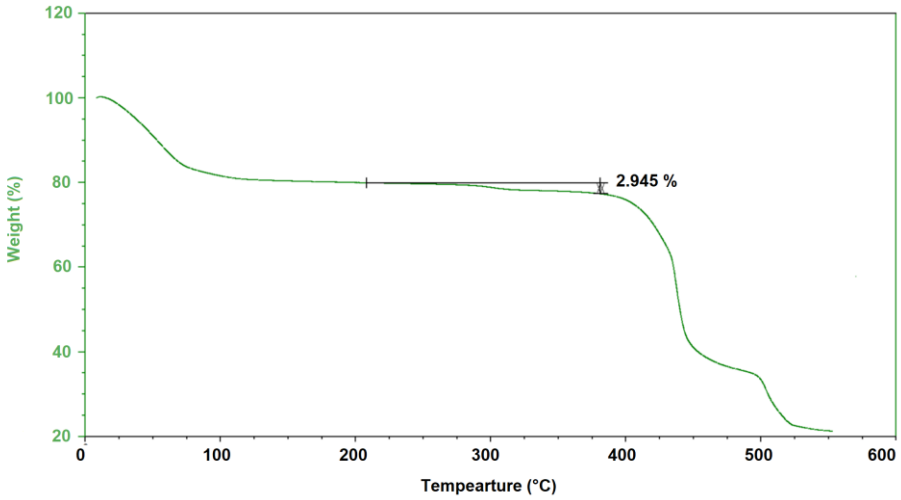

Figure 2.5 TGA curve of MUF-15 showing a 2.95% weight loss equivalent to calculated weight loss for one coordinated water molecule.

A N_2 adsorption isotherm at 77 K illustrated the permanent porosity of MUF-15 (Figure 2.6) and gave a BET surface area of 1130 m^2/g and a pore volume of 0.51 cm^3/g (See appendix A for the calculations).

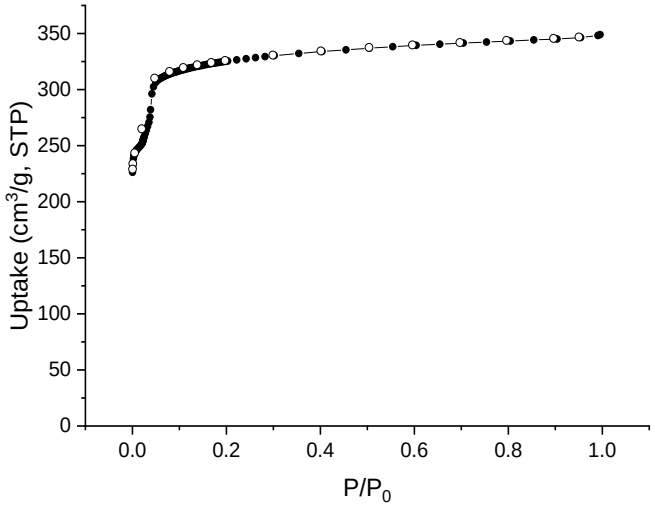

Figure 2.6 Experimental adsorption (filled circles) and desorption (open circles) of N_2 at 77 K by MUF-15.

These values are nearly identical to the geometric surface area of 1260 m^2/g and pore volume of 0.46 cm^3/g calculated from the crystallographic coordinates. These data together as well as the limiting pore diameter (i.e., the diameter of smallest pore window) and the largest cavity diameter (i.e., the diameter of the largest sphere that can fit within the pores) are presented in Table 2.2.

Table 2.2 Calculated and experimentally determined structural characteristics of MUF-15.

Geometric surface area calculated (RASPA2)	1260 m^2/g
BET surface area from experimental N_2 isotherm/77K	1130 m^2/g
Pore volume calculated (RASPA2)	0.46 cm^3/g
Pore volume from experimental N_2 isotherm/77K	0.51 cm^3/g
Largest cavity diameter calculated (Zeo++)	5.2 Å
Pore limiting diameter calculated (Zeo++)	3.6 Å
Crystallographic crystal density	1.245 g/cm^3

The accessible surface of the MUF-15 channels is largely defined by the phenyl rings of the ipa ligands. Together with the pore dimensions, this surface chemistry signals promise for the capture of the more polarizable ethane in preference to ethylene. Single-component C_2H_6 and C_2H_4 adsorption isotherms were measured on guest-free MUF-15 at 293 K (Figure 2.7a) and other temperatures (see Appendix A). These isotherms exhibit type I character with a smooth increase with pressure and full reversibility. Importantly, the isotherms remain identical after exposing a sample to a laboratory atmosphere overnight (Figure 2.7c), and can be reproduced over multiple cycles (Figure 2.7d). MUF-15 has a distinct preference for adsorbing ethane over ethylene: the uptake reaches 4.69 mmol/g (105 cm^3/g) and 4.15 (93 cm^3/g) for C_2H_6 and C_2H_4, respectively, at 293 K and 1 bar. As was mentioned in chapter 1, there are three overall mechanisms for separation systems. Separation based on the difference in equilibrium adsorption uptake, kinetic of adsorption and size of adsorbates. According to appreciable adsorption of both C_2H_6 and C_2H_4, the mechanism of separation cannot be molecular sieving as both C_2H_6 and C_2H_4 can enter the pores of MUF-15. To investigate the kinetics of adsorption for C_2H_6 and C_2H_4, their kinetic uptakes were measured versus time and results are presented in Figure 2.7b. Since the uptake kinetics of the two gases are nearly identical, it can be concluded that separation mechanism in MUF-15 can be ascribed to thermodynamic effect, where due to the favourable adsorption sites, MUF-15 adsorbs C_2H_6 more stronger than C_2H_4.

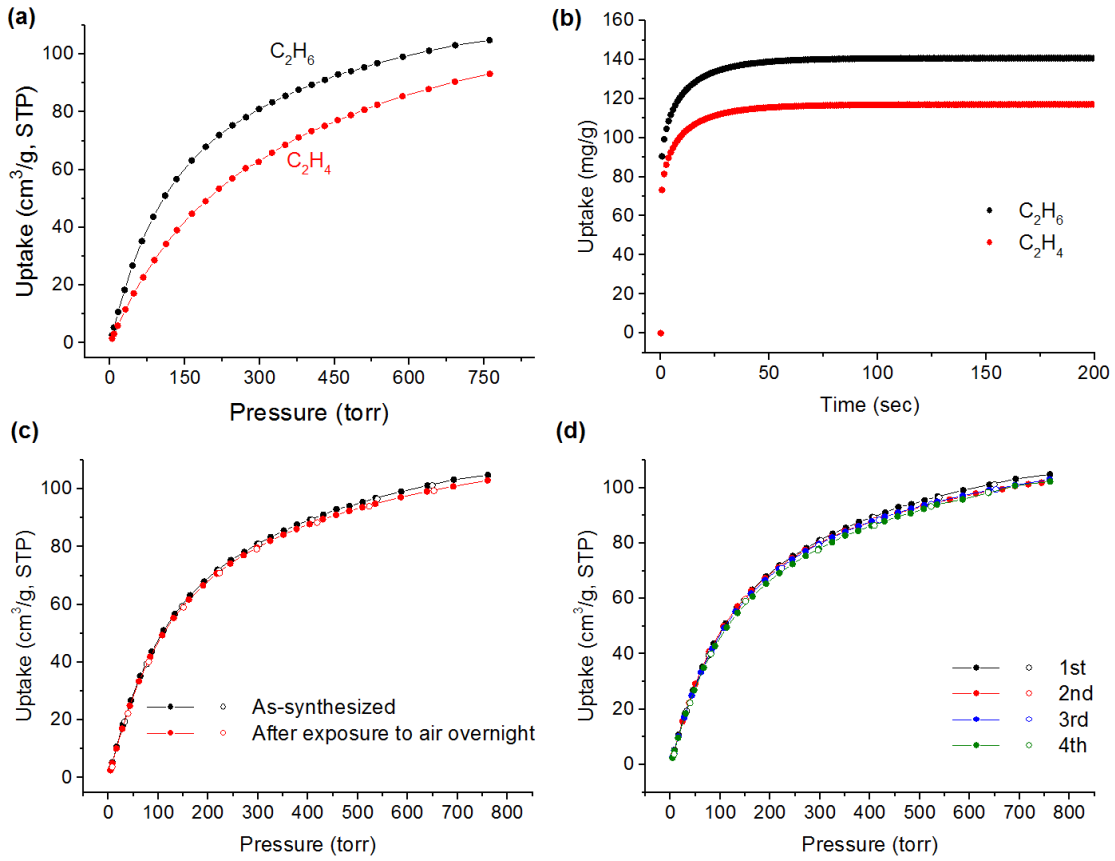

Figure 2.7 (a) Experimental C_2H_6 and C_2H_4 adsorption isotherms of MUF-15 at 293 K (desorption points not presented for clarity – see Appendix A). (b) Kinetic profiles of gas uptake by MUF-15 at 293 K upon exposing an evacuated sample to a dose of gas equal to its measured total adsorption of that gas at 760 torr. (c) Volumetric C_2H_6 adsorption (filled circles) and desorption (open circles) adsorption isotherms of MUF-15 at 293 K before and after exposing a sample to a laboratory environment with ~80% humidity overnight. (d) Volumetric C_2H_6 adsorption (filled circles) and desorption (open circles) isotherms of MUF-15 at 293K measured on the same sample over multiple cycles.

The C_2H_6 uptake capacity of MUF-15 at 1 bar (4.69 mmol/g) is notably higher than that of the benchmark adsorbents $Cu(Qc)_2$ (1.85 mmol/g)[227], ZIF-7 (1.85 mmol/g)[225] and MAF-49 (1.73 mmol/g).[119] The ethane capacity of MUF-15 stems from its large pore volume (0.51 cm^3/g) compared to that of $Cu(Qc)_2$ (0.11 cm^3/g)[227], ZIF-7 (0.078 cm^3/g)[231] and MAF-49 (0.2 cm^3/g; calculated by RASPA2[232] simulation software using a helium probe) (Table 2.4). There is frequently a trade-off between pore dimensions and pore volumes in adsorbent materials. Pore dimensions on par with small guest molecules often correlate with small pore volumes, which in turn lead to low uptake capacities. On the other hand, high pore volumes usually arise from large pores which cannot discriminate between molecules of similar sizes. However, the topology features of MUF-15 embody a rare combination of voluminous pores and wall-to-wall distances on par with small guest molecules. This allows it to simultaneously adsorb a significant quantity of ethane and discriminate it from ethylene.

Coverage-dependent adsorption enthalpies (Q_{st}) of MUF-15 for C_2H_6 and C_2H_4 were evaluated experimentally from pure component isotherms collected at 288, 293, and 298 K, by the implementation of a virial equation (Figure 2.8a). The resultant Q_{st} at near-zero coverage is 29.2 and 28.2 kJ/mol for C_2H_6 and C_2H_4, respectively, which underscores the enhanced uptake of C_2H_6. At higher coverage, the Q_{st} values rise for both gases, with the increase for C_2H_6 being markedly steeper. This implies that the adsorption process benefits from intermolecular interactions amongst the adsorbates, which is fully consistent with the crystallographically-observed pore dimensions. In fact, because of the packed accommodation of C_2H_6 and C_2H_4 in the pores, the intermolecular distance between these gases is very short, and they orientate in a way that hydrogen atoms of a molecules interact strongly with carbon atoms of adjacent molecules. These interactions increase with the adsorption of more molecules, thus increasing the binding energy.

Motivated by the high uptake and preferential binding of ethane by MUF-15, the adsorption selectivity of C_2H_6/C_2H_4 mixtures was predicted on the basis of ideal adsorbed solution theory (IAST)[118] using a range of starting compositions (50/50, 25/75 and 10/90 C_2H_6/C_2H_4, Figure 2.8b, see Appendix A for the rest).

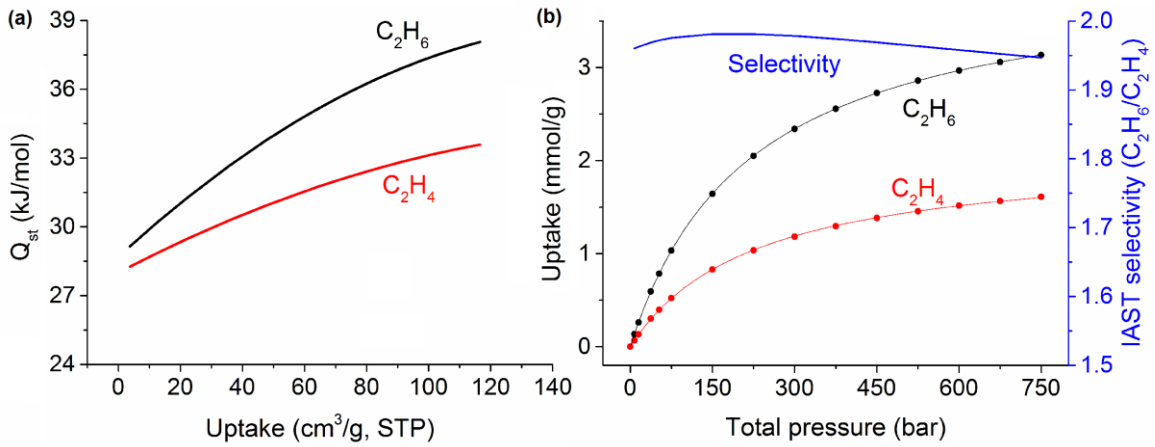

Figure 2.8 (a) Isosteric heat of adsorption plots for the adsorption of C_2H_6 and C_2H_4 by MUF-15. (b) Predicted mixture adsorption isotherms and selectivity of MUF-15 predicted by IAST method for a 50/50 C_2H_6/C_2H_4 mixture at 293 K.

MUF-15 exhibits a C_2H_6/C_2H_4 selectivity of around two for all three mixtures. Achieving this combination of good selectivity and high capacity is rare in an adsorbent material. Previously-reported ethane-selective MOFs typically exhibit either very low gas uptakes or poor selectivity (Table 2.4).[119, 220-221, 223, 225-226]

First-principles dispersion-corrected density functional theory (DFT-D3)[233] calculations as implemented in the software package VASP[234] were performed to gain further insight into

the mechanism of selective C_2H_6/C_2H_4 adsorption in MUF-15. The calculated static binding energy for C_2H_6 at its most preferred binding site is around -36.7 kJ/mol, whereas it is −35.0 kJ/mol for C_2H_4. The stronger host-guest interactions with ethane are in accord with experimental observations. This can be attributed to van der Waals interactions between the ethane and neighbouring π electron clouds. As shown in Figures 2.9a and b, based on DFT calculations, the C_2H_6 molecules are bound in a pocket defined by four phenyl rings.

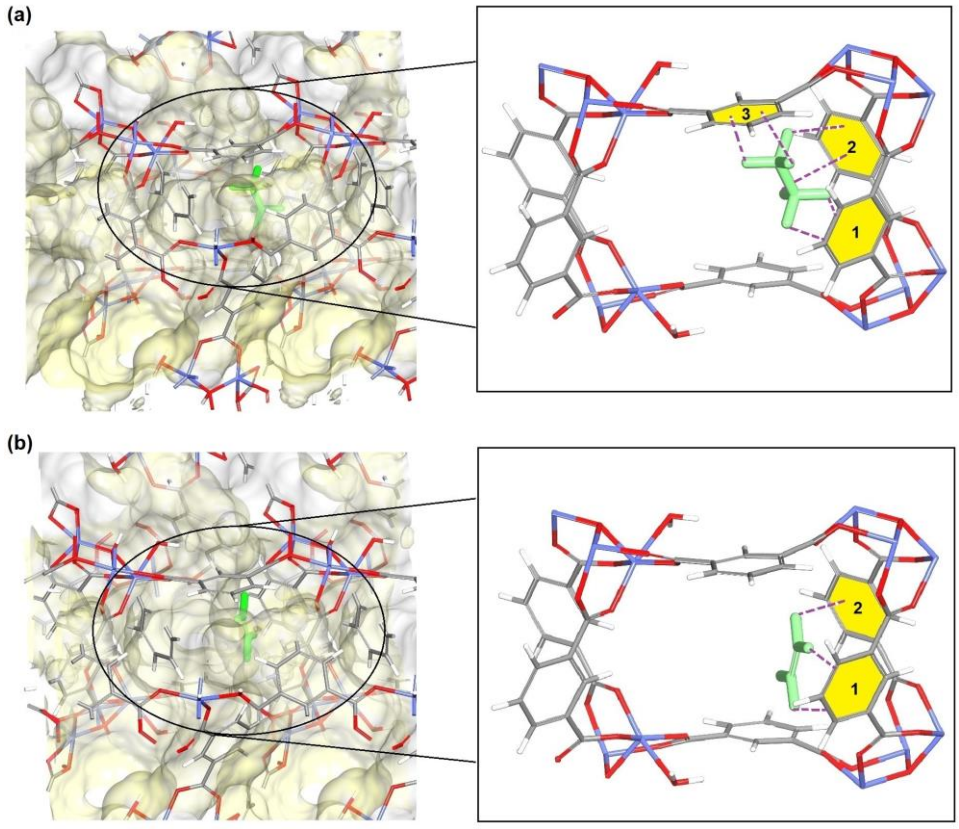

Figure 2.9 Comparison of the preferential (a) C_2H_6 and (b) C_2H_4 adsorption sites (Co blue, O red, C dark gray, H white) observed by DFT-D3 calculations.

C−H···π interactions exist between the C_2H_6 molecule and the phenyl rings within the cavity. Although C−H···π interactions are dominated by dispersion, as compared to other noncovalent interactions involving permanent dipoles/quadrupoles, the cavity of MUF-15 complements the size of the C_2H_6 molecule to enable C−H···π interactions between all six hydrogens of C_2H_6 and three adjacent phenyl rings. In contrast, the C_2H_4 molecule shows short contacts only with two parallel edges of the cavity. Thus, its lower binding energy can be attributed to the lack of strong permanent dipoles on the framework and the reduced number of C−H···π interactions. Beside the number of C−H···π interactions, C_2H_6 as a more polarizable molecule can interact more strongly by induced dipole interactions with the framework compared to the less polarizable C_2H_4 molecule.

The underlying mechanism behind C_2H_6-selective behaviour of MUF-15 was further investigated by the adsorption behaviour of acetylene, as another guest molecule from C2 hydrocarbons family which has the highest polarity and lowest polarizability (Table 2.3).

Table 2.3 Physicochemical properties of various gases.[110, 235-236]

	Boiling point (K)	Molecular dimensions (Å)	Polarizability (Å^3)	Quadrupole moment× 10^{26}/esu cm^2	Dipole moment ×10^{18}/esu cm^2
C_2H_2	188.4	3.32×3.34×5.70	3.33-3.93	+7.5	-
C_2H_4	169.4	3.28×4.18×4.84	4.25	+1.5	-
C_2H_6	184.5	3.81×4.82×4.08	4.43-4.47	+0.65	-

Adsorption isotherms of C_2H_2 for MUF-15 were measured, and interestingly MUF-15 adsorbed less C_2H_2 than both C_2H_4 and C_2H_6 at low pressure (Figure 2.10a).

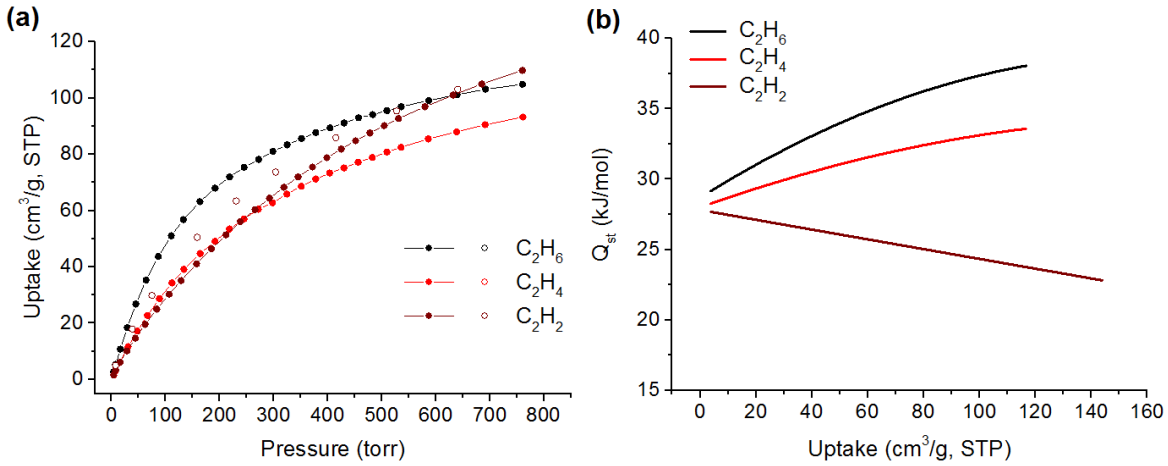

Figure 2.10 (a) Experimental adsorption isotherm of C_2H_2 in comparison to C_2H_6 and C_2H_6 by MUF-15 at 293 K. (b) Isosteric heat of adsorption plots for the adsorption of C_2H_2 in comparison to C_2H_6 and C_2H_4 by MUF-15.

The shape of C_2H_2 adsorption isotherm also was more linear than other two, which implies less interaction of C_2H_2 with framework. To calculate adsorption strength of C_2H_2 quantitatively, Q_{st} of C_2H_2 was calculated. Expectedly, Q_{st} of C_2H_2 (27.5 kJ/mol) was much lower than that of C_2H_4 and C_2H_6 (28.2 kJ/mol and 29.2 kJ/mol, respectively) (Figure 2.10b). This lower affinity for C_2H_2 again confirms that the dominating guest-host interaction in MUF-15 is dispersive (van der Waals) interactions rather than the interaction between permanent dipoles of pore surface and quadrupoles of guest molecules. It is a rare phenomenon for a porous material to selectively adsorb a molecules of low polarity

(quadrupole moment) over polar molecules. To best of our knowledge, MUF-15 is the first MOF reported that exhibits the selective adsorption of C_2H_6 over *both* C_2H_4 and C_2H_2.

Building on these results, we then demonstrated the feasibility of using MUF-15 for C_2H_6/C_2H_4 separations under the dynamic conditions encountered in industrial processes. A home-built breakthrough apparatus was designed and constructed to measure the gas separation performance of the MOFs under dynamic conditions (Figure 2.11 and 2.12).

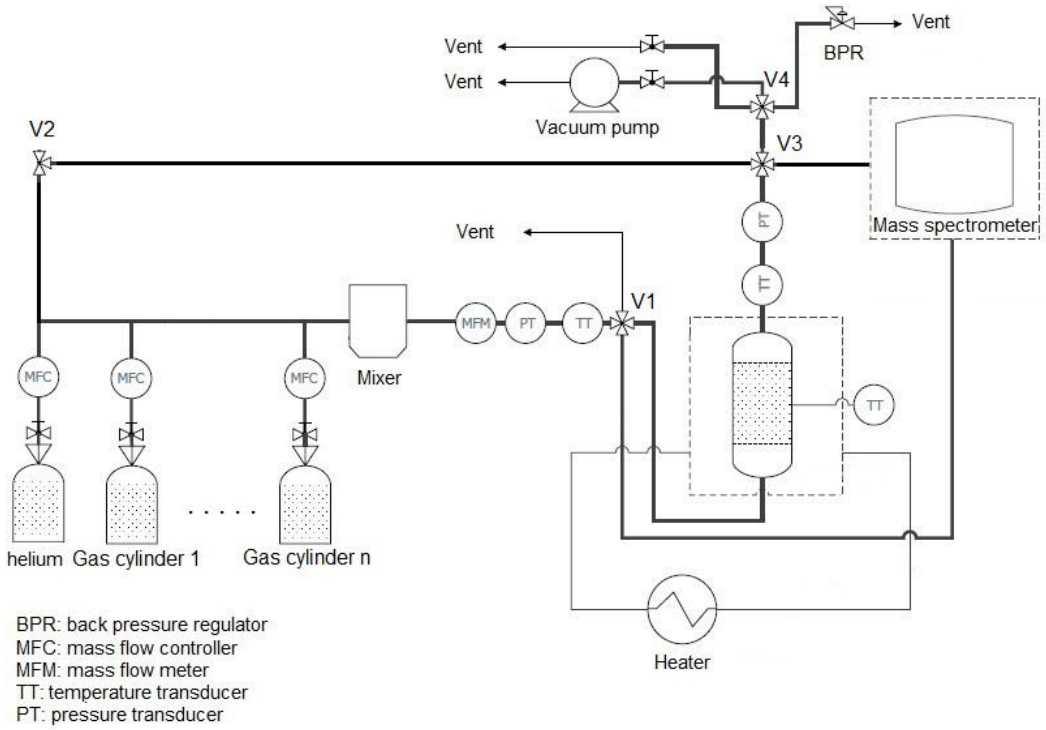

Figure 2.11 A schematic of the experimental column breakthrough apparatus.

A SRS UGA200 mass spectrometer was used to analyse the composition of the feed and outlet gases at 1-1.1 bar at 20 °C. The mass spectrometer was first calibrated to give a reliable quantitative result. As the instrument was factory-calibrated for nitrogen, a nitrogen reservoir with known pressure was introduced to the system to calibrate the instrument for pressure reduction effect (caused by capillary tube and the performance curve of the pumps) and head sensitivity. One of these factors can be kept constant to be able to fix the other one. Both factors cannot be determined; therefore, each time the instrument is calibrated, one of the factors will be assumed to be correct. Here, sensitivity factor was kept as its default number, and reduction factor was adjusted until the pressure determined by mass spectrometer was equal to pressure shown by pressure gauge. After fixing the pressure reduction factor, the mass spectrometer was calibrated for all the gases using in the experiment one by one. This was done by determining scaling factor for each gas in the instrument. To do this, single gas

of all the components with known pressure were introduced to the mass spectrometer and their scaling factors were manipulated until pressure monitored by mass spectrometer was equal to pressure shown by pressure gauge. In the case of ethane/ethylene separation, a mass of 30 was used for ethane, 2 for helium and 28 for ethylene. It should be noted that ethane spectrum also generates a peak at mass 28 with an intensity 47% of that of the total peak. Therefore, during the calculation of composition for ethylene, the contribution of this peak from ethane should be subtracted.

Figure 2.12 A photo of our breakthrough test apparatus (It should be noted that the upper part of the apparatus is used for the measurement of membrane permeability).

The performance and accuracy of our homemade breakthrough apparatus was established by reproducing breakthrough results reported in the literature and consistent results were obtained.[201, 226, 237] As an example, our breakthrough results for the separation of ethane from ethylene by ZIF-4 is compared with that of Hartmann's group[226] and CO_2 from CH_4 by 13X zeolite is compared with that of Yi's group[237]. The exact feed characteristics and adsorbent amounts was employed to mimic the breakthrough experiments reported by Hartmann's group.

ZIF-4 experiment

Before starting the measurement, an empty bed experiment was performed to obtain the elapsed times of the gas mixture to pass through the adsorption column and reach the mass

spectrometer (Dead volume measurements). At this stage, bed was free of adsorbents and a gas mixture containing 0.1 ml_N/min of helium, 0.45 ml_N/min of ethane and 0.45 ml_N/min of ethylene (the same flow rate as presented in literature[226]) was passed through the bed at 1 bar and 293 K. Mass flow meters were set on the desired flowrates and the composition of the mixture was monitored by mass spectrometer (by opening the V1 to mass spectrometer). Once the intended gas compositions were obtained and they were steady state, V1 was closed and mass flowmeters were set on zero (keeping the gas feed behind the adsorption column). Upstream and adsorption column was then kept under vacuum for 15 min by opening V3 and V4 to the bed, and then filled with helium gas at 1 bar by closing V4, opening V2 and opening V3 to adsorption column. Once the bed and upstream pipes were filled with helium at 1 bar, V2 was closed, V1 was opened to the bed and mass flow controllers were set again to the previous flowrates. It should be noted that back pressure regulator was connected to the system to maintain the pressure around 1.1 bar during the whole processes (except vacuuming the bed). The outlet gas stream from the bed was monitored by mass spectrometer. The following raw data was obtained from mass spectrometer (Figure 2.13).

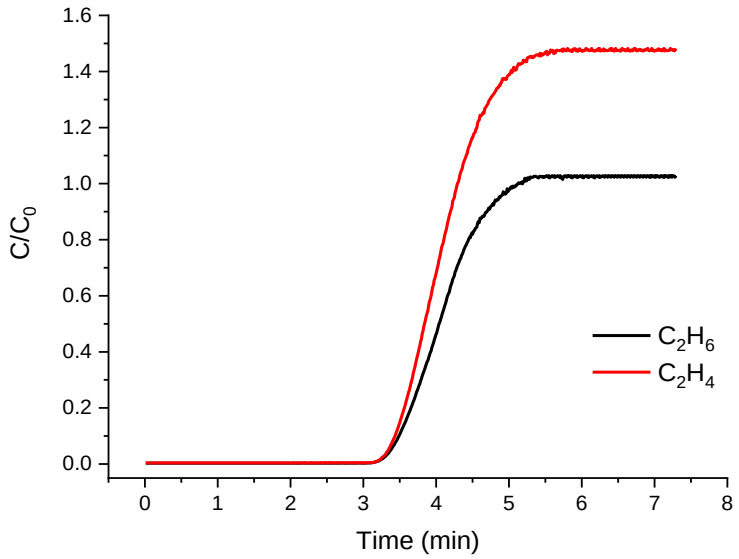

Figure 2.13 Raw breakthrough data after doing an empty breakthrough test (with no adsorbent present) for an equimolar mixture of ethane/ethylene at 1.05 bar and 293 K. C_0 is the initial concentration of the component.

As can be seen from Figure 2.13, all the gases are detected by the mass spectrometer in the same time (as a result of good mixing) after approximately three minutes. This three minute dead time must be subtracted from the breakthrough curves obtained from the bed packed with adsorbent. While an equimolar mixture of ethane/ethylene passes through the bed, the outlet concentration of ethylene seems to be significantly higher than that of ethane.

Obviously, this is because of the 47% contribution of 28 mass generated by ethane ionization, and then need to be subtracted from ethylene 28 mass. After subtraction, an identical breakthrough curves were observed for ethylene, as expected (Figure 2.14).

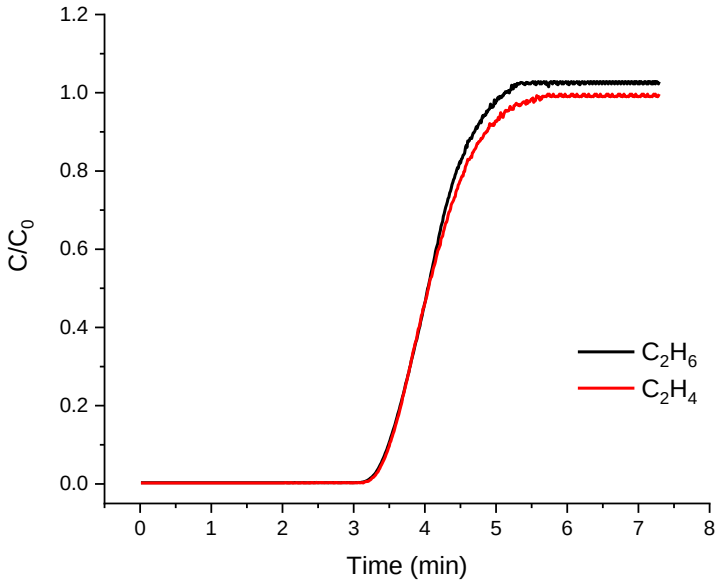

Figure 2.14 Breakthrough curves of C_2H_6 and C_2H_4 from an empty bed after correcting 47% contribution of 28 mass generated by ethane ionization at 1.05 bar and 293 K.

In a typical breakthrough experiment, 0.450 g of activated ZIF-4 (The synthesis of ZIF-4 was performed according to the procedure published by Park et al.[238]) were placed in an adsorption column (6.4 mm in diameter × 11 cm in length) to form a fixed bed. The column then is left under vacuum for another 5 hours at 150 °C. After the bed was cooled to the 20 °C, the column was purged under a 20 mL_N/min flow of He gas for 1 hr at 1.05 bar prior to the breakthrough experiment. The same gas compositions and the preparation procedure was employed but for the packed bed this time. The outlet composition was continuously monitored by the mass spectrometer until complete breakthrough was observed (Figure 2.15a). After subtracting the time required by adsorbates to pass through an empty bed and reach mass spectrometer and correcting for ethane mass 28 contribution the following breakthrough curves were obtained (Figure 2.15b).

These breakthrough curves were then compared with the breakthrough curves reported by Hartmann and co-workers and as can be seen from Figure 2.16, they are identical to the previously reported breakthrough curves.

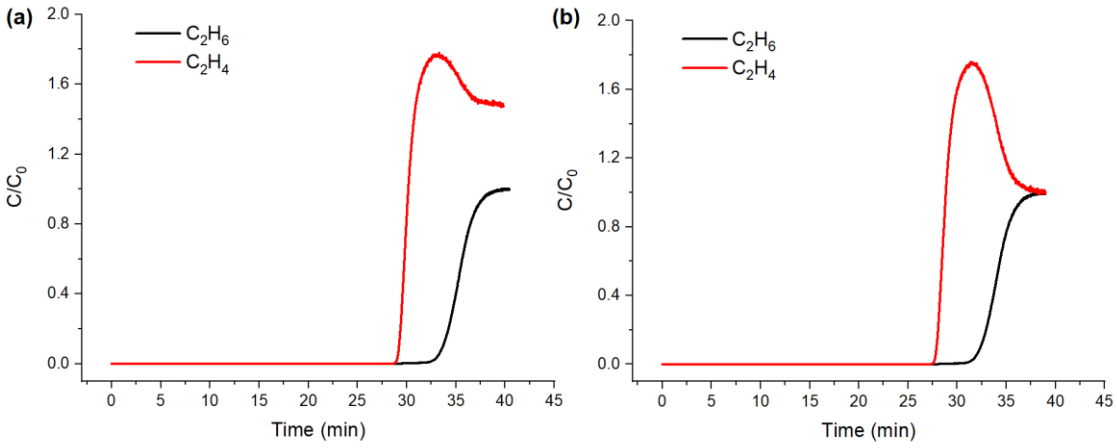

Figure 2.15 Breakthrough curves of C_2H_6 and C_2H_4 in and adsorption column packed with ZIF-4 at 1.05 bar and 293 K (a) before correcting for ethane mass 28 contribution and elapsed time obtained from empty bed test and (b) after correcting for ethane mass 28 contribution and elapsed time obtained from empty bed test.

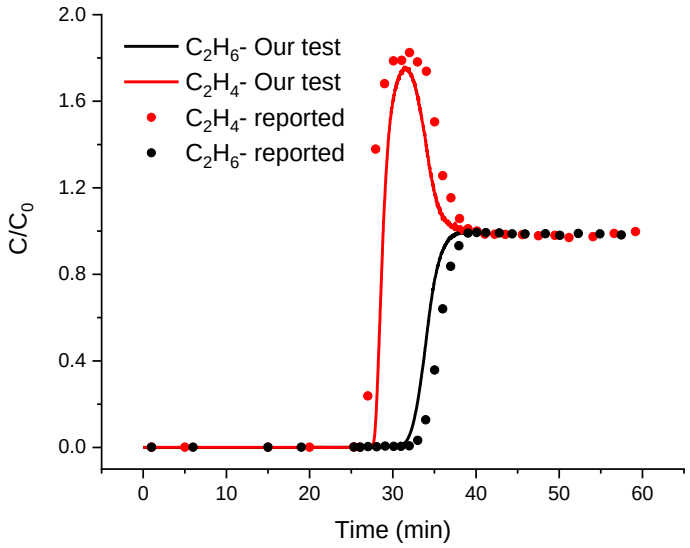

Figure 2.16 Breakthrough curves obtained from our apparatus for a mixture of ethane/ethylene in an adsorption column packed with ZIF-4 at 293 K and 1.05 bar in comparison with the reported breakthrough curved by Hartmann and co-workers in the exact same operational conditions and feed characteristics.

13X experiment

The same procedure and data processing used for ZIF-4 experiment was employed for 13X experiment. As the adsorption column used in the Yi's group was large and flowrate was higher, we scaled down the bed characteristics and flow rate equally to mimic their breakthrough performance. In this regard, flowrate, adsorption column volume and amount of adsorbents was divided by 10. Our adsorption bed (6.4 mm in diameter × 11 cm in length) was packed with 1 g of 13X zeolite and a flowrate of 1.1 ml_N/min for CH_4 and 0.9 ml_N/min

for CO_2 and 0.2 ml_N/min for He was passed through the adsorption bed at 1.05 bar and 293 K. A mass of 44 was chosen for CO_2 and 15 for CH_4. The following empty bed breakthrough curves was achieved (Figure 2.17), thus 1.9 min was subtracted from packed bed breakthrough experiments. The final breakthrough also was achieved and is compared with the literature in Figure 2.18.

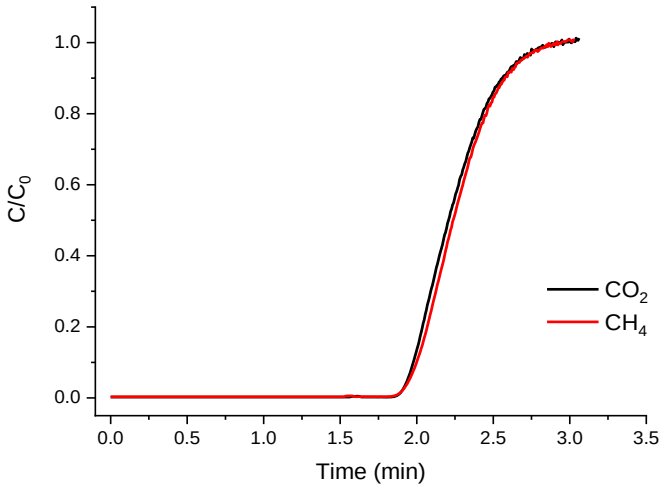

Figure 2.17 Breakthrough curve of CO_2 and CH_4 from empty bed at 1.05 bar and 293 K.

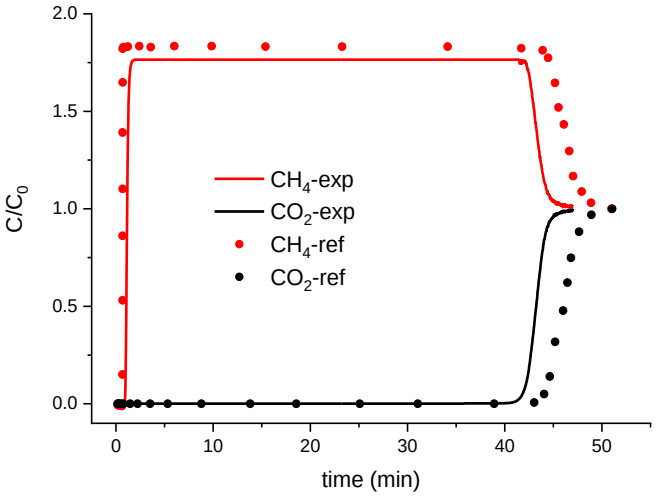

Figure 2.18 Breakthrough curves obtained from our apparatus for a mixture of CO_2/CH_4 in an adsorption column packed with 13X at 293 K and 1.05 bar in comparison with the reported breakthrough curved by Yi and co-workers.

After validating our breakthrough apparatus, breakthrough measurements using a fixed adsorbent bed containing ~1 g of MUF-15 were conducted at room temperature. C_2H_6/C_2H_4 mixtures of 50/50, 25/75 and 10/90 were used as feeds to mimic a range of industrial process conditions (Figures 2.19a, and see Appendix A for the rest). C_2H_4 eluted through the bed first to yield an outflow of pure gas. Conversely, because C_2H_6 is more efficiently adsorbed

by the MUF-15 bed, it breaks through following a substantial time lapse. These results indicate that MUF-15 can efficiently trap C_2H_6 to yield pure C_2H_4. The separation performance of MUF-15 was quantified in terms of its productivity for comparison with other high-performance C_2H_6-selective MOFs. The productivity of these adsorbents is defined as the quantity of ethylene with a purity in excess of 99.95% produced per unit mass of material starting from an equimolar ethane/ethylene mixture.[119, 227] Productivity was calculated based on both experimental and simulated breakthrough curves for MUF-15 and materials previously reported in the literature (Table 2.4). MUF-15 possesses a productivity of 14 litres of polymer-grade ethylene gas per kg of material with a single adsorption step, which exceeds that of other top-performing ethane-selective MOFs such as MAF-49[119] (5.3 L/kg), $Cu(Qc)_2$[227] (4.3 L/kg), IRMOF-8[216] (2.5 L/kg) and PCN-250[222] (10 L/kg), but trails the recently-reported MOF $[Fe_2(O_2)(dobdc)]$[229] (19.3 L/kg).

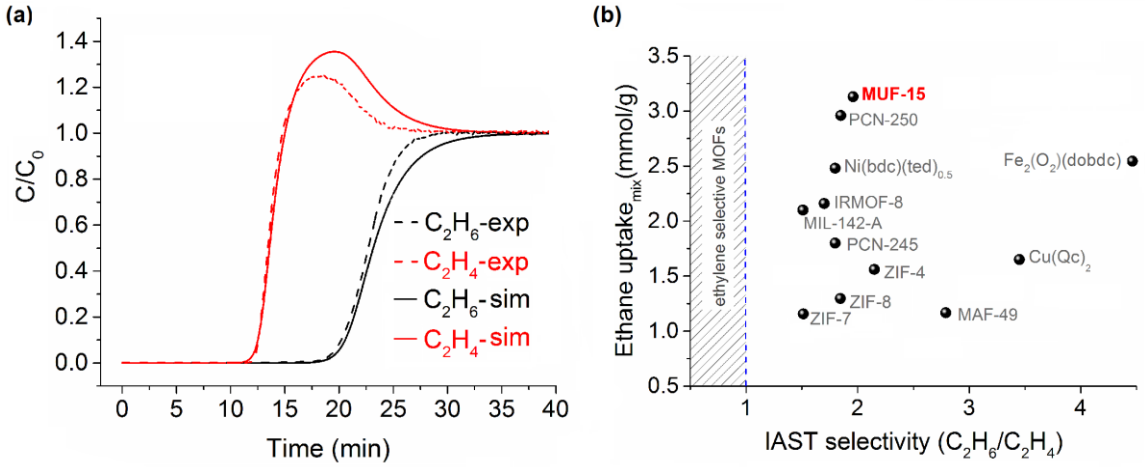

Figure 2.19 (a) Simulated and experimental breakthrough curves for a 50/50 C_2H_6/C_2H_4 mixture at 293 K and 1.1 bar in an adsorption column packed with MUF-15. (b) Ethane uptake from an equimolar mixture of C_2H_6/C_2H_4 as a function of IAST selectivity for the best ethane-selective materials reported to date.

Table 2.4 Separation metrics of C_2H_4-selective MOFs reported in the literature.

MOF	T (°C)	P (bar)	$Q_{st,ethane}$ (kJ/mol)	$Q_{st,ethylene}$ (kJ/mol)	$q_{ethane,mixed}$ (mmol/g)	$q_{ethylene,mixed}$ (mmol/g)	Selectivity (C_2H_6/C_2H_4)	$Productivity_{sim}$ (L/kg)	$Productivity_{exp}$ (L/kg)
IRMOF-8[119]	25	1	52.5	50	2.16	1.25	1.7	20.3	2.5
MAF-49[119]	43	1	61	48	1.21	0.44	2.7	17.2	5.3[a]
MIL-142A[219]	25	1	27.2	26.2	2.1	1.39	1.51	15.9	6.7
Ni(bdc)(ted)[224]	25	1	21.5	18.3	2.48	1.38	1.8	24.6	-
PCN-245[220]	25	1	22.8	21	1.8	1	1.8	17.9	5.8
ZIF-4[226]	20	1	-	-	1.56	0.73	2.15	18.5	6.6
PCN-250[222]	25	1	23.2	21.1	2.96	1.6	1.85	30.4	10
ZIF-7[225]	25	1	-	-	1.2	0.8	1.5	21	2
ZIF-8[223]	22	1	17.2	16.1	1.26	0.7	1.8	13.4	0.4
$Cu(Qc)_2$[227]	25	1	30	25.4	1.65	0.48	3.45	26.2	4.34 [b]
Fe_2O_2dobdc[229]	25	1	66.8	36.5	2.53	0.57	4.4	45.02	19.3[c]
MUF-15	**20**	**1**	**29.2**	**28.2**	**3.13**	**1.6**	**1.96**	**34.2**	**14**

[a] The reported productivity value is 6.2 L/kg. [b] The reported productivity value is 4.4 L/kg. [c] The reported productivity value is 19.93 L/kg.

In isolation, neither high uptake nor good selectivity are sufficient for highly productive MOFs. Both attributes are required in tandem, but they are seldom simultaneously combined in the same material. Relative to other materials, MUF-15 benefits from particularly good uptake. As highlighted in Figure 2.19b, the uptake of ethane from a 50/50 mixture of ethane and ethylene at 1 bar (ethane uptake$_{mix}$) calculated for MUF-15 exceeds that of other known ethane-selective adsorbents. This results in a longer period of time during which pure C_2H_4 can be obtained from the column outlet i.e. it underpins the excellent productivity of MUF-15. Looking ahead, since improvements in selectivity tend to come associated with costs relating to regeneration and instability, high-performance materials that can operate under realistic operating conditions in the future are likely to arise from further enhancements in ethane capacity.

To investigate separations at low C_2H_6 concentrations and higher operating pressures, we simulated breakthrough curves under these conditions. First, a reliable mass transfer coefficient for the simulated breakthrough curves was estimated from experimental data (see the section 1.4 of the Chapter 1for further detail about this calculations). Upon optimization, this coefficient leads to an excellent match between simulated and experimental breakthrough curves. We subsequently predicted breakthrough curves using feed compositions of 1/99 and 0.1/99.9 C_2H_6/C_2H_4 (Figures 2.20a and see Appendix A for the 0.1/99.9 mixture). These calculations revealed that MUF-15 is capable of eliminating trace quantities of C_2H_6 from C_2H_4, as often required in industrial settings, and we anticipate that this result could be verified experimentally. To investigate the performance of MUF-15 at higher pressure, as required by pressure-swing adsorption processes, breakthrough curves were predicted at different pressures. Firstly, isotherms of C_2H_6 and C_2H_4 were measured at 298 K up to 10 bar (Figure 2.20b). From IAST calculations for a 25/75 C_2H_6/C_2H_4 mixture (Figure 2.20c) at 10 bar, we found that MUF-15 maintains its preferential adsorption of C_2H_6 over C_2H_4 with a selectivity of 1.79. This selectivity result was then used to predict breakthrough curves of C_2H_6 and C_2H_4 across a range of elevated pressures (Figure 2.20d). These predicted breakthrough curves demonstrate that MUF-15 is capable of removing C_2H_6 from C_2H_4 at high pressures under dynamic conditions. This is notable since productivity gains arise from working at higher pressures. For example, the productivity of MUF-15 nearly doubles in going from atmospheric pressure to 20 bar (See appendix A).

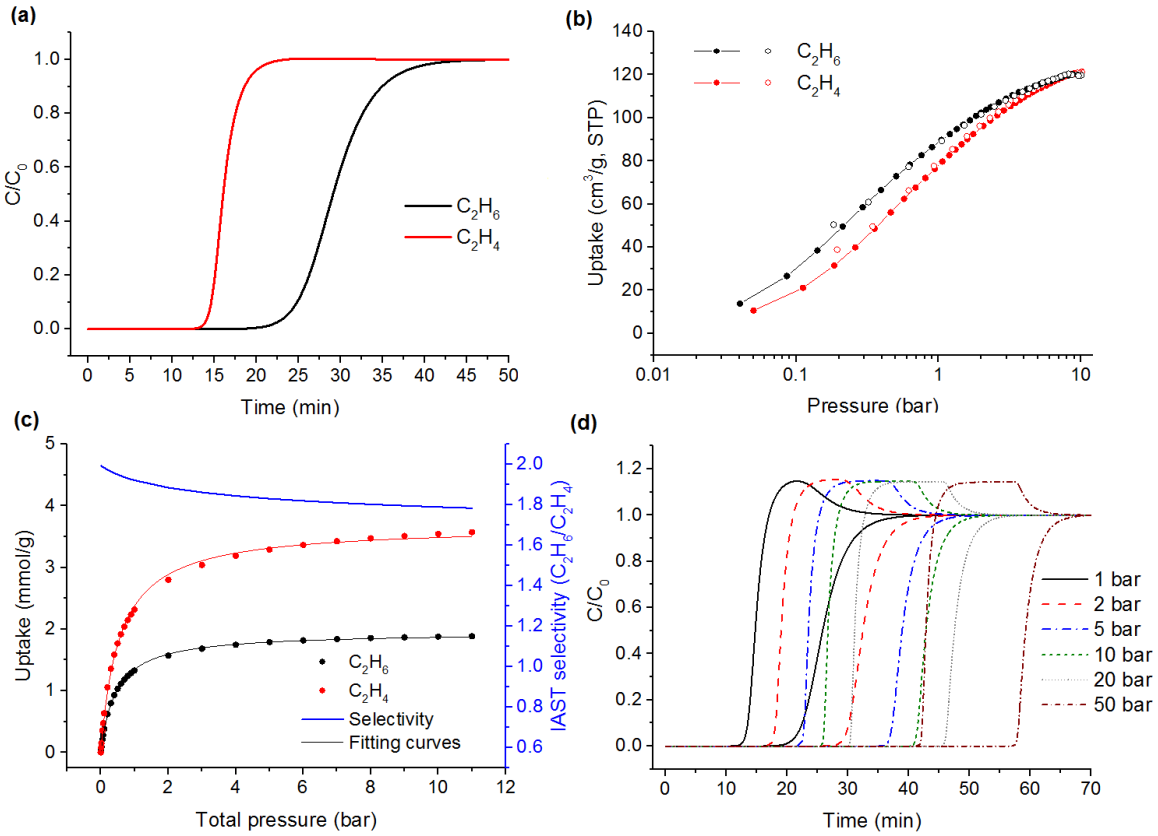

Figure 2.20(a) Simulated breakthrough curves for a mixture of 0.1/99.9 C_2H_6/C_2H_4 at 293 K and 1.1 bar. (b) High pressure C_2H_6 and C_2H_4 adsorption (filled circles) and desorption (open circles) isotherms of MUF-15 at 298 K. (c) Mixed isotherms and selectivity of MUF-15 predicted by IAST for a mixture of 25/75 C_2H_6/C_2H_4 at 293 K at high pressures. (d) Predicted breakthrough curves at different operating pressures for a 25/75 mixture of C_2H_6/C_2H_4 at 298 K.

To enable economical deployment in industrial settings, the adsorbent should also possess good regenerability and recyclability. To test the recyclability of MUF-15, breakthrough separation experiments were cycled numerous times (Figure 2.21a). The experimental cycling results indicate that there was no noticeable loss in the C_2H_6 adsorption and separation capacity for MUF-15 over 12 cycles. The regenerability of MUF-15 was also investigated by either placing it under vacuum or by purging with an inert gas. The framework can be fully regenerated between cycles in this manner, specifically by placing it under vacuum for around 10-15 mins or by purging with helium at 70 °C and 1.1 bar (Figure 2.21b).

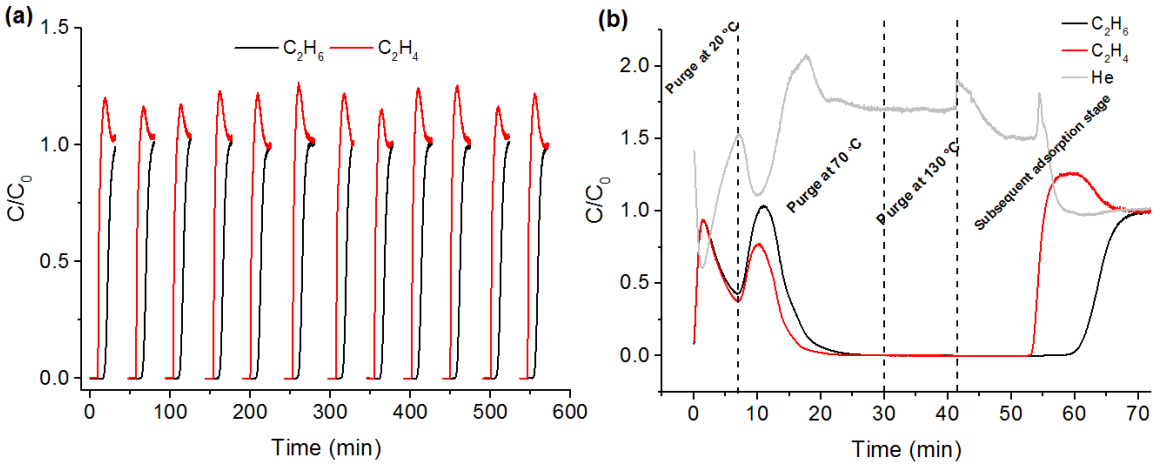

Figure 2.21 (a) C_2H_6/C_2H_4 separation cycles for a 25/75 C_2H_6/C_2H_4 mixture lasting for 600 min. Each separation process was carried out at 293 K and 1.1 bar and MUF-15 was regenerated by being kept under vacuum at ambient temperature for 20-30 min. (b) Desorption behaviour of the adsorbates through heating the column at 1.1 bar under a helium flow of 5 mL_N/min. Ethane and ethylene are both completely removed from the column upon heating to 70 °C. No adsorbates are removed upon further heating to 130 °C.

2.3 Conclusion

We have targeted a unique MOF for the direct production of C_2H_4 by selectively adsorbing C_2H_6 over C_2H_4 from a C_2H_6/C_2H_4 mixture at ambient condition. Owing to its high selectivity and appreciable C_2H_6 uptake, MUF-15 possesses one of the highest C_2H_4 productivity among those found in the well-established C_2H_6-selective MOFs. The underlying mechanism behind this C_2H_6 selectivity are the close contacts between guest molecules and pore surfaces decorated with aromatic rings (inert surface) that induce optimal van der Waal's interactions. Furthermore, due to its moderate heat of adsorption, MUF-15 can be easily regenerated by purging at moderate temperatures or introduction of vacuum for a short time. MUF-15 is readily synthesized from simple and inexpensive reagents and can be recycled for repeated separations cycles without any loss of performance. The combination of these attributes represents significant addition to the portfolio of known C_2H_6-selective MOFs. By providing a clear illustration of how such selectivity and uptakes may be achieved using simple components, this framework defines the way forward for challenging separations.

2.4 Experimental and computational section

2.4.1 General procedures

All starting compounds and solvents were used as received from commercial sources without further purification unless otherwise noted. Zeolite 13X with a batch number of

84107 was purchased in the form of 4-8 mesh beads from Ajax chemicals. Elemental analyses were performed by the Campbell Microanalytical Laboratory at the University of Otago, New Zealand. Care was taken to limit the exposure of all MOFs to the atmosphere.

2.4.2 Thermogravimetric Analysis (TGA)

Thermogravimetric analyses were performed on a TA Instruments Q50 instrument. Freshly prepared MOF samples were washed with MeOH, and then activated at 120 °C under vacuum for 10 hours. Samples were exposed to air for 1 hour and then transferred to an aluminum sample pan, and then measurements were commenced under an N_2 flow with a heating rate of 5 °C /min.

2.4.3 Single crystal X-ray diffraction

A Rigaku Spider diffractometer equipped with a MicroMax MM007 rotating anode generator (Cu_α radiation, 1.54180 Å), high-flux Osmic multilayer mirror optics, and a curved image plate detector was used to collect SCXRD data. As-synthesized samples were washed several times with MeOH before being mounted on the instrument. All the data were collected at room temperature. The SCXRD data were integrated, scaled and averaged with FS Process.[239] SHELX[240] (under OLEX[241]) was used for structure solution and refinement. The Solvent Mask function in OLEX was used to mask out contributions from guest molecules occluded in the framework pores.

All atoms were found in the electron density difference map. Electron density difference maps were carefully analyzed for the possible presence of disordered framework components. All non-hydrogen atoms and coordinated waters were refined anisotropically A solvent mask was calculated and 582.0 electrons were found in a volume of 2654 $Å^3$ in 1 void. This is consistent with the presence of 4[CH_3OH] per formula unit which accounts for 576.0 electrons. Methanol was chosen as uncoordinated molecules in the pores as it was the main solvent used for MUF-15 synthesis.

2.4.4 Powder X-ray diffraction patterns

All powder X-ray diffraction experiments were carried out on a Rigaku Spider X-ray diffractometer with Cu K_α radiation (Rigaku MM007 microfocus rotating-anode generator), monochromated and focused with high-flux Osmic multilayer mirror optics, and a curved image plate detector. The data were obtained from freshly prepared MOF samples that had been washed several times with MeOH.. The two-dimensional images of the Debye rings were integrated

with 2DP to give 2θ vs I diffractograms. Predicted powder patterns were generated from single crystal structures using Mercury.

2.4.5 Low-pressure gas adsorption measurements

Gas adsorption isotherms were measured with a volumetric adsorption apparatus (Quantachrome-Autosorb-iQ2). Ultrahigh-purity gases were used as received from BOC Gases. The as-synthesized samples were washed with anhydrous methanol several times and about 100 mg was transferred into a pre-dried and weighed sample tube and heated at rate of 10°C/min to a temperature of 120 °C under a dynamic vacuum with a turbomolecular pump for 20 hours. Accurate sample masses were calculated using degassed samples after sample tubes were backfilled with nitrogen. Surface areas were determined from the N_2 (77 K) adsorption isotherm collected by application of the BET model. Bath temperatures of 273 K and 293 K were precisely controlled with a recirculating control system containing a mixture of ethylene glycol and water. The low temperature (77 K) was controlled by a Dewar filled with liquid N_2.

2.4.6 High-pressure gas adsorption measurements

High-pressure adsorption isotherms were measured on a PCT Pro instrument from Setaram. About 0.4 g of activated sample (activated at 120 ^{o}C under vacuum overnight) was transferred into a 4 mL stainless steel sample holder inside a glove box under an Ar atmosphere, the sample mass was weighed using decrement method due to the insufficient measuring range of the balance for the sample holder. The sample holder was then transferred to the PCT Pro, connected to the instrument's analysis station via a VCR fitting, and evacuated at 40 ^{o}C for at least 2 h. The sample holder was placed inside a stainless-steel recirculating dewar connected to a Julabo F12-E0 isothermal bath filled with Ethylene glycol aqueous solution (1:3, v/v), for which the temperature stability is $\pm$ 0.02 °C.

To eliminate the influence of fluctuations in room temperature, the manifold was set as 40 ^{o}C. He was used to determine the void volume in the sample holder by using the method of expanding from the dosing manifold to the evacuated sample holder and recording the change in pressure, assuming He adsorption is negligible. The PCT Pro is equipped with a 15 bar transducer (accuracy of ± 0.12% of the reading) for the measurements up to 10 bar. By default, the direct method was used to calibrate the void volume. Ultrahigh grade (99.999%) of C_2H_6, C_2H_4 and He were used for all the adsorption measurements. The background adsorption was measured with empty holder at 273 and 298 K by the direct

method. The background correction on all isotherms was performed with the "subtract" function directly within Origin.

2.4.7 Physical properties and pore characteristics calculations

The Zeo++[242] code and RASPA2[232] were used to characterize the geometric features of the crystal structure of MUF-15 by calculating the pore volume with the use of a helium probe atom, the pore limiting diameter (i.e., the diameter of smallest pore window), the largest cavity diameter (i.e., the diameter of the largest sphere that can fit within the pores), and the surface area accessible to a H_2 probe (a N_2 probe produce a surface area of zero) using the coordinated found by X-ray crsytallography. The Accelrys Materials Studio 7.0 software package was used to visualize the MOF structure and pore topology.

2.4.8 IAST selectivity calculations for binary gas mixtures

Mixed gas adsorption isotherms and gas selectivities for five different mixtures of C_2H_6/C_2H_4 (25/75, 50/50, 10/90, 1/99, 0.1/99.9) were calculated at 293 K based on the ideal adsorbed solution theory (IAST) proposed by Myers and Prausnitz (See selected experimental and computational methods in chapter 1 for more details)[118]. The pyIAST package[182] was used to perform the IAST calculations. In order to predict the sorption performance of MUF-15 towards the separation of binary mixed gases, the single-component C_2H_6 and C_2H_4 adsorption isotherms were first fit to a dual site angmuir model as below:

$$q = \frac{q_1 b_1 P}{1 + b_1 P} + \frac{q_2 b_2 P}{1 + b_2 P} \quad (1)$$

Where q is the uptake of a gas; P is the equilibrium pressure and q_1, b_1, q_2 and b_2 are constants. The fitting parameters are shown in Appendix A, section IAST. These parameters were used subsequently to carry out the IAST calculations.

2.4.9 Breakthrough separation experiment

In a typical breakthrough experiment, 1 g of an activated sample of MUF-15 was placed in an adsorption column (6.4 mm in diameter × 11 cm in length) to form a fixed bed. The adsorbent was activated *in situ* at 120 °C under high vacuum for 6 hours and then the column was left under vacuum for another 2 hours while being cooled to 20 °C. The column was then purged under a 20 mL_N/min flow of He gas for 1 hr at 1.1 bar prior to each breakthrough

experiment. A gas mixture containing different mixtures of C_2H_6, C_2H_4 and He gas was introduced to the column at 1.1 bar and 20 °C at 8 mL_N/min. The flow rate of inert He gas in all the experiments was kept constant at 4 mL_N/min. The operating pressure was controlled at 1.1 bar with a back-pressure regulator. The outlet composition was continuously monitored by the mass spectrometer until complete breakthrough was observed. The adsorbent was regenerated under vacuum for 15-20 minutes between each cycle.

Regeneration profile

The desorption behaviour of ethane and ethylene from the adsorption column was also investigated. Once the adsorbent was saturated with an equimolar mixture of ethane and ethylene, the column was purged with a helium flow of 5 mL_N/min for 7 mins at 20 °C at 1.1 bar. Then column was then heated to 70 °C with a ramp of 10 °C/min for 23 mins. Finally it was heated to 130 °C with the same ramping for 12 min before cooling to 20 °C. A breakthrough measurement was then performed, which showed that the absorbent had been fully regenerated.

2.4.10 Breakthrough curve simulations

Breakthrough curves were simulated based on the procedure presented earlier. Adsorption bed characteristics and other related parameters for simulation are presented in Table 2.5.

Table 2.5 Adsorption column parameters and feed characteristics used for the simulations.

Adsorption bed	***Feed***
Length: 110 mm Diameter: 6.4 mm Amount of adsorbent in the bed: 1 g Bed voidage: 0.77 Adsorbent average radius: 0.2 mm k_{ethane}: 0.009 s^{-1} $k_{ethylene}$: 0.013 s^{-1}	Flow rate: 8 mL_N/min Temperature: 293 K Pressure: 1.1 bar Carrier gas (He) flow rate: In all the simulated breakthrough curves feed was diluted with 4 mL_N/min of helium unless otherwise stated. Purge gas: He with a flow rate of 20 mL_N/min
Langmuir fitting	
See Appendix A	

2.4.11 Comparison of separation performance for different MOFs

To unambiguously compare the separation performance of different materials, ethylene productivity, IAST selectivity and mixture uptakes (the amount of gas uptake taken by adsorbent in presence of other gases, $q_{i,mix}$) for an equimolar mixture of ethane/ethylene and isosteric heats of adsorption for the top-performing ethane-selective MOFs reported in the literature were compared. The C_2H_4 productivity was defined by the breakthrough amount of ethylene (defined as a volume of gas at STP) from an adsorption bed packed with 1 kg of MOF. The breakthrough amount was calculated by integration of the breakthrough curves during a period from t_1 to t_2 during which the C_2H_4 purity is higher than or equal to a threshold value of 99.95%:

$$(C_2H_4)_{\text{Productivity}}: \frac{\int_{t_1}^{t_2} F_{C_2H_4,out}\, dt}{m_{MOF}} \qquad (2)$$

Where $F_{C_2H_4,out}$ the flowrate of effluent ethylene and m_{MOF} is the amount of MOF packed in the bed. Ethylene productivity was calculated based on both experimental and simulated breakthrough curves (termed as $\text{Productivity}_{exp}$ and $\text{Productivity}_{sim}$). Simulated breakthrough curves for an equimolar mixture of ethane/ethylene (without helium as a carrier gas) at 293 K and 1 bar were estimated using the method outlined earlier and assuming that gases quickly reach their equilibrium uptake during the dynamic breakthrough process. The single gas isotherms presented in the references were used to calculate IAST selectivity and to simulate breakthrough curves. Experimental breakthrough curves presented in the references were used to calculate $\text{Productivity}_{exp}$. It should be noted that experimental breakthrough curves data were extracted from these literature references using a plot digitizer program. Therefore, the $\text{Productivity}_{exp}$ values are estimates and not strictly based on threshold values of exactly 99.95% as we did not have the breakthrough data with sufficient precision.

2.4.12 DFT calculations

Static binding energies for ethane and ethylene in MUF-15 framework were calculated using density functional theory (DFT) as implemented in the software package VASP 5.4.4.[234] It is well-known that standard DFT methods based on generalized gradient approximation do not fully account for the long-range dispersion interactions between the framework and the bound gaseous adsorbates. To accurately estimate static binding energies for the guest molecules with MUF-15 framework, we implemented dispersion corrections

using DFT-D3 method.[233] Electron exchange and correlation were described using the generalized gradient approximation Perdew, Burke, and Ernzerhof (PBE)[243] form and the projector-augmented wave potentials were used to treat core and valence electrons. In all cases, we used a plane-wave kinetic energy cutoff of 600 eV and a Gamma-point mesh for sampling the Brillouin zone. The ionic coordinates were relaxed until the Hellman-Feynman ionic forces were less than 0.02 eV/Å. The initial location of the guest molecule (one guest molecule per cell) in the unit cell of MUF-15 was obtained from the classical simulated annealing technique using classical force field as implemented in sorption module in *Materials Studio.*[244] In the simulated annealing method, the temperature was lowered stepwise, allowing the gas molecule to reach a desirable configuration based on different moves such as rotation, translation and repositioning with preset probabilities of occurrence. This process of heating and cooling the system was repeated in several heating cycles to find the local minima. Forty heating cycles were performed where the maximum temperature and the final temperature were 10^5 K and 100 K, respectively. Static binding energies (ΔE) at 0 K in vacuum and in solvent (both water and methanol) were calculated using the following expression:

$$\Delta E = E_{MOF+Guest} - E_{MOF} - E_{Guest} \quad (3)$$

Where E_x refers, respectively, to the total energies of the MOF + guest complex, the MOF alone, and guest molecule.

Chapter 3

Isoreticular Analogues of MUF-15: Pore Tuning, Flexibility and C2 hydrocarbon separations

3.1 Introduction

The ability to tune the pore size and nature of MOF structures without changing their underlying topology has given rise to the isoreticular principle.[132, 135] Some of the most fascinating families of MOFs are porous compounds whose physical structure and chemical affinity can be fine-tuned, whilst keeping the basic topology of the framework unchanged.[35, 70, 135] This has allowed for the design of MOFs with a wide variety of applications. For instance, isoreticular chemistry enables design of MOFs with precise pore dimensions and favourable affinity by the right selection of organic linkers or metal ions so that they selectively adsorb specific guest molecules, while excluding other gases.[36-41] As an example, Chen and co-workers developed two isoreticular MOFs, [Cu(ina)$_2$] (Hina = isonicotinic acid) and [Cu(Qc)$_2$] (HQc = quinoline 5-carboxylic acid), to demonstrate the control of pore electrostatics and dimensions for improving C_2H_6/C_2H_4 selectivity through isoreticular approach.[37] Substitution of HQc ligand with Hina ligand resulted in an isoreticular MOF but with smaller pore size and stronger affinity towards C_2H_6, thus leading to a preferential adsorption of C_2H_6 over C_2H_4. These capabilities also enable substantial enhancement of gas storage in MOFs and have led to the design of materials with exceptional surface areas and pore volumes.[135, 245-248] Additionally, the isoreticular approach has been a great help for design and development of effective MOFs for catalysing reactions,[64, 249-250] luminescence,[70, 251] drug deliveries,[252-254] sensing,[74, 255-256] and so on. This unique ability has also led to significant improvements in design and development of MOFs with high thermal and physical stability compared to that of the parent MOF.[42-45] As one of the main strategies to design isoreticular MOFs, ligand functionalization in MOFs has been studied extensively and has been demonstrated to enhance gas adsorption and chemical stability of many MOFs.[45, 257-265] More interestingly, ligand functionalization can induce interesting gas adsorption behaviour by designing flexible/dynamic MOFs. When exposing to certain stimuli, the structure of some MOFs can change. These frameworks which are referred as

flexible/dynamic MOFs are a unique subclass of these materials while other solid porous materials such as zeolites have a rigid framework.[46-47, 266-268]

Suitable pore characteristics and chemistry of MUF-15 motivated us to investigate the effect of different functional groups on its structural properties and gas separation performance. Based on the result of Chapter 2, crystal structure of MUF-15 shows that the hydrogen atom of 5-position carbon in phenyl ring is positioned towards the pore aperture. Thus substituting it with different functional groups may drastically change the properties and adsorption performance of MUF-15. For example, introduction of flouro group in the structure of MUF-15 may improve pore affinity towards CO_2 molecules through strong electrostatic interactions between fluorine and CO_2 molecules. As another example, introduction of large methoxy group in the structure of MUF-15 can significantly affect the pore dimensions and pore volume of MUF-15 as these groups occupy part of the pore volumes. Thus, different organic groups such as fluoro, hydroxy, bromo, nitro, methyl and methoxy, representing a broad range of different sizes and functionalities, were incorporated to the structure of MUF-15 to achieve six isostructural materials to MUF-15 as shown in Figure 3.1. It should be noted that phenyl ring itself has a significant impact on the electrostatics and affinity of the framework towards guest molecules as it was previously demonstrated by close interaction of C_2H_6 and C_2H_4 with phenyl rings revealed by DFT.

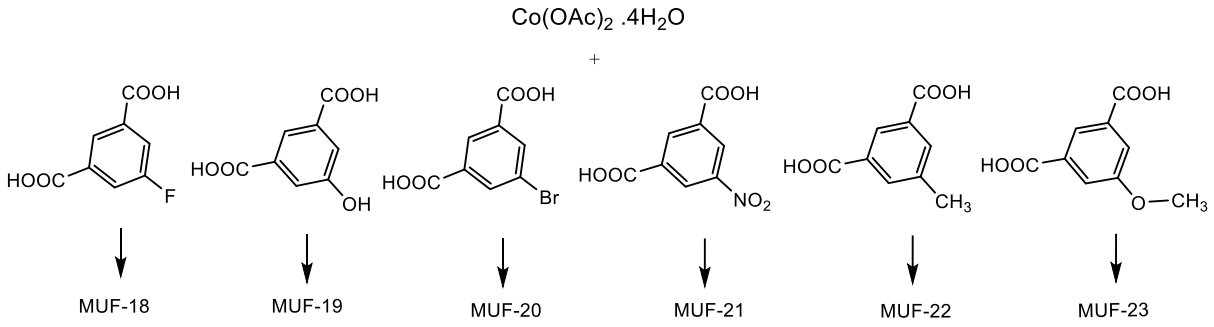

Figure 3.1 Composition of MUF-18-23 by introducing six different functional groups to the 5-position carbon of the phenyl ring.

3.2 Results and discussion

3.2.1 Design and synthesis of functionalized MUF-15 series

As described in the previous chapter, MUF-15 defines three intersected narrow zigzag 1-dimensional pores. These orthogonal channels run along the a, b, and c axes with pore-limiting windows of 8.5 × 3.5, 7 × 3.8, and 3.2 × 1.2 Å, respectively. As shown in Figure 3.2, phenyl rings of isophthalic ligands are pointing towards the pore windows. Such an interesting orientation of phenyl rings in the structure of MUF-15 suggests the introduction

of functional groups into these rings may hugely change the pore dimension of MUF-15 as illustrated in Figure 3.2. Moreover, as these functional groups are well located in the pore surface they can largely enhance the affinity of frameworks to guest molecules through electrostatic interactions. Therefore, we decided to fabricate an isoreticular series of MOF-15 by substituting the hydrogen atom of 5-position carbon atom in phenyl rings with different functional groups as it has the highest impact in pore aperture size and closest contact with guest molecules.

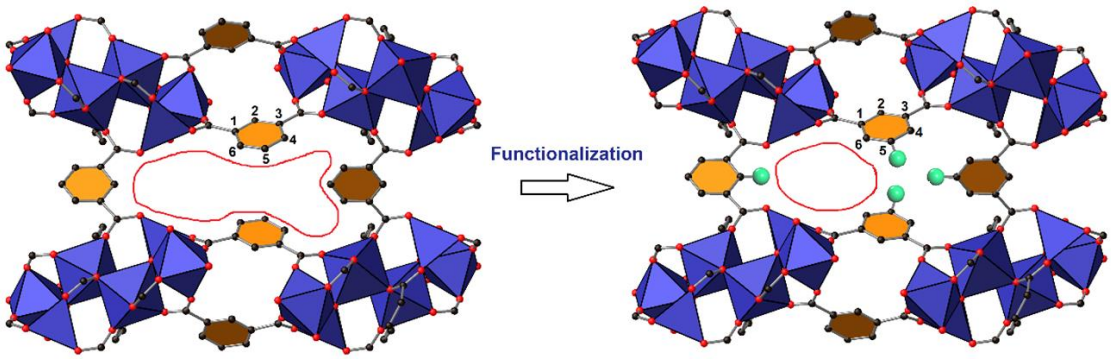

Figure 3.2 A schematic of MUF-15 pore architecture, showing the effect of ligand functionalization on the pore aperture size.

Six different functional groups, including fluoro, hydroxy, bromo, nitro, methyl and methoxy were incorporated into the structure of MUF-15 to represent a broad range of functionalities in terms of size and polarity. Functionalized MUF-15 series were synthesized based on a procedure similar to that of MUF-15 with slightly modification as shown in Table 3.1. A mixture of $Co(OAc)_2.4H_2O$ (0.125 g, 0.5 mmol), ligand (refer to Table 3.1 for the quantity), MeOH (6 mL), and H_2O (0.5 mL) were sonicated for 10 min and sealed in a 25 ml Teflon-lined autoclave and heated according to the conditions mentioned in Table 3.1.

Table 3.1. Synthesis conditions for analogous MUF-15 series and corresponding naming.

MOFs	ligand	ligand/salt ratio	Reaction temperature (°C)	Duration of reaction (h)
MUF-18	5-fluoroisophthalic acid	1.75	120	24
MUF-19	5-hydroxyisophthalic acid	2	120	48
MUF-20	5-bromoisophthalic acid	2	120	48
MUF-21	5-nitroisophthalic acid	1.75	120	48
MUF-22	5-methylisophthalic acid	1.75	140	36
MUF-23	5-methoxyisophthalic acid	1.75	120	36

After cooling to room temperature, the resulting purple crystals were washed with methanol for several times and dried under vacuum. Table 3.1 shows the synthesis conditions for each MOF and assigned naming. It should be noted that we tried to synthesize the amino-functionalized version of MUF-15 as well, but amino-functionalized MUF-15 was not achieved under the same conditions of MUF-15. We tried to change the synthesis conditions, but either no crystals formed or different phases were obtained.

3.2.2 X-ray crystal structure and pore architecture of analogous MUF-15 series

After synthesizing the isoreticular MUF-15 series with different functional groups, PXRD pattern was first obtained to investigate the structural similarity of these MOFs to parent MOF. As can be seen from Figure 3.3, the powder pattern of MUF-18 and MUF-21 are nearly identical to that of MUF-15 and they are clearly isostructural to MUF-15. Other structures show slightly change either in number of peaks or peak angles, but they all possess the main low-angle peak in the same position with MUF-15.

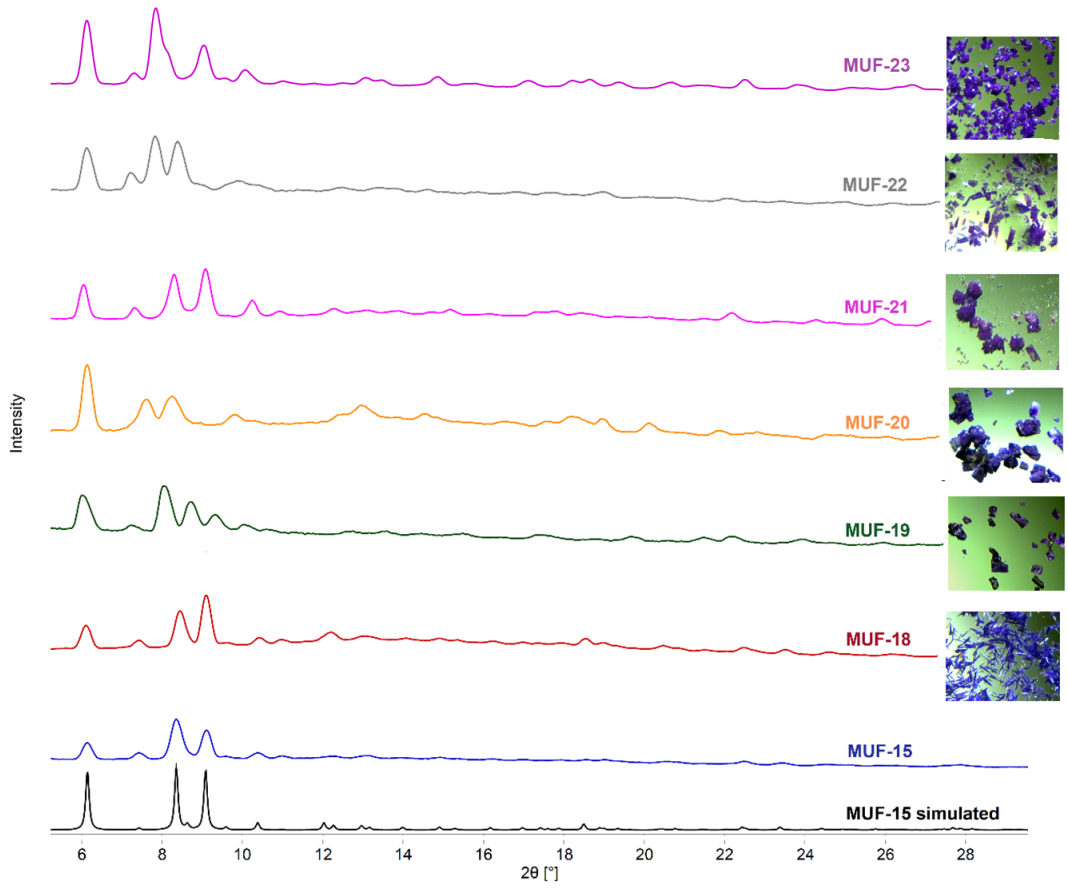

Figure 3.3 Simulated PXRD pattern of MUF-15 and experimental patterns and optical micrograph of MUF-15 and its derivatives.

Positional change in other peaks of PXRD patterns is not fully understood. Our initial guess was that the introduced functional groups in the structure of MUF-15 has caused these changes. However, the simulated PXRD of hypothetically functionalized MOFs (simply introducing the functional groups into the structure of MUF-15 and simulating their PXRD) revealed that introduction of functionalized groups would not change the major peaks in PXRD patterns (Figure 3.4). These peak changes might be attributed to the effects of functional groups indirectly, where incorporation of these groups has slightly changed the position and orientation of atoms in the framework due to the new electrostatic interactions between functionalization groups and MUF-15 framework atoms. Similar changes were seen in the PXRD patterns of solved structure of MUF-18, MUF-22 and MUF-23. While the topology and main structure of these frameworks remained same as MUF-15, but their PXRD patterns is still different with MUF-15.

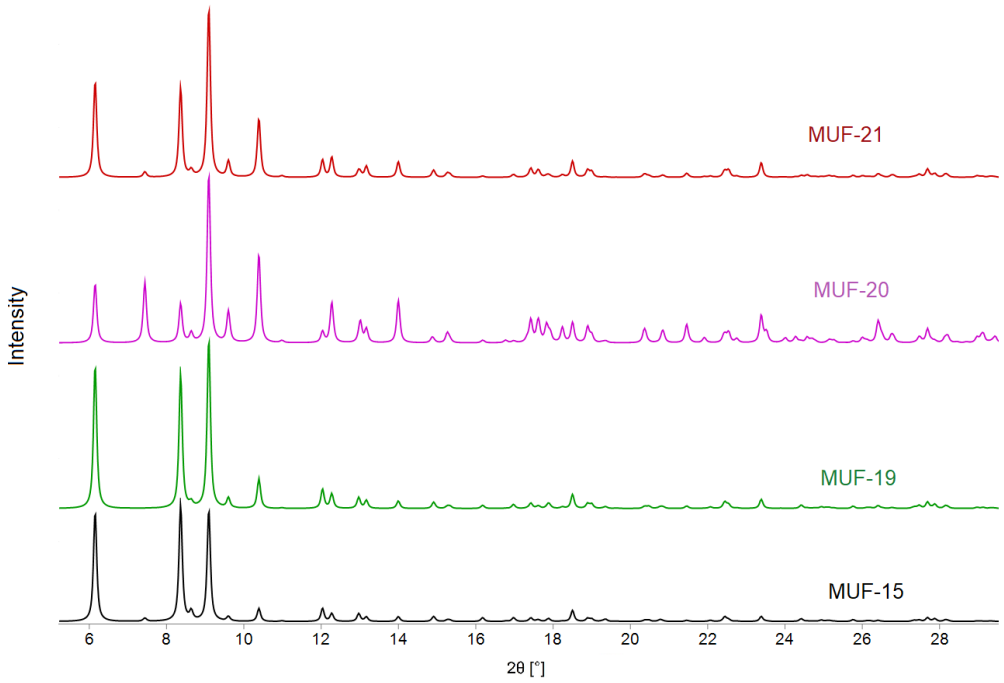

Figure 3.4 Simulated PXRD patterns of simulated MUF-15, MUF-19, MUF-20 and MUF-21. These patterns were obtained from a hypothetically determined structure of MUF-19, MUF-20 and MUF-21 by simply introducing a hydroxyl, bromo or nitro group in an appropriate position in the structure of MUF-15.

SCXRD experiments were implemented to obtain the structure of MUF-18 to MUF-23. Out of these six derivative MOFs, we were only able to solve the structure of MUF-18, MUF-22 and MUF-23. Crystal structures and refinement details of MUF-18, MUF-22 and MUF-23 are shown in Table 3.2.

Table 3.2 Crystal data and structure refinement of MUF-18, MUF-22 and MUF-23 in comparison to those of MUF-15.

	MUF-15	MUF-18	MUF-22	MUF-23
Formula	$Co_6(\mu_3\text{-}OH)_2(ip)_5(H_2O)_2$	$Co_6(\mu_3\text{-}OH)_2(ip\text{-}F)_5(H_2O)_4$	$Co_6(\mu_3\text{-}OH)_2(ip\text{-}Me)_5(H_2O)_4$	$Co_6(\mu_3\text{-}OH)_2(ip\text{-}OMe)_5(H_2O)_4$
Empirical formula	$C_{40}H_{26}Co_6O_{24}$	$C_{40}H_{23}Co_6F_5O_{26}$	$C_{45}H_{40}Co_6O_{26}$	$C_{45}H_{40}Co_6O_{31}$
Formula weight	1244.18	1368.16	1350.35	1428.33
Temperature/K	293.15	293(2)	273.15	293.15
Crystal system	orthorhombic	orthorhombic	monoclinic	orthorhombic
Space group	*P*nna	*P*na2_1	*P*2_1/n	*P*$2_1$$2_1$2
a/Å	28.714(2)	28.668(6)	10.909(2)	22.6822(15)
b/Å	21.1265(7)	10.875(2)	28.582(6)	28.614(2)
c/Å	10.9460(3)	20.623(4)	21.999(4)	10.9041(7)
α/°	90	90	90	90
β/°	90	90	98.74(3)	90
γ/°	90	90	90	90
Volume/Å^3	6640.1(5)	6430.0(2)	6780.0(2)	7077.1(8)
Z	8	4	4	4
ρ_{calc} /g cm^{-3}	1.245	1.413	1.323	1.341
μ/mm^{-1}	12.006	1.595	1.501	11.411
F(000)	2480.0	2712.0	2720.0	2872.0
Radiation	λ = 1.54178	λ = 0.71073	λ = 0.71073	λ = 1.54178
2Θ range for data collection/°	12.044 to 70.240	3.460 to 60.264	5.104 to 45.970	11.256 to 60.948
Index ranges	$-21 \le h \le 21, -15 \le k \le 15, -8 \le l \le 8$	$-40 \le h \le 40, -15 \le k \le 15, -28 \le l \le 28$	$-11 \le h \le 11, -31 \le k \le 31, -24 \le l \le 24$	$-14 \le h \le 14, -18 \le k \le 18, -7 \le l \le 7$
Reflections collected	16306	89636	55287	18857
Independent reflections	1426 [R_{int} = 0.1075, R_{sigma} = 0.0582]	16227 [R_{int} = 0.1049, R_{sigma} = 0.0595]	9124 [R_{int} = 0.1219, R_{sigma} = 0.0820]	2088 [R_{int} = 0.2735, R_{sigma} = 0.1566]
Data/restraints/parameters	1426/219/296	16227/1/699	9124/0/705	2088/1003/664
Goodness-of-fit on F^2	1.126	1.096	1.814	1.032
Final R indexes [I>=2σ (I)]	R_1 = 0.0867, wR_2 = 0.2409	R_1 = 0.0536, wR_2 = 0.1344	R_1 = 0.1680, wR_2 = 0.4518	R_1 = 0.0938, wR_2 = 0.2388
Final R indexes [all data]	R_1 = 0.1043, wR_2 = 0.2606	R_1 = 0.0596, wR_2 = 0.1409	R_1 = 0.1979, wR_2 = 0.4810	R_1 = 0.1214, wR_2 = 0.2643
Largest diff. peak/hole / e Å^{-3}	0.73/-0.42	0.71/-0.76	1.76/-1.20	0.43/-0.38

The rest did not show high stability in air and after few hours their structure collapsed. Soaking these MOFs in non-volatile solvents such as DMF or DBF also was not a practical solution as these solvents changed the structure of these MOFs. As an example, PXRD patterns of as-synthesized MUF-19 in methanol and after soaking it in DMF for 10 minutes are presented in Figure 3.5.

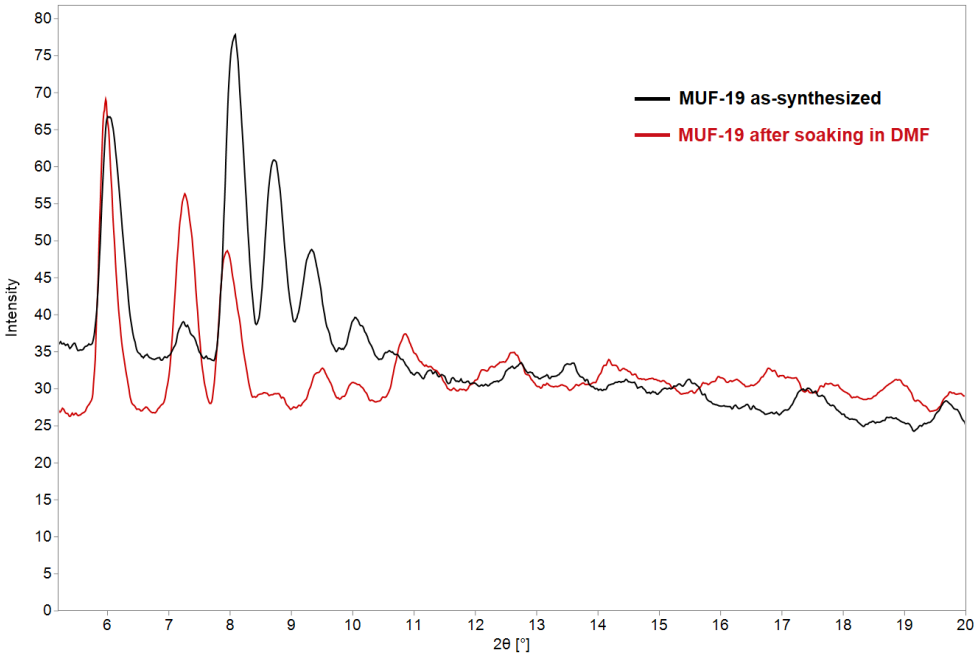

Figure 3.5 PXRD patterns of as-synthesized MUF-19 in comparison to its pattern after soaking in DMF for 10 minutes.

The validity of crystal structure solution and phase purity of MUF-18, MUF-22 and MUF-23 was firstly validated by the comparison of simulated PXRD pattern and experimental ones as shown in Figure 3.6.

Although the crystal system and space group of these MOFs are different from those of MUF-15, they all share the same topology, i.e., having the same cluster. These clusters have been connected to each other with the same coordination and geometry of MUF-15 and they have the similar unit cells. Similar to MUF-15, they are assembled from a hexacobalt cluster connected by ten organic linkers. The cluster nodes are built up from two symmetry-related sets of three cobalt(II) ions. The ions within each set coordinate to a μ_3-bridging hydroxide ion, and the two sets are connected to each other through shared carboxylate groups. There is one terminal H_2O ligand per set of three cobalt ions, which is disordered over two sites. By considering the cobalt clusters as 10-connected nodes linked by organic linkers, all of

these MOFs can be depicted as porous coordination polymers. Therefore, these structures are topologically identical and can be regarded as isoreticular structures.

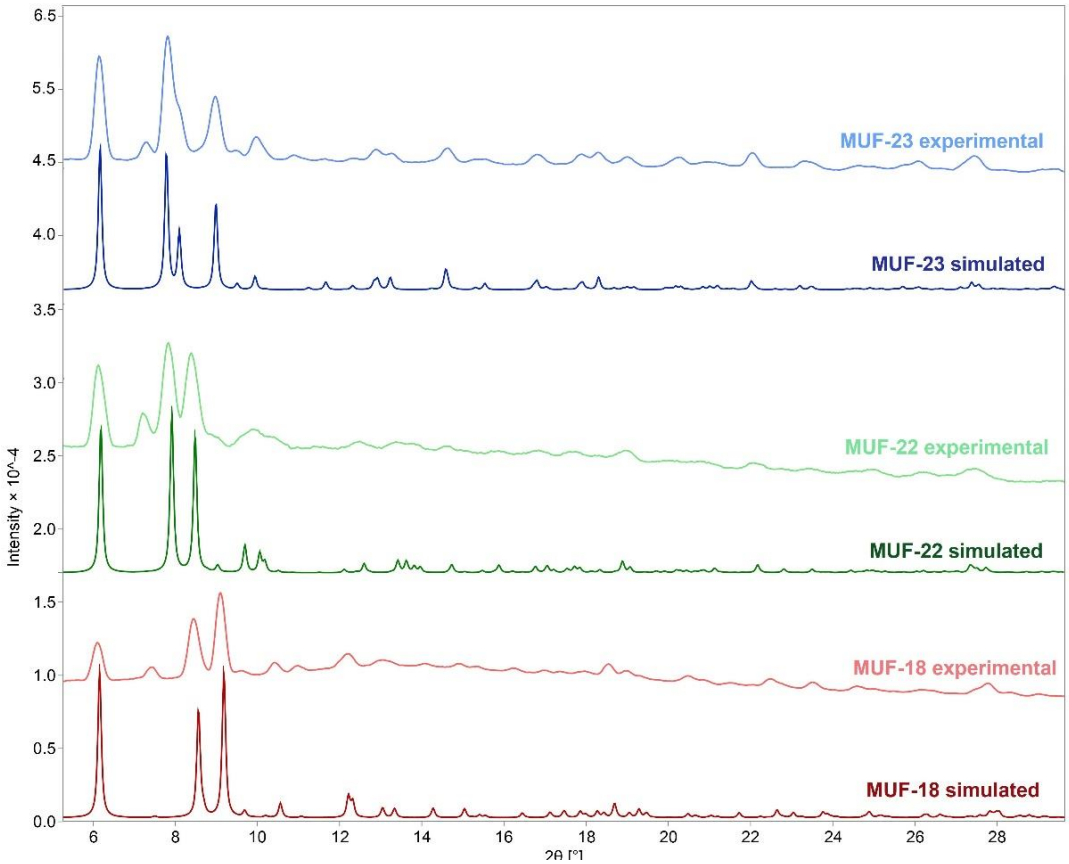

Figure 3.6 Experimental PXRD patterns of MUF-18, MUF-22 and MUF-23 in comparison with simulated patterns derived from single-crystal structure data.

3.2.3 Thermal and physical stability and pore characteristics

Guest-free derivatives of MUF-15 can be readily produced by placing them under vacuum overnight at 120 °C (except MUF-19, which was activated under vacuum at room temperature for two hours), which preserves the coordinated water molecules. These water ligands are lost, together with crystallinity and porosity, by heating above 200 °C. As shown in Figure 3.7, a N_2 adsorption isotherm at 77 K illustrated the permanent porosity of these MOFs. Calculated BET surface area and pore volume based on N_2 isotherm at 77 K are shown in Table 3.3. These values are nearly identical to the geometric surface area and pore volume calculated from the crystallographic coordinates. It should be noted that the metrics derived from the structure data of MUF-19, MUF-20 and MUF-21 are not presented here because the single crystal structures of these materials could not be determined.

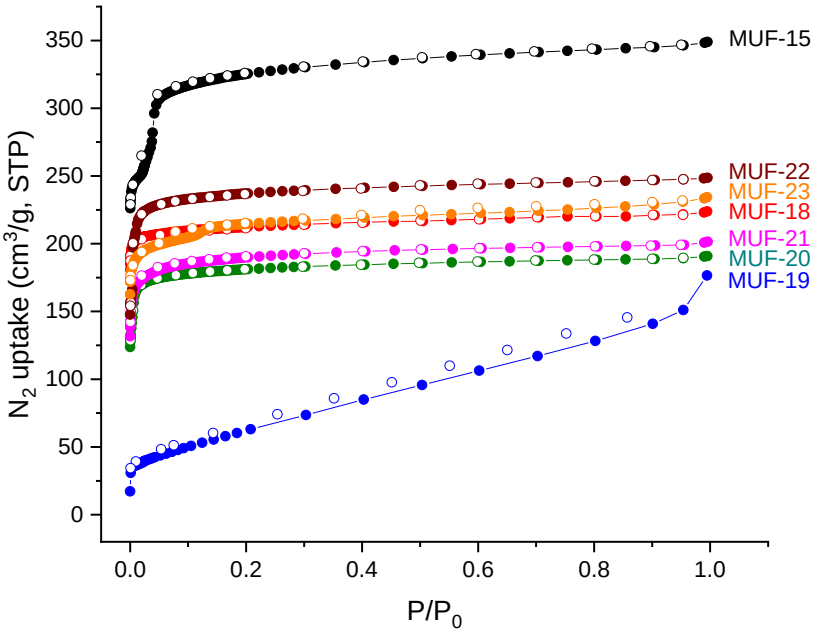

Figure 3.7. Volumetric N_2 adsorption (filled circles) and desorption (open circles) isotherms measured at 77 K for MUF-15 and its derivatives.

Table 3.3. Some calculated and experimentally determined structural characteristics of MUF-15 and its derivatives.

MOFs	BET surface area from experimental N_2 isotherm/77 K (m^2/g)	Calculated geometric surface area (RASPA2) (m^2/g)	Pore volume from experimental N_2 isotherm/77 K (cm^3/g)	Calculated pore volume (Raspa) (cm^3/g)	PLD/LCD (Å)
MUF-15	1130	1207	0.51	0.46	3.6/5.2
MUF-18	874	927	0.35	0.36	3.4/5.0
MUF-19	190	-	0.25	-	-
MUF-20	734	-	0.29	-	-
MUF-21	762	-	0.31	-	-
MUF-22	967	1084	0.38	0.40	3.5/5.1
MUF-23	837	999	0.36	0.38	3.4/5.0

As expected, introduction of the functional group into the structure of MUF-15 reduces the pore volume and surface area of all the derivative MOFs in comparison to MUF-15. This decrease can be simply explained by the occupancy of a portion of void space by functional groups. Moreover, BET surface area calculations showed that introduction of more bulky functional groups is not proportionally in line with the decrease of surface area and pore volume. For instance, both BET surface area (gravimetric) and pore volume of MUF-22 (methyl-functionalized MUF-15) are higher than those of MUF-18 (fluoro-functionalized

MUF-15), while the size of methyl group is relatively larger than that of fluoro group. MUF-15 N_2 adsorption isotherm shows a stepped one. The reason behind this is not fully understood. It may come from some sort of flexibility or by the filling of multiple layers of pore space. MUF-19 shows the lowest surface area and pore volume amongst the derivatives. We believe it is because of its structural change and/or partial structural collapse after removal of guest molecules as its N_2 isotherm at 77 K is completely different from other derivatives both in shape and adsorption capacity. To investigate structural collapse or change of MUF-19 upon activation, PXRD pattern after activation (and further gas adsorption) was measured and compared with as-synthesized states (Figure 3.8). As expected, MUF-19 shows some peak shift upon activation compared to its as-synthesized pattern. It should be noted that, PXRD patterns cannot prove whether the structure of all MUF-19 crystals is not collapsed. In fact, structure of MUF-19 could be partially collapsed while PXRD patterns still show that the structure remains intact.

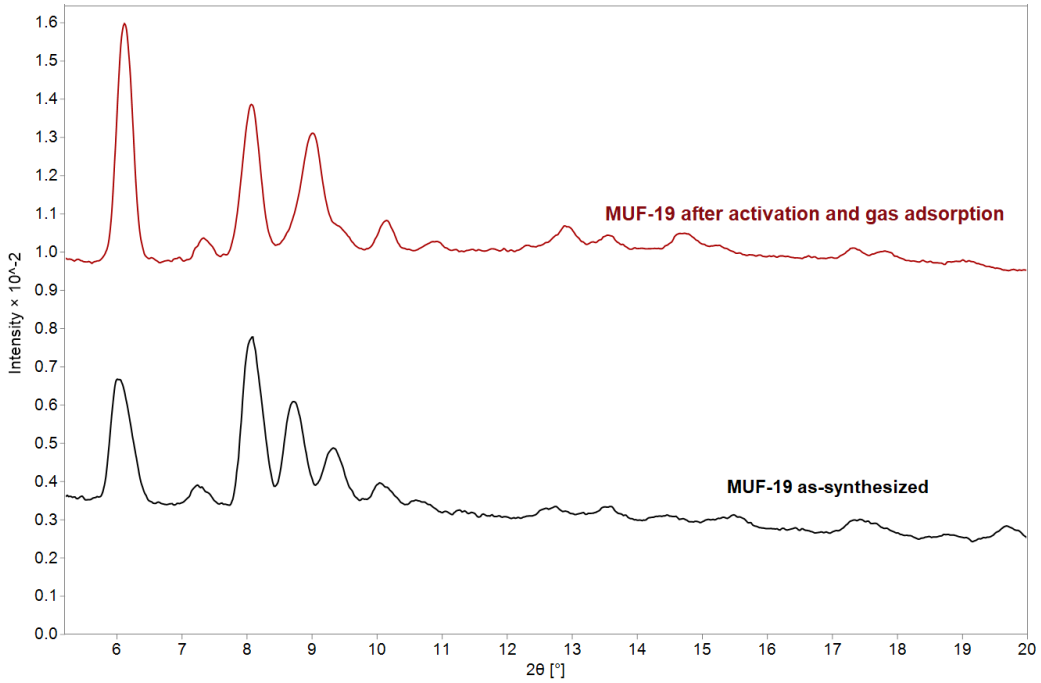

Figure 3.8 PXRD patterns of as-synthesized MUF-19 and after gas adsorption.

Next, to compare the pore architecture and dimensions of MUF-15 before and after functionalization, a Connolly surface with a probe of 1 Å was plotted for MUF-15 and its derivatives as illustrated in Figure 3.9.

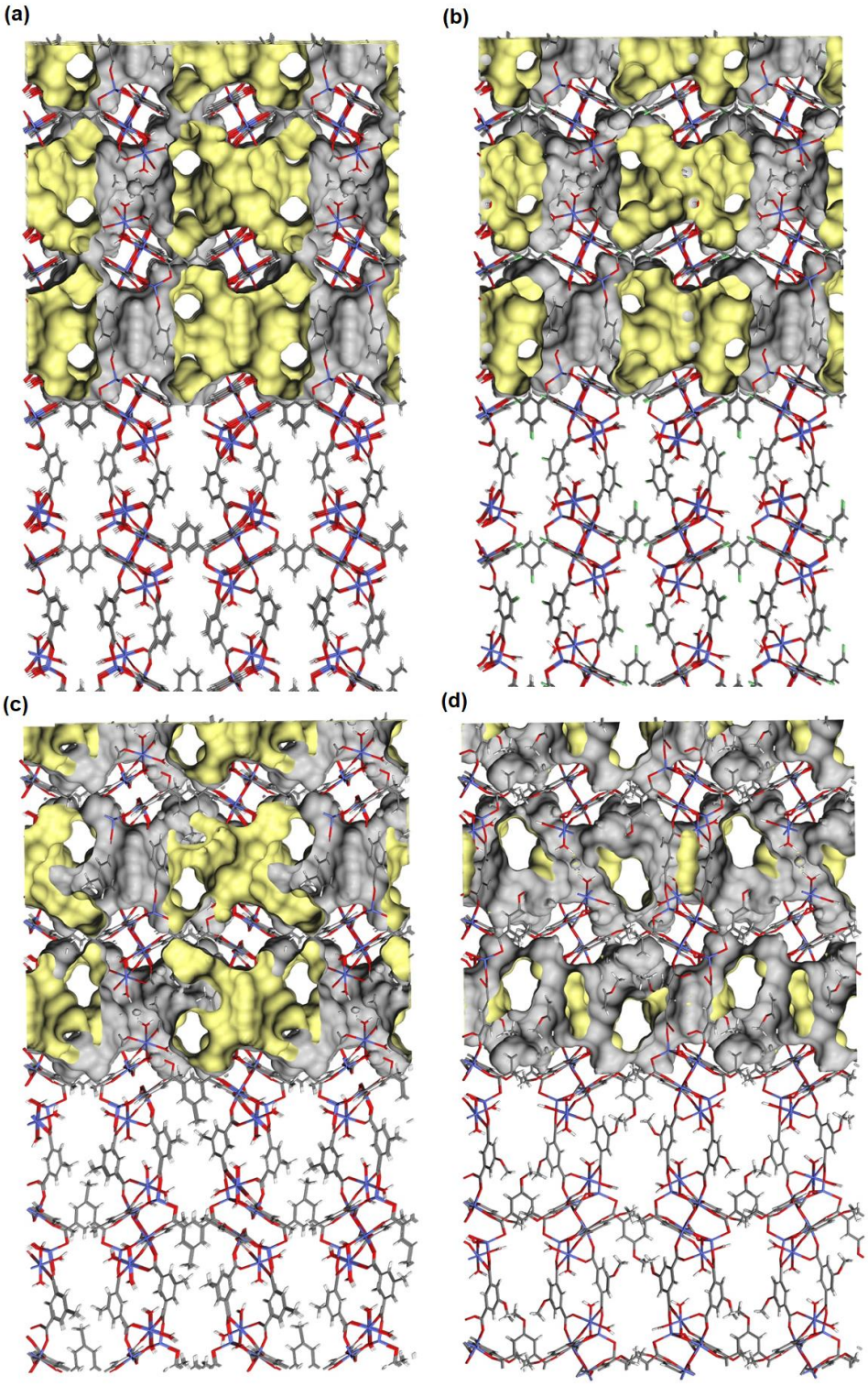

Figure 3.9. Pore structure and void space of (a) MUF-15, (b) MUF-18, (c) MUF-22 and (d) MUF-23 illustrated by Connolly surface using a probe of diameter of 1 Å.

Comparing the MUF-15 pore structure with its derivatives, it can be seen that MUF-15 has the widest channels compared to its derivatives due to less occupancy of its pore space (only hydrogen atoms in 5-position carbon atom of phenyl rings). In comparison, pore structure of MUF-18 is very similar to that of MUF-15 with respect to its shape (Figure 3.9a,b), but substitution of hydrogen atom with fluoro has led to a decrease in channel size

and a subsequent drastic reduction of both surface area and pore volume from 1130 m^2/g and 51 cm^3/g to 783 m^2/g and 0.36 cm^3/g, respectively (Table 3.3). Unlike fluoro group, introduction of methyl and methoxy group not only changed the pore metrics, but also altered the shape of the pores (Figure 3.9c,d). MUF-22 and MUF-23 both show lower surface area and pore volume compared to MUF-15, which is again an indicator of occupancy of a portion of void space by these bulky groups. Interestingly, although more bulky groups have been incorporated to the structure of MUF-15, both MUF-22 and MUF-23 possess higher surface area and pore volume compared to MUF-18, which has been functionalized with relatively small fluoro group. It can be explained by the formation of larger cavities in MUF-22 and MUF-23 compared to MUF-18, thus accommodating larger volumes of guest molecules.

In addition to their high porosity and ability to take up gases, MUF-15 derivatives also display excellent thermal and water stability. Thermogravimetric analysis (TGA) of activated MUF-15 derivatives crystals shows a mass loss of 10-20% (depending on the adsorbed water content in the pores and the duration they have been exposed to air) when the samples were heated to 100 °C, due to the escape of guest molecules.

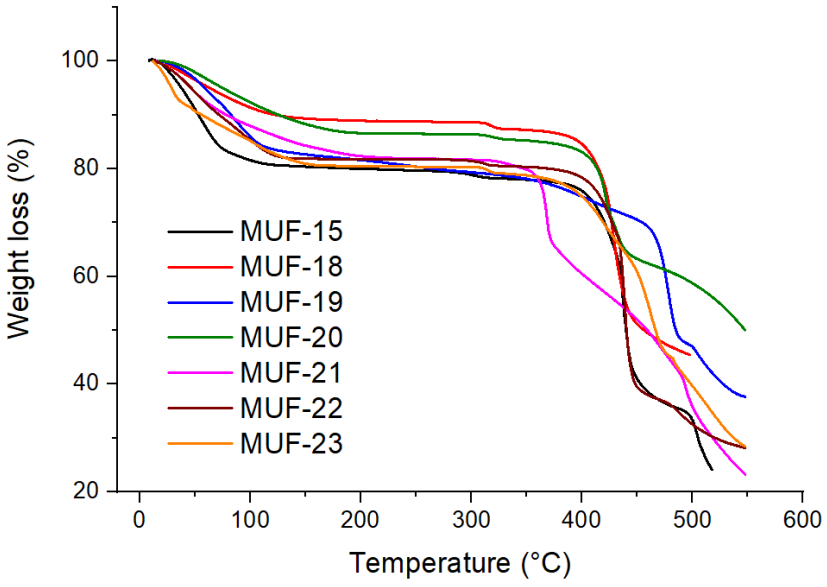

Figure 3.10 TGA curves of MUF-15 and its derivatives showing complete removal of guest molecules at 130 °C.

A complete removal of guest molecules can be seen for all the derivative MOFs at 130 °C. The remaining desolvated framework is stable up to 300 °C before the removal of coordinated water is observed (Figure 3.10). MUF-21 shows an earlier structural collapse, which might be attributed to the departure of NO_2 group.

We were delighted to find that MUF-22 and MUF-23 showed extraordinary stability towards water vapour. Following the removal of occluded solvent, a sample was exposed to ambient air (70-80 % RH) at 20 °C for 180 days. No changes to the morphology or transparency of the crystals were detected by optical microscopy (Figure 3.11).

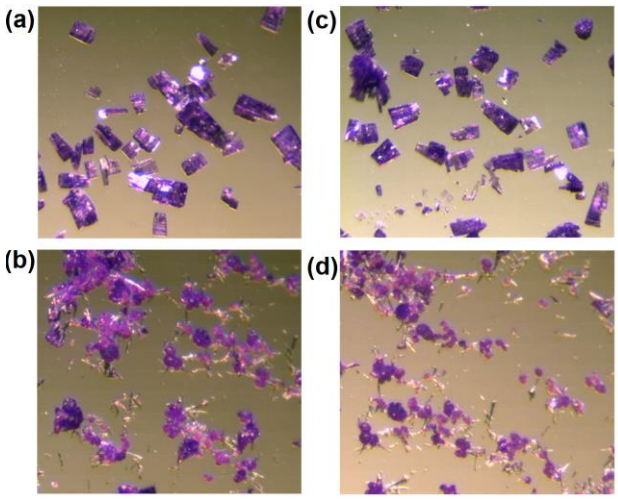

Figure 3.11. Microscopy images of MUF-22 (a) before and (b) after and MUF-23 (c) before and (d) after being aged at 70-80 % RH for 180 days.

PXRD patterns were recorded throughout the exposure period and they were found to remain unchanged (Figure 3.12 and 3.13). As a point of comparison, activated MUF-15 is stable in air for only a week and PXRD pattern indicates a loss of crystallinity.

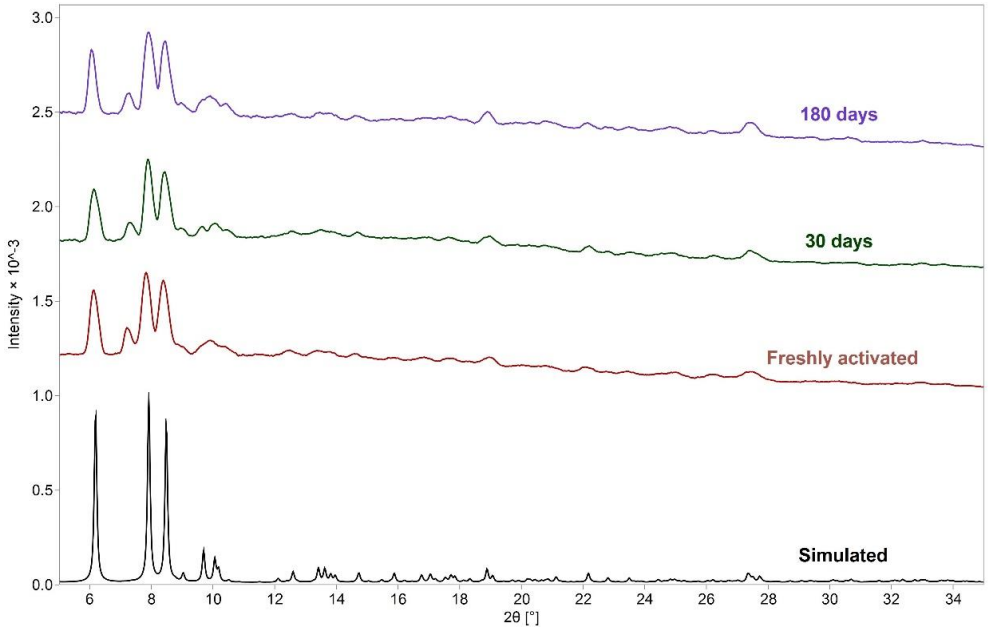

Figure 3.12. Powder X-ray diffraction patterns of MUF-22; freshly activated and aged samples exposed to 70-80 % relative humidity at 20 °C for the stated period.

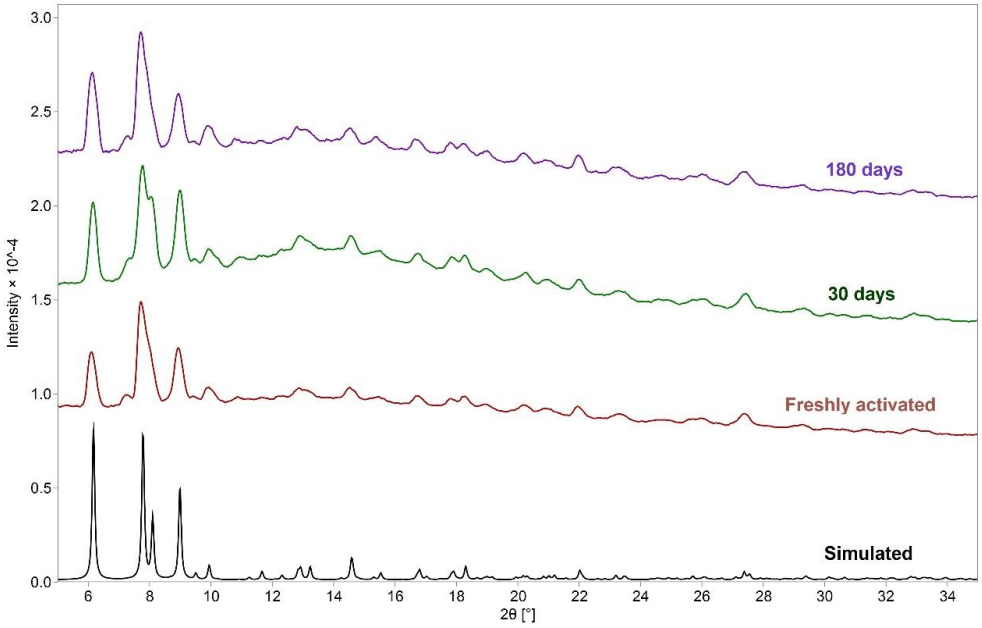

Figure 3.13. Powder X-ray diffraction patterns of MUF-23; freshly activated and aged samples exposed to 70-80 % relative humidity at 20 °C for the stated period.

To quantify the stability of MUF-22 and MUF-23 towards humid air, we turned to the measurement of gas adsorption isotherms before and after periods of exposure to ambient air. This allows the porosity of an aged sample to be compared to its pristine state. Following the exposure of MUF-22 and MUF-23 to humid air (RH = 70-80%) for 180 days, CO_2 isotherm was measured at 293 K (Figure 3.14). The uptake of CO_2 by aged MUF-22 and MUF-23 after 180 days are 63.6 and 60.2 cm^3/g (at 1 bar), respectively, which are almost identical to their pristine samples (64.7 cm^3/g for MUF-22 and 60.6 cm^3/g for MUF-23).

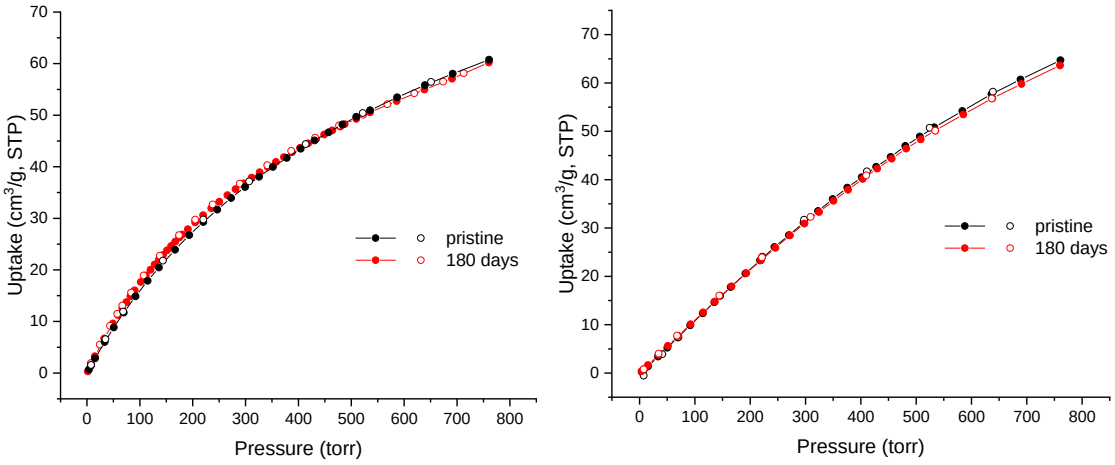

Figure 3.14. Left: CO_2 adsorption (filled circles) and desorption (open circles) isotherms measured at 293 K for pristine and aged MUF-22 under 70-80% relative humidity. Right: CO_2 adsorption (filled circles) and desorption (open circles) isotherms measured at 293 K for pristine and aged MUF-23 under 70-80% relative humidity.

The water vapour stability was investigated for other derivatives as well. Unlike MUF-22 and MUF-23, they did not show great stability in presence of humidity. MUF-18 maintains its crystallinity for about a week, MUF-19 loses its crystalinity in few minutes and MUF-20 and MUF-21 are stable in air not for more than 4 hours and 14 hous (based on their PXRD patterns, see Appendix B for PXRD patterns). The observed stability of MUF-22 and MUF-23 indicates that they can be handled indefinitely under typical laboratory conditions, which is a surprising revelation. MUF-15, MUF-22 and MUF-23 are built from similar ligand sets and identical SBUs. Why does their stability towards humid air differ so remarkably? The procedure of MOF degradation in water vapour or liquid water can be considered as a series of substitution reactions in which the metal-coordinated linkers are replaced by water or hydroxide ions. On this basis, there are two plausible reasons behind the superior stability of MUF-22 and MUF-23: isolation of SBUs by functionalized ligands and introduction of hydrophobic groups into the ligands. In MUF-22 and MUF-23, SBUs are excluded from exposure to water and other guest molecules. As can be seen from Figure 3.15, hexa-cobalt clusters are surrounded by more bulky methoxy and methyl groups, thus preventing water molecules to attack the clusters, while pore channels in MUF-15 are open to the surface of SBUs. Secondly, methyl and methoxy groups are known as hydrophobic groups and have lower affinity for adsorbing water vapour. Therefore, introduction of these groups increase water resistance by enhancing the hydrophobicity of these frameworks.

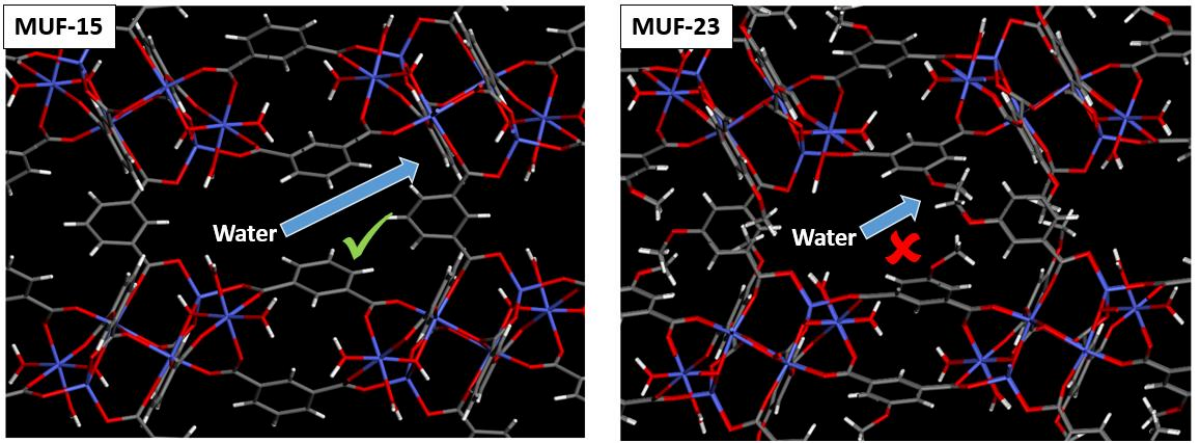

Figure 3.15. Left: Water molecules route towards hexa-cobalt clusters in MUF-15 showing their easy access to the surface of clusters. Right: Water molecules route towards hexa-cobalt clusters in MUF-23, which is blocked by methoxy groups.

3.2.4 Gas sorption studies, heat of adsorption and IAST selectivity calculations

Motivated by great separation performance of parent MOF (MUF-15) for $C_2H_6/C_2H_4/C_2H_2$ separations, gas adsorption studies were performed to evaluate separation

performance of functionalized MOFs. Hence, single gas adsorption isotherms of C_2H_6, C_2H_4, C_2H_2 and CO_2 were measured up to 1 bar at various temperatures for these MOFs (Figure 3.16).

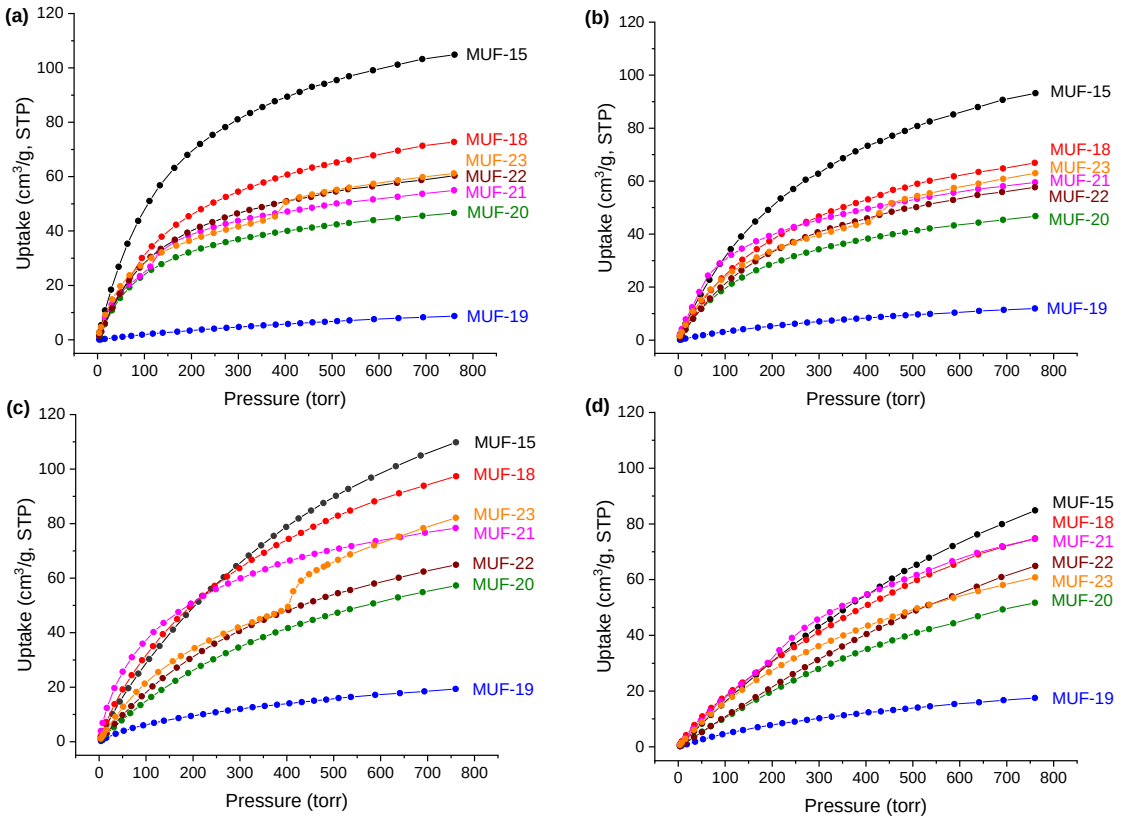

Figure 3.16. Volumetric (a) C_2H_6, (b) C_2H_4, (c) C_2H_2 and (d) CO_2 adsorption isotherms of MUF-15 and its derivatives measured at 293 K (desorption points are removed for clarity).

As observed by N_2 isotherms at 77 K, MUF-15 also exhibits the highest uptake amongst derivatives for C_2H_6, C_2H_4, C_2H_2 and CO_2 at 1 bar and 293 K because of its higher pore volume and surface area. As expected, MUF-18 has the closest gas uptake to MUF-15 for all the gases because fluoro and hydrogen atoms have similar size. MUF-19 also shows the poorest adsorption capacity, which can be again explained by its structural change or collapse (partially) after activation. Interestingly, the difference in gas uptakes of derivative MOFs compared to MUF-15, reduces moving from non-polar gases to polar ones. As can be seen from Figure 3.16, C_2H_6 uptake of MUF-15 is 105 cm^3/g, which is at least two-thirds of that of other derivatives. This difference decreases to atleast 75% and (almost identical) for C_2H_4 and C_2H_2, respectively. An initial conclusion of these results is that introduction of functional groups increases the polarity of the pore surface, thus enhancing the affinity of framework towards more polar gases and a subsequent increase in gas uptake (bearing in mind that overall pore volume is reduced by functionalization). Additionally, it was again

confirmed that the separation mechanism in MUF-15 is based on the recognition of non-polar but highly polarizable molecules over polar molecules, as the difference between the uptake of C_2H_6, C_2H_4 and C_2H_2 decreases with the introduction of more polar groups. Another interesting observation from Figure 3.16 is the affinity of frameworks for different gases. This can be discussed based on the uptake of gases at low pressure, i.e., the steepness of isotherm curves. For C_2H_6, MUF-15 exhibits the highest uptake capacity and steepness in comparison to its derivatives. It can be explained by the high aromatic pore surface of MUF-15 compared to its derivatives, which favours non-polar but polarizable C_2H_6 molecules. In fact, introduction of functional groups does not play a key role in the framework's affinity towards C_2H_6, because all the derivative MOFs show similar steepness of C_2H_6 isotherm and their uptakes vary mostly because of their different pore volumes. Moving towards more polar gases, the effect of functional groups can be clearly seen. For instance, MUF-21 shows similar affinity towards C_2H_4 and higher affinity towards C_2H_2 compared to MUF-15, or MUF-18 with highly electronegative fluoro groups indicates stronger interaction with C_2H_2 and CO_2 compared to MUF-15. The effect of pore surface polarity after introduction of functional groups can be observed by the adsorption behaviour of C_2H_2 molecules (as the most polar molecules of the C2 adsorbates). As can be seen from Figure 3.17, among functionalized MOFs, MUF-21 and MUF-18 that are functionalized by relatively more polar groups of nitro and fluoro possess the highest affinity to C_2H_2 molecules.

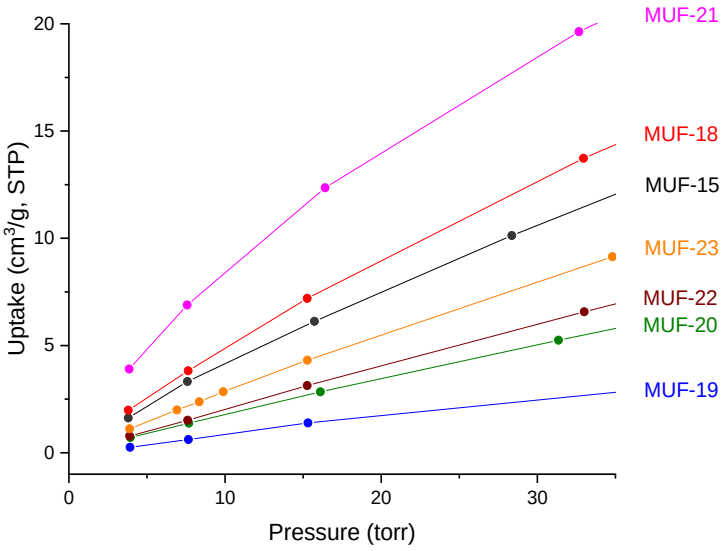

Figure 3.17. Volumetric C_2H_2 adsorption isotherms measured at 293 K for MUF-15 and its derivatives in low pressure range (desorption points are not presented for clarity).

Then, as expected, MUF-23 which is functionalized by methoxy group (which is less polar than flouro and nitro group but more polar than methyl group) surpasses MUF-22 which is functionalized by methyl group. And at the end, MUF-20 functionalized by

relatively less polar group of bromo shows the lowest C_2H_2 uptake at low pressures. The affinity of these MOFs towards different gases will be compared quantitatively by calculation of their isosteric heat of adsorptions in the next sections.

More interestingly, we were excited by observing the sign of flexibility in gas adsorption isotherms of C_2H_6, C_2H_4, C_2H_2 and CO_2 by MUF-21 and MUF-23 at low pressures (0-1 bar). Flexible (or dynamic) MOFs are referred as a class of MOFs that response to an external stimuli such as pressure, heat, solvent, and electric field or magnetic field through changing its internal structure without breaking the overall network. This structural transformation generally occurs by bond breaking/making, change of coordination number of the metal ion, change of coordination mode of ligand, ligand length squeezing, solvent exchange, solvent removal, etc.[46, 269]

To evaluate the binding strength between MUF-15 derivatives and guest molecules, coverage-dependent isosteric heat of adsorptions (Q_{st}) for C_2H_6, C_2H_4, C_2H_2 and CO_2 were evaluated experimentally from pure component isotherms collected at 273 and 293 K by the implementation of a virial equation.[122] These results are presented in Figure 3.18.

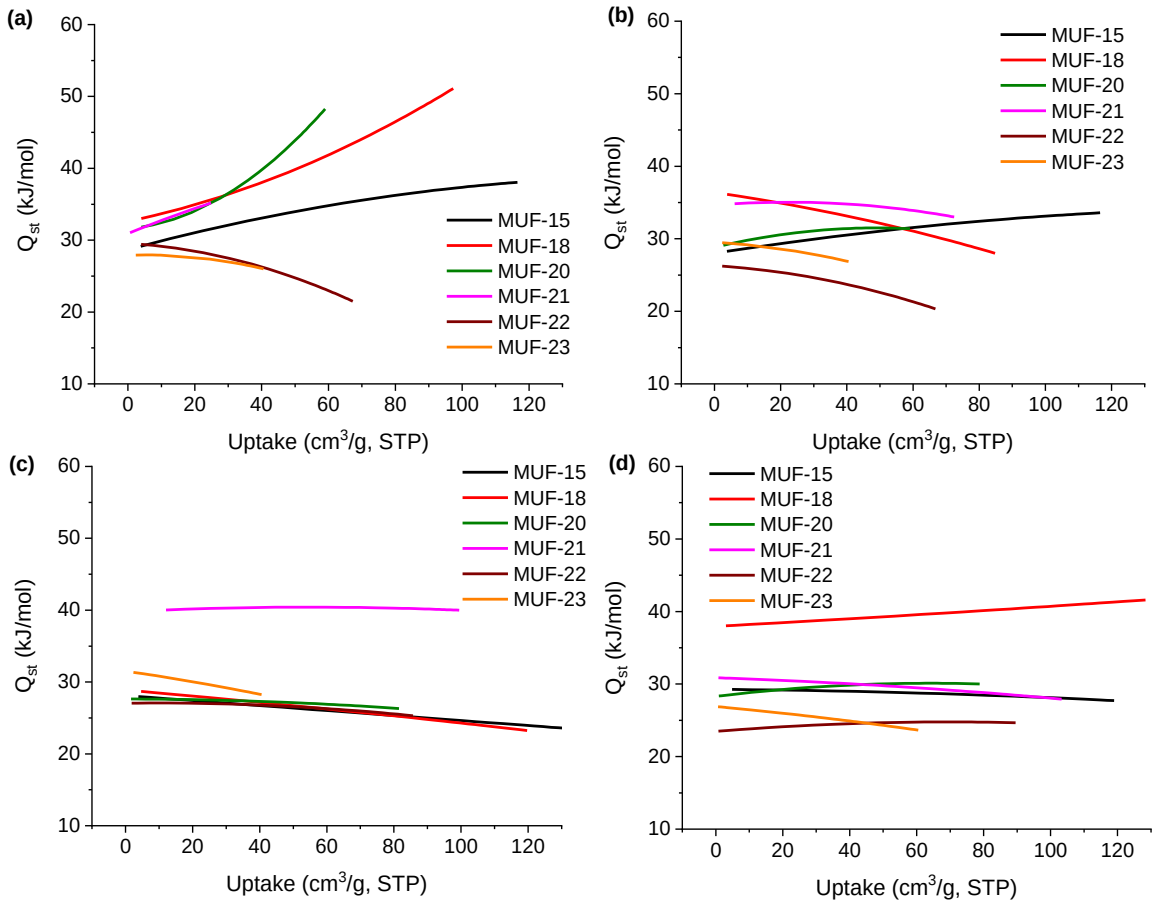

Figure 3.18. Isosteric heat of adsorption plots for the adsorption of (a) C_2H_6, (b) C_2H_4, (c) C_2H_2 and (d) CO_2 by MUF-15 and its derivatives.

It should be noted that low pressure areas, just before breathing point, were chosen for flexible MOFs (to achieve a better fit with virial equation) to calculate Q_{st}. A Q_{st} calculation is not presented for MUF-19, as the adsorption uptakes were low and isotherms were not smooth. As can be seen from Figure 3.18, functionalization has not significantly affected the Q_{st} values of C_2H_6 for derivatives compared to that of MUF-15 at low loadings. At higher loadings, MUF-18 and MUF-20 show considerably higher Q_{st} values for C_2H_6, which can be attributed to the intermolecular interaction of C_2H_6 molecules.

C_2H_4 is a more polar molecule compared to C_2H_6, and hence MUF-18 and MUF-21 show a comparatively high heat of adsorption (~35 kJ/mol) at low loadings which is higher than that of MUF-15 and other derivatives (less than 30 kJ/mol). As was discussed earlier, it can be attributed to the highly polar surface of MUF-18 and MUF-21, which are functionalized by fluoro and nitro groups, respectively. Moving towards C_2H_2, as shown earlier by a steep adsorption isotherm, MUF-21 exhibits a considerably high Q_{st} for C_2H_2 (40 kJ/mol) which drastically surpasses all the other derivatives and MUF-15. Such a high Q_{st} of MUF-21 for C_2H_2 originates from the strong interaction of nitro groups with highly polar C_2H_2 molecules. For CO_2, MUF-18 shows the highest heat of adsorption (38 kJ/mol), which was significantly higher than that of other MOFs (less than 31 kJ/mol). High interaction of fluorinated MOFs with CO_2 has been observed several times in literature.[176, 270-273] Such an appreciable affinity of these MOFs for CO_2 are explained by strong hydrogen bonding of fluoro atoms with carbon atoms of CO_2 molecules.

Motivated by interesting adsorption behaviour of functionalized MOFs, the adsorption selectivity of C_2H_6/C_2H_4, C_2H_4/C_2H_2 and C_2H_2/CO_2 mixtures at 293 K was predicted on the basis of ideal adsorbed solution theory (IAST)[118]. First, single gas adsorption isotherms of C_2H_6, C_2H_4, C_2H_2 and CO_2 for MUF-15 and its derivatives are presented in Figure 3.19.

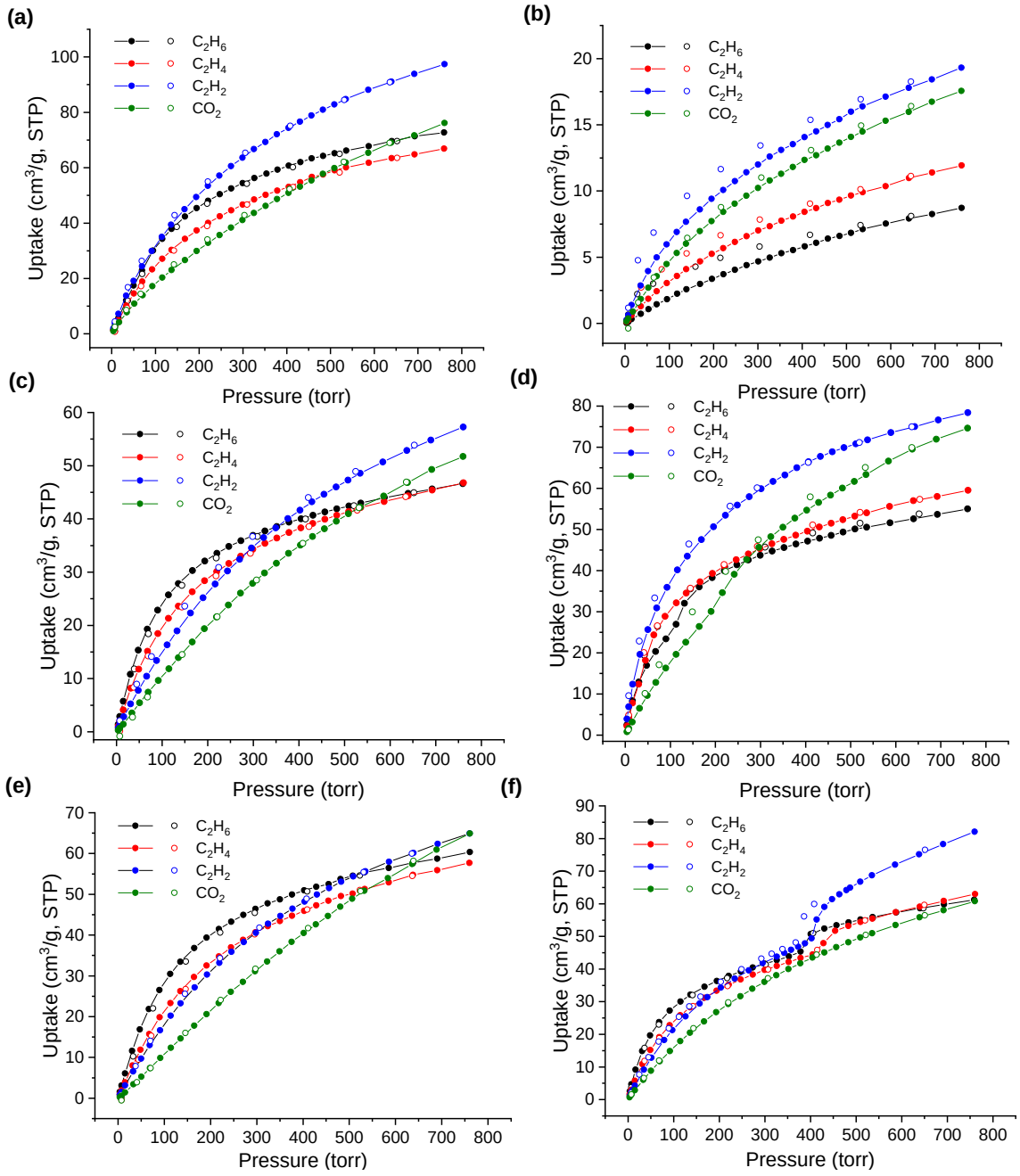

Figure 3.19. Volumetric adsorption (filled circles) and desorption (open circles) isotherms measured at different temperatures for (a) MUF-18, (b) MUF-19, (c) MUF-20, (d) MUF-21, (e) MUF-22, (f) MUF-23 at 293 K.

A Dual-Site Langmuir-Freundlich model was used to fit the single gas isotherms. An equimolar mixture was chosen as a representative mixture composition to evaluate the selectivity of MUF-15 and its derivatives. The result of these calculations are presented in Figure 3.20.

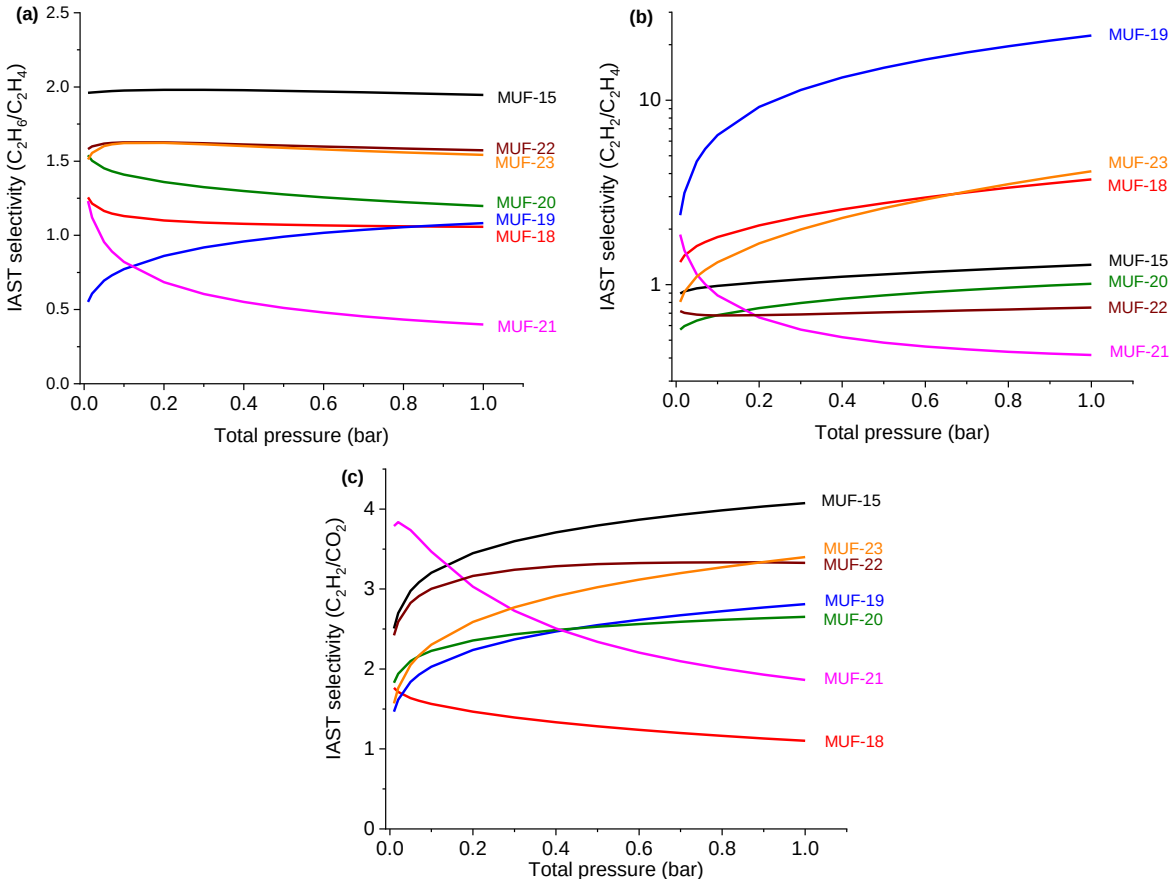

Figure 3.20. Predicted IAST selectivity of MUF-15 and its derivatives for an equimolar mixture of (a) C_2H_6/C_2H_4, (b) C_2H_2/C_2H_4 and (c) C_2H_2/CO_2 at 293 K.

For C_2H_6/C_2H_4 separation, MUF-15 indicates the highest selectivity (~2) over the whole range of pressures. This again confirms that the introduction of functionalized groups does not improve the C_2H_6/C_2H_4 separation performance of MUF-15. As these functional groups enhance the polarity of pore surface, they mainly increase the interaction of frameworks with C_2H_4 as the more polar gas, thus decreasing the selectivity of frameworks for adsorption of C_2H_6 over C_2H_4. This can be clearly seen from Figure 3.20a, where MOFs functionalized with less polar groups, including methyl, methoxy and bromo show greater C_2H_6/C_2H_4 selectivity (1.57, 1.54 and 1.19, respectively, at 1 bar) compared to MOFs functionalized with more polar groups, such as fluoro and nitro (1.08 and 0.39, respectively at 1 bar). Interestingly, MUF-21, which is functionalized with nitro group shows reveres selectivity for C_2H_6/C_2H_4, where its selectivity for C_2H_6/C_2H_4 drop to 0.39 at 1 bar. It can be explained by the introduction of polar nitro groups into the structure of MUF-15 that interact more strongly with more polar C_2H_4 molecules. These results again support the underlying mechanism proposed for ethane-selectivity of MUF-15: More inert surfaces enhance the C_2H_6 selectivity of the frameworks, while a highly polar surface favours the adsorption of C_2H_4.

As another industrially relevant gas separation application, MUF-15 and its derivatives were evaluated for C_2H_2/C_2H_4 separations.[198] As can be observed from Figure 3.20b, functionalization has affected the selectivity of MOFs for C_2H_2/C_2H_4 separation significantly. MUF-15 shows virtually no selectivity towards C_2H_2 and C_2H_4, while MUF-23 and MUF-18 are C_2H_2 selective with a selectivity of around 3, and three other MOFs (MUF-20, MUF-21 and MUF-22) exhibits reverse selectivity, i.e. they adsorb C_2H_4 over C_2H_2. The underlying mechanism behind these selectivities is not easy to be explained. MUF-18 is functionalized by electronegative fluoro groups that probably interact strongly with the electropositive hydrogen atoms of C_2H_2. MUF-23 also shows gate opening behaviour with rapid increase of C_2H_2 uptake compared to C_2H_4 that might account for its C_2H_2 selective nature (C_2H_2 molecules interact with framework more strongly and thus induce the flexibility of the structure stronger). On the other hand, MUF-21 shows C_2H_2 selective behaviour at low pressures, while selectivity unexpectedly drops below 1 with the increase of pressure. Such adsorption behaviour might be originated from the intermolecular interactions. At low pressures MUF-21 interact favourably with polar C_2H_2 molecules and therefore shows a selectivity towards C_2H_2, while at high pressures intermolecular interaction of C_2H_4 molecules favours the adsorption of C_2H_4 over C_2H_2.

Interestingly, MUF-19 shows the highest selectivity of 22 at 1 bar and 293 K for an equimolar mixture of C_2H_2/C_2H_4. As MUF-19 does not show high stability and we are not sure of it has been activated properly or its structure has changed during the activation, it is hard to be fully confident about its high calculated selectivity. Moreover, the adsorption uptake of this MOF is quite low compared to other MOFs.

The final gas pair that was investigated was C_2H_2/CO_2, which is another important gas separation application for producing high purity C_2H_2.[198] The first observation from Figure 3.20c is that all of these MOFs are selective towards C_2H_2. Comparing their selectivity at low pressures, MUF-21 indicates the highest selectivity of 3.8. Its selectivity rapidly decreases to 1.8 at 1 bar; the same behaviour that was observed for C_2H_4/C_2H_2 mixture. Interestingly, MUF-15 shows the highest selectivity (~4) At 1 bar followed by MUF-23 and MUF-22. The selectivity drops to its lowest value by MUF-18 (~1). Such a low selectivity of MUF-18 for C_2H_2 over CO_2 can be readily explained by strong adsorption of CO_2 by the fluoro functionalized materials. To sum up, apparently, MOFs functionalized with less polar groups such as methoxy and methyl show higher selectivity of C_2H_2 over CO_2, while the selectivity drops upon the introduction of polar groups such as nitro and fluoro. Such a behaviour is not well understood at a molecular level but may relate to the effect of intermolecular interactions, or pore geometry and orientation of guest molecules in the pores.

3.2.5 Flexible analogues of MUF-15 and their separation performance

Among the various unique characteristics of MOFs, the flexibility of the framework and their dynamic behaviour have recently attracted great attention. In comparison to non-flexible porous materials, such as zeolites or activated carbons, some MOFs show structural flexibility when they are exposed to certain stimuli. This flexibility generally comes from at least one of these factors: a) the nature of the organic ligands, b) the moderate metal–ligand interactions, c) the versatile configuration of metal ions/clusters, and d) the movement of interpenetrated subnets.[46, 269] One of the characteristics of the ligands that can trigger flexibility in MOFs is its ability to rotate i.e., the spatial alignment of a linker is changed by turning around a rotational axis.[46, 269] Such flexible behaviour has been revealed in ZIF-8 (Zeolitic Imidazolate Framework, $[Zn(mIm)_2]n$, mIm = 2-methylimidazole). A series of comprehensive experimental and theoretical studies have underscored the conclusion that the rotation of the organic linkers in the structure of ZIF-8 leads to the expansion of the pore windows, thus resulting in the adsorption of molecules that are larger than the pore size of framework.[274]

The first sign of flexibility in the MUF-15 family was observed by a slight change of its structure upon exposure to some solvents such as DMF and DEF (Figure 3.5). The flexible nature of MUF-15 was then further confirmed by measuring its PXRD pattern under vacuum. As can be seen from Figure 3.21, the PXRD pattern of MUF-15 under vacuum shows a peak at $2\theta = 7.5°$ completely disappears and the peak at $2\theta = 9.2°$ is shifted in comparison to as-synthesized state. MUF-15 structure turns back to its as-synthesized state after removing vacuum and exposing it to the atmosphere.

We believe this flexibility originates from the rotation of phenyl rings upon the reversible inclusion of guest molecules, such as water, resulting in a structural deformation. A schematic of a possible transition is shown in Figure 3.22. It should be noted that these explanations are based on our observations and limited studies. Future comprehensive studies are needed to be done to investigate the mechanism behind these flexibilities.

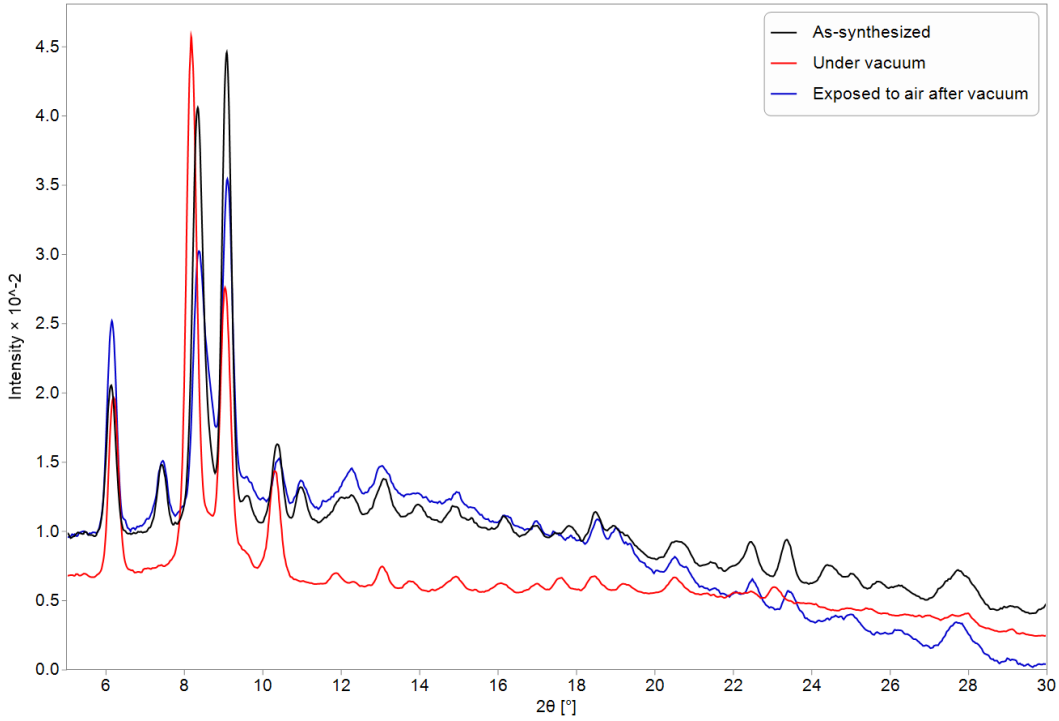

Figure 3.21. PXRD pattern of MUF-15 under vacuum in comparison to its as-synthesized state and exposed to air after vacuum.

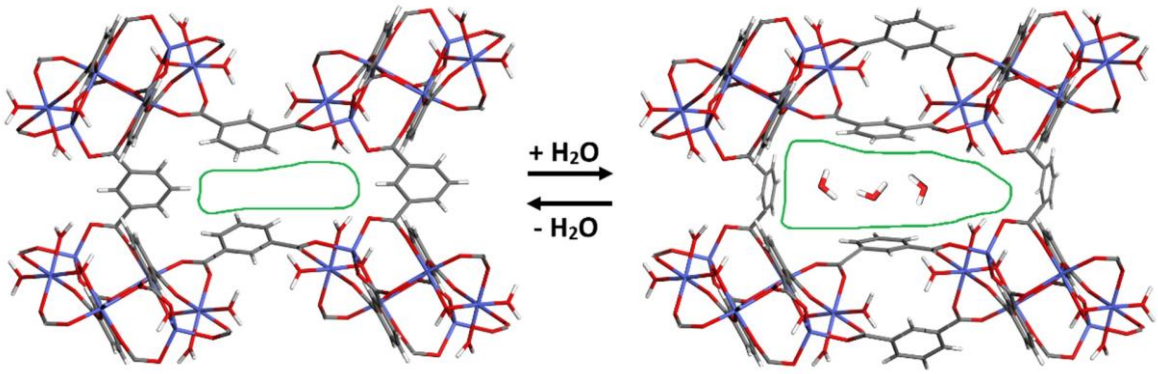

Figure 3.22. A hypothetical schematic of the pore shape in MUF-15, showing the rotation of phenyl rings upon adsorption of water molecules opens up more space.

However, MUF-15 exhibits no sign of flexibility upon the adsorption of guest molecules such as CO_2, C_2H_6, C_2H_4 and C_2H_2 at different temperatures ranging from 195 K to 323 K and low pressures (0-1 bar). Recent studies have demonstrated that flexibility of MOFs can be tuned by substituent effects at the linker, i.e., by introducing functional groups.[46, 266-268, 275-277] An early example of introducing different groups at the backbone of the ligand for inducing the flexibility was demonstrated in the prototypical MIL-53-series proposed by Férey et al.[277] The bdc ligand was functionalized with $–CH_3$, –Br, –Cl, $–NO_2$, and $–(OH)_2$ groups. It was revealed that these functionalities, varying in polarity, hydrophilicity, and acidity, can trigger the flexibility of MIL-53 through the presence of intraframework

interactions. Another series of functionalized MOFs, $[Zn_2(L)_2\text{-}(dabco)]_n$ (where L is ligand) prepared by Henke et al. showed adjustable flexibility through functionalization of the ligands with a series of dialkoxy groups.[276] It was demonstrated that the flexibility of the frameworks is dependent on the length, polarity, and grade of saturation of the added alkoxy chains. A similar behaviour was observed through functionalization of MUF-15 by different groups. As demonstrated earlier by measuring adsorption isotherms of different gases, MUF-21 and MUF-23 functionalized by nitro and methoxy group, respectively, shows flexibility upon adsorption of guest molecules.

The flexibility of these MOFs was further confirmed by measuring their PXRD patterns under vacuum and comparing them to as-synthesized MOF. MUF-21 shows weak stability in the atmosphere, so we were not able to measures its PXRD pattern under vacuum as sample preparation involves loading the MOF into a capillary, and the sample gets exposed to the atmosphere several times.

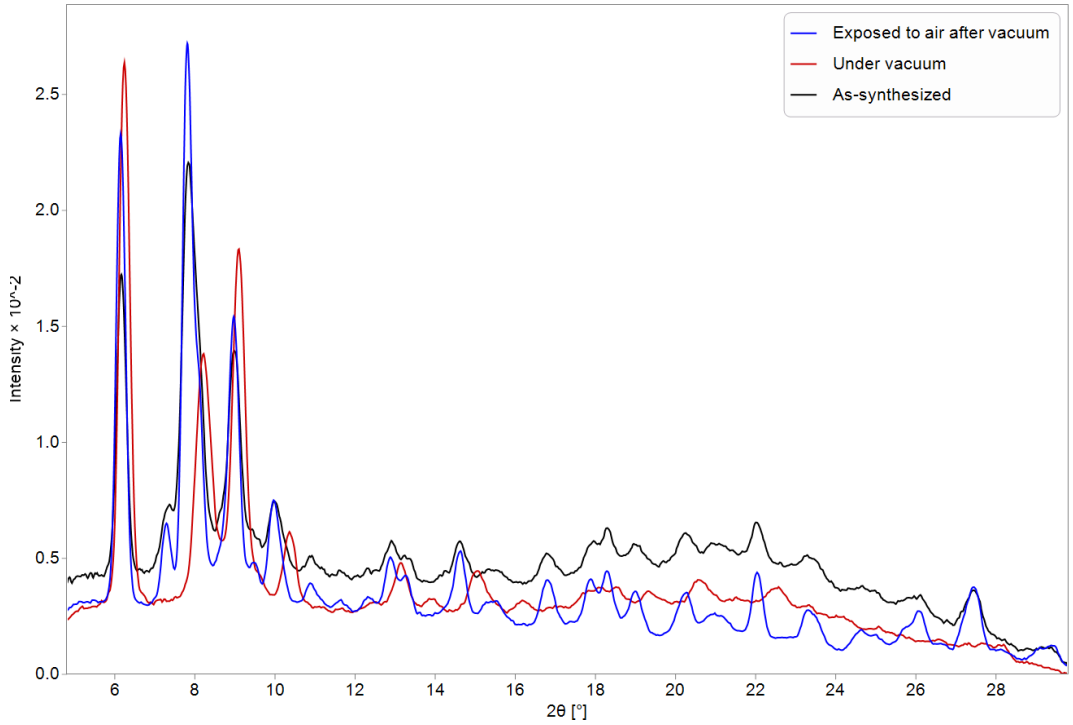

Figure 3.23. PXRD pattern of MUF-23 under vacuum in comparison to its as-synthesized state and after removing vacuum and exposing to atmosphere.

As can be seen from Figure 3.23, the PXRD patterns of MUF-23 under vacuum shows that peak at 2θ = 7.5° completely disappears and the one at 2θ = 8° and 2θ = 9 ° are shifted to high angles compared to as-synthesized state. MUF-23 structure turns back to its as-synthesized state after removing vacuum and exposing it to atmosphere. MUF-21 shows flexibility during the adsorption of CO_2 and C_2H_6. MUF-23 shows flexibility upon

adsorption of C_2H_6, C_2H_4, C_2H_2 and CO_2 in a range of different temperatures and low pressures (0-1 bar). These isotherms are presented in Figure 3.24 and 3.25.

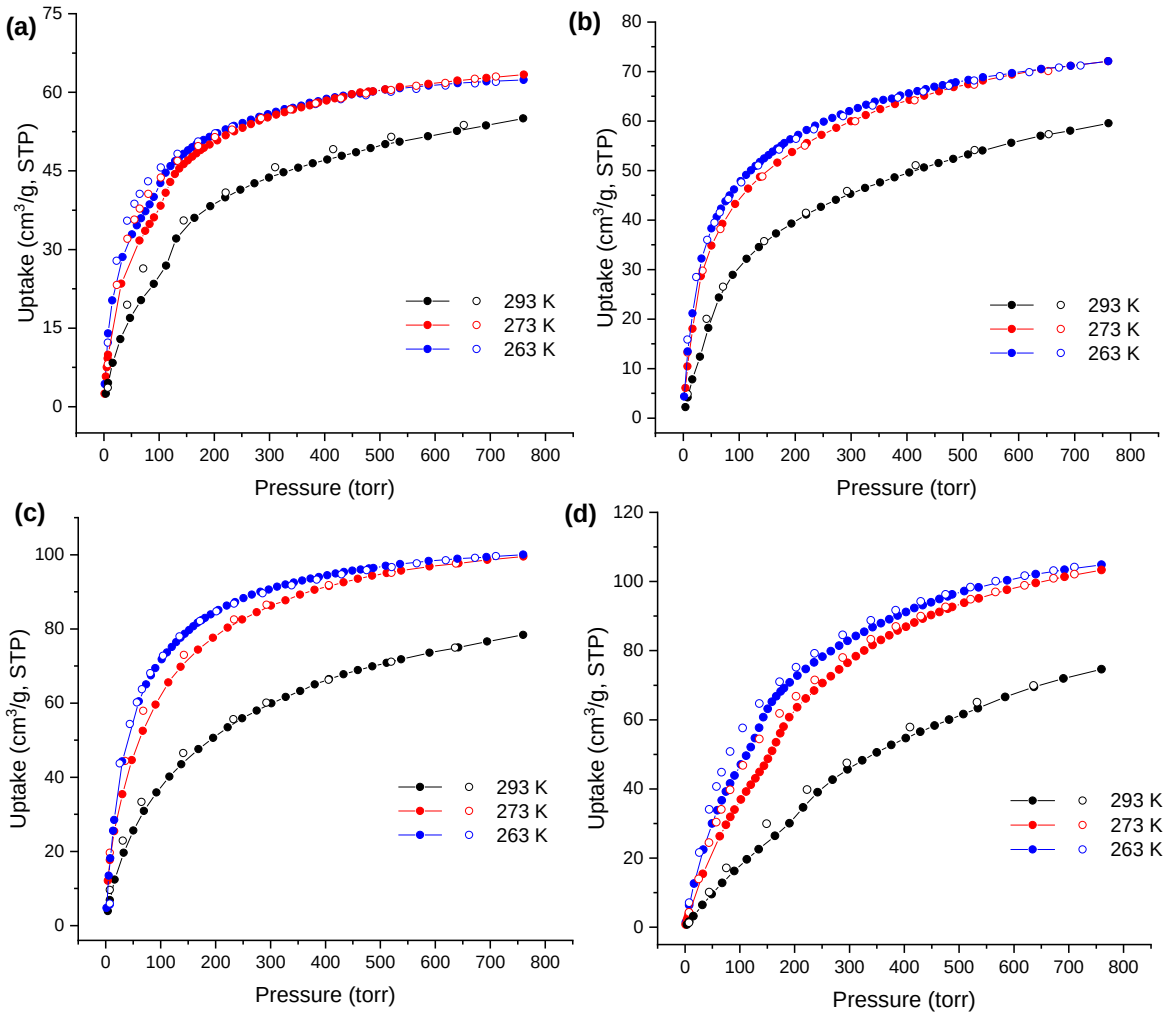

Figure 3.24. Volumetric (a) C_2H_6, (b) C_2H_4, (c) C_2H_2 and (d) CO_2 adsorption (filled circles) and desorption (open circles) isotherms measured at different temperatures for MUF-21.

Apparently, interaction of guest molecules and pore surfaces in a certain gas uptake (or pressure) triggers a rotation of functionalized linkers and opens up more space for further adsorption of guest molecules. This uptake (pressure) at which frameworks open up more space (so-called gate opening point) varies upon inclusion of different guest molecules or by the change of temperatures. Generally, inclusion of polar molecules at low temperatures can increase the interaction energy between framework and guest molecules and consequently induce the frameworks flexibility. In the case of MUF-21, we were able to see flexibility upon adsorption of C_2H_6 and CO_2 by measuring their adsorption isotherms at three different temperatures of 293, 273 and 263 K, while C_2H_2 and C_2H_4 shows type I Langmuir isotherms

at these temperatures in the whole pressure range. As both C_2H_4 and C_2H_2 are more polar than C_2H_6 and CO_2, we believe these gases can induce framework for gate opening behaviour right after they are introduced to the pores as the interaction between them and frameworks is strong enough to trigger the rotation of linkers, while CO_2 and C_2H_6 need to reach a certain uptake (pressure) to induce framework flexibility. This behaviour can be clearly justified by comparing the shape of C_2H_6 adsorption isotherm at different temperatures of 293, 273 and 263 K. At 293 K, the gate opening pressure can be clearly observed showing a smooth jump in uptake capacity before and after frameworks expansion. Moving towards lower temperatures, the interaction between C_2H_6 molecules and framework increases and the boundary before and after expansion is disappearing leading to an isotherm shape similar to the type I Langmuir isotherm.

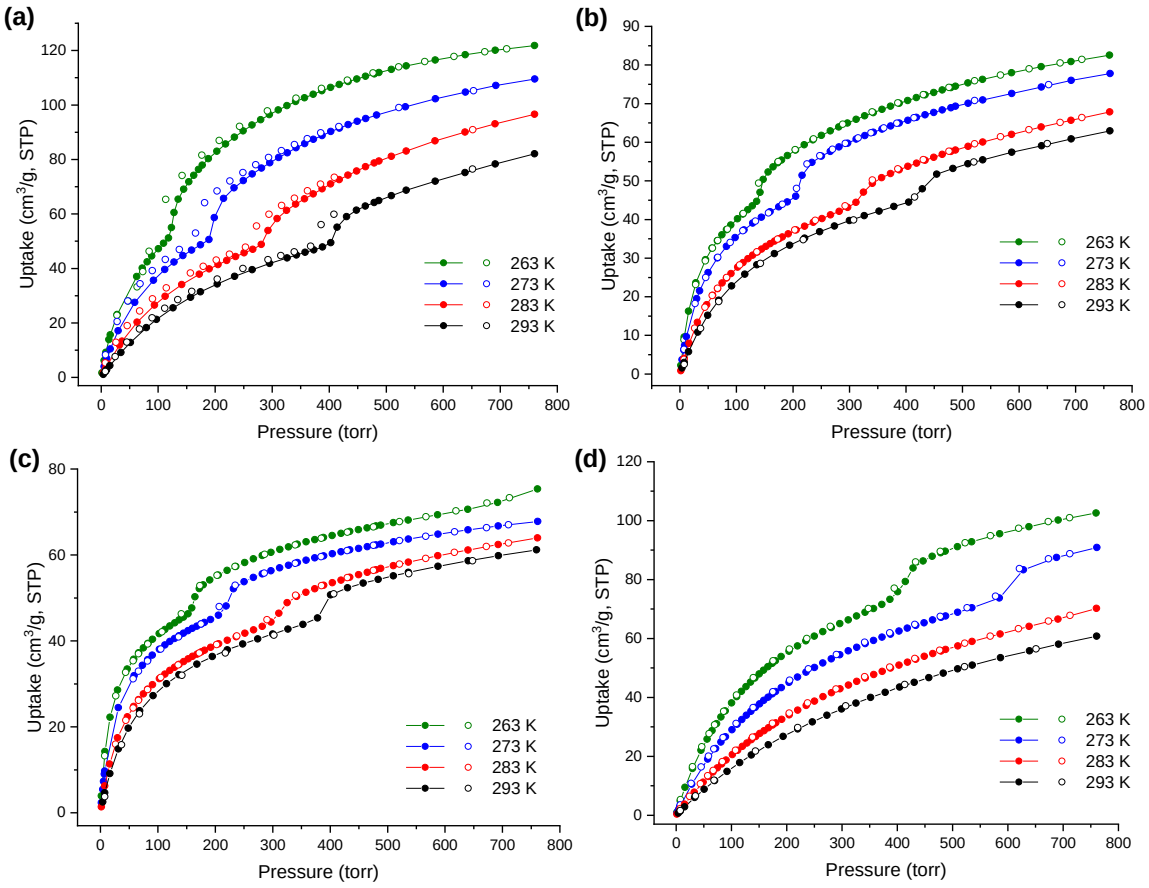

Figure 3.25. Volumetric (a) C_2H_2, (b) C_2H_4, (c) C_2H_6 and (d) CO_2 adsorption (filled circles) and desorption (open circles) isotherms measured at different temperatures for MUF-23.

In contrast to MUF-21, MUF-23 indicates flexibility for all the four gases of C_2H_6, C_2H_4, C_2H_2, and CO_2 at different temperatures. In addition, the gate opening behaviour is more pronounced in MUF-23 compared to MUF-21. MUF-23 indicates a sharp jump in gas uptake at gate opening pressure (an uptake of 45 cm^3/g for acetylene at 263 K), pointing out a

significant structural change. This abrupt change compared to the gradual gate opening of MUF-21 might be explained by two factors. Rotation of lengthy methoxy group can open up more spaces compared to smaller nitro groups and different polarity of these substituent, thus resulting in different host-guest interactions. More interestingly, MUF-23 shows a clear dependence of the gate-opening pressure to temperature. As can be seen from Figure 3.25a, reducing temperature from 293 K to 263 K, the gate opening pressure decreases from 400 torr to 100 torr for adsorption of C_2H_2 molecules. This is obviously because of stronger interaction of guest molecules with framework at low temperatures, at which only a small quantity of adsorbed guest molecules are required to trigger framework flexibility. As observed by adsorption isotherms of MUF-21, MUF-23 also shows that gate opening behaviour disappears at a certain temperatures. For instance, we measured C_2H_4 and CO_2 adsorption isotherm at 195 K and as can be seen from Figure 3.26, there is no sign of gate opening phenomena at this temperature for C_2H_6. CO_2 isotherm at this temperature also exhibits gate opening behaviour at much lower pressure (85 torr) and a high uptake (130 cm^3/g). The gate opening uptake of CO_2 at 195 K is much higher than that of other temperatures (263-293 K). It can be attributed to insufficient thermal energy at this temperature, thus higher amount of CO2 is required to induce the flexibility.

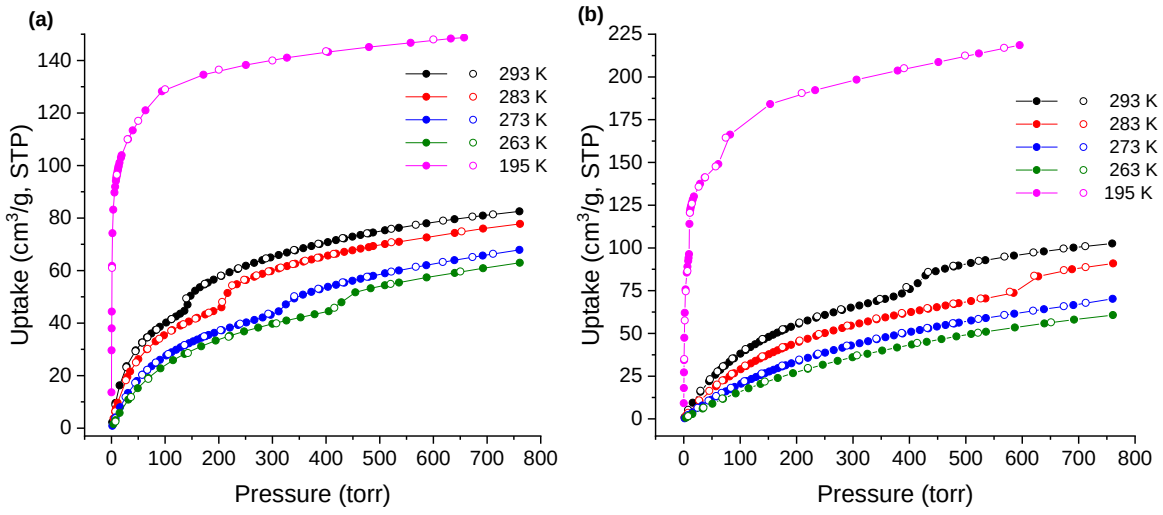

Figure 3.26. Volumetric adsorption (filled circles) and desorption (open circles) isotherms of (a) C_2H_4 and (b) CO_2 by MUF-23 at 195 K in comparison with higher temperatures, showing the disappearance of gate opening phenomena.

Moreover, MUF-23 shows different gate opening pressure upon inclusion of different guest molecules. As can be seen from Figure 3.27, C_2H_2 has the lowest gate opening pressure (190 torr) with an uptake of 70 cm^3/g, while C_2H_4 and C_2H_6 open up the frameworks in almost the same pressures (210 torr) and uptakes (43 cm^3/g). Compared to the rest, CO2

exhibited the highest gate opening pressure (600 torr) and uptakes (70 cm^3/g). Such a trend of gate opening pressures for these molecules can be attributed to their polarity as C_2H_2 with higher polarity triggers framework flexibility at lower pressures and uptakes, and less polar CO_2 (compared to C_2H_2) at relatively higher pressures and uptakes.

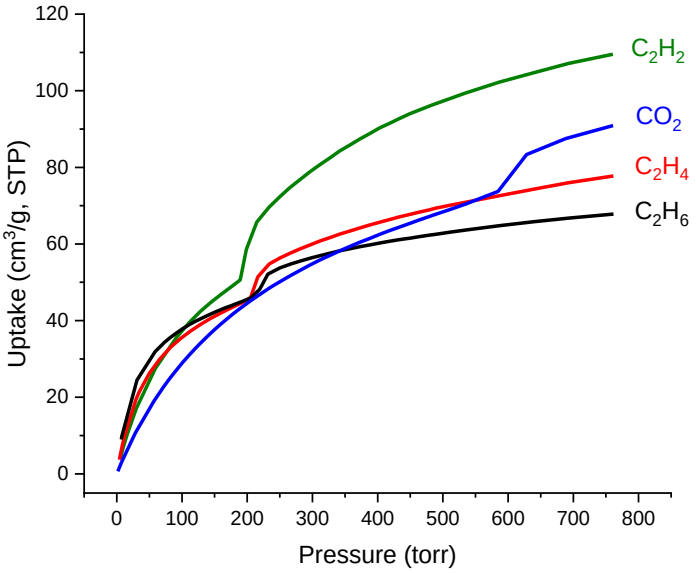

Figure 3.27. Volumetric adsorption isotherms measured at 273 K for MUF-23, showing different gate opening pressures for various gases.

Such gas-induced behaviour and resulting differences in gate opening pressure caused by host–guest interactions could be a unique advantage for gas separation. As a promising application for flexible MOFs, energetically favourable pressure swing adsorption processes can be employed to separate gases as a result of adsorption discrepancy of different gases in these frameworks. Adsorptive separation of CO_2 over O_2 and N_2 on a flexible two-dimensional framework CID-3 (constructed from interdigitated $[Zn(2,7\text{-ndc})\text{-}(bipy)]_n$ layers (2,7-ndc = 2,7-naphthalene dicarboxylate) is a good example proposed by Kitagawa and co-workers.[278] The flexible MOF, MIL-53(Al) was also employed to study CO_2/N_2 separation. Rodrigue et al., incorporated MIL-53(Al) and its amino-functionalized analogues into the mixed matrix membranes for CO_2/CH_4 separation.[279] This membrane (6FDA–ODA polyimide (6FDA = 4,40 -(hexafluoroisopropylidene)-diphthalic anhydride; ODA = 4,40 -oxydianiline) used as polymers) exhibits a high ideal selectivity of up to 77 with a separation factor up to 53. [280] In another interesting work, Chen and co-workers, discovered a microporous material $[Zn(dps)_2(SiF_6)]$ (UTSA-300, dps = 4,4'-dipyridylsulfide) with two-dimensional channels of about 3.3 Å in size, well-matched for the separation of small molecules such as C_2H_2. The network is transformed to its closed-pore phase upon activation, while inclusion of C_2H_2 molecules opens up its structure, resulting in an appreciable

adsorption of C_2H_2 molecules. More interestingly, the structure remains closed upon exposure of CO_2 and C_2H_4 molecules, making this material an excellent adsorbent for C_2H_2/C_2H_4 and C_2H_2/CO_2 separations.[281]

As an example of such flexible behaviour for gas separation applications, we have investigated the application of MUF-23 for separating CO_2 from N_2 at 273 K. The reason why we chose these two gases and this temperature was that MUF-23 shows gate opening behaviour at 273 K for CO_2 while N_2 isotherm at this temperature shows no sign of flexibility. Adsorption isotherms of CO_2 and N_2 at 273 and DSLF fitting parameters are presented in Figure 3.28. It should be noted that the CO_2 isotherm at entire pressure range has been considered to predict IAST selectivity (considering the flexible nature of MUF-23).

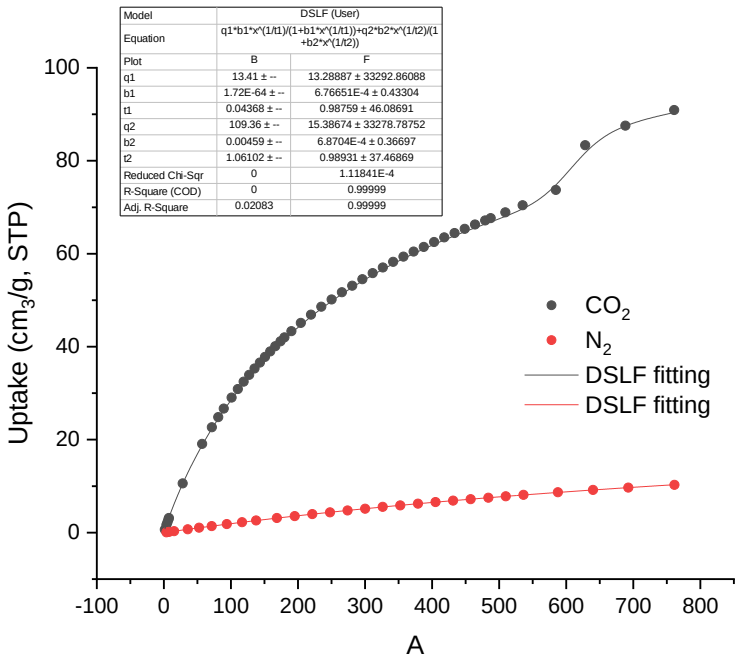

Figure 3.28. (a) Volumetric adsorption isotherms of CO_2 and N_2 at 273 K for MUF-23 fitted with DSLF model.

These isotherms show MUF-23 can be a good candidate for efficient separation of CO_2 from N_2 at 273 K and 1 bar, as it shows an abrupt jump at 600 torr in gas uptake, resulting a CO_2 uptake of 90 cm^3/g at 750 torr. However, single gas adsorption isotherms are not the ideal metrics to evaluate an adsorbent for its separation performance in real operating conditions, as it does not consider the kinetics of adsorption and possible competitive adsorption by other impurities in the mixture. This is even more prominent in case of flexible MOFs, as upon gate opening, there would be more space for other existing gases in the mixture as well. In addition, as the guest-host interaction is one of the main factors for

inducing the framework, existence of other gases in the mixture may affect drastically on the occurrence or the pressure of gate opening. On the other hand, single gas isotherms hint at the dependency of separation performance of MUF-23 on pressure. Hence, to demonstrate the effect of flexibility on separation performance of MUF-23 under dynamic conditions and pressure-dependent separation performance of MUF-23, we measure its breakthrough curve before and after gate opening pressures.

Firstly, we measured the single gas breakthrough curves of CO_2 at different partial pressures to see if we can detect different gate opening behaviour which may then underlie a pressure-dependent separation performance. To do this, a mixture of CO_2 and an inert gas (helium) was introduced to an adsorption column packed with 0.85 g of MUF-23 at 273 K and 1.02 bar. Four different mixtures of CO_2/He as shown in Table 3.4 were introduced to the column. Three of them have a CO_2 partial pressure before gate opening pressure and the other one has a CO_2 partial pressure after gate opening pressure. It should be noted that in all of these experiments, the inlet flow rate of CO_2 was kept constant (3 ml_N/min).

Table 3.4. Feed composition for single gas breakthrough experiments.

Inlet mixture (CO_2/He)	CO_2 partial pressure (torr)	CO_2 flow rate (ml_N/min)	Helium flow rate (ml_N/min)	Total pressure (bar)
50/50	375	3	3	1.02
60/40	450	3	2	1.02
70/30	525	3	1.28	1.02
95/5	720	3	0.16	1.02

Single gas breakthrough curves are presented in Figure 3.29. As expected, CO_2 broke through from the column earlier in a mixture of CO_2/He 50/50, compared to the mixture with higher percentage of CO_2. This is due to the lower CO_2 uptake capacity at low partial pressures, which leads to an early saturation of adsorption column i.e. the bed takes up a lower amount of CO_2, thus leading to an earlier breakthrough of CO_2. This breakthrough time increases to 22 min for the mixture with 95% CO_2. Comparing the breakthrough time between two inlet feeds with 70 and 95% CO_2, there seems to be a significant difference in breakthrough time. This might correspond to the abrupt jump in gas uptake brought about by the structural deformation of the MOF which is expected in this region.

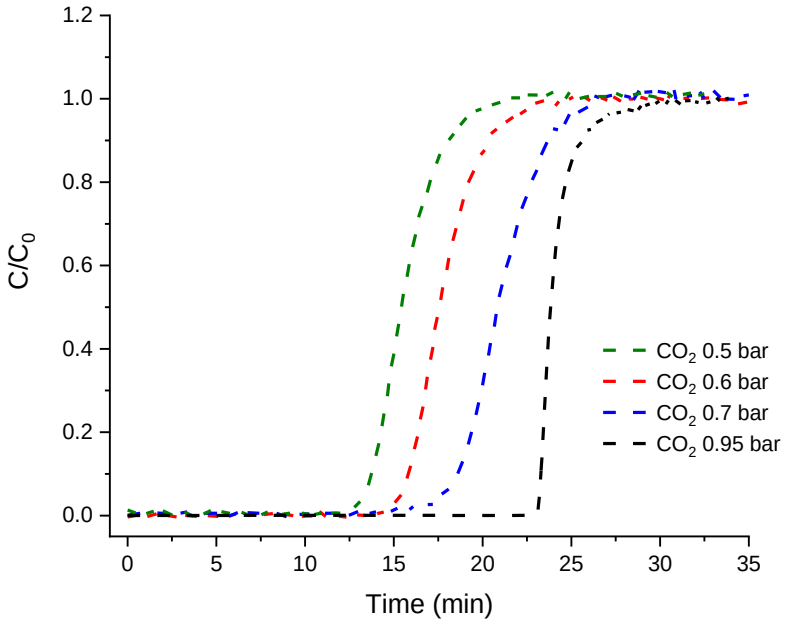

Figure 3.29. Experimental single-component breakthrough curves of CO_2 for gas streams with different partial pressures of CO_2 in a column packed with MUF-23 at 273 K and 1.02 bar. Non-adsorbing He gas was used to bring the pressure up to 1.02 bar in all cases.

To investigate this, we decided to simulate the breakthrough curves of CO_2, assuming there is not any jump in its adsorption isotherm, i.e. no gate opening phenomena and compare it with experimental breakthrough and simulated breakthrough with the assumption that there is gate opening phenomena. If CO_2 breaks through earlier for MUF-23 under the assumption of no gate opening phenomena compared to the inclusion of the gate opening phenomena, then it can be concluded that the flexible nature of MUF-23 has improved its separation performance through a pressure-dependent mechanism. First, a reliable mass transfer coefficient should be obtained. We proceeded under the assumption that the mass transfer coefficient before and after flexing should be different. Breakthrough curves were simulated for the four mixtures of CO_2 and compared with the experimental breakthrough curves (Figure 3.30). It should be noted that the simulated breakthrough for the 95% CO_2 mixture is predicted considering the flexible nature of MUF-23 (using the DSLF model, Figure 3.28). Also we assumed zero adsorption of helium by MUF-23. A reliable mass transfer coefficient for the simulated breakthrough curves was then estimated from the experimental breakthrough curves. A mass transfer coefficient of 0.0085 s^{-1} and 0.0133 s^{-1} was found to be the optimum value, leading to a satisfactory match between predicted and experimental breakthrough curves before and after flexing, respectively (Figure 3.30).

Identical operating conditions, feed characteristics, adsorbent amount and bed dimension was used to predict these breakthrough curves.

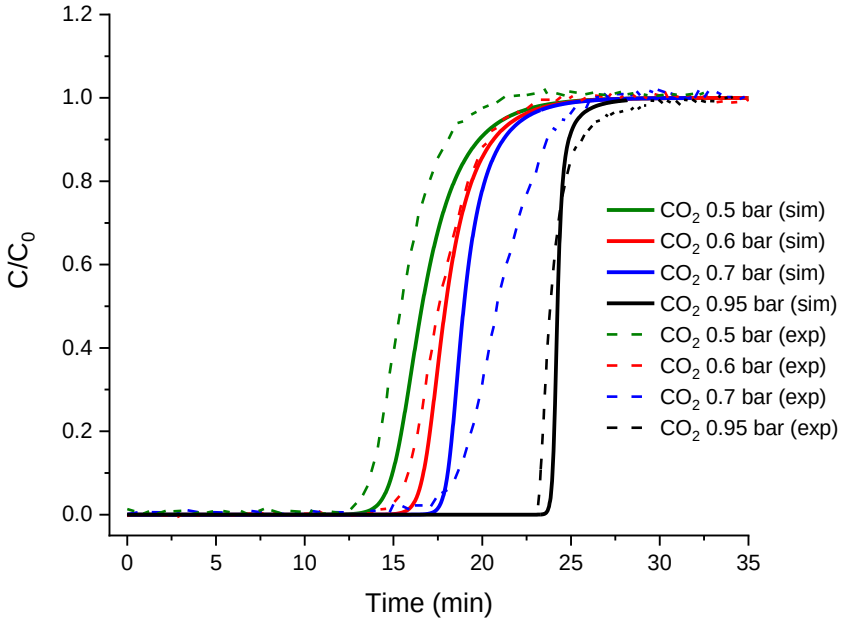

Figure 3.30. Predicted single-component breakthrough curves of CO_2 for gas streams with different partial pressure of CO_2 in a column packed with MUF-23 at 273 K and 1.02 bar in comparison with experimental breakthrough curves (from Fig. 3.29).

Having the tuned mass transfer coefficient in hand for the framework structure prior to flexing, a breakthrough curve was then estimated for a mixture of 95/5 CO_2/He (at 1 bar). This assumes no gate opening process occurs (Figure 3.32). To simulate breakthrough curve with this assumption, the CO_2 adsorption isotherm of MUF-23 was refitted only using the adsorption data points up to the gate opening pressure, as indicated in Figure 3.31 (red line).

These new fitting parameters were used further for the simulation of breakthrough curves. A comparison of breakthrough curves for MUF-23 that both consider (black line) and neglect (pink line) the gate opening phenomena are presented in Figure 3.32. It shows the flexibility of MUF-23 has improved the performance of MUF-23 by increasing the CO_2 breakthrough time from 20 min to 24 min. This jump in breakthrough time corresponds to the gate opening phenomena in MUF-23. In this way the flexibility of MOFs can be used to enhance gas separation performance under dynamic conditions.

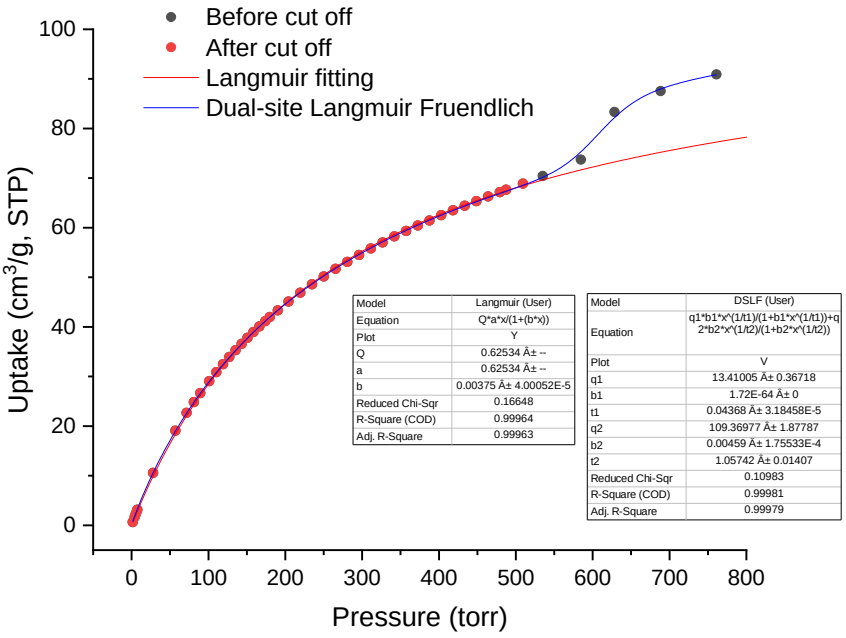

Figure 3.31. Fitting parameters for CO_2 adsorption isotherm by MUF-23 at 273 K before and after cut-off. DSLF model was used before cut-off and Langmuir model after cut-off.

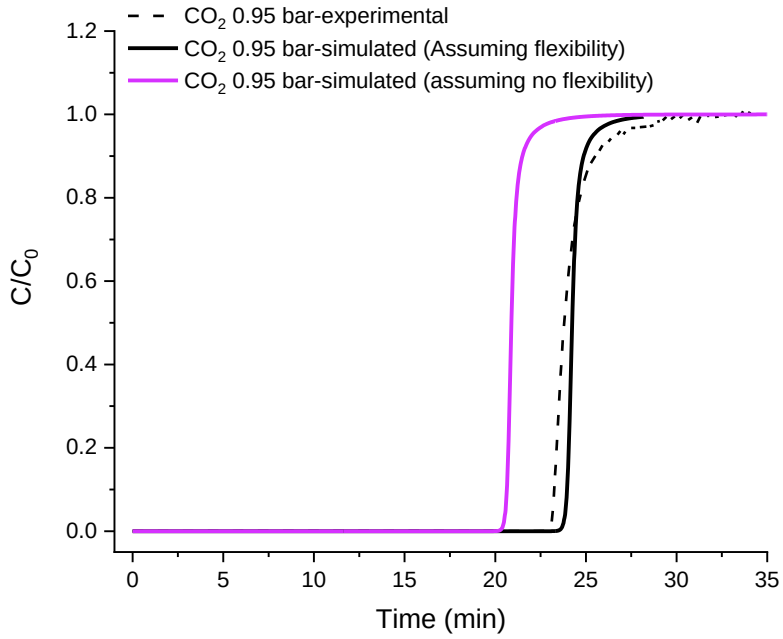

Figure 3.32. Predicted single gas breakthrough curves of CO_2 for a mixture of 95/5 CO_2/He in a column packed with MUF-23 at 273 K and 1.02 bar, assuming MUF-23 as a rigid MOFs in comparison with a flexible model.

At the end of this chapter, the performance of MUF-23 for separation of CO_2 from N_2 is presented as an example of a binary mixture with only one of the components (CO_2) benefitting from the gate opening behaviour. This case study exemplifies the positive effect

gate opening phenomena can have on competitive gas separation processes. Thus, experimental breakthrough curves were measured for two mixtures - 60/40 and 85/15 CO_2/N_2 - at 273 K and 1.02 bar. The CO_2 partial pressure in the 60/40 mixture is lower than the gate opening pressure, while its partial pressure in the 85/15 mixture is expected to induce gate opening.

The experimental breakthrough curves are shown in Figure 3.33. These breakthrough curves show MUF-23 can successfully separate CO_2 from N_2, as N_2 elutes through the bed first to yield an outflow of pure N_2 gas. Mass transfer coefficients were then obtained by tuning the predicted breakthrough curves to best match the experimental ones. A mass transfer coefficient of 0.0133 s^{-1} was deduced for CO_2 in this way.

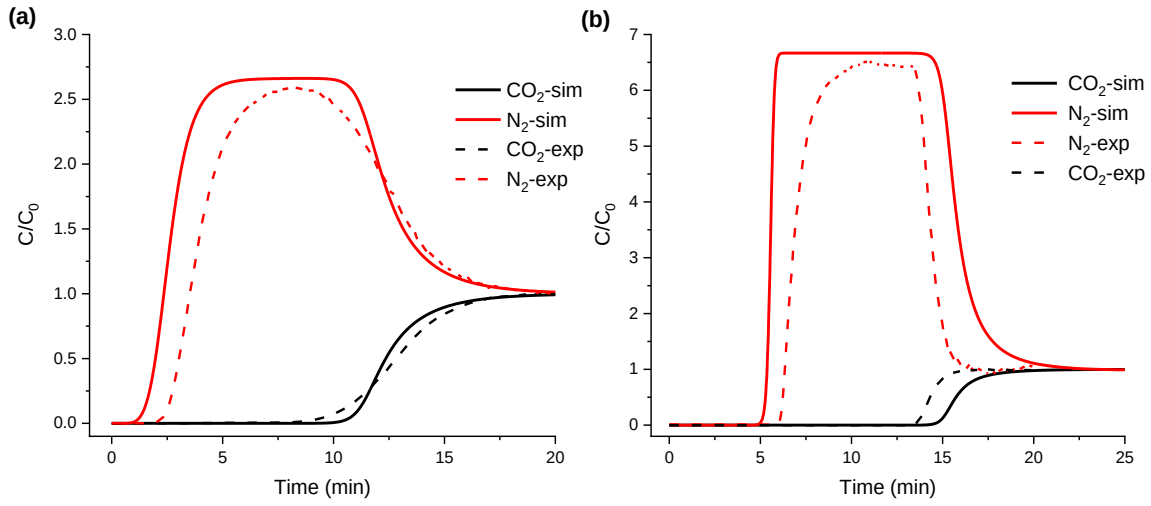

Figure 3.33. Experimental and predicted breakthrough curves for a mixture of (a) 60/40 CO_2/N_2 and (b) 85/15 CO_2/N_2 in column packed with MUF-23 at 273 K and 1.02 bar.

As before, this mass transfer coefficient was then used to predict breakthrough curves for a mixture of 85/15 CO_2/N_2 under two different assumptions: (i) that MUF-23 is inflexible (red line) and (ii) that MUF-23 is flexible (Figure 3.34). The predicted breakthrough curves assuming no flexibility shows that CO_2 elutes 2.5 min earlier than MUF-23 compared to assuming flexibility. This 2.5 min difference correspond to the beneficial effect of the gate opening phenomenon, where framework opens up more space, thus resulting in an enhanced preferential adsorption of CO_2. The elution times of N_2 passing through a bed of MUF-23 are similar considering both flexibility and inflexibility. This indicates that little extra N_2 is adsorbed upon framework expansion, and CO_2 is the main beneficiary of the additional pore space created in the gate-opened framework. This is consistent with the high calculated selectivity for CO_2 over N_2 at 1 bar based on single-component isotherms (Figure 3.28).

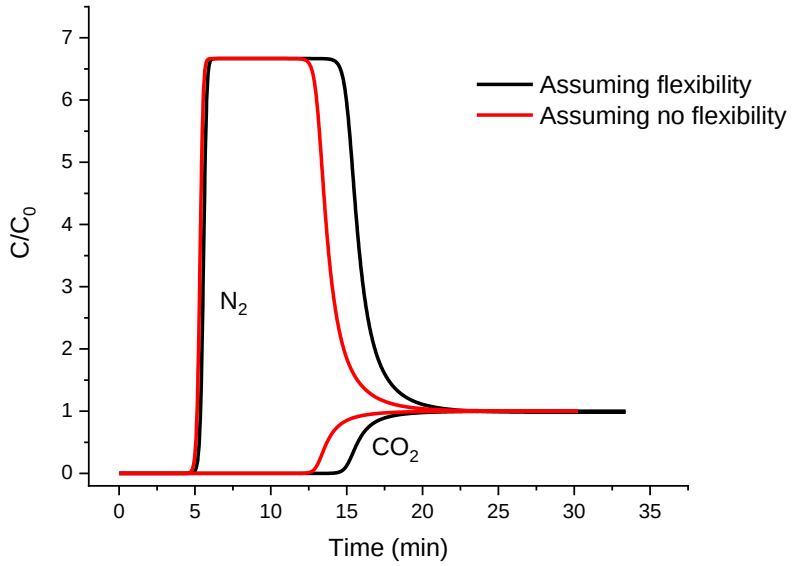

Figure 3.34. Predicted breakthrough curve for a mixture of 85/15 CO_2/N_2 for a bed packed with MUF-23 at 273 K and 1.02 bar assuming no flexibility for MUF-23 in comparison to MUF-23 showing flexibility.

3.3 Conclusion

In this chapter, the synthesis, characterization and separation performance of an isoreticular family of MUF-15 frameworks functionalized with a series of different functional groups, namely fluoro (MUF-18), hydroxy (MUF-19), bromo (MUF-20), nitro (MUF-21), methyl (MUF-22) and methoxy (MUF-23), representing a broad range of sizes and functional properties, was reported. As these functionalities point into the void spaces, the pore characteristics and surface polarities of these MOFs vary significantly, resulting in different adsorption behaviour for guest molecules. As expected, introducing the functional groups into MUF-15 reduces the pore volume and surface area. However, BET surface area and void fraction calculations based on N_2 isotherms at 77 K showed that the introduction of bulkier functional groups is not proportionally in line with the decrease of surface area and pore volume. For instance, both the BET surface area and pore volume of MUF-22 (methyl functionalized MUF-15) are higher than that of MUF-18 (fluoro functionalized MUF-15), while the methyl group is larger than the fluoro group. Isosteric heat of adsorptions calculation demonstrated that MUF-18 and MUF-21 interact stronger with guest molecules (C_2H_2, CO_2, C_2H_4 and C_2H_6) compared to MUF-15 and other derivatives. Interestingly, the water stability of these derivatives also significantly changed upon introduction of different functional groups. MUF-22 and MUF-23 indicated extraordinary water stability, i.e. these frameworks maintains their porosity and structure after six months exposure to humid air, which is much longer than the one week stability of MUF-15.

Further, the separation performance of these MOFs was evaluated based on IAST for three binary mixtures of C_2H_6/C_2H_4, C_2H_2/C_2H_4 and C_2H_2/CO_2. MUF-15 indicated the highest selectivity (~2) at the whole range of pressures for C_2H_6/C_2H_4 mixture, showing that introduction of functionalized groups do not improve the C_2H_6/C_2H_4 separation performance of MUF-15. As these functional groups mainly enhance the polarity of pore surface, they increase the interaction of frameworks with C_2H_4 as more polar gas, thus decreasing the selectivity of the frameworks for adsorption of C_2H_6 over C_2H_4. Interestingly, MUF-21 which is functionalized with nitro groups shows reverse selectivity for C_2H_6/C_2H_4, wherein its selectivity for C_2H_6/C_2H_4 drops to 0.39 at 1 bar. That can be explained by the introduction of polar nitro groups that interact more strongly with the polar C_2H_4 molecules. These results proves the underlying mechanism of ethane-selective MOFs: More inert surfaces enhance the ethane selectivity of frameworks, while a highly polar surface favours the adsorption of C_2H_4.

Surprisingly, MUF-21 and MUF-23 showed flexibility upon inclusion of guest molecules such as C_2H_2, CO_2, C_2H_4 and C_2H_6 at ambient conditions. We believe this flexibility originates from the rotation of phenyl rings upon the inclusion of guest molecules, thus opening up more space. This is also believed that MUF-15 and all of its family have flexible structures varying in the gate opening pressure and temperature. MUF-23 was further investigated to see the effect of flexibility on its separation performance. A combination of predicted and experimental breakthrough proved that the gate opening process improves the performance of MUF-23 for the separation of CO_2 from N_2.

3.4 Experimental and computational section

3.4.1 General procedures

All starting compounds and solvents were used as received from commercial sources without further purification unless otherwise noted.

3.4.2 Thermogravimetric Analysis (TGA)

Thermogravimetric analyses were performed on a TA Instruments Q50 instrument. Measurements were made under a N_2 flow with a heating rate of 5 °C /min. The mother liquor of the as-synthesized MOF crystals was replaced with fresh methanol multiple times. The MOF crystals were then evacuated under high vacuum to afford desolvated MOFs. The exposure time to atmosphere for these MOFs before doing TGA was around 5-20 minutes.

3.4.3 Single crystal X-ray diffraction

As per Chapter 2, except that MUF-18 and MUF-22 data were collected at the Australian Synchrotron.

As-synthesized MUF-18, MUF-22 and MUF-23 were soaked in fresh methanol and was replenished few times within a day to produce crystals suitable for single crystal X-ray diffraction analyses. MOF crystals were analysed right after removing them from methanol.

Room temperature data collection also produced better refinement statistics than low temperature data collection.

3.4.4 Powder X-ray diffraction patterns

As per Chapter 2. The data were obtained from freshly prepared MOF samples that had been washed several times with MeOH. MOF crystals were analysed right after removing them from methanol. Predicted powder patterns were generated from single crystal structures using Mercury.

3.4.5 Powder X-ray diffraction patterns under vacuum

The PXRD pattern for samples were measured under vacuum using a 0.5 mm capillary. After washing as-synthesized samples several times with methanol, they were dried under vacuum at room temperature for 2 hours. Then they were ground gently using a pestle and mortar. The ground samples were then transferred to a 0.5 mm. The very top of capillary was then blocked with glass wool to make sure MOFs are kept in the capillary upon vacuum. The capillary was connected to a Quantachrome Autosorb iQ2 and kept under vacuum for 10 hours while being heated at 110 °C. The very top of the capillary was then burned using a flame gun. The burned capillary was then mounted to Rigaku Spider X-ray diffractometer for further PXRD studies.

3.4.6 Aging experiments on activated frameworks

After washing as-synthesized samples several times with MeOH, they were activated and were aged in air at 70-85% relative humidity and 20 °C.

3.4.7 Modeling, calculations and simulations

Single crystal structures of MUF-18, MUF-22 and MUF-23 were used directly for all the calculations and simulations without modification. The Zeo++ code and RASPA were used to characterize the geometric features of the crystal structures and its derivatives by calculating the pore volume with the use of a helium probe atom, the pore limiting diameter), the largest cavity diameter, and the surface area accessible to a H_2 probe (a N_2 probe produce a surface area of zero) using the coordinated found by X-ray crsytallography.

3.4.8 Gas adsorption measurements

As per Chapter 2. The as-synthesized samples were washed with anhydrous methanol several times and about 25-100 mg was transferred into a pre-dried and weighed sample tube and heated at rate of 10°C/min to a temperature of 120-130 °C under a dynamic vacuum with a turbomolecular pump for 20 hours (MUF-19 was activated at room temperature).

3.4.9 IAST calculations

As per Chapter 2.

3.4.10 Breakthrough curve measurements

In a typical breakthrough experiment, 0.85 g of activated MUF-23 was placed in an adsorption column (6.4 mm in diameter × 11 cm in length) to form a fixed bed. The adsorbent was activated at 130 °C under high vacuum for 12 hours and then the column was left under vacuum for another 3 hours while being cooled to 20 °C. The column was then purged under a 20 mL_N/min flow of He gas for 1 hr at 1.1 bar prior to the breakthrough experiment. A gas mixture containing either CO_2/He or CO_2/N_2 with different compositions was introduced to the column at 1.02 bar and 20 °C (See table 3.4). The operating pressure was controlled at 1.1 bar with a back-pressure regulator. The outlet composition was continuously monitored by the mass spectrometer until complete breakthrough was observed.

Table 3.5. Feed composition for single and multiple gas breakthrough experiments.

Inlet mixture	CO_2 partial pressure (torr)	CO_2 flow rate (ml_N/min)	N_2 flow rate (ml_N/min)	Total pressure (bar)
60/40	375	3	2	1.02
85/15	450	3	0.52	1.02

3.4.11 Breakthrough curve simulations

As per Chapter 2. A bed with dimension of 100 mm in length and 6.4 mm in diameter with 0.85 g adsorbent was considered for simulation.

Chapter 4

A Series of Isostructural Metal-Organic Frameworks for Efficient Adsorption of CO_2

2.1 Introduction

One of the most critical environmental issues of our age is the escalating release of CO_2 into the atmosphere. CO_2 release principally stems from the combustion of fossil fuels.[282-283] Atmospheric CO_2 levels can be reduced by using less petroleum and natural gas, sequestering the CO_2 at point sources where significant quantities are released, or capturing it directly from air. In addition to fossil fuel combustion, significant amounts of CO_2 are released during the production of electricity from geothermal vents and the sweetening of natural gas and biogas (natural gas produced from biomass).[284] Currently, state-of-the-art technology for CO_2 capture involves absorption of CO_2 using wet amine chemisorptions such as primary and secondary alkyl because of their large capacity and high selectivity for acidic gas.[139-140] However, implementation of these methodologies is associated with several drawbacks including high energy consumption during the regeneration, solvent loss due to the degradation and evaporation, and corrosive nature of amines.[138, 141] Hence, the search for materials that not only show high CO_2 capacity and selectivity but also require mild regeneration condition is of major importance. More broadly, adsorbents that are specific to CO_2 can also be implemented for the purification of important industrial gas streams such as syngas and to eliminate CO_2 from enclosed atmospheres.

Many MOFs are effective CO_2 sequestration materials.[24, 97, 132, 134, 203, 285-289] Unlike the classical zeolites, which have a limited number of structures, more than 75,000 MOFs have been synthesized through the selection availability of a rich library of inorganic and organic building blocks. Moreover, thanks to their inherent modularity, MOFs can enable exquisite control over pore-size and pore-chemistry.[37, 40, 134, 285, 290-291] Several strategies have been employed to improve the CO_2 capture performance of MOFs for carbon capture processes, such as functionalization of the pores with highly polar groups or introduction of exposed metal sites within the framework. These endow the frameworks with electric dipoles that align with the CO_2 quadrupole to enhance the uptake and selectivity towards this guest. Even though these approaches have led to materials with enhanced separation performance, they

typically suffer from low selectivities, particularly at high pressures, or a loss in capacity in the presence of water due to the competitive adsorption of other impurities in the mixture.[38, 142, 292-301] Furthermore, the underlying mechanism of such a separation originates from the increased affinity of the material for CO_2 which incurs high energy penalty during regeneration when it is removed from the framework. For example, CuBTTri with a pores functionalized by N,N'-dimethylethylenediamine shows adsorption enthalpies of −96 kJ/mol.[302]

As an alternative to enhancing the affinity for CO_2 through strong electrostatic interactions, it can be adsorbed through cooperative effect of appropriate pore size and optimal electrostatic interactions. A pore dimension of similar to molecular size of CO_2 molecule enables close contact of CO_2 and pore surface, and favourable host-guest interaction guarantee an efficient adsorption of CO_2. However, this is very hard to achieve in practice since it requires exquisite control over the structure of materials to produce rigid pores with apertures fixed precisely between the kinetic diameters of the species of interest, and in the same time a favourable orientation of electrostatics forces between adsorbate and adsorbent. Please refer to Chapter 1 regarding CO_2 adsorption in MOFs and their different adsorption behaviour.

4.2 Results and discussion

A family of MOFs with the formula of $[M(Haip)_2]$, where M = Co(II), Mn(II), or Ni(II) and H_2aip is 5-aminoisophthalic acid, was synthesized. These materials are coordination polymers built up from reaction of metal salts and 5-aminoisophthalic acid. This structure was first reported in 2006 with cobalt(II) as the metal ion.[303] We have termed this material MUF-16. Few years later, its manganese(II) analogous was synthesized in 2015 (termed MUF-16(Mn)).[304] We also added the nickel(II) version to this family, MUF-16(Ni). MUF-16(Mn) and MUF-16(Ni) were synthesized based on the reported procedure with slightly modification.[304]

A mixture of $M(ClO_4)_2 \cdot 6H_2O$ (where M = Mn or Ni) (1.25 mmol), 5-aminoisophthalic acid (2.50 mmol, 0.45 g), and NH_4NO_3 (2.50 mmol, 0.20 g) with a mixed-solvent of CH_3CN (20 mL) and CH_3OH (15 mL) were sonicated for 20 min and sealed in 100 mL of Teflon-lined stainless steel vessel, and heated at 160 °C for two days under autogenous pressure. After cooling the oven to room temperature, the resulting brownish crystals were isolated by decanting off the mother liquor, washed with methanol several times and dried under

vacuum at 130 °C for 20 h. It yielded 0.21 g (36% based on Mn) of guest free MUF-16(Mn) and 0.28 g (47% based on Ni) of guest-free MUF-16(Ni) (Figure 4.1).

MUF-16 synthesis procedure was developed in our group to afford higher yield, shorter reaction time and milder synthesis condition. A mixture of $Co(OAc)_2.4H_2O$ (0. 625 g, 2.5 mmol), 5-aminoisophthalic acid (1.8 g, 10 mmol), methanol (80 mL), and H_2O (5 mL) were sonicated for 20 min in a sealed in a 500 mL Schott bottle then heated in a pre-heated oven at 85 °C for 2 hours under autogenous pressure. After cooling the oven to room temperature, the resulting pink crystals were isolated by decanting off the mother liquor, washed with methanol several times and dried under vacuum at 130 °C for 20 h, yielding 0.99 g (90% based on cobalt) guest-free MUF-16 (Figure 4.1).

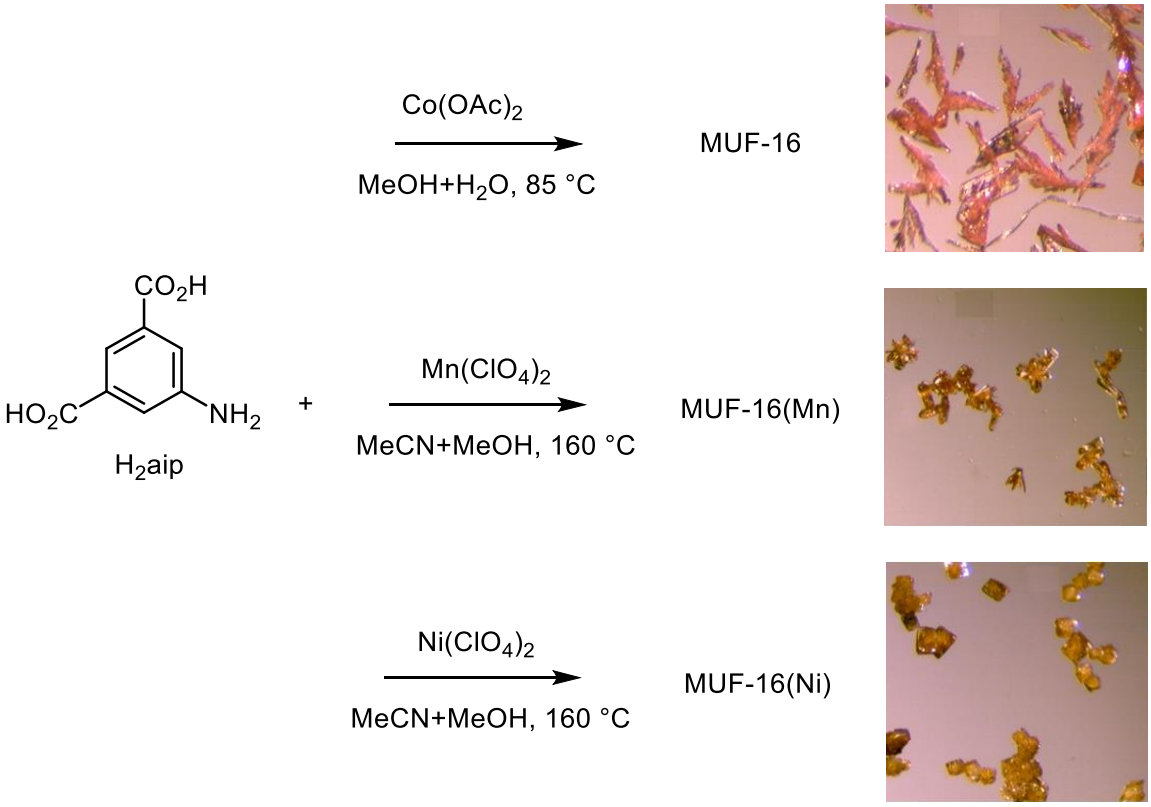

Figure 4.1 Synthetic routes to the MUF-16 family and optical micrographs of the reaction products.

The crystal structures of MUF-16 family were resolved by single crystal X-ray diffraction analysis thanks to their excellent crystallinity. The MUF-16 family is isostructural, crystalizing in the *I*2/a space group (Table 4.1), in agreement with the previous reports.[303-304] The frameworks consist of M(II) atoms with octahedral geometry lining up into a 1D chain along the crystallographic b axis through sharing two carboxylate groups from two Haip ligands (Figure 4.2a). Two adjacent chains are further pillared into 2D sheets by Haip ligands spreading along the bc plane (Figure 4.2b).

Table 4.1. Crystal data and structure refinement for MUF-16, MUF-16(Mn) and MUF-16(Ni).

	MUF-16	**MUF-16(Mn)**	**MUF-16(Ni)**
Formula	$Co(Haip)_2.2H_2O$	$Mn(Haip)_2.3H_2O$	$Ni(Haip)_2.3H_2O$
CCDC deposition #			
Empirical formula	$C_{16}H_{16}CoN_2O_{10}$	$C_{16}H_{18}MnN_2O_{11}$	$C_{16}H_{18}N_2NiO_{11}$
Formula weight	455.24	471.28	473.3
Temperature/K	292	292	293
Crystal system	monoclinic	monoclinic	monoclinic
Space group	*I2/a*	*I2/a*	*I2/a*
a/Å	15.3514(15)	25.2367(14)	15.4963(11)
b/Å	4.4232(4)	4.57990(10)	4.5780(2)
c/Å	25.614(4)	15.4895(11)	25.230(2)
α/°	90	90	90
β/°	94.294(10)	96.046(8)	96.177(8)
γ/°	90	90	90
Volume/$Å^3$	1734.4(4)	1780.34(17)	1779.5(2)
Z	4	4	4
ρ_{calc} /g cm^{-3}	1.743	1.758	1.832
μ/mm^{-1}	8.357	6.682	2.020
F(000)	932.0	972.0	856.0
2Θ range for data collection/°	11.56 to 100.864	7.044 to 143.852	11.488 to 88.944
Index ranges	$-13 \le h \le 15$, $-4 \le k \le 4$, $-25 \le l \le 24$	$-24 \le h \le 30$, $-5 \le k \le 5$, $-18 \le l \le 18$	$-14 \le h \le 14$, $-3 \le k \le 4$, $-22 \le l \le 22$
Reflections collected	5496	14132	5778
Independent reflections	908 [R_{int} = 0.0848, R_{sigma} = 0.0719]	1668 [R_{int} = 0.1054, R_{sigma} = 0.1158]	698 [R_{int} = 0.0863, $R_{□□}$ = 0.0668]
Data/restraints/parameters	908/2/137	1668/1/149	698/0/126
Goodness-of-fit on F^2	1.159	1.152	1.685
Final R indices [I>=2σ (I)]	R_1 = 0.0822, wR_2 = 0.2236	R_1 = 0.0740, wR_2 = 0.1821	R_1 = 0.1344, wR_2 = 0.3363
Final R indices [all data]	R_1 = 0.1020, wR_2 = 0.2763	R_1 = 0.1350, wR_2 = 0.2421	R_1 = 0.1714, wR_2 = 0.4053
Largest diff. peak/hole / e $Å^{-3}$	0.81/-0.49	0.57/-0.51	0.76/-0.81

Interestingly, only one of the two carboxylate groups of each Haip ligand coordinates, while the other one acts as a hydrogen-bond acceptor and donor (Figure 4.2a). This hydrogen bond assembles the layers into a 3D supramolecular open framework (figure 4.2c), exhibiting one-dimensional channels running along the crystallographic *a* axis with an approximate dimension of ~ 3.1 × 5.9 $Å^2$ (Figure 4.2d,e).

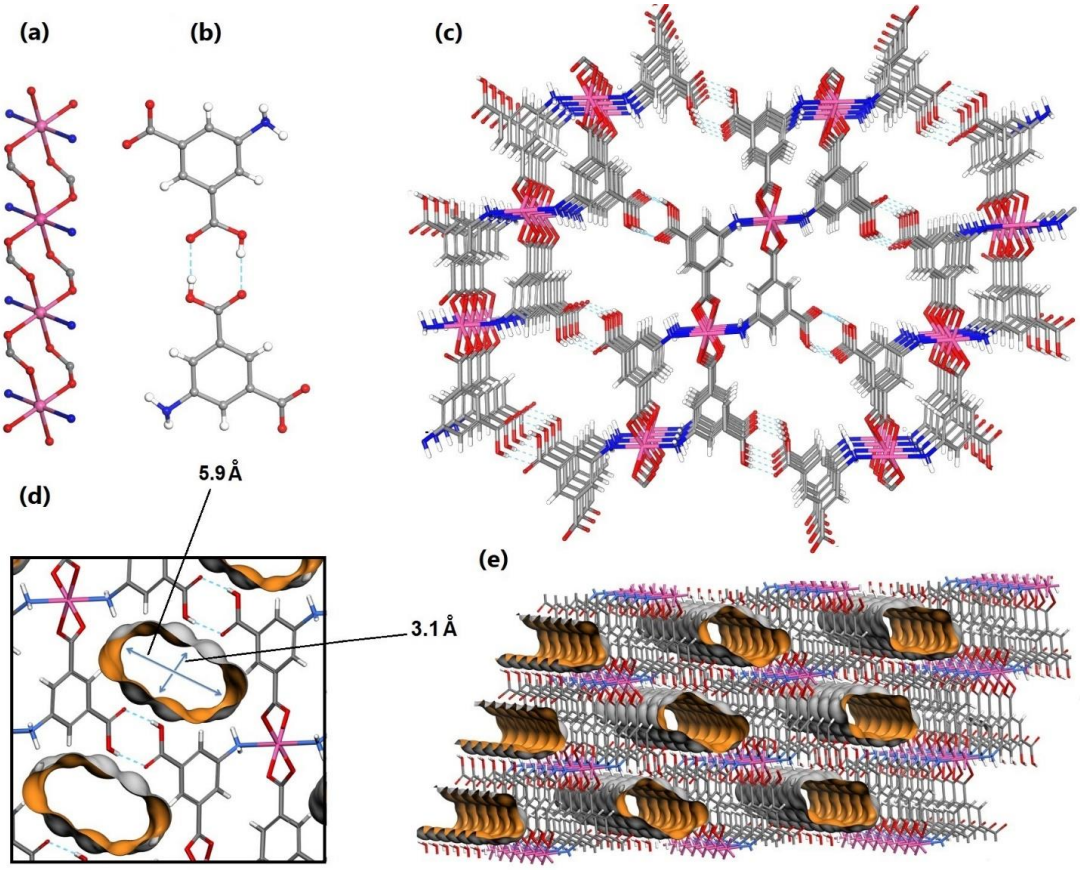

Figure 4.2 The structure of MUF-16 can be viewed as the connection of 1D Co−O−C−O chains (a) by Haip ligands pillared by strong hydrogen bonds (b), resulting in a 3D framework (c) (cobalt, cyan; oxygen, red; carbon, grey; hydrogen white). (d,e) 1D channels and pore dimension of MUF-16 illustrated by the Connolly surface defined with a probe of diameter 1.0 Å.

Guest-free MUF-16 was readily produced at 130 °C *in vacuo*. The phase purity of activated MUF-16 was confirmed by matching the experimental and simulated powder X-ray diffraction patterns (Figure 4.3-4.5) and elemental analysis (Table 4.2).

Table 4.2 Elemental analysis of MUF-16 family

	C: calcd./found	H: calcd./found	N: calcd./found
MUF-16.H_2O	43.91/43.49	3.20/3.23	6.40/6.40
MUF-16(Mn).H_2O	44.31/44.05	3.23/3.42	6.46/6.64
MUF-16(Ni).H_2O	43.93/44.18	3.20/3.57	6.40/6.90

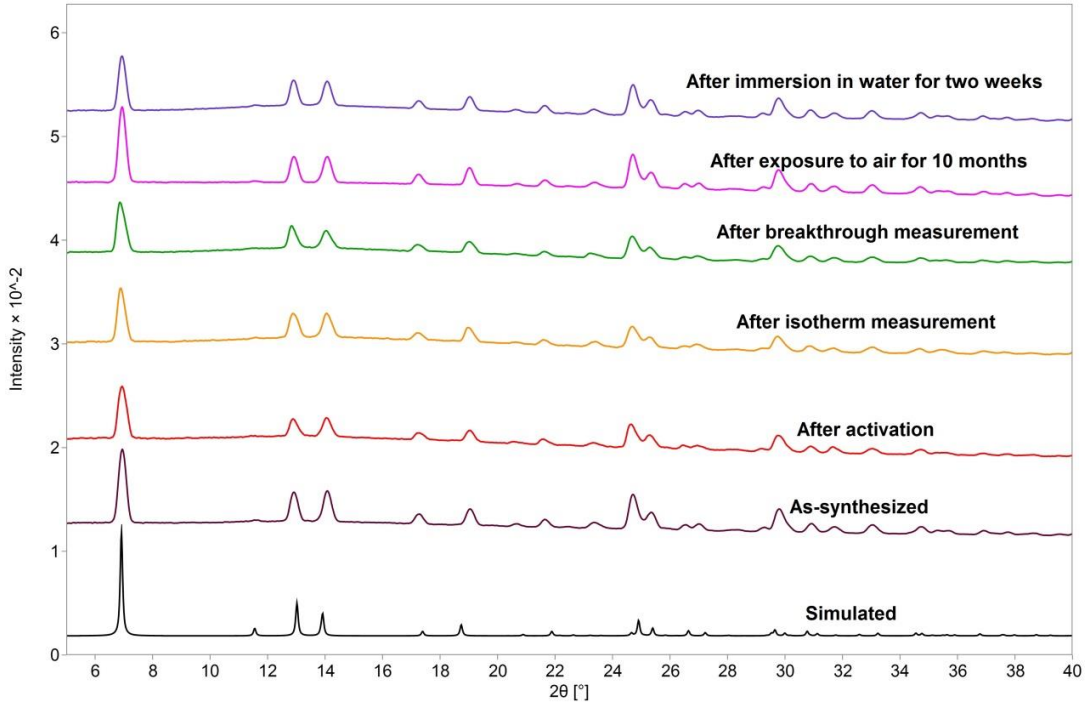

Figure 4.3 PXRD patterns of MUF-16 showing that its structure remains unchanged after activation at 130 °C under vacuum, after isotherm measurements, after breakthrough experiments, after exposure to an air with relative humidity of >80% for at least 10 months and after immersion in water for two weeks.

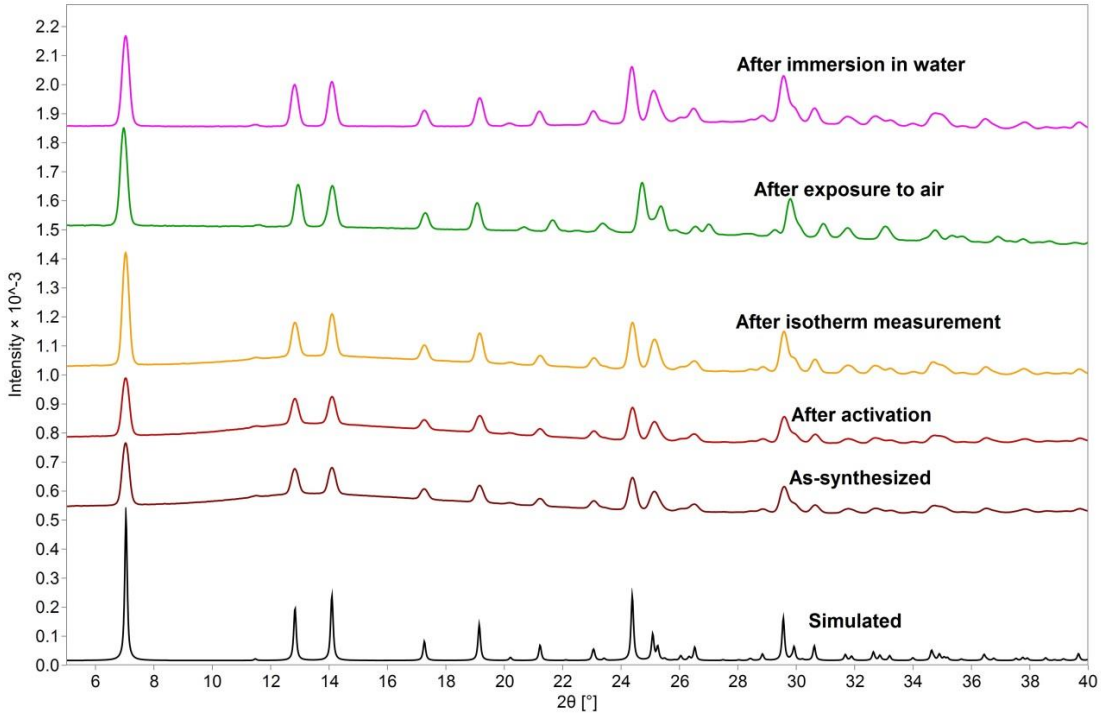

Figure 4.4. PXRD patterns of MUF-16(Mn) showing that its structure remains unchanged after activation at 130 °C under vacuum, after isotherm measurements, after exposure to an air with relative humidity of >80% for at least 6 months and after immersion in water for 40 days.

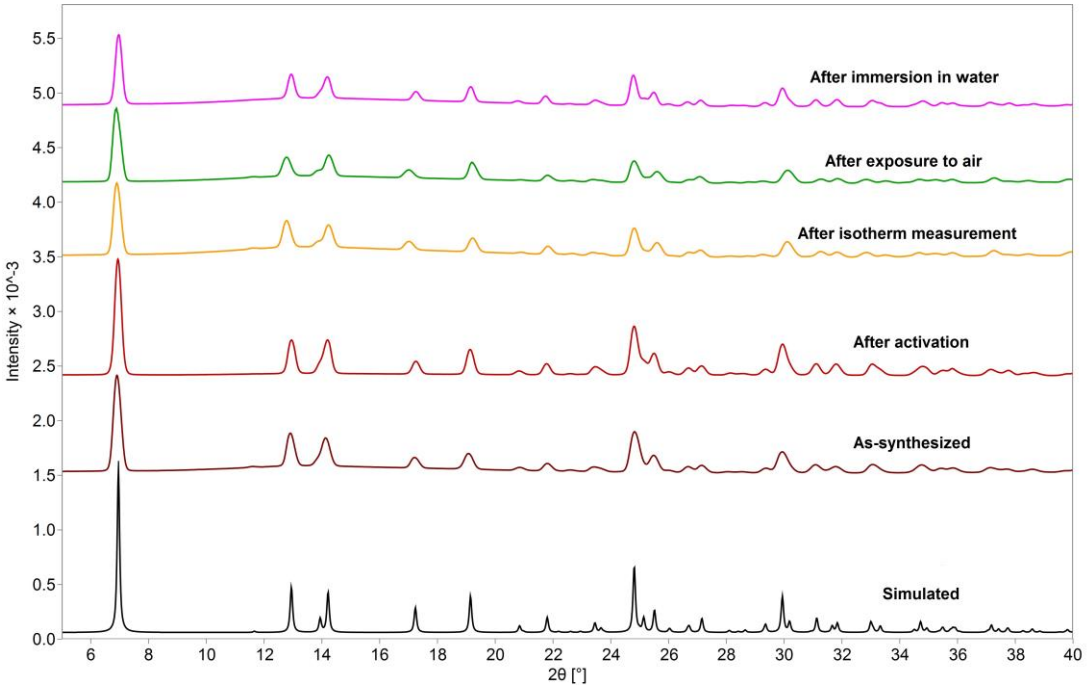

Figure 4.5 PXRD patterns of MUF-16(Ni) showing that its structure remains unchanged after activation at 130 °C under vacuum, after isotherm measurements, after exposure to an air with relative humidity of >80% for at least 6 months and after immersion in water for 40 days.

Thermogravimetry and PXRD demonstrated that the MUF-16 family is stable up to 350 °C under nitrogen (Figure 4.6), in a laboratory atmosphere (80% humidity) for at least six months (Figure 4.3-4.5) and in water for two weeks (Figure 4.3-4.5).

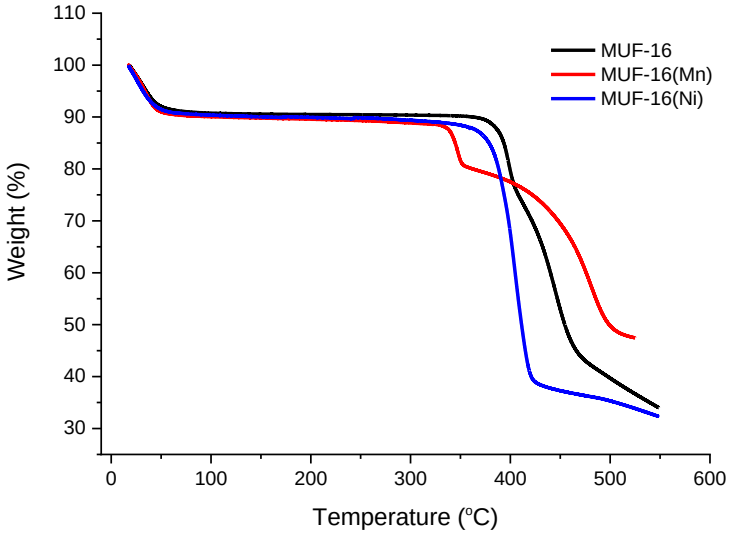

Figure 4.6 TGA curve of MUF-16, MUF-16(Mn), and MUF-16(Ni).

The high stability of MUF-16 towards water can be attributed to the strong metal-ligand bonds including nitrogen- and oxygen-bonding with metal ions as well as strong hydrogen bonding between ligands. The stability of MUF-16 family was further confirmed by

measuring CO_2 adsorption isotherms of MUF-16 after exposure to a humid laboratory atmosphere for 6 months or soaking in water for 48 hours, where the adsorption capacity remained constant.

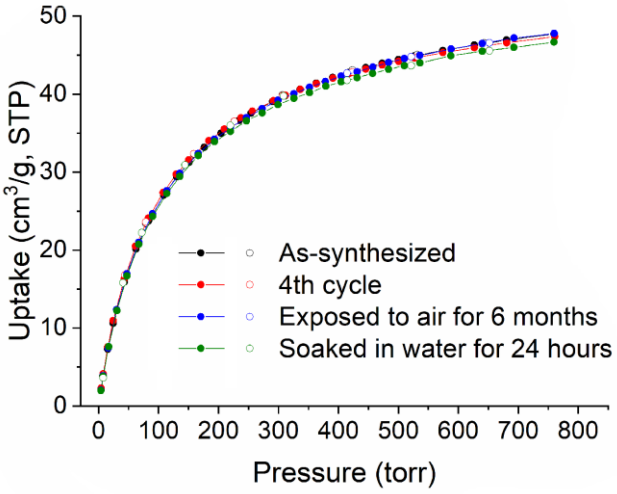

Figure 4.7 CO_2 adsorption isotherms (293 K) of as-synthesized MUF-16 after four consecutive adsorption-desorption cycles, after exposing it to air with ~80% humidity for 6 months, and after immersion in water for 48 hours.

A N_2 adsorption isotherm at 77 K established the permanent porosity of the MUF-16 family and gave BET surface areas of 215, 209 and 238 m^2/g for Co, Mn and Ni, respectively, and a pore volume of around 0.11 cm^3/g for all of them (Figure 4.8 and see appendix C for BET calculations). These values are comparable with the geometric surface area and pore volume calculated from the crystallographic coordinates (Table 4.3).

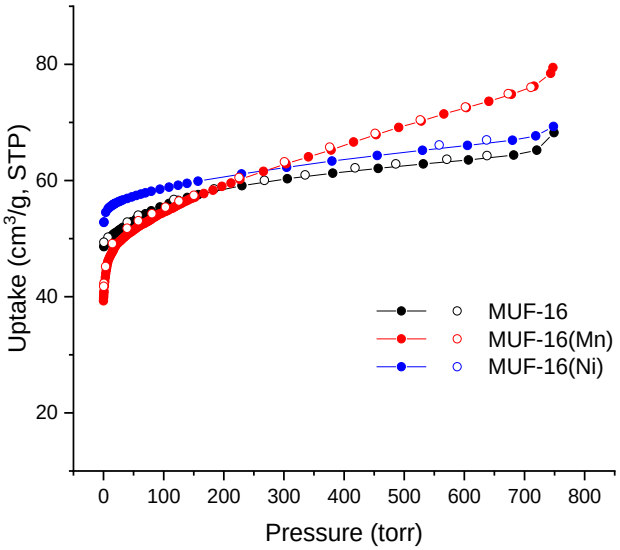

Figure 4.8 Volumetric adsorption (filled circles) and desorption (open circles) isotherms of N_2 for MUF-16 (black), MUF-16(Mn) (red) and MUF-16(Ni) (blue) measured at 77 K.

Table 4.3. Some calculated and experimentally determined properties of MUF-16 family.

	MUF-16	MUF-16(Mn)	MUF-16(Ni)
Geometric surface area (m^2/g, Zeo++)	313	315	313
BET surface area (m^2/g, from experimental N_2 isotherm/77 K)	215	209	238
Pore volume (cm^3/g, RASPA2)	0.10	0.11	0.11
Pore volume (cm^3/g, from experimental N_2 isotherm/77 K)	0.11	0.12	0.11
Largest cavity diameter (Å)	3.63	3.58	3.61
Pore limiting diameter (Å)	2.95	2.95	2.96

The pore dimension is perfectly matched with that of CO_2 molecules (3.32 × 3.34 × 5.7 $Å^3$), enabling excellent accommodation of CO_2 molecules. Equally important, the pore surface of MUF-16 possesses a favourable distribution of electrostatic forces. In the middle, the electron-donor oxygen atoms of non-coordinated carboxyl groups create a negatively charged environment, while on the corners electron-acceptor hydrogen atoms of amine group and phenyl rings make a strong positive adsorption sites. Such an arrangement of electrostatics forces in narrow channels of MUF-16 is particularly favourable for adsorption of molecules like CO_2 with an electropositive carbon atom at the centre and partially negatively charged oxygen atoms in the termini. Hence, low-pressure CO_2 adsorption isotherms were collected on MUF-16 at two temperatures of 293 K and 273 K (Figures 4.9). These frameworks take up a considerable amount of CO_2 for MUF-16 and MUF-16(Ni) (2.13 mmol g^{-1}, 48 cm^3(STP) g^{-1}), and slightly higher for MUF-16(Mn) (2.25 mmol g^{-1}, 50.5 cm^3(STP) g^{-1}) at 293 K and 1 bar (Figure 4.9a), which equates to approximately 0.9 molecules of CO_2 per metal site and occupation of 50% of the overall pore volume by CO_2 molecules (Table 4.4).

Table 4.4 Uptake capacity of CO_2 at 293 K and 1 bar for MUF-16.

	Uptake (Wt%)	Molecules of adsorbate per unit cell	Molecules of adsorbate per cobalt	Occupied fraction of void volume*
CO_2	9.38	3.58	0.90	0.50

*This the fraction of the total free volume of MUF-16 that is occupied by adsorbate molecules. This was calculated from the accessible void volume given by the N_2 isotherms at 77K, the molecular volume of the adsorbates and the total number of adsorbate molecules.

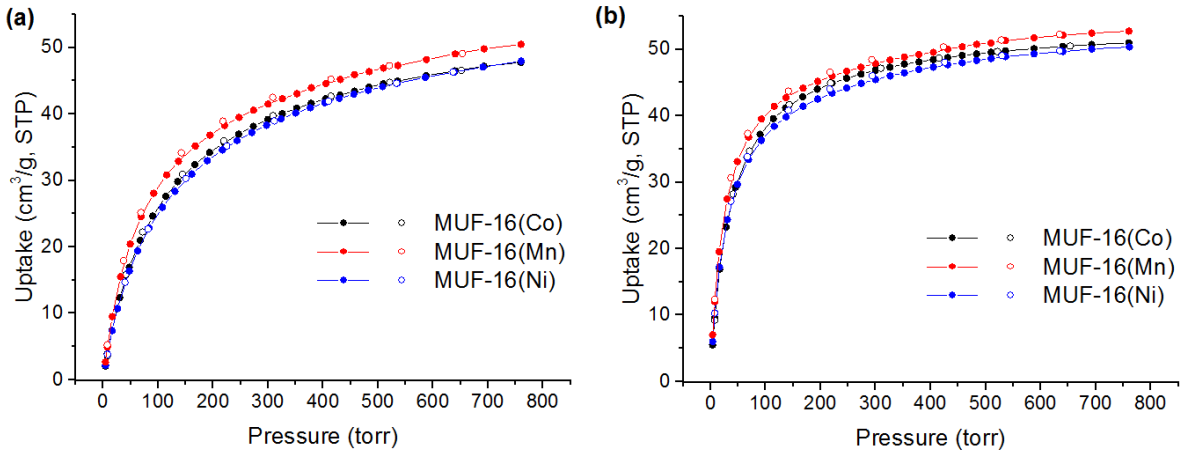

Figure 4.9 Volumetric adsorption (filled circles) and desorption (open circles) isotherms of CO_2 measured at (a) 293 K and (b) 273 K for MUF-16 (black), MUF-16(Mn) (red), and MUF-16(Ni) (blue).

The slightly higher adsorption uptake of MUF-16(Mn) can be attributed to stronger interaction of Mn sites with CO_2 molecules or larger pore volume of MUF-16(Mn). CO_2 adsorption isotherms of MUF-16 family at 293 K are relatively steep at low pressures and becomes almost plateau at higher pressures, indicating strong affinity of frameworks with CO_2 molecules and thus saturation at pressures around 1 bar. In other words, due to the high affinity of MOF for CO_2, framework can adsorb quite a high amount of CO_2 even at very low pressures leading to an early saturation of framework. This can be confirmed with the adsorption isotherm at 273 K, where CO_2 adsorption uptake at saturation is not enhanced much for this family (2.32 mmol g^{-1}, 52 cm^3(STP). g^{-1}).

To evaluate the binding strength between MUF-16 and CO_2, the isosteric heat of adsorption (Q_{st}) was calculated from experimental adsorption isotherms using a virial method. The Q_{st} at zero-coverage is around 32 kJ/mol for MUF-16 and 37 kJ/mol for MUF-16(Mn) and MUF-16(Ni), which increases at higher loadings (Figure 4.10). This rise can be attributed to the intermolecular interactions amongst the adsorbates, which is fully consistent with the crystallographically-observed pore dimensions and the requirement for close packing of adsorbate molecules in the pores as the adsorbent approaches saturation. This was experimentally verified by SCXRD (*vide infra*).

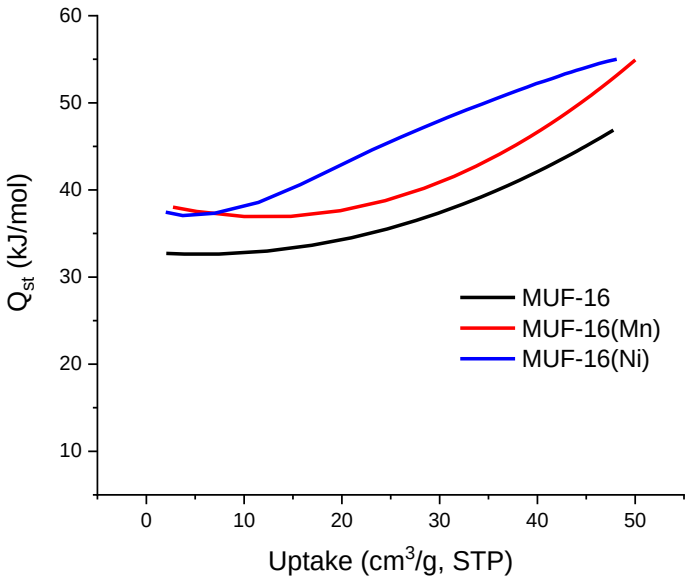

Figure 4.10 Isosteric heat of adsorption for CO_2 plotted as a function of gas uptake by MUF-16, MUF-16(Mn) and MUF-16(Ni).

The Q_{st} for CO_2 is moderately high compared to other MOFs that lack open metal sites or polar functional groups and lower than that of MOFs with open metal sites. For example CO_2 heat of adsorption by Mg-MOF-74 at low coverage is around 43 kJ/mol which is quite higher than that of MUF-16 family.[305] From a practical standpoint, the moderately high value of Q_{st} at different loadings is a positive attribute as regeneration energies in separation processes are expected to be low and the risk of irreversible poisoning by impurities such as H_2O and H_2S is diminished.

To visualize and structurally understand this adsorption behaviour of MUF-16, single-crystal studies was conducted to determine binding conformation of CO_2 molecules in MUF-16. Single crystal structure, PXRD patterns and CO_2 adsorption isotherms of MUF-16 family confirmed earlier that they are isostructural with similar CO_2 adsorption behaviour, so individual single crystals of MUF-16(Mn), which are brown colour, were used for single crystal X-ray studies (single crystals of MUF-16 were not visible in the capillary due to their light colour). We successfully loaded CO_2 molecules in the channel of MUF-16(Mn) using a flame-sealed glass capillary. After transferring the single crystal into the capillary, it was first activated in *vacuo* and the guest-free structure was determined crystallographically (Table 4.4). By backfilling the capillary with CO_2 to a pressure of around 1 bar following activation, the structure of MUF-16(Mn) loaded with this guest was determined crystallographically (Table 4.5 and see section 4.4 of this chapter for further details). The

great challenge in this experiment was making sure there is not any water left in the capillary as could be adsorbed over CO_2 even if a tiny amount of it exists.

Table 4.5 SCXRD data and refinement details of vacuumed and CO_2-loaded MUF-16(Mn).

MOF	Under vacuum (Mn)	Loaded with CO_2 (Mn)
Formula	$Mn(Haip)_2$	$Mn(Haip)_2.CO_2$
Empirical formula	$C_{16}H_{12}MnN_2O_8$	$C_{17}H_{12}MnN_2O_{10}$
Formula weight	415.22	459.23
Temperature/K	292	292
Crystal system	monoclinic	monoclinic
Space group	*I*2/a	*I*2/a
a/Å	15.4872(11)	15.5719(10)
b/Å	4.51930(10)	4.52010(10)
c/Å	25.4913(13)	25.438(2)
α/°	90	90
β/°	97.080(16)	97.108(8)
γ/°	90	90
Volume/Å^3	1770.56(17)	1776.7(2)
Z	4	4
ρ_{calc} /g cm^{-3}	1.558	1.717
μ/mm^{-1}	6.512	6.646
F(000)	844.0	932.0
2Θ range for data collection/°	11.514 to 117.84	12.672 to 91.092
Index ranges	$-17 \le h \le 11$, $-4 \le k \le 4$, $-28 \le l \le 28$	$-14 \le h \le 14$, $-4 \le k \le 4$, $-23 \le l \le 23$
Reflections collected	7515	8177
Independent reflections	1214 [R_{int} = 0.1632, R_{sigma} = 0.1964]	713 [R_{int} = 0.1104, R_{sigma} = 0.0804]
Data/restraints/parameters	1214/0/129	713/90/136
Goodness-of-fit on F^2	0.862	1.216
Final R indexes [I>=2σ (I)]	R_1 = 0.0510, wR_2 = 0.0954	R_1 = 0.0868, wR_2 = 0.2280
Final R indexes [all data]	R_1 = 0.1341, wR_2 = 0.1112	R_1 = 0.1278, wR_2 = 0.2915
Largest diff. peak/hole / e Å^{-3}	0.35/-0.48	0.56/-0.58

Analysis of the diffraction data revealed little change to the framework itself. The CO_2 guest molecules were clearly visible in its 1D channels in the Fourier difference map. There was found, in total, one CO_2 molecules per cobalt ion which is in agreement with the adsorption isotherms. The CO_2 molecules are positioned at an angle to the pore axis (Figure 4.11a). Individual CO_2 molecules occupy either of two sites that are related by crystallographic symmetry. A strong electron density was observed in the middle of pore and two weaker dense area in the angles. The central dense area then was assigned to be oxygen with a fixed occupancy of 1, while the other two area were set to be oxygen and carbon atoms with a fixed occupancy of half. It equates with one CO_2 molecules with occupancy of one.

In accord with the increase contribute to the moderately high Q_{st}, the oxygen atoms of one of the CO_2 guest molecules forms close N-H···O and C-H···O interactions with the phenyl and amino functionalities of Haip ligand with a distance of 2.42 and 2.83 Å, respectively (Figure 4.11a). Similarly, the carbon atom of adsorbed CO_2 molecule forms a C···O interaction with oxygen atom of uncoordinated carboxylate group with a distance of 3.04 Å. This suggests that the adsorbed CO_2 molecules are perfectly surrounded by favourable adsorption sites both in the corners and middle of pores in MUF-16(Mn). Notably, due to the diagonally-oriented adsorption sites of the pores, adsorbed CO_2 molecules are distributed in the 1D channels in a Z-shaped manner (Figure 4.11b). Such an orientation of CO_2 molecules in the channels lead to intermolecular $C\delta^{+}\cdots O\delta^{-}$ interactions between adjacent CO_2 molecules with a C···O distance of 3.91 Å. These underlie the observed increase in Q_{st} as a function of gas loading.

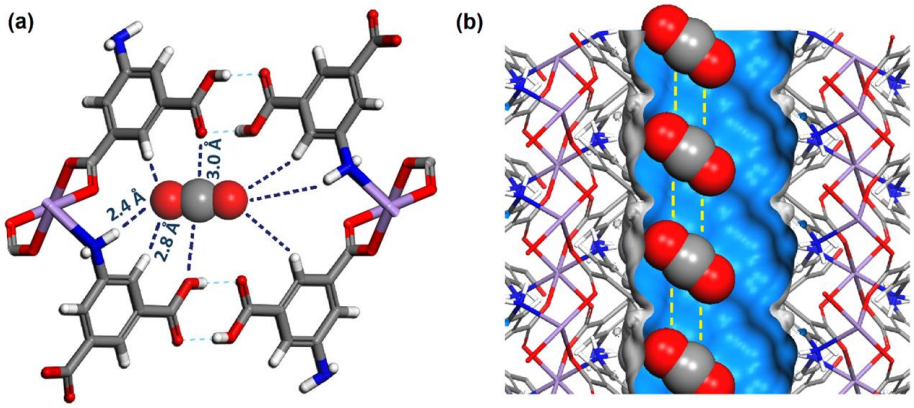

Figure 4.11 (a) The adsorption sites of CO_2 molecules in MUF-16(Mn) as determined experimentally by single-crystal X-ray diffraction (The other CO_2 site is equivalent by symmetry). (b) The intermolecular interactions observed between adsorbed CO_2 molecules in the channels of MUF-16(Mn). The dashed lines indicate a C···O distance of 3.91 Å. The CO_2 molecules are shown in representative orientations that do not take the crystallographic disorder into consideration (manganese, light purple; nitrogen, blue; oxygen, red; carbon, grey; hydrogen, white; pore surface, light blue).

The propensity of MUF-16 to adsorb CO_2 can be also explained by the complementarity of its electric dipole with the polarization of the MUF-16 pore surface. The electron-rich oxygen atoms of the non-coordinated carboxyl groups of the framework create an environment with a build-up of partial negatively charge, while at the pore corners the electron-deficient hydrogen atoms of the amino group and the phenyl rings generate regions of partial positive charge. Now, considering the adsorption of CO_2, this guest molecule will occupy sites that are compatible in terms of both size and electrostatics. The CO_2 adsorbates can align their quadrupole to in the channels so that its regions of high electron density on

its oxygen atoms sit alongside the positively charged regions of the pore surface. In addition, the carbon atom of CO_2, which has a partial positive charge, complements the framework oxygen atoms. This framework pocket has an ideal size to optimize the noncovalent interactions with the CO_2 guests (Figure 4.12).

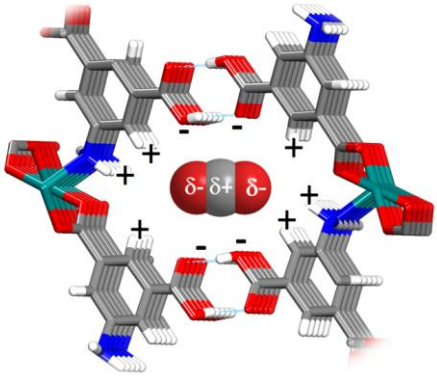

Figure 4.12 Complementarity of CO_2 molecule electrostatic distribution with the polarization of the MUF-16 pore surface.

The validity of this model of CO_2 binding in MUF-16 was strengthened by assessing its adsorption of nitrous oxide. N_2O was chosen as a reference gas as its molecular size and electrostatic distribution is nearly identical to that of CO_2 (Figure 4.13 and Table 4.6).

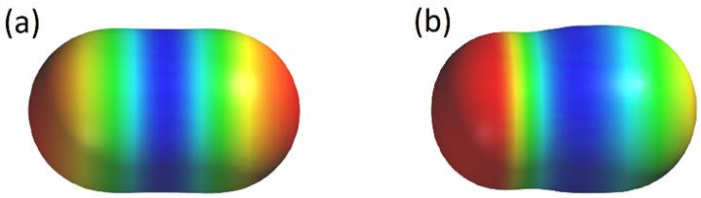

Figure 4.13 Electrostatic potential maps of (a) CO_2 and (b) N_2O. Blue/green = positive; red/orange = negative.

Table 4.6. Physicochemical characteristics of CO_2 and other relevant gases.[110, 235-236]

	Boiling point (K)	Molecular dimensions (Å)	Molecular volume (from CPK model) (Å^3)	Polarizability (Å^3)	Dipole moment ×10^{18}/esu cm^2	Quadrupole moment× 10^{26}/esu cm^2
CO_2	216.5	3.18×3.33×5.36	38.84	2.91	0	-4.3
N_2O	184.6	3.03×3.04×5.32	32.35	3.03	0.16	-3.3

Adsorption isotherms of N_2O were measured at different temperatures (Figure 4.14). MUF-16 adsorbs a significant amount of N_2O (1.91 mmol/g, 43 cm^3/g) at 1 bar and 293 K. This is only slightly less than the uptake of CO_2. In parallel with CO_2, N_2O possesses atoms

with partial negative charges at its termini that can bind to positively-charged regions of the pore surface, and vice-versa for its central positive nitrogen atom.

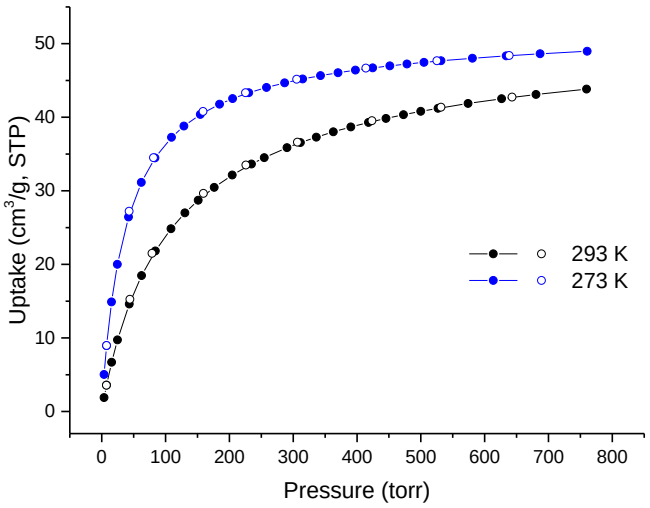

Figure.4.14. Volumetric adsorption isotherms of N_2O measured at two temperatures for MUF-16.

4.3 Conclusion

We have discovered a series of isostructural porous metal−organic frameworks, MUF-16 family, towards efficient adsorption of CO_2 molecules. In principle, fine-tuning of pore size and appropriate surface chemistry in MOFs can gain favourable adsorbate-adsorbent interactions and sieving effects for gas separation. For such an approach to work, the small and size-matched pores of MUF-16 lead to an intimate contact between gas molecules and the pore environment. In addition, the favourable orientation of electrostatic potential in the pore surface enables strong interaction between polarized surface of the framework and quadrupole of CO_2 molecules. The recognition mechanism of MUF-16 for gas molecules is well supported by direct crystallography studies and adsorption isotherm measurement in which the adsorption sites within the framework interact favourably with CO_2 molecules. This approach is likely applicable to other gas mixtures with impurities that possess opposite electrostatic distribution, which will facilitate the design and implementation of novel porous MOF materials for other important gas separations. Moreover, easy and inexpensive preparation of MUF-16 as well as its low heat of adsorption and high stability offer this material as a promising candidate for future industrial separation processes.

4.4 Experimental and computational section

4.4.1 General procedures

All starting compounds and solvents were used as received from commercial sources without further purification unless otherwise noted. Elemental analyses were performed by the Campbell Microanalytical Laboratory at the University of Otago, New Zealand.

4.4.2 Thermogravimetric Analysis (TGA)

As per chapter 2. Freshly prepared MOF samples were washed with MeOH, and then activated at 130 °C under vacuum for 10 hours. Samples were exposed to air for 1 hour and then transferred to an aluminum sample pan, and then measurements were commenced under an N_2 flow with a heating rate of 5 °C /min.

4.4.3 Single crystal X-ray diffraction

As per Chapter 2. MOF crystals were analysed right after removing them from methanol. Room temperature data collection also produced better refinement statistics than low temperature data collection.

All atoms were found in the electron density difference map. Electron density difference maps were carefully analyzed for the possible presence of disordered framework components. All atoms were refined anisotropically, except hydrogen atoms, loaded CO_2 molecules in MUF-16(Mn) and one of the uncoordinated water in MUF-16.

4.4.4 Single crystal X-ray crystallography under vacuum and loaded with CO_2

Capillary SCXRD was performed for a single crystal of MUF-16 both under vacuum and loaded with CO_2 at around 0.8 bar and 20 °C based on the following steps:

1. First a single crystal was chosen with an appropriate size (~ 0.1 × 0.1 × 0.1 mm).

2. A small capillary tube with around 0.2 mm in diameter and 50 mm in length (which is open at both ends) was made by burning and shaping the neck of a glass pipette (referred as the ‘home-made capillary’).
3. The crystal was soaked in Fomblin oil and then the home-made capillary was used to trap the crystal inside it. Normally, the crystal will flow through the capillary by the oil stream.
4. Then home-made capillary was transferred into a standard 0.3 mm capillary. A lengthy capillary with 0.2 mm in dimeter was used to push the home-made capillary to the very bottom of the 0.3 mm capillary.

5. Around 6 or 7 crystals of cobalt chloride was then transferred to the 0.3 mm capillary and placed on the top of home-made capillary. The cobalt chloride was used a visual indicator of the level of water vapour in the capillary base on its pink/blue colour change.
6. The top of the 0.3 mm capillary was then covered by glass wool to avoid the elutriation of cobalt chloride crystals during activation.
7. The capillary assembly was then connected to adsorption apparatus (Quantachrome-Autosorb-iQ2) using appropriate Swagelok fittings (Figure 4.15) and was kept under vacuum and a temperature of 140 °C for around 5 hours so that the vacuum level reached 0.0008 torr. At this point the cobalt chloride crystals were blue in colour.

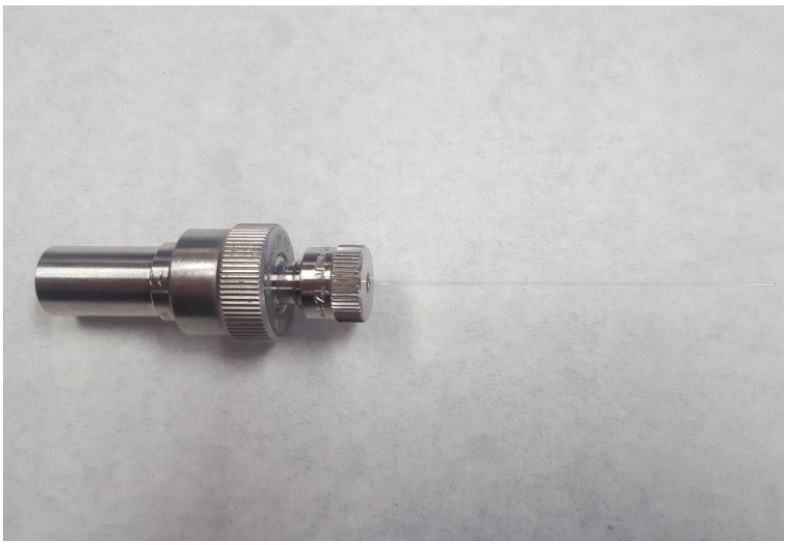

Figure 4.15 Swagelok fittings for connecting capillary to Quantachrome-Autosorb-iQ2.

8. The capillary was flame sealed at this point to trap the crystal under vacuum test. Alternatively, the capillary can be filled with CO_2 and then flame sealed to trap the crystal under CO_2.

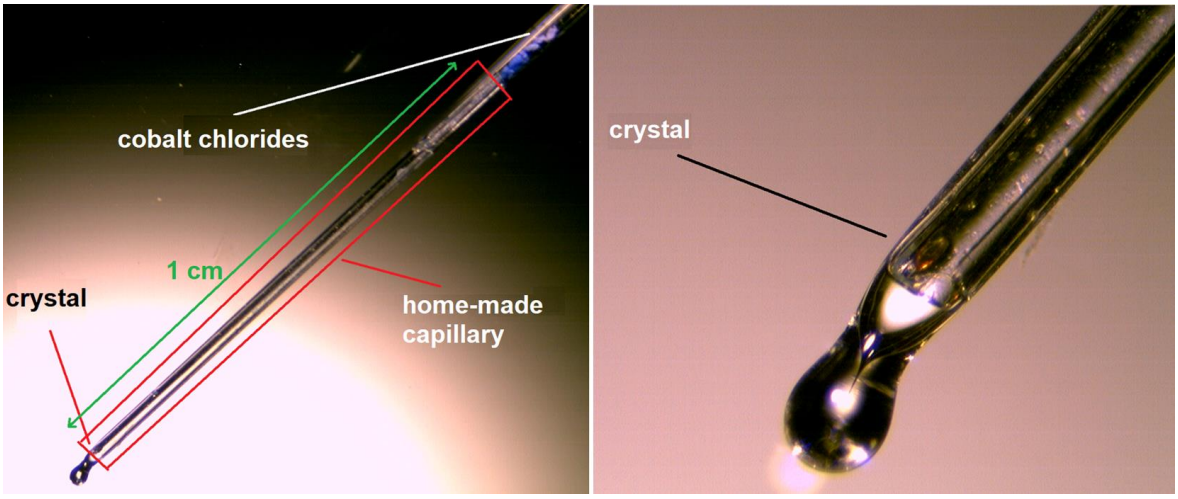

Figure 4.16. Schematic and dimensions of capillaries used for SCXRD.

4.4.5 Powder X-ray diffraction patterns

As per Chapter 2. The data were obtained from freshly prepared MOF samples that had been washed several times with MeOH. MOF crystals were analysed right after removing them from MeOH.The two-dimensional images of the Debye rings were integrated with 2DP to give 2θ vs I diffractograms. Predicted powder patterns were generated from single crystal structures using Mercury.

4.4.6 Aging experiments on activated frameworks

After washing as-synthesized samples several times with MeOH, they were activated and were aged in air at 70-85% relative humidity or water at 20 °C.

4.4.7 Low-pressure gas adsorption measurements

As per Chapter 2. The as-synthesized samples were washed with anhydrous methanol several times and about 50-100 mg was transferred into a pre-dried and weighed sample tube and heated at rate of 10°C/min to a temperature of 130 °C under a dynamic vacuum with a turbomolecular pump for 20 hours.

4.4.8 Structure, physical properties and pore shape

Single crystal structures of MUF-16, MUF-16(Mn) and MUF-16(Ni) were used directly for all the calculations and simulations without modification. The Zeo++[242] code and RASPA2[232] were used to calculate their pore volumes and surface areas with the use of H_2 and He probes, respectively, pore limiting diameter (i.e., the diameter of smallest opening along the pore) and largest cavity diameter (i.e., the diameter of the largest sphere that can fit within the pores). Accelrys Materials Studio 7.0 software package was performed to visualize the MOF structures and pore topologies.

Chapter 5

Application of MUF-16 for Adsorptive Separation of CO_2 from Different Gas Mixtures

5.1 Introduction

The selective trapping of CO_2 is of prime importance in industrial and environmental settings. For example, it is estimated that 50% of the volume of known natural gas reservoirs contain more than 2% CO_2.[306] Reducing the levels of carbon dioxide in natural gas allows transportation and prevents the corrosion of equipment and pipeline. Moreover, CO_2 has no heating value and it has to be removed to meet gas quality specifications before distribution to end users *via* pipelines.[306-307]

CO_2 impurities in acetylene, ethylene and ethane streams need to be removed before they can be used as feedstocks for the production of fine chemicals, fuels and polymers. This contamination is not only a barrier to optimal heat release from gas combustion, it adversely influences reactions involving these feedstocks.[306, 308-309]

In terms of the environment, the amount of carbon dioxide in the atmosphere continues to rise, which underlies the greenhouse gas effect and subsequent temperature increases.[144, 158] It is necessary to develop economical and practical pathways to reduce both carbon dioxide emissions and current carbon dioxide levels in the atmosphere. Atmospheric CO_2 levels can be reduced by using less petroleum and natural gas, decarbonizing fossil fuel (pre-combustion capture), capturing CO_2 by at point sources where significant quantities are released (post-combustion carbon), or capturing it directly from air (direct air capture).[138, 310]

Currently, conventional separation methods involve absorption using aqueous amines, solvent extraction or cryogenic distillation.[138] However, implementation of these methodologies is associated with several drawbacks including high capital cost, high energy consumption, difficult and expensive maintenance, solvent loss due to the degradation and evaporation, and the corrosive nature of solvents.[138, 141, 286, 311-312] Hence, the search for materials that not only show high CO_2 capacity and selectivity but also require mild

operational conditions and are economical to be implemented is of major importance. Unfortunately, traditional porous materials, such as activated carbon and zeolites, exhibit poor characteristics against some of these metrics. For example, the surface area of these materials are relatively low, thus resulting in lower CO_2 capacity and they are not tunable, i.e., their structure cannot be modified for enhancing their selectivity or surface area.[95] Conversely, metal–organic frameworks (MOFs) are effective materials for highly challenging separations.[7, 24, 207, 290, 313] More than 75,000 MOFs have been synthesized by combining a rich library of inorganic and organic building blocks.[1] Thanks to their inherent modularity, MOFs can enable exquisite control over pore sizes and electrostatics.[95, 110, 134, 285, 314-317]. The current challenge in MOF area for gas separation is their expensive end price, which can be overcome with the development of less expensive MOFs.

While dozens of MOFs are now known for CO_2/C2 hydrocarbon separations, most of them have shown strong affinity towards the hydrocarbon component rather than CO_2. This has been achieved through the implementation of strategies including the formation of host-guest hydrogen-bonds and coordinative bonds between π electrons on the hydrocarbons and unsaturated metal sites on the framework.[314, 318-329] On the other hand, the selective adsorption of CO_2 over C2 hydrocarbons have been seldom reported[235, 327, 330-336] phenomenon despite the fact that adsorbents that selectively capture CO_2 from C2 hydrocarbons are likely to be more energy efficient: High purity products can be achieved only through one single breakthrough step, while hydrocarbon-selective MOFs require additional processes involving the capture of the desired hydrocarbon and its subsequent release (Figure 5.1). In addition, further purification is demanded if the eluent is contaminated by adsorbed CO_2 during this desorption step.[327, 337-338]

Despite these advantages, the separation performance of most of the CO_2-selective MOFs that have been identified so far are restricted to cryogenic temperatures, or their separation performance has not been assessed experimentally under dynamic conditions but simply inferred from single-component adsorption isotherms.[235, 330-335] For the separation of CO_2 from C_2H_2, we are aware of only three reported materials, CD-MOF-1[336], CD-MOF-2[336] and SIFSIX-3-Ni[327] that have shown such ability at ambient conditions through experimental breakthrough measurements, where a mixture of CO_2 and C_2H_2 passes through an adsorption column and pure acetylene is obtained through selective adsorption of the CO_2 by the dsorbent. Furthermore, to best of our knowledge, there are not any MOFs reported in the literature that selectively adsorb CO_2 over all three C2 hydrocarbons; previously reported materials are confined to either CO_2/C_2H_2 or CO_2/C_2H_4 and CO_2/C_2H_6 separations.

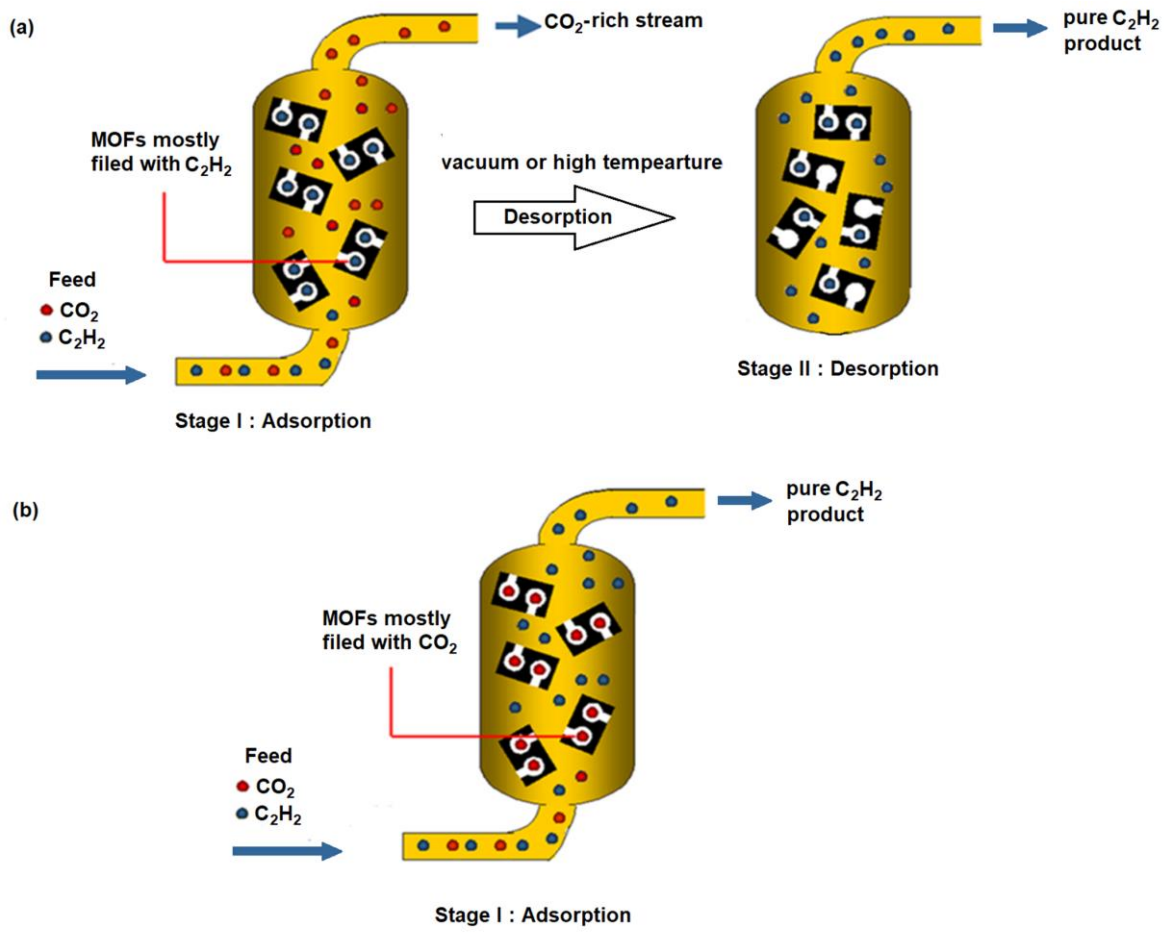

Figure 5.1 A simplified adsorption processes for production of pure acetylene by (a) a C_2H_2-selective MOFs through multiple adsorption-desorption stages and (b) a CO_2 selective OFs through one single adsorption stages.

In the first section of this chapter, MUF-16 is presented as an effective material for selective adsorption of CO_2 over C2 hydrocarbon. As was discussed in Chapter 4, MUF-16's high affinity and selective recognition for CO_2 arises from complementary electrostatic properties and perfectly-matched pore dimensions. In contrast, C2 hydrocarbons has an opposite electrostatic distribution, so MUF-16 may show a very low adsorption of these gases.

Additionally, the potential of MUF-16 derivatives for carbon capture applications by selectively capturing CO_2 from N_2 and natural gas sweetening processes through adsorptive removal of CO_2 from CH_4 is investigated in the second section of this chapter. Its performance to selectively adsorb CO_2 from air and natural is then compared with that of benchmark materials in the literature.[40, 142, 147, 291, 305, 339-351] The efficiency of MUF-16 for direct air capture is also investigated at the end of this section.

5.2 Results and discussion

5.2.1 CO_2/C2 hydrocarbons separation

As was discussed earlier in Chapter 4, efficient adsorption of CO_2 by MUF-16 family stems from suitable distribution of electrostatic potential, where CO_2 molecules can orientate their electric quadrupoles to complement the electrostatic potential of the pore surface. In contrast to CO_2, C2 hydrocarbons including C_2H_2, C_2H_4, and C_2H_6 have an opposite quadrupole moments as shown in Figure 5.2. This would lead to repulsive interactions between these molecules and the same framework pore spaces. In turn, the affinity for these guests would be substantially reduced.

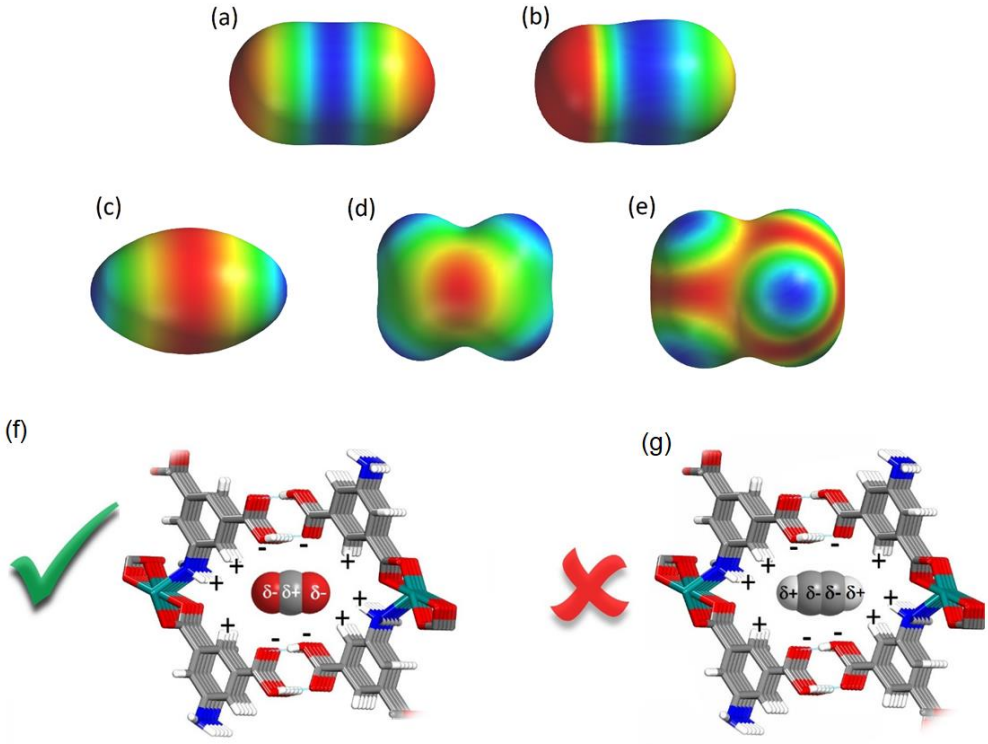

Figure 5.2 Electrostatic potential maps of (a) CO_2, (b) N_2O, (c) C_2H_2, (d) C_2H_4 and (e) C_2H_6 (Blue/green = positive; red/orange = negative). (a) Attractive interaction between pore surface of MUF-16 with CO_2 and (g) repulsive forces with C_2H_2.

This unique pore chemistry of MUF-16 and opposite quadrupole of C2 hydrocarbons provided us the initial motivation to evaluate its sorption performance for adsorption of CO_2 over C2 hydrocarbons. Adsorption isotherms of C2 hydrocarbons were measured at two temperatures of 293 K and 273 K. In contrast to CO_2, only minor quantities of C2 hydrocarbons are adsorbed by MUF-16 (3.1, 3.2 and 4.0 $cm^3\ g^{-1}$, for C_2H_6, C_2H_4 and C_2H_2, respectively, at 293 K, Figure 5.3).

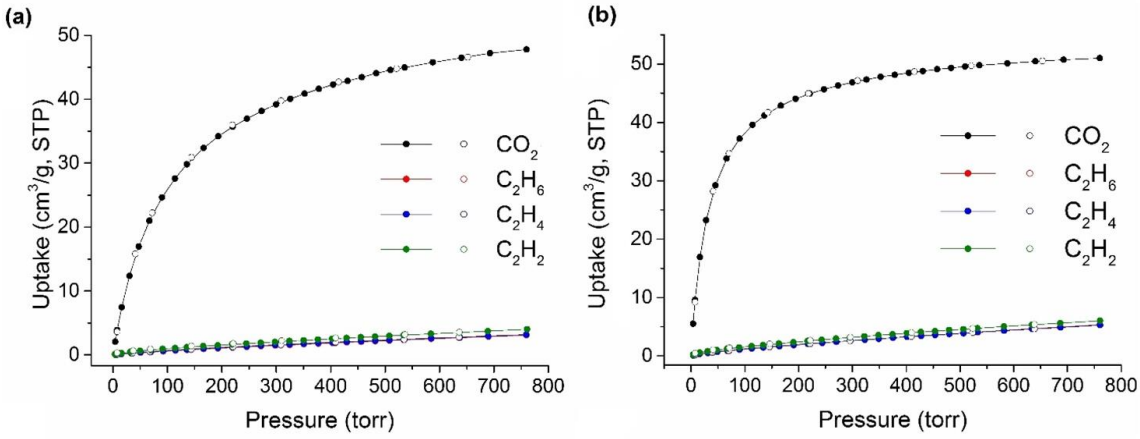

Figure 5.3 Experimental C_2H_6, C_2H_4, and C_2H_2 adsorption and desorption isotherms of MUF-16 at (a) 293 K and (b) 273 K in comparison with that of CO_2.

The CO_2/C2 uptake ratios are 15.7 (C_2H_6), 15.1 (C_2H_4) and 12.0 (C_2H_2). These metrics indicate that MUF-16 drastically outperforms other MOF materials that have been reported to be selective for CO_2 (Figure 5.4 and Table 5.1), including SIFSIX-3-Ni (CO_2/C_2H_2 = 1.2 at 298 K and 0.1 bar),[327] [Mn(bdc)(dpe)] (CO_2/C_2H_2 = 6.4 at 273 K and 1 bar),[333] $K_2[Cr_3O(OOCH)_6(4\text{-ethylpyridine})_3]_2[aSiW_{12}O_{40}]$ (CO_2/C_2H_2 = 4.8 at 278 K and 1 bar)[235] and CDMOF-2 (CO_2/C_2H_2 = 1.3 at 298 K and 1 bar).[336]

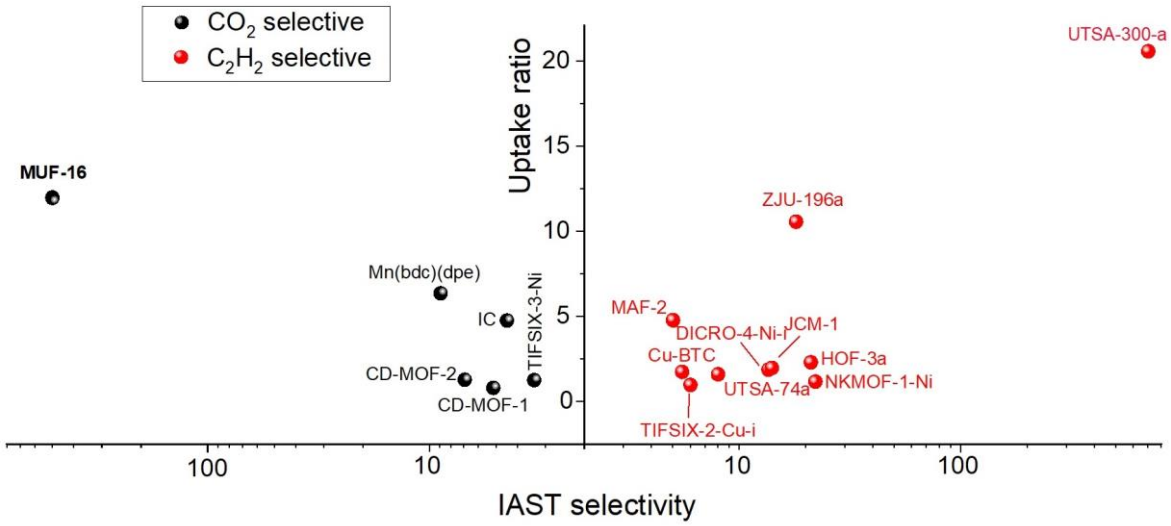

Figure 5.4 Predicted IAST selectivity from an equimolar mixture of CO_2/C_2H_2 and uptake ratio at 1 bar and 293-298 K (except for IC (278 K) and Mn(bdc)(dpe) (273 K)) for MUF-16 in comparison to the best materials reported to date. Selectivity and uptake ratios are defined as CO_2/C_2H_2 and C_2H_2/CO_2 for CO_2-selective and C_2H_2-selective materials, respectively.

The separation performance of MUF-16 also exceeds that of benchmark materials that show an inverted selectivity (preference for C_2H_2 over CO_2) such as MAF-2 (4.7),[323] HOF-

3 (2.3),[320] and UTSA-74 (1.6)[322] (Figure 5.4). The CO_2 adsorption capacity of MUF-16 at 1 bar (2.14 mmol/g) and ambient temperature is comparable to other CO_2-selective materials (in the range of 0.5-2.87 mmol/g).

Table 5.1 Separation metrics of MUF-16 in comparison to other top-performing materials reported in the literature.

MOF	T (°C)	P (bar)	CO_2 uptake (mmol/g)	C_2H_2 uptake (mmol/g)	IAST selectivity*	Uptake ratio*	Q_{st} of CO_2 (kJ/mol)	Q_{st} of C_2H_2 (kJ/mol)
CO_2-selective MOFs								
MUF-16	**20**	**1**	**2.142**	**0.178**	**513**	**12.0**	**34**	-
Mn(bdc)(dpe)[333]	0	1	2.08	0.32	9	6.4	29.5	27.8
$K_2[Cr_3O(OOCH)_6$ Ionic crystal[235]	5	1	0.50	0.10	4.52	4.8	38	30
SIFSIX-3-Ni[327]	25	1	2.80	3.30	5.2	0.84	51	36.5
CD-MOF-1[336]	25	1	2.87	2.23	3.4	1.3	41	17
CD-MOF-2[336]	25	1	2.67	2.03	7	1.3	67.5	25
C_2H_2-selective MOFs								
ZJU-10a[328]	25	1	3.66	7.58	4	2.1	26	39
TIFSIX-2-Cu-i[327]	25	1	4.2`0	4.10	6	0.97	36	46
DICRO-4-Ni-i[326]	25	1	1.02	1.91	13.5	1.9	34	38
NKMOF-1-Ni[325]	25	1	2.27	2.67	22	1.2	41	60
ZJU-196a[324]	25	1	0.35	3.70	18	10.6	-	39
MAF-2[323]	25	1	0.82	3.90	5	4.7	27	33
UTSA-74a[322]	25	1	3.00	4.80	8	1.6	25.5	31.5
UTSA-300a[281]	25	1	0.15	3.10	700	20.6	-	57.6
ZJU-60a[329]	23	1	3.12	6.69	4	2.1	15.5	17.5
JCM-1[321]	25	1	1.69	3.34	14	2	33	36.5
HOF-3a[320]	23	1	0.93	2.14	21	2.3	42	19.5
UTSA-50a[320]	23	1	3.10	4.10	5	1.3	27.8	32
Cu-BTC[305, 319-320]	25	1	5.10	8.90	5.5	1.7	26.9	30
MFM-188[318]	25	1	5.35	10.20	3.7	1.9	20.8	32.5
$[Ni_3(HCOO)_6]$[352]	25	1	3.00	4.20	21	1.4	24.5	40.9
FJU-90a[353]	25	1	4.92	8.03	4.3	1.63	21	25.3

* IAST selectivities and uptake ratios are given with respect to the ratio of the highly adsorbed component to the weakly adsorbed component.

Additionally, for better comparison, a good summary of adsorption performance of top-performing MOFs, including adsorption uptakes, uptake ratio, IAST selectivity and isosteric heat of adsorption at low coverage for CO_2/C_2H_2 separation has been presented in Table 5.1. Owing to its exceptional adsorption performance, the selectivities calculated for MUF-16 by the ideal adsorbed solution theory (IAST) are 603, 596 and 513 for equimolar mixtures of CO_2/C_2H_6, CO_2/C_2H_4 and CO_2/C_2H_2, respectively, at 293 K and 1 bar (Figure 5.5 and see appendix D for other compositions). This remarkable selectivity for CO_2 sets new

benchmarks for all three CO_2/C2 hydrocarbon separations (Table 5.1). This is highlighted in Figure 5.4 for the case of C_2H_2, where the performance of MUF-16 exceeds all frameworks that are selective towards CO_2.

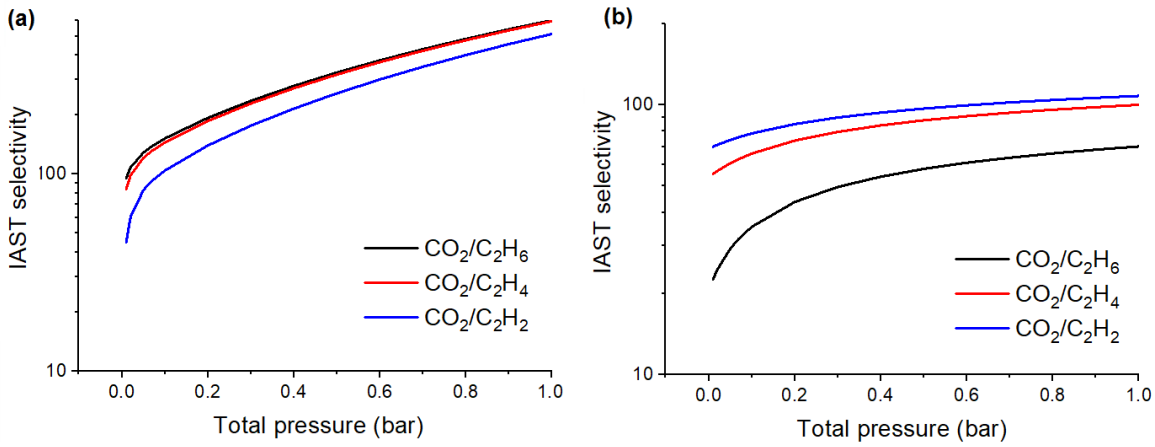

Figure 5.5 Predicted IAST selectivity of MUF-16 for a 50/50 CO_2/C2 hydrocarbon mixtures at (a) 293 K and (b) 273 K.

While the pore characteristics of MUF-16 clearly favour the uptake of CO_2 over C2 hydrocarbons, the adsorption mechanism could potentially be molecular sieving where the hydrocarbon adsorbates are excluded from the framework on the basis of their size. This was ruled out by measuring gas adsorption isotherms at 195 K, which revealed that MUF-16 can take up significant amounts of large molecules such as C_2H_6 at this temperature (Figure 5.6). Thus, these molecules can freely enter the pore network of MUF-16 around room temperature but their interactions with the framework are weak so their uptake is low.

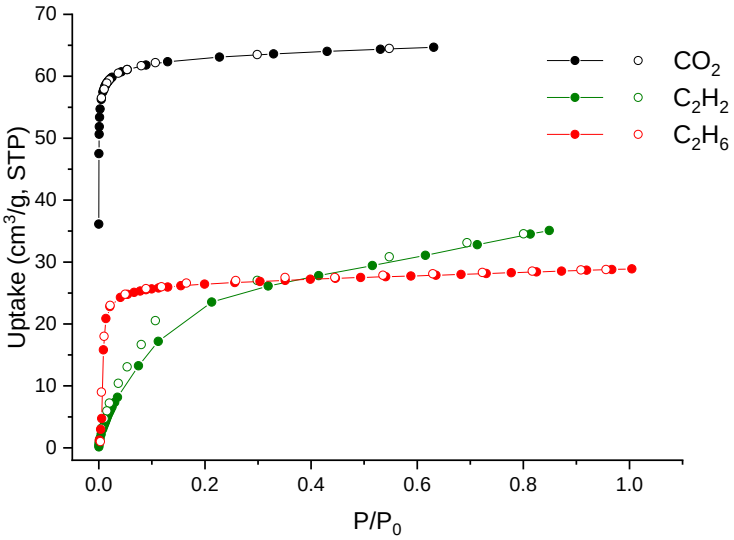

Figure 5.6 Volumetric adsorption (filled circles) and desorption (open circles) isotherms of CO_2 (black), C_2H_2 (red), C_2H_6 (blue) and CH_4 (purple) measured at 195 K for MUF-16.

Further, the kinetics of adsorption of all four guest molecules were measured. Since the uptake kinetics of CO_2 and C2 hydrocarbons are nearly identical (Figure 5.7), the differences in their differential affinity for MUF-16 can be ascribed to thermodynamic – rather than kinetic – effects.

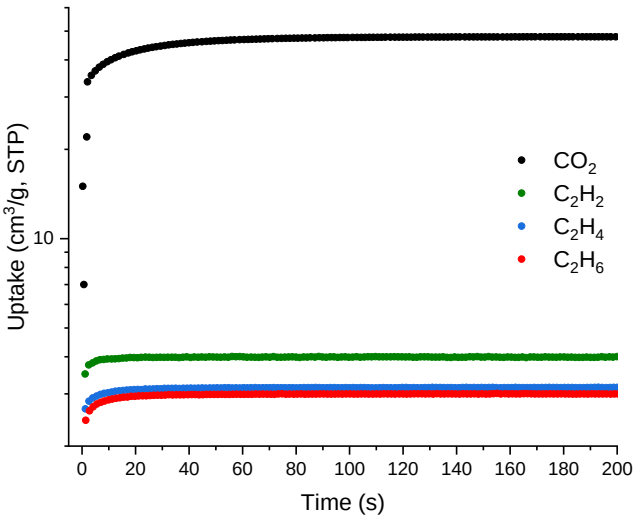

Figure 5.7 Kinetic profiles of gas uptake by MUF-16 at 293 K upon exposing an evacuated sample to a dose of gas equal to its measured total adsorption at 760 torr.

As can be seen from Figure 5.7 all the gases reach their equilibrium gas uptake in less than 50 seconds, thus exhibiting a fast kinetics of MUF-16 for adsorbing CO_2 and C2 hydrocarbons. However, the equilibrium adsorption capacity of MUF-16 is significantly higher than C2 hydrocarbons which confirms that the mechanism of adsorption is differences in the equilibrium capacity of CO_2 with these gases.

Building on these results, we then investigated the feasibility of CO_2/C2 hydrocarbon separations under dynamic conditions. We measured experimental breakthrough curves for various gas mixtures at 293 K and 1.1 bar: CO_2/C_2H_6 (50/50), CO_2/C_2H_4 (50/50) and CO_2/C_2H_2 (50/50 and 5/95). Figure 5.8 shows the relative concentration of CO_2 and the three C2 hydrocarbons (measured independently) exiting the adsorbent bed packed with 0.9 gram of MUF-16 as a function of time.

Complete separation was realized by MUF-16, whereby the C2 hydrocarbons broke through from the column at an early stage because of their low affinity for the framework. Conversely, the signal of CO_2 was not detected for at least 12 minutes due to its adsorption by MUF-16 (Figure 5.8a). It equates to a dynamic adsorption capacity of 1.8 mmol/g which is very close to its equilibrium adsorption capacity of 1.92 mmol/g at studied partial pressure. Significant volumes of pure C2 hydrocarbons can be obtained in this way.

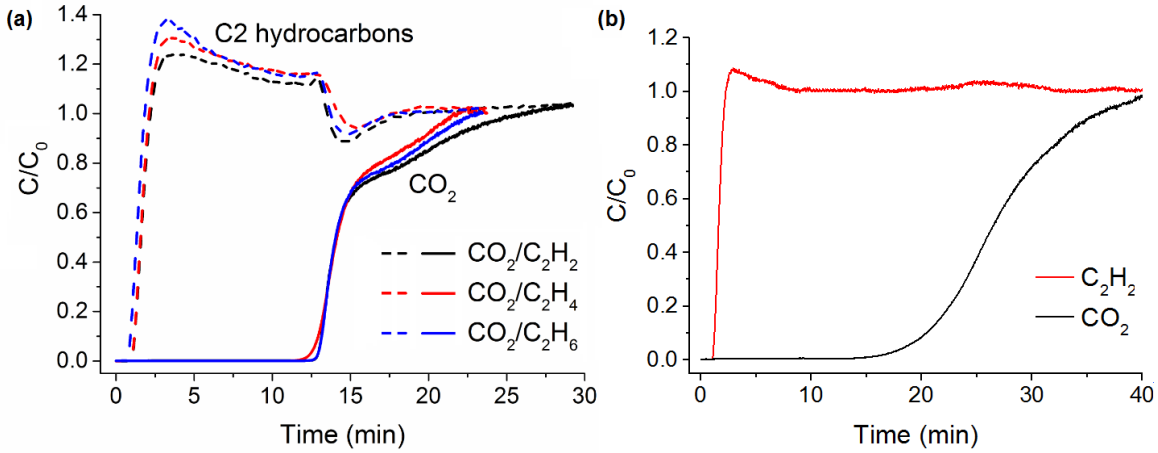

Figure 5.8 Experimental breakthrough curves for (a) 50/50 mixtures of CO_2 and the three C2 hydrocarbons (measured independently) and (b) 5/95 mixtures of CO_2/C_2H_2 and at 293 K and 1.1 bar in an adsorption column packed with MUF-16.

The ability of MUF-16 to selectively adsorb CO_2 is an important advantage of this MOF as pure C2 hydrocarbons can be produced directly in a single adsorption step using a fixed-bed adsorption operation. For the other MOFs that have been suggested in the literature as C_2H_2-selective materials, pure C_2H_2 can only be produced in the desorption step, which is considerably more difficult and burdensome. Subsequent multiple breakthrough tests revealed that MUF-16 maintained its CO_2 uptake and complete removal of CO_2 over 12 cycles (Figure 5.9a).

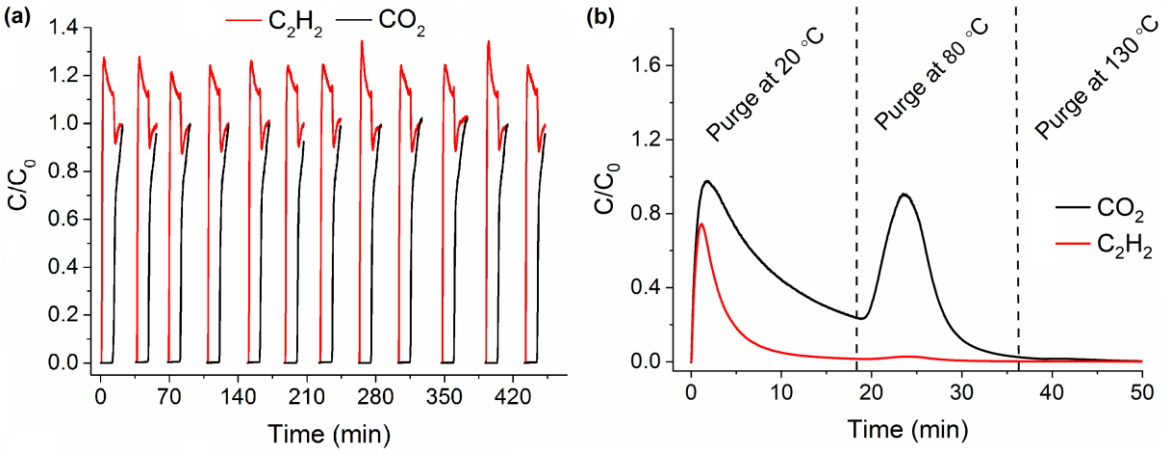

Figure 5.9 (a) Twelve separation cycles for a CO_2/C_2H_2 mixture (50/50 mixture). Each separation process was carried out at 293 K and 1.1 bar. MUF-16 was regenerated between cycles by placing it under vacuum at ambient temperature for 20-25 min. **(b)** Experimental desorption profile of MUF-16 following the separation of CO_2 and C_2H_2 upon heating under a helium flow of 5 ml_N/min at 1.1 bar. No adsorbates were removed upon further heating at 130 °C indicating that they had been fully expelled at lower temperatures.

The regeneration of MUF-16 was achieved by placing it under vacuum or purging with an inert gas. Full regenerated was observed under vacuum for around 25 mins (Figure 5.9a). As an alternative, regeneration by purging with a helium gas at elevated temperatures also was investigated. First CO_2 adsorption isotherms of MUF-16 at different temperatures were obtained Figure 5.10. As can be seen from Figure 5.10, temperature increase from 353 K (80 °C) does not decrease much the CO_2 adsorption uptake of MUF-16 so this temperature was found to be an optimum temperature for regenerating MUF-16 under helium flow.

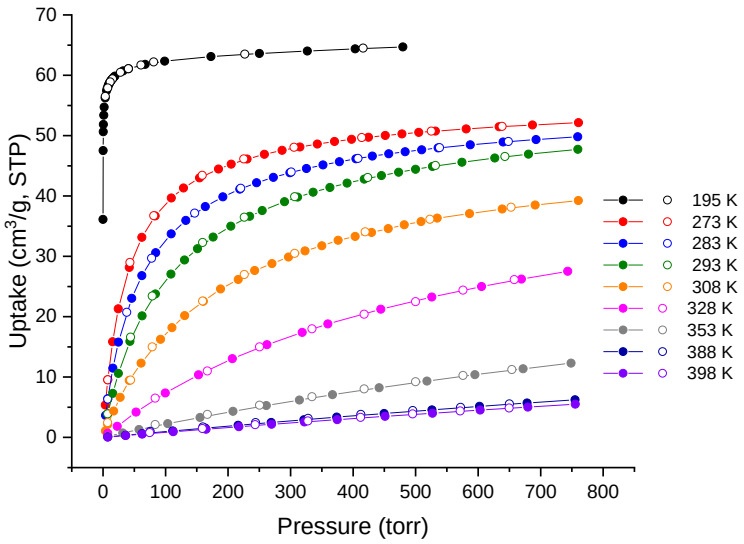

Figure 5.10. Volumetric adsorption (filled circles) and desorption (open circles) isotherms of CO_2 at different temperatures for MUF-16.

As can be seen from Figure 5.9b, in the case of acetylene, all of the adsorbed hydrocarbon and half of the CO_2 can be removed from the bed by purging at room temperature. The remainder can be fully desorbed at 80 °C. Such a low temperature of activation makes MUF-16 an economical adsorbent for TSA processes where all the adsorbed CO_2 gases can be completely removed from adsorbent. This temperature is much lower than required regeneration temperature with conventional materials.[354]

To investigate separations at low CO_2 concentrations, we simulated breakthrough curves under these conditions. First, the mass transfer coefficient used for the simulated breakthrough curves was empirically tuned based on experimental breakthrough curves (as the overall mass transfer coefficient is in proportion to the steepness of breakthrough curves, the accurate value of it was obtained empirically by tuning its value until the steepness of the predicted and experimental breakthrough curves were the same). This produces an excellent match between simulated and experimental breakthrough curves. With this realistic mass transfer coefficient in hand, we predicted breakthrough curves using feeds containing

trace CO_2 (0.1%) in the three C2 hydrocarbons (Figure 5.11). These calculations revealed that MUF-16 is capable of eliminating such small quantities of CO_2, as often required in industrial processes.

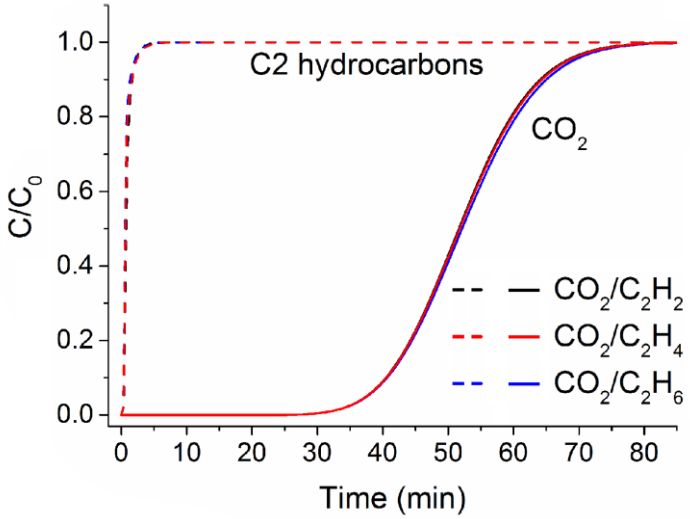

Figure 5.11 Simulated breakthrough curves for a mixture of 0.1/99.9 CO_2/C2 hydrocarbons at 293 K and 1.1 bar.

Pelletized MOFs are generally more compatible with industrial processes than MOF crystals. In this light, we investigated the feasibility of pelletizing MUF-16 using various polymers and found polyvinylidene fluoride (PVDF) to be an effective binder. A photo of pelletized MOFs is presented in Figure 5.12. Further details about practical procedure of making MUF-16 in pellets are discussed in the last section of this chapter. The PXRD patterns and CO_2 adsorption isotherm exhibit no notable differences compared to MUF-16 powders, indicating that the separation performance of MUF-16 is maintained (Figure 5.13).

Figure 5.12 A photograph of MUF-16/PVDF pellets.

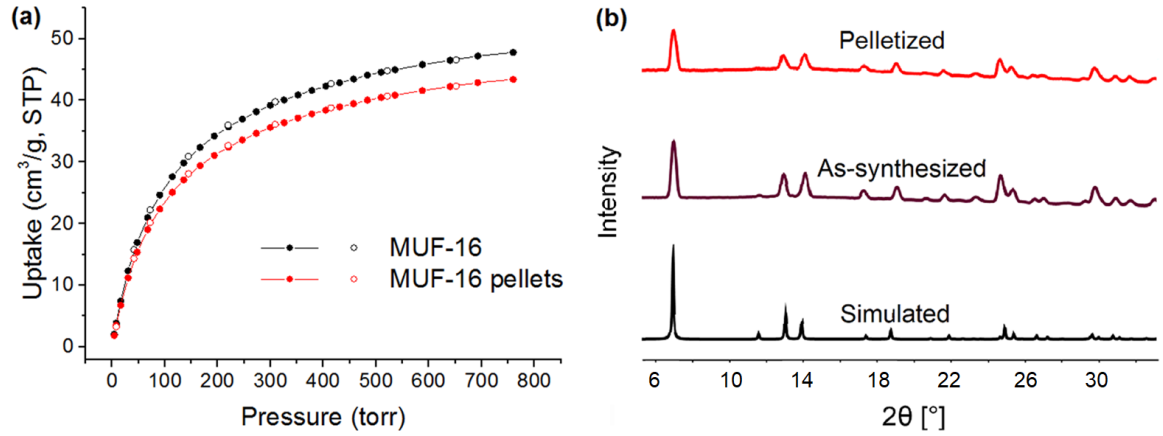

Figure 5.13 (a) PXRD patterns of MUF-16 showing that its structure remains unchanged after making it into pellet with a PVDF binder. (b) CO_2 adsorption isotherm of MUF-16 at 293 K showing that the inherent adsorption performance of the MOF towards CO_2 remains unchanged after making it into pellet with a PVDF binder. The observed drop in capacity for the pellets arises from the 10 wt% PVDF, which is non-adsorbing.

5.2.2 CO_2/N_2 and $CO_2/CH_4+C_2H_6$ separations

Similar to the case of CO_2/C2 hydrocarbons separation, the unique pore chemistry and appropriate pore aperture size of MUF-16 family for adsorbing CO_2, motivated us to evaluate its sorption performance for separation CO_2 over N_2 and CH_4. Hence, low-pressure N_2 and CH_4 sorption data at two temperatures of 293 K and 273 K were measured. These isotherm together with C_2H_6 are compared with that of CO_2 in Figure 5.14.

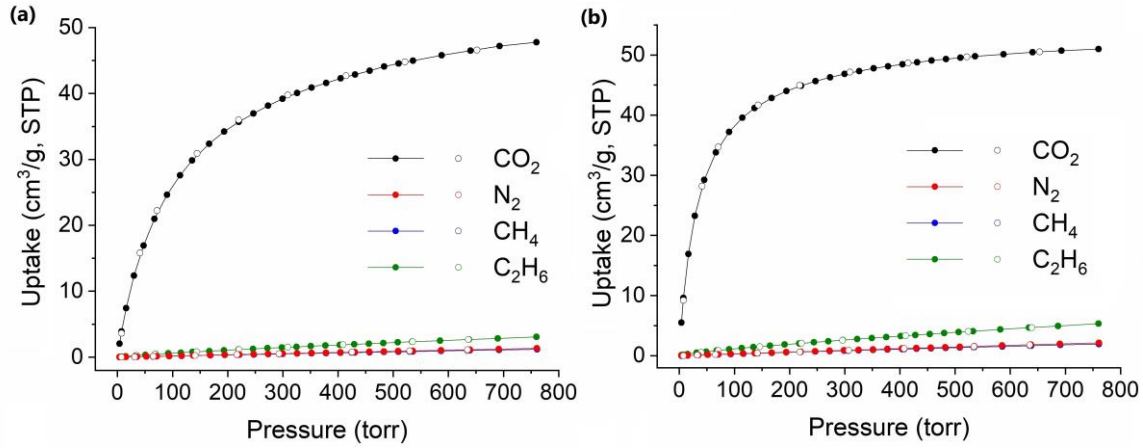

Figure 5.14 Experimental CO_2, N_2, CH_4, and C_2H_6 adsorption (solid) and desorption (open) isotherms of MUF-16 at (a) 293 K and (b) 273 K.

The MUF-16 family showed highly selective adsorption of CO_2 by taking up a large amount of CO_2 at ambient conditions, while adsorbing negligible amounts of N_2, CH_4 and C_2H_6. MUF-16 with cobalt(II) centres was superior to its Mn(II) and Ni(II) analogues because if its limited uptake of N_2 and CH_4 (1.32 and 1.20, respectively). MUF-16(Mn) and MUF-16(Ni) adsorb similar quantities of CO_2 (50.5 and 48 cm^3/g, respectively) but relatively higher amounts of N_2, CH_4 and C_2H_6 (Figure 5.15, Table 5.2). Therefore, we focused on the separation performance of MUF-16 and investigated its potential to separate CO_2 from N_2 and CO_2 from CH_4.

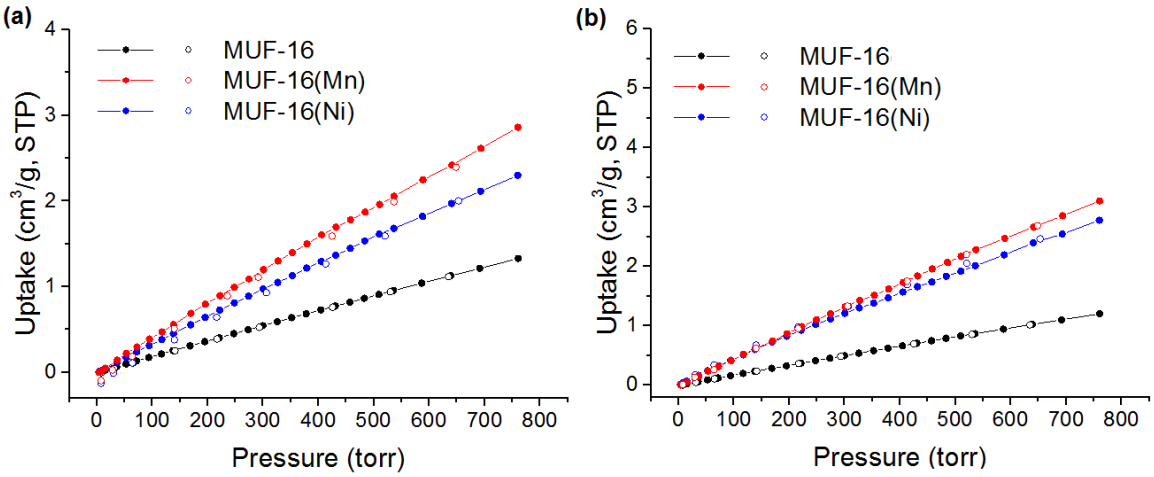

Figure 5.15 Volumetric adsorption (filled circles) and desorption (open circles) isotherms of (a) N_2 and (b) CH_4 measured at 293 K for MUF-16 (black), MUF-16(Mn) (red), and MUF-16(Ni) (blue).

Table 5.2 Summary of gas adsorption data and associated metrics for the MUF-16 family.

MOF	BET surface area (m^2/g)[a]	CO_2 uptake (cm^3/g)[b]	N_2 uptake (cm^3/g)[b]	CH_4 uptake (cm^3/g)[b]	CO_2/N_2 uptake ratio	CO_2/CH_4 uptake ratio	Q_{st} of CO_2 (kJ/mol)	S_{CN} [c]	S_{CM} [c]
MUF-16	215	47.78	1.32	1.20	36.2	39.8	32.7	554	4327
MUF-16(Mn)	209	50.50	2.86	3.10	17.6	16.3	38.0	254	322
MUF-16(Ni)	238	47.97	2.30	2.77	20.8	17.3	37.4	280	573

[a] From the N_2 adsorption isotherm at 77 K. [b] At 1 bar and 293 K. [c] CO_2/N_2 and CO_2/CH_4 selectivity for a 15/85 and 50/50 mixture, respectively, at 1 bar and 293 K as calculated by IAST.

As a result of the difference between its uptake capacity of CO_2 and other gases, MUF-16 exhibits uptake ratios of 36.2 and 39.8 for CO_2/N_2 and CO_2/CH_4, respectively, at 293 K and 1 bar. Such a separation performance is unprecedented, and the framework outperforms benchmark adsorbents including Cu-BTC[305, 355] (uptake ratio of 23 and 5.5 for CO_2/N_2 and CO_2/CH_4, respectively), Mg-MOF74[40, 142] (uptake ratio of 11.8 and 7.2 for CO_2/N_2 and CO_2/CH_4, respectively), SIFSIX-3-Zn[40] (uptake ratio of 11.2 and 3.3 for CO_2/N_2 and

CO_2/CH_4, respectively), and zeolite 13X[339] (uptake ratio of 18.7 and 8.6 for CO_2/N_2 and CO_2/CH_4, respectively) (Table 5.2). The performance of MUF-16 is comparable with top-performing MOFs such as SIFSIX-2-cu-i[40] (uptake ratio of 34 and 12 for CO_2/N_2 and CO_2/CH_4, respectively), DICRO-3-Ni-i[349] (uptake ratio of 20 for CO_2/N_2), and en-Mg-dobpdc[147] (uptake ratio of 47 for CO_2/N_2).

In addition, MUF-16 also takes up negligible amount of C_2H_6, which makes it suitable for removing CO_2 from natural gas which mainly consists of CH_4 and C_2H_6.[306] Composition of natural gas in three different locations are presented in table 5.3.[356]

Table 5.3 Composition of natural gas in three different locations.

Components	Canada	Kansas	Texas
methane	77.1	73	65.8
ethane	6.6	6.3	3.8
C3+	8.1	5.7	3.0
H_2S	3.3	trace	trace
CO_2	1.7	trace	trace
N2	3.2	14.7	25.6
He	trace	0.5	1.8

In light of appreciable adsorption of CO_2 over other gases, MUF-16 shows an extraordinary ideal adsorbed solution theory (IAST) selectivity of 554, 4327 and 539 for 15/85 mixture of CO_2/N_2, 50/50 mixture of CO_2/CH_4 and 10/10+80 mixture of CO_2/C_2H_6+CH_4, respectively, at 293 K and 1 bar. These selectivity values together with those of other member of MUF-16 family are presented in Figure 5.17 (see Appendix D for other mixture compositions and temperatures). As anticipated, based on their higher CH_4 and N_2 uptake, they showed lower selectivity compared to MUF-16.

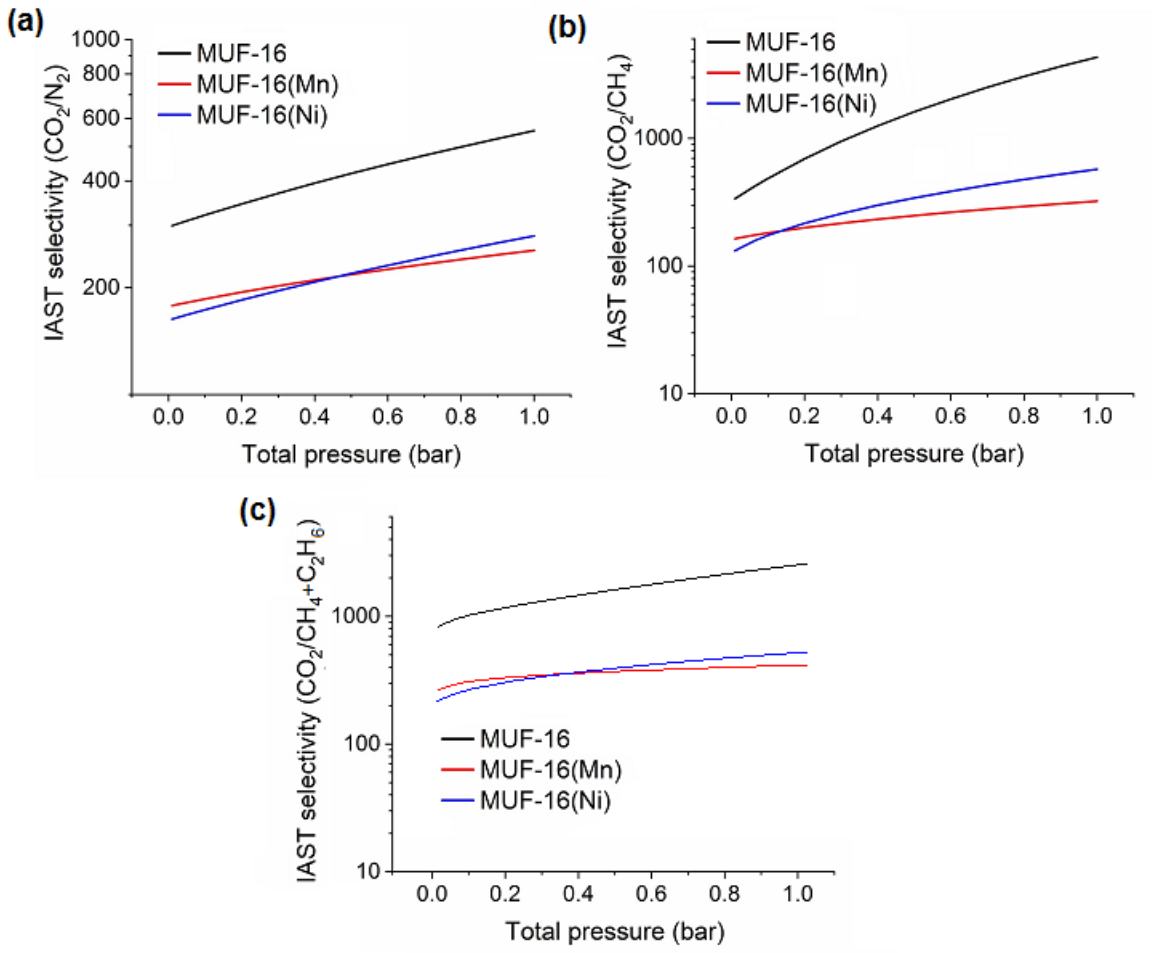

Figure 5.16 IAST calculations for (a) a 15/85 mixture of CO_2/N_2, (b) an equimolar mixture of CO_2/CH_4 and (c) 10/80+10 $CO_2/CH_4+C_2H_6$ at 293 K for the MUF-16 family.

This exceptional selectivity for CO_2, surpassing the majority of reported CO_2 selective materials, positions MUF-16 as one of the top-performing materials for CO_2/N_2 and a new benchmark for CO_2/CH_4 and $CO_2/CH_4+C_2H_6$ separations. Remarkably, IAST selectivity of 4327 for equimolar mixture of CO_2/CH_4 at 293 K and 1 bar is the highest value ever reported for porous materials. For the case of CO_2/CH_4, separation performance of MUF-16 family is compared with top-performing MOFs in the Figure 5.17.

As can be seen from both Figure 5.17a and 5.17b, MUF-17 has the highest IAST selectivity compared to the top-performing MOFs ever reported. The second high selective MOF is also still from MUF-16 family, MUF-16(Ni). Comparing to other MOFs, MUF-16 family has a medium CO_2 uptake of 2.14 mmol/g at 1 bar and 293 K, which is lower than Mg-dobdc (7.2 mmol/g) and CAU-13 (6.1 mmol/g), but still higher than half of top-performing MOFs (Figure 5.17a). MUF-16 also has one of the highest CO_2/CH_4 uptake ratio (39.8 for MUF-16, the highest ones are SIFSIX-14-Cu-I and $[Cd_2L(H_2O)]2.5H_2O$ with an uptake ratio of 116 and 42.9, respectively. They are not presented in Figure 5.17 because

their IAST selectivity is not reported). MOF with the second high uptake ratio is [Cu(tba)$_2$] with an uptake ratio of 23.2 which is much lower than MUF-16. The third and fourth one also are from MUF-16 family, MUF-16(Ni) and MUF-16(Mn) respectively.

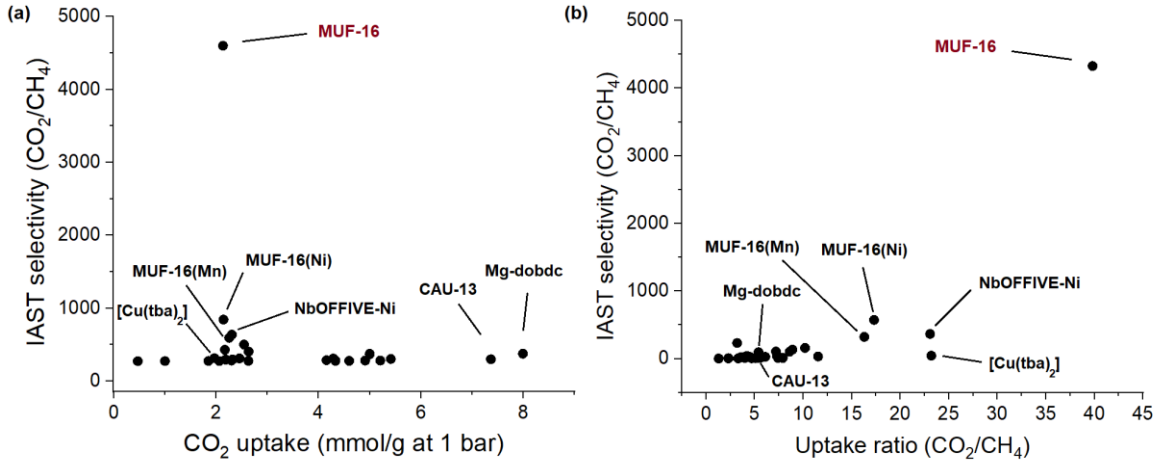

Figure 5.17 IAST selectivity of MUF-16 family for an equimolar mixture of CO_2/CH_4 in comparison to top top-performing MOFs at 1 bar and ambient temperature versus their (a) CO_2 uptake and (b) uptake ratio at 1 bar.

The CO_2/N_2 and CO_2/CH_4 separation parameters of MUF-16 in comparison to theses top-performing MOFs also are presented in Table 5.4. IAST selectivities are presented for a 15/85 mixture of CO_2/N_2 and 50/50 CO_2/CH_4 at 1 bar, unless otherwise stated. Q_{st} values are reported at low loading, unless otherwise stated. Uptake ratios are calculated by dividing the uptake of CO_2 by that of N_2 or CH_4 (all at 1 bar and specified temperature in the Table 5.4). These were taken from either a direct statement of relevant details in the manuscript or were extracted from figures by a digitizer software.

Table 5.4 Separation metrics of MUF-16 in comparison to other top-performing materials reported in the literature.

	MOF	T (°C)	P (bar)	CO_2|N_2|CH_4 uptakes (cc/g)	IAST selectivity		Uptake ratio		$Q_{st}(CO_2)$ (kJ/mol)
					CO_2/N_2	CO_2/CH_4	CO_2/N_2	CO_2/CH_4	
Commercial adsorbents and zeolites	Zeolite 13X[40, 339]	25	1	112 | 6.0 | 13	420	103	18.7	8.6	44-54
	BPL Activated carbon[340-341]	25	1	46.2 | 6.5 | 20.2	23*	4	7.1	2.3	21[c]
	Cu-SSZ-13[357]	25	1	71.3 | 7.6 | n/a	72	n/a	9.4	n/a	34
	Zeolite 5A[358-359]	30	1	75.5 | 5.2 | 11.8	n/a	n/a	14.5	6.4	23[c]
	Zeolite 4A[360-361]	30-32	1	105.3 | 7.4 | 15	n/a	n/a	14.2	7	39
Conventional MOFs	Mg-dobdc[40, 142, 305, 342]	40	1	179 | 15.2 | 25	182	105	11.8	7.2	47-52
	en-Mg-dobpdc[147]	25	1	103 | 2.2 | n/a	230[a]	n/a	47	n/a	49-51
	mmen-Mg-dobdc[343]	25	1	86.3 | 2.35 | n/a	n/a	n/a	36.7	n/a	71[c]
	HKUST-1[305, 355, 362]	25	1	103 | 4.5 | 18.7	n/a	7.4	23	5.5	35[c]
	CAU-1[363]	0	1	165 | 5.6 | 27	101[b]	28[b]	29.5	6.1	48
	PCN-88[364]	23	1	97 | 3.1 | 19	15	7	31.3	5.1	27
	ZIF-78[365]	25	1	51.5 | 3.9 | 13	50[b]	10.6[b]	13.2	4	29
	MIL-101(Cr)[366]	20	1	22.4 | 2.3 | 6.7	n/a	4	9.7	3.3	26
	mmen-Cu-BTTri[344]	25	1	90 | 2.35 | n/a	327*	n/a	38.3	n/a	96
	ZIF-8[367-368]	25	1	10.5 | 2.3 | 8	6.5	2.5	4.6	1.3	19
	bio-MOF-11[345]	25	1	92 | 2.9 | n/a	75[b]	n/a	31.7	n/a	45
SI(TI)FSIX and Hybrid ultra-porous materials	SIFSIX-1-Cu[346-347]	25	1	116.6 | 6.4 | 14.8	27[#]	10.6	18.2	7.9	27
	SNIFSIX-1-Cu[347]	25	1	97 | 6 | 12.2	22[#]	12	16.2	7.9	27
	SIFSIX-2-Cu[40]	25	1	41.4 | 3.9 | 8.7	14	5.3	10.6	4.7	22
	SIFSIX-2-Cu-i[40]	25	1	121.2 | 3.4 | 10.5	140	33	35.6	11.54	32
	SIFSIX-3-Zn[40]	25	1	57 | 5.1 | 17.6	1820	231	11.2	3.2	45
	SIFSIX-3-Cu[152]	25	1	58 | 4.3 | n/a	15500[#]	n/a	13.5	n/a	54
	SIFSIX-3-Ni[369]	25	1	59 | n/a | 6.6	n/a	134	n/a	8.9	45
	TIFSIX-3-Ni[369]	25	1	48.6 | n/a | 4.8	n/a	158	n/a	10.2	50
	TIFSIX-1-Cu[347]	25	1	110 | 6.5 | 14.9	30[#]	11	17	7.4	27
	TIFSIX-2-Cu-i[369]	25	1	93.1 | n/a |16.7	n/a	16	n/a	5.6	36
	SIFSIX-14-Cu-i[348]	25	1	109 | 0.13 | 1.1	n/a	n/a	838	116	38

	NbOFFIVE-Ni[369]	25	1	51.69 | n/a | 2.24	n/a	366	n/a	23.07	54
	UTSA-120[370]	23	1	112 | 5.6 | 20.8	600	96	20	5.4	27
	DICRO-3-Cu-i[349]	20	1	40.3 | 0.51 | n/a	146[a]	n/a	79	NA	37
	MOOFOUR-1-Ni[350]	25	1	55 | 5.5 | 13	96[#]	40[#]	10	4.2	56
	WOFOUR-1-Ni[371]	25	1	52 | 3.5 | 11.5	179[#]	26[#]	14.8	4.5	66
	Qc-5-Ni-dia[291]	20	1	58.9 | 7.1 | 25.6	36	7	8.3	2.3	32
Other MOFs	$[Cd_2L(H_2O)]_2.5H_2O$[372]	20	1	47.2 | 1.3 | 1.1	n/a	n/a	36.3	42.9	37
	$[Cu(tba)_2]$[351]	20	1	44 | 1.6 | 1.9	45	45[&]	27.5	23.2	36
	$[Cu(bcppm)H_2O]$[373]	20	1	33.6 | 1.5 | n/a	590	NA	22.4	n/a	29
	UTSA-16[305, 374]	23	1	96 | 4.5 | 13.2	314	38	21.3	7.3	33
	IITKGP-5a[375]	22	1	49 | 4 | 13.6	148	23.8	12.3	3.6	23
	Cu-TDPAT[376]	25	1	132 | 8.7 | 24	79[#]	n/a	15.2	5.5	42
	PPN-6-CH_2DETA[377]	22	1	98.6 | 0.7 | n/a	442	n/a	140	n/a	63
	IISERP-MOF2[378]	30	1	88.48 | 5.1 | n/a	1860	n/a	17.3	n/a	33
	ZnAtzOx[379]	0	1	94.80 | 5.5 | n/a	n/a	n/a	17.2	n/a	40
	SGU-29[380]	25	1	79.18 | n/a | n/a	3515[#]	n/a	n/a	n/a	50
This work	**MUF-16**	**20**	**1**	**47.8 | 1.3 | 1.2**	**554**	**4327**	**36.2**	**39.8**	**32.7**
	MUF-16(Mn)	**20**	**1**	**50.5 | 2.9 | 3.1**	**254**	**322**	**17.6**	**16.3**	**38**
	MUF-16(Ni)	**20**	**1**	**48 | 2.3 | 2.8**	**280**	**573**	**20.8**	**17.3**	**37.4**

[a] Selectivity is calculated from the uptake ratio/partial pressure ratio. [b] Selectivity is calculated from the slope of isotherms at low pressures (Henry constant). [C] Heat of adsorption averaged over CO_2 uptakes. *IAST is calculated for a 15/75 mixture (10% other gases assumed). [#] IAST is calculated for a 10/90 mixture. [&] IAST is calculated for a 15/85 mixture. [¥] Molecular sieving mechanism.

Based on these results, we then investigated the feasibility of CO_2/N_2 (post-combustion carbon capture), CO_2/CH_4 (biogas separation) and $CO_2/CH_4+C_2H_6$ (natural gas upgrading) separations under dynamic conditions through experimental breakthrough tests. For the case of CO_2/N_2, five different mixtures of 50/50, 15/85, 1/99, 0.4/99.6, and 0.2/99.8 (relevant to the composition of flue gas and the carbon dioxide content in enclosed atmospheres such as submarines) were passed through an adsorption column packed with MUF-16 and their breakthrough curves were obtained (Figure 5.18 and see Appendix D for 0.2/99.8 mixture).

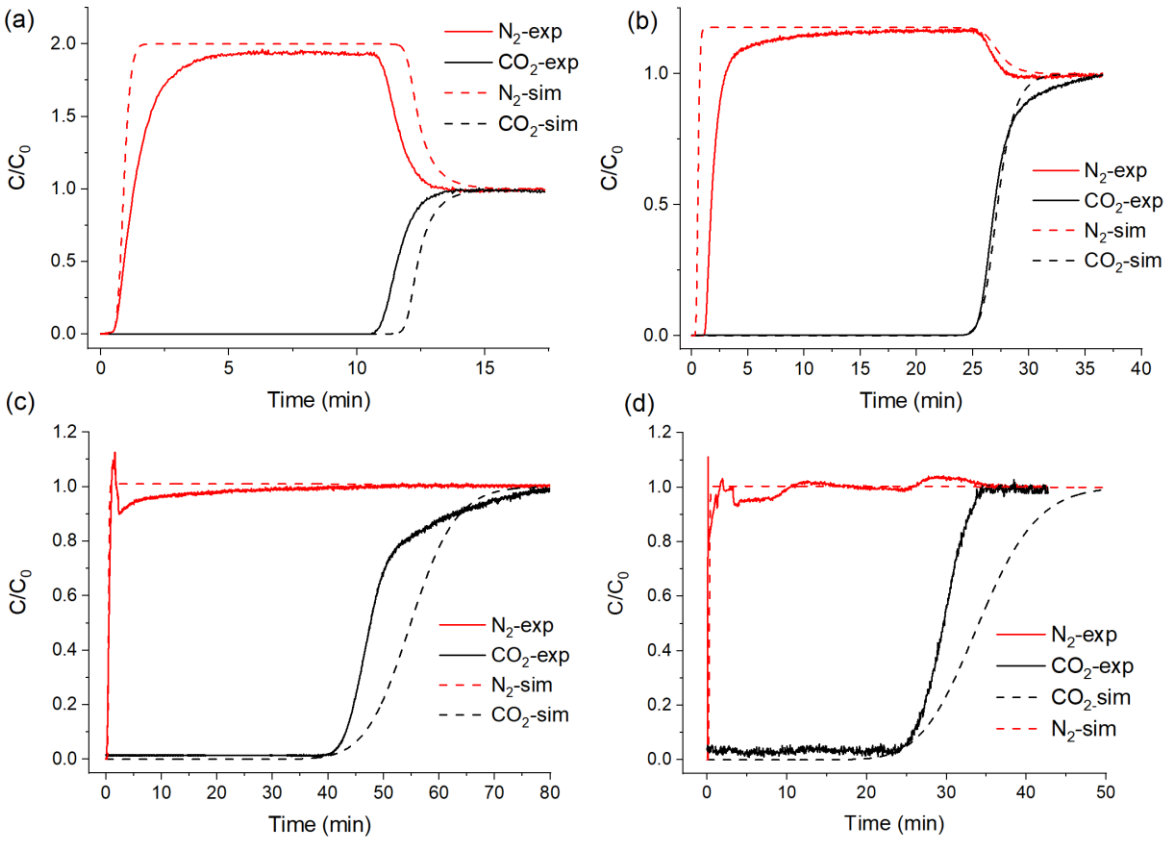

Figure 5.18 Experimental breakthrough curves for (a) 50/50 mixture, (b) 15/85 (c) 1/99 and (d) 0.4/99.6 mixture of CO_2/N_2 at 293 K and 1.1 bar in an adsorption column packed with MUF-16 in comparison to simulated breakthrough curves.

In all of these mixtures, MUF-16 efficiently separate CO_2 from N_2, with a stream of pure N_2 for 11, 24, 40 and 22 minutes for 50/50, 15/85, 1/99, and 0.4/99.6 CO_2/N_2 mixture, respectively. It equates to a dynamic capacity of 1.40, 1.00, 0.17 and 0.044 mmol/g for 50/50, 15/85, 1/99, and 0.4/99.6 CO_2/N_2 mixture, respectively, which are nearly identical to the equilibrium capacity of MUF-16 at these partial pressures of CO_2. Breakthrough curves also were simulated and were compared to the experimental ones and a good agreement was found between them.

Experimental breakthrough curves for different mixture of CO_2/CH_4 (50/50, 15/85) and $CO_2/CH_4+C_2H_6$ (10/80+10, relevant to the composition of natural gas) at 293 K and 1.1 bar. was also measured in an adsorption column packed with MUF-16. Figure 5.19 (see appendix D for 15/85 CO_2/CH_4 mixture) shows a complete separation by MUF-16, whereby CH_4 and C_2H_6 broke through quickly because of low uptake capacity; nevertheless, the signal of CO_2 was not detected longer than 10 for 50/50 and 20 min for 10/10+80 mixture of $CO_2/CH_4+C_2H_6$, denoting that pure CH_4 and $CH_4+C_2H_6$ could be obtained until CO_2 was eluted. The dynamic uptake capacity of CO_2 by MUF-16 obtained from breakthrough curves equates to 1.47 and 0.53 mmol/g which is nearly identical to its equilibrium capacity at the studied partial pressure of CO_2. Simulated breakthrough also was calculated and compared with experimental ones. A good agreement was found for the case of CO_2/CH_4 mixture, but predicted breakthrough curves for $CO_2/CH_4+C_2H_6$ were slightly different from the experimental breakthrough curves. In particular, the CO_2 broke through from the colum much earlier than expected. This can be attributed to the deviation of IAST selectivity from real selectivity of CO_2 over a $CH_4+C_2H_6$ mixture

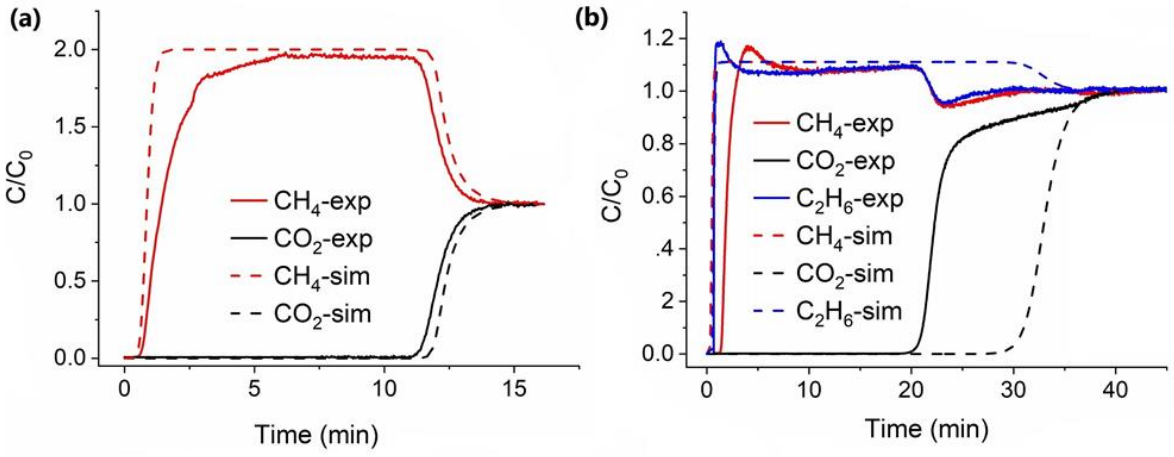

Figure 5.19 Experimental breakthrough curves for (a) 50/50 mixture of CO_2/CH_4 and (b) 10/80/10 mixture of $CO_2/CH_4/C_2H_6$ at 293 K and 1.1 bar in an adsorption column packed with MUF-16.

Subsequently, multiple breakthrough tests revealed that MUF-16 maintained its CO_2 uptake and complete removal of CO_2 over 12 cycles for a CO_2/N_2 50/50 mixture (Figure 5.20). This illustrates the recyclability of MUF-16 for the separation of CO_2/N_2 mixtures (as shown in previous section for CO_2/C_2H_2 mixture as well).

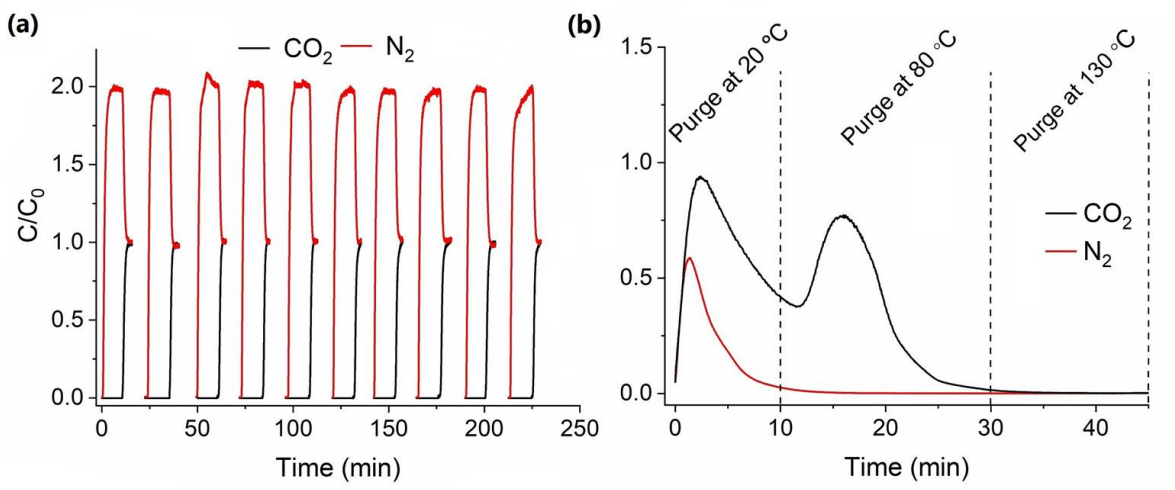

Figure 5.20 (a) CO_2/N_2 separation cycles for a 50/50 mixture lasting for 10 cycles. Each separation process was carried out at 293 K and 1.1 bar and MUF-16 was regenerated by being kept under vacuum at ambient temperature for 20-25 min. (b) Desorption profile of CO_2 and N_2 upon heating under a helium flow of 8 mlN/min at 1.1 bar. No adsorbates removed upon further heating at 130 °C.

The regenerability of MUF-16 was also investigated by placing it under vacuum or purging with an inert gas. The framework can be fully regenerated between cycles by placing it under vacuum for around 15-20 mins (Figure 5.20a) or by purging with a helium gas at 1 bar. As can be seen from Figure 5.20b, the whole N_2 and half of adsorbed CO_2 can be removed from the bed by purging at room temperature and the rest can be fully desorbed at 80 °C. We did the same experiment for two mixtures of CO_2/N_2 0.4/99.6 and 0.2/99.8 and again same results were achieved. All of the adsorbed CO_2 was desorbed at 80 °C (see appendix D for the desorption profiles). Facile regeneration of MUF-16 motivated us to investigate the regenerability of MUF-16 at ambient temperature by a purge gas other than helium (helium is not a practical gas for purging in industrial gas adsorption units). Thus, we further investigated the regenerability of MF-16 at ambient temperature by purging with N_2 or dry air. A higher flowrate of 15 ml_N/min of either N_2 or dry air (water content less than 20 ppm, CO_2 content less than 200 ppm) passed through the adsorption column packed with MUF-16 which is already saturated with CO_2 (A mixture of CO_2/N_2 0.15/0.85 at room temperatures was passed through the column). The CO_2 profile eluting from adsorption column after regeneration is presented in Figure 5.21 for both N_2 and dry air.

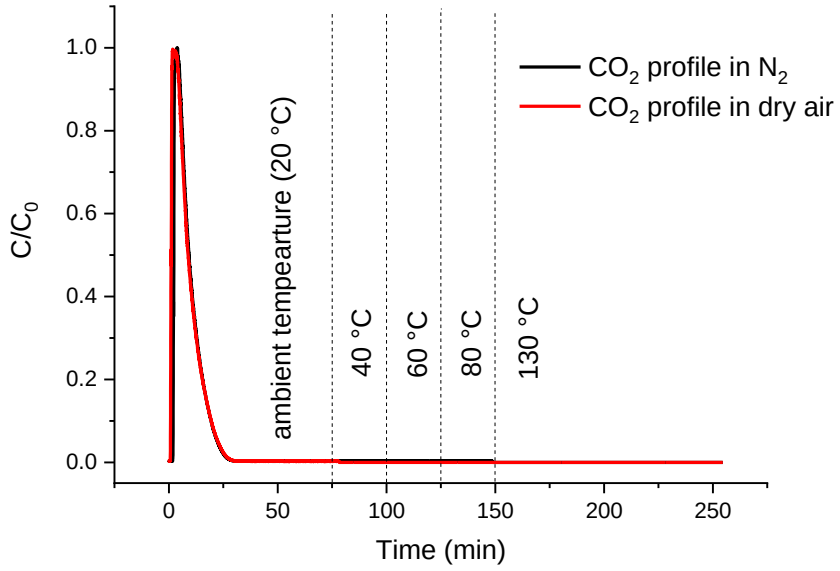

Figure 5.21 Desorption profile of CO_2 in N_2 (purging with N_2) and dry air (purging with dry air) upon purging under a flow of 15 ml_N/min at 1.1 bar. No adsorbates removed upon further heating at 40, 60, 80 and 130 °C.

A flow of either N_2 or dry air was passed through the column at ambient temperature (20 °C) for 75 minutes. The concentration of CO_2 dropped to almost zero after 25 minutes purging showing no further desorption of CO_2 happens after this time. The bed was then heated to elevated temperatures (40, 60, 80 and 130 °C to see if any possible CO_2 that has left in the bed will be desorbed). Interestingly, no further CO_2 desorbed from the bed at these elevated temperatures, showing that bed had already fully desorbed upon purging at ambient temperature. This experiment confirms that MUF-16 can be easily regenerated at ambient temperature through purging by N_2 or dry air during a relatively short period.

5.2.3 Direct air capture

As was mentioned earlier, CO_2 can be captured from air directly. This approach, referred to as direct air capture (DAC), has the advantage of location flexibility and a cleaner environment where the concentrations of SO_x and NO_x are low compared to post-combustion processes.[381-382] However, DAC has the distinct disadvantage that the concentration of CO_2 in air is only 400 ppm.[383] The relatively high affinity of MUF-16 for CO_2 encouraged us to investigate the efficiency of MUF-16 for direct air capture processes. To do this, ambient air (N_2:0.778, O_2:0.195, Ar:0.008, CO_2:400 (ppmv), H_2O: 0.0188) with a flowrate of 3.5 mL_N/min was passed through the column packed with MUF-16. The obtained breakthrough curves for water, CO_2, Ar, N_2 and O_2 are presented in Figure 5.22.

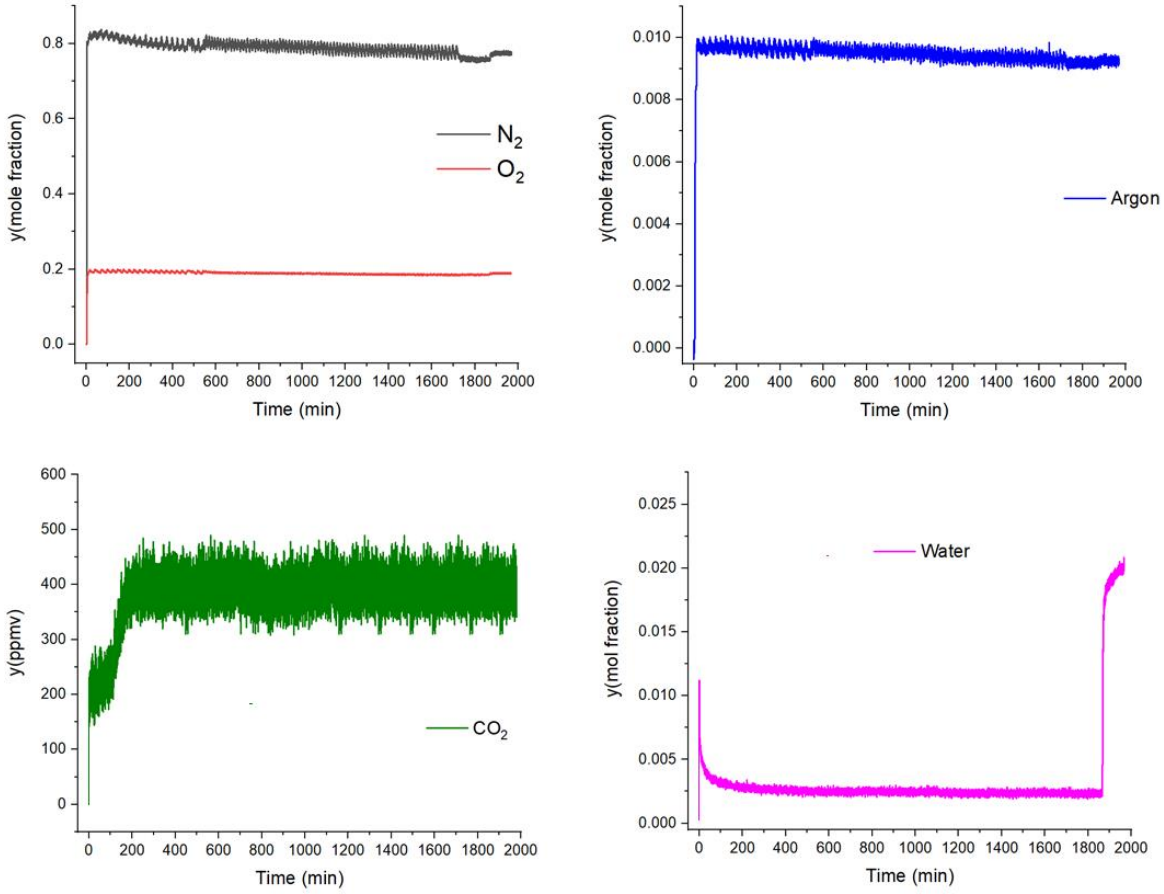

Figure 5.22 Experimental breakthrough curves of different compounds in the air after passing air through an adsorption column packed with MUF-16 at 1 bar and 293 K.

As can be seen from Figure 5.22., N_2, O_2 and Ar break through very quickly because of their near zero adsorption by MUF-16. The breakthrough curve of CO_2 shows MUF-16 has two steps. The first one from zero concentration of CO_2 to 200 ppmv, and the second from 200 ppmv to 400 ppmv (its initial concentration in the feed stream). The first breakthrough occurs just after starting the experiment, indicating MUF-16 is unable to produce much eluent air with a zero concentration of CO_2. The second breakthrough lasts around 50 minutes, producing effluent with a CO_2 concentration of 200 ppmv. Here, MUF-16 can capture about half of the CO_2 present in air. Its inability to *capture* all of the CO_2 probably stems from its low adsorption uptake at low partial pressures of CO_2 (and/or co-adsorption of water molecules).

The breakthrough curve of water is interesting. In the beginning, the water concentration is relatively high, showing weak adsorption of water. It then gradually drops to below 0.0025 (mole fraction). Comparing breakthrough curves of water and CO_2, one scenario could be competition of water with CO_2. In the beginning (First 50 minutes), CO_2 will be mostly

adsorbed in competition with water, thus the CO_2 concentration in the effluent is low and water concentration remains high. Later, the water concentration decreases, while CO_2 starts breaking through, indicating a displacement of previously-adsorbed CO_2 adsorption by incoming water. To investigate this better, single-component breakthrough curves for CO_2 and water were predicted, assuming only one gas passes through the bed with an infinite mass transfer coefficient (quick adsorption). These breakthrough curves are presented in Figure 5.23 in comparison with their experimental breakthrough curves (which involve the above-stated gas mixture).

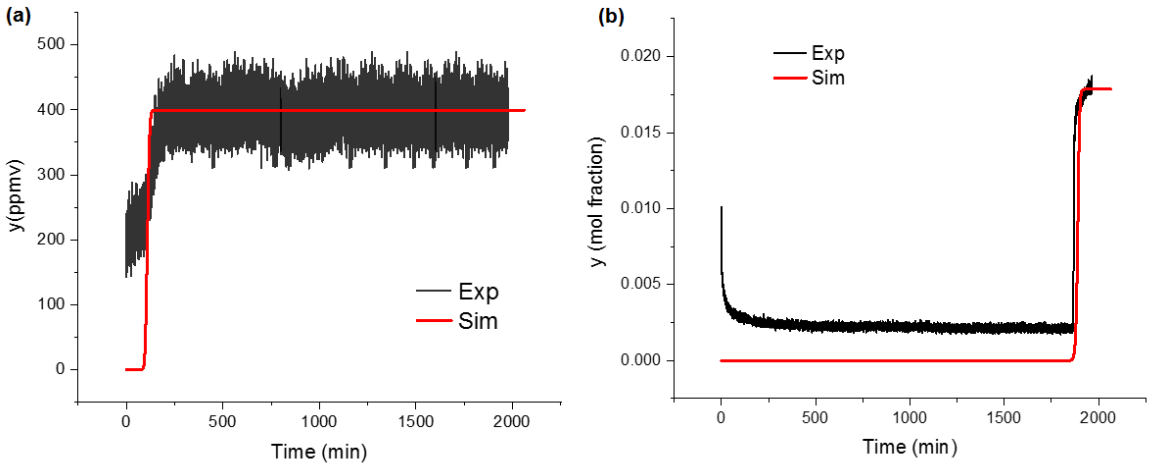

Figure 5.23 Single gas predicted breakthrough curves for (a) CO_2 and (b) water after passing a 0.0004/0.9996 CO_2/He or 0.0188/0.9812 H_2O/He mixture through an adsorption column packed with MUF-16 at 1.02 bar and 293 K in comparison to their mixture experimental breakthrough curve.

The single breakthrough curves of CO_2 (simulated) indicates that MUF-16 could produce air with near zero concentration of CO_2 in absence of water for a short period of time (60 minutes). On the other hand, predicted and experimental breakthrough curves of water match, showing that water is adsorbing ideally and all the capacity of MUF-16 is taken by water. Therefore, water displaces CO_2 during the breakthrough measurement.

Superior adsorption of water compared to CO_2 was demonstrated by the adsorption isotherms of water, indicating water adsorption uptake at low pressure is much higher than that of CO_2 (Figure 5.24a). Kinetic traces for water and CO_2 adsorption were compared and they showed that the rates of uptake of CO_2 is slightly higher than water molecules (Figure 5.24b).

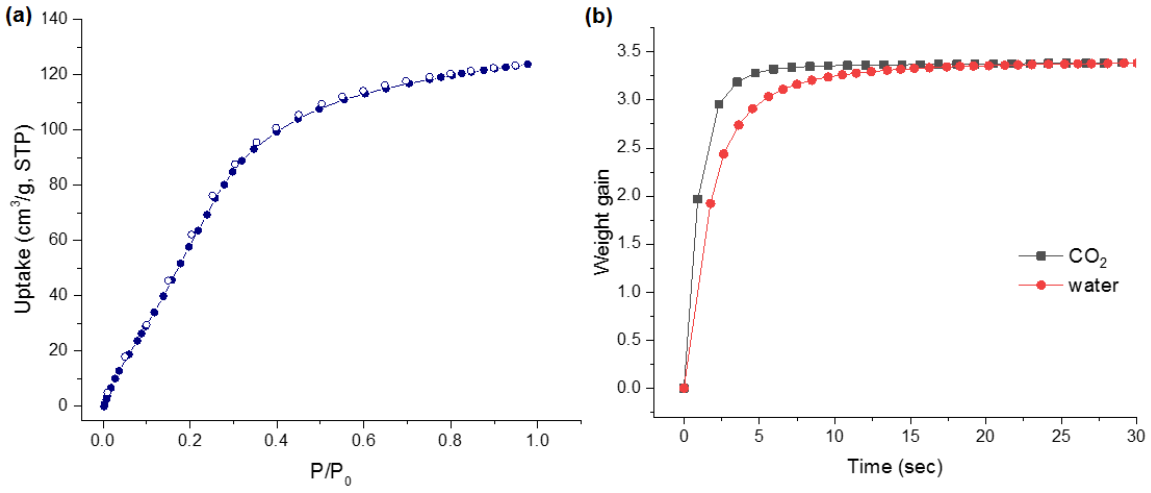

Figure 5.24 (a) Volumetric adsorption (filled circles) and desorption (open circles) isotherm of water measured at 298 K for MUF-16. (b) Kinetic profiles of gas uptake by MUF-16 at 293 K upon exposing an evacuated sample to a dose of gas equal to taking up 3.27 mg of CO_2 or H_2O.

5.3 Conclusion

In this chapter, the performance of MUF-16 for selective adsorption of CO_2 over C2 hydrocarbon, N_2 and CH_4 was investigated. MUF-16 exhibits appreciable selectivity for CO_2 by taking up significant amount of CO_2, while adsorbing near zero amount of C2 hydrocarbons. In the context of CO_2/C2 hydrocarbons separation, the favourable orientation of electrostatic potential in the pore surface has enlarged the tiny difference of CO_2 and C2 hydrocarbons that have opposite electrostatic distribution, i.e., C2 hydrocarbons have quadrupole moment of different signs. This results in an attractive interaction of CO_2 molecules and thus a high adsorption of CO_2 molecules, while the interaction of C2 hydrocarbons with framework is repulsive, resulting in negligible adsorption of them. For the case of CO_2/N_2 and CO_2/CH_4, the same mechanism is applied. The combined effect of small pore size of MUF-16 and the weaker interaction of N_2 and CH_4 with framework leads to a negligible adsorption of these gases.

The efficiency of MUF-16 for separating CO_2 from C2 hydrocarbon, CH_4+C_2H_6 and N_2 was well demonstrated by breakthrough experiments. Complete separation was achieved by very early breakthrough of N_2, CH_4 and C2 hydrocarbons, while CO_2 was being adsorbed on the bed up to its near equilibrium capacity. The ability of MUF-16 for capturing CO_2 from air also was investigated through breakthrough experiment and MUF-16 was not successful to produce an air with near zero concentration of CO_2 mostly because of co-adsorption of water by framework.

Pelletized MUF-16 also was successfully achieved by incorporating a PVDF binder. Besides, MUF-16 indicated an easy regeneration, excellent recyclability and stability

towards water. Therefore, MUF-16 shows great potential in the practical separation of CO_2 from different gas streams.

5.4 Experimental and computational section

5.4.1 General procedures

Heat of adsorption and BET calculation were calculated based on the methods presented in Chapter 2. See appendix D for related curves and fitting parameters.

5.4.2 Gas adsorption isotherm measurements

The same instrument as mentioned in Chapter 2 was used to measure adsorption isotherms. 500-1000 mg was transferred into a pre-dried and weighed sample tube and heated at rate of 10°C/min to a temperature of 130 °C under a dynamic vacuum with a turbomolecular pump for 20 hours.

5.4.3 IAST selectivity calculations

Mixed gas adsorption isotherms and gas selectivities for different mixtures of CO_2/C2 hydrocarbons, CO_2/N_2, CO_2/CH_4 and $CO_2/CH_4/C_2H_6$ at 293 K were calculated based on the method and procedure explained in chapter 1. For binary and ternary mixtures, the adsorption selectivity is defined as follows[384]:

$$S_{binary} = \frac{q_1/p_1}{q_2/p_2} \quad (1)$$

$$S_{ternary} = \frac{q_1/p_1}{(q_2 + q_3)/(p_2 + p_3)} \quad (2)$$

5.4.4 Breakthrough separation experiment and simulation

CO_2/C2 hydrocarbon separations

In a typical breakthrough experiment, 0.9 g of activated MUF-16 was placed in an adsorption column (6.4 mm in diameter × 11 cm in length) to form a fixed bed. The adsorbent was activated at 120 °C under high vacuum for 7 hours and then the column was left under vacuum for another 3 hours while being cooled to 20 °C. The column was then purged under a 20 mL_N/min flow of He gas for 1 hr at 1.1 bar prior to the breakthrough experiment. A gas mixture containing different gas pair of CO_2, C_2H_2, C_2H_6 and C_2H_4 along with He as a carrier gas was introduced to the column at 1.1 bar and 20 °C. A feed flowrate of 6 and 6.85 mL_N/min (including helium) was set for the experiments with 50/50 and 5/95 mixture of

gases, respectively, and the flowrate of He in the feed was kept constant at 2 mL_N/min for all the experiments except for CO_2/C_2H_2 5/95 mixture which no helium was used. The operating pressure was controlled at 1.1 bar with a back-pressure regulator. The outlet composition was continuously monitored by the mass spectrometer until complete breakthrough was observed. The adsorbent was regenerated under vacuum for 20-25 minutes between each cycle.

The desorption behaviour of CO_2 and C_2H_2 from the adsorption column was also investigated. Once the adsorbent was saturated with an equimolar mixture of CO_2 and C_2H_2, the column was purged with a helium flow of 5 mL_N/min for 18 mins at 20 °C at 1 bar while monitoring the effluent gas. Then the column was then heated to 80 °C with a ramp of 10 °C/min for 20 mins. Finally, the column was heated to 130 °C with the same ramping for 15 min before cooling to 20 °C.

Breakthrough curves simulation was performed based on the method presented previously. A summary of Adsorption column parameters and feed characterizations are presented in table 5.5.

Table 5.5 Adsorption column parameters and feed characterizations used for the simulations for MUF-16.

Adsorption bed	***Feed***
Length: 110 mm Diameter: 6.4 mm Amount of adsorbent in the bed: 0.9 g Bed voidage: 0.84 Adsorbent average radius: 0.2 mm K_{CO2}: 0.021 s^{-1} K_{C2H2}: 0.024 s^{-1} K_{C2H4}: 0.017 s^{-1} K_{C2H6}: 0.018 s^{-1}	Flow rate: 6 mL_N/min for equimolar and 0.1/99.9 mixture, and 6.85 mL_N/min for 5/95 mixture. Temperature: 293 K Pressure: 1.1 bar Carrier gas (He) flow rate: 2 mL_N/min for equimolar and 0.1/99.9 mixture, and no He for 5/95. Purge gas: He with a flow rate of 20 mL_N/min

CO_2/N_2, $CO_2/CH_4+C_2H_6$ separations

In a typical breakthrough experiment, 0.9 g of activated MUF-16 was placed in an adsorption column (6.4 mm in diameter × 11 cm in length) to form a fixed bed. The adsorbent was activated at 130 °C under high vacuum for 7 hours and then the column was left under vacuum for another 3 hours while being cooled to 20 °C. The column was then purged under a 20 mL_N/min flow of He gas for 1 hr at 1.1 bar prior to the breakthrough experiment. A gas mixture containing different mixture of CO_2/N_2, CO_2/CH_4 and $CO_2/C_2H_6/CH_4$ was introduced to the column at 1.1 bar and 20 °C. A feed flowrate of 10 mL_N/min and 6

mL_N/min was set for the experiments with gas mixture containing 1% or less CO_2 and more than 1%, respectively. The operating pressure was controlled at 1.1 bar with a back-pressure regulator. The outlet composition was continuously monitored by the mass spectrometer until complete breakthrough was observed.

The desorption behaviour of CO_2 and N_2 from the adsorption column packed with MUF-16 was also investigated. Once the adsorbent was saturated with a mixture of CO_2/N_2, the column was purged with a helium flow of 8 mL_N/min and 20 mL_N/min for the experiments with gas inlet mixture containing 1% or less CO_2 and more than 1%, respectively, at 20 °C at 1 bar while monitoring the effluent gas. Column was first purged with helium at ambient temperature (20 °C). The column was then heated to 80 °C with a ramp of 10 °C/min for 20 mins. Finally, the column was heated to 130 °C with the same ramping before cooling to 20 °C.

Breakthrough curves simulation was performed based on the method presented previously. A summary of Adsorption column parameters and feed characterizations are presented in table 5.6.

Table 5.6 Adsorption column parameters and feed characterizations used for the simulations for MUF-16.

Adsorption bed	**Feed**
Length: 110 mm Diameter: 6.4 mm Amount of adsorbent in the bed: 0.9 g Bed voidage: 0.84 adsorbent density: 1.674 g/cm^3 Adsorbent average radius: 0.2 mm K_{CO2}: 0.029 s^{-1} K_{N2}: 0.00012 s^{-1} K_{CH4}: 0.00021 s^{-1} K_{C2H6}: 0.0018 s^{-1}	Flow rate: 6 mL_N/min for all the mixture containing 1% or more CO_2 and 10 mL_N/min for all the mixture containing less than 1% CO_2 Temperature: 293 K Pressure: 1.1 bar Carrier gas flow rate: No carrier gas was used for all the experiments. Purge gas: He with a flow rate of 20 mL_N/min

Direct air capture

In a typical breakthrough experiment, 0.9 g of activated MUF-16 was placed in an adsorption column (6.4 mm in diameter × 11 cm in length) to form a fixed bed. The adsorbent was activated at 130 °C under high vacuum for 7 hours and then the column was left under vacuum for another 3 hours while being cooled to 20 °C. Ambient air (N_2:0.778, O_2:0.195, Ar:0.008, CO_2:400 (ppmv), H_2O: 0.0188) with a flowrate of 3.5 mL/min was passed through the column.

Single gas breakthrough curves were predicted for water and CO_2 at 1.1 bar and 293 K. To simulate CO_2 and water composition relevant to typical air, water and CO_2 were

diluted with He to achieve gas mixtures of 0.0004/0.9996 CO_2/He and 0.0188/0.9812 H_2O/He to introduce to the adsorption column.

5.4.5 Pelletisation

MOF pellets were fabricated based on the following procedure:

1. MUF-16 (~0.5 g) was gently ground using mortar and pestle.
2. The ground sample was transferred to a 20 mL vial and 0.5 mL of DMF was added. A viscous suspension was obtained after sonicating for half an hour. The suspension was stirred for another 30 mins.
3. PVDF powder (~ 50 mg) was gradually added over the course of 1 hour to make a viscus paste.
4. The paste was transferred into a plastic syringe using a spatula and pressed it out in one thin noodle onto a glass slide.
5. The noodle was cut into small pellets and dried under vacuum at 120 °C for 4 hours.

Chapter 6

A Multipurpose Metal-Organic Framework MUF-17 for Selective Adsorption of Acetylene over Ethylene and Carbon Dioxide

6.1 Introduction

Ethylene (C_2H_4) and acetylene (C_2H_2) are two major petrochemical products. They have been widely used as fuels and as feedstocks for the production of valuable compounds such as polyethylene and 1,4-butanediol.[190, 385-386] Ethylene is produced by the pyrolysis of hydrocarbons, and crude streams contain trace acetylene that acts as a catalyst poison during polymerization to polyethylene.[387-388] When acetylene is required, it is typically generated by the combustion of natural gas or the cracking of hydrocarbons. Both methods generate a suite of gaseous impurities.[389-390] Acetylene purification is thus important from two distinct angles: the removal of trace quantities of it from ethylene mixtures and its isolation in pure form by eliminating contaminants. Conventional separation and purification methods for acetylene[391] involve solvent extraction,[392] cryogenic distillation,[393] or chemical reactions.[394] These technologies incur several drawbacks. Solvent absorption technologies typically show low selectivities and high energy consumption during regeneration. They also suffer from rapid degradation and environmental pollution due to volatile organic solvents. Cryogenic distillation is expensive and incurs a high energy penalty due to the similarity of the boiling points of acetylene and ethylene, ethane, and carbon dioxide (Table 6.1).

Table 6.1 Physicochemical characteristics of different gases.[110, 235-236]

	Boiling point (K)	Molecular dimensions (Å)	Polarizability (Å^3)	Dipole moment $\times10^{18}$/esu cm^2	Quadrupole moment $\times10^{26}$/esu cm^2
C_2H_2	188.4	3.32×3.34×5.7	3.33-3.93	0	+7.5
CO_2	216.5	3.18×3.33×5.36	2.91	0	-4.3
C_2H_4	169.4	3.28×4.18×4.84	4.25	0	+1.5
C_2H_6	184.5	3.81×4.82×4.08	4.43-4.47	0	+0.65

Significant challenges thus remain in the development of effective, sustainable and energy-efficient methods for the separation and purification of acetylene. One process that

meets many of these goals is selective adsorption in porous media. Adsorption can take place efficiently at ambient temperature and pressures. It can be employed for both gas separation and purification by adsorbing either the major or trace component, respectively. In this light, we targeted a single material that can be used to both trap low levels of acetylene in ethylene *and* to take up large quantities of acetylene when it is in the presence of unwanted gases such as carbon dioxide. The key challenge here is to develop a porous material that possesses both a high selectivity and adsorption capacity for acetylene, particularly at low pressures. The similar sizes, shapes and physicochemical properties of acetylene and the competing guest molecules mean that such an adsorbent must present pores that are specific to acetylene.[110] This can be achieved by a complementary match between the host and guest in terms of both size and electric polarity. Unfortunately, traditional porous materials, such as activated carbon and zeolites, exhibit poor characteristics in this regard. Conversely, metal–organic frameworks are effective materials for highly challenging separations.[7, 24, 207, 290, 313] More than 75,000 MOFs have been synthesized by combining a rich library of inorganic and organic building blocks.[1] Thanks to their inherent modularity, MOFs can enable exquisite control over pore sizes and electrostatics.[95, 110, 134, 285, 314-317]

Recently, MOFs and related materials have been developed for C_2H_2/C_2H_4[281, 317, 395-407] and C_2H_2/CO_2[318, 320, 322, 324-327, 329, 333, 352-353] separations. For example, the mixed MOFs (M'MOFs)[402] family and hydrogen-bonded framework (HOF-3)[320] exhibit very high selectivities for C_2H_2/C_2H_4 (up to 45) and C_2H_2/CO_2 separations (up to 21). However, a common drawback is a relatively low capacity for C_2H_2 narrow micropore windows and low pore volumes. In contrast, the well-known MOF-74 series shows exceptionally high C_2H_2 uptake capacity (e.g., 6.66 mmol/g for Fe-MOF-74 at 45 °C)[408] due to their high density of open metal sites. However, since the pores are too wide to achieve size-discriminating effects, both C_2H_2 and C_2H_4 show strong interactions with the pore surfaces and thus the selectivity is low (2.1, at 1 bar and 45 °C). This underscores a key notion. Both high uptake and good selectivity are jointly necessary in high-performance materials. In addition, in the case of trace gas removal, a steep adsorption isotherm is desired for the target impurity, so it can be removed when present at low partial pressures.

6.2 Results and discussion

Similar to MUF-16, MUF-17 also is built up from solvothermal reaction of cobalt acetate and 5-aminoisophthalic acid but at different synthesis condition and different ligand/metal salt ratio. Specifically, a mixture of $Co(OAc)_2.4H_2O$ (0.125 g, 0.5 mmol), 5-

aminoisophthalic acid (H_2aip, 0.046 g, 0.25 mmol), MeOH (7 mL), and H_2O (0.5 mL) were sonicated for 20 min and sealed in a 50 mL Schott bottle and heated at 85 °C for 24 hours. After cooling the oven to room temperature, the resulting purple crystals (Figure 6.1) of MUF-17 [$Co_5(OH)_2(aip)_4(H_2O)_2$] were isolated by decanting off the mother liquor, then washed with methanol several times and dried under vacuum at 130 °C for 20 h. It yields 62 mg of guest-free MUF-17 with a reaction yield of 92% based on H_2aip.

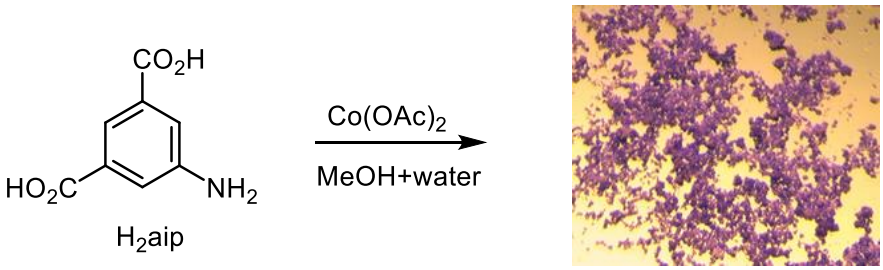

Figure 6.1 Synthetic route to MUF-17 with an optical microscopy image of its single crystals.

As can be seen from Figure 6.1, single crystals of MUF-17 obtained from this synthesis procedure are very small, thus not appropriate for single crystal X-ray diffraction studies. We developed another method to yield bigger crystals. A mixture of $Co(OAc)_2.4H_2O$ (0.125 g, 0.5 mmol), H_2aipBoc (0.281 g, 1 mmol), MeOH (6 mL), and H_2O (0.5 mL) were sonicated for 20 min and sealed in a Teflon-lined autoclave and heated at 120 C for 3 days. After cooling the oven to room temperature, the resulting product was isolated by decanting off the mother liquor, then washed with methanol several times and dried under vacuum to give approximately 0.3 g of MUF-17 as a dark purple solid (Figure 6.2). Appropriate single crystals were chosen for SCXRD studies.

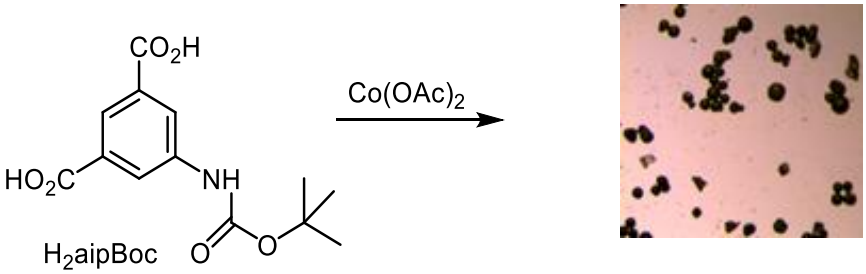

Figure 6.2 Synthetic route to MUF-17 with bigger crystals and an optical microscopy image of its single crystals.

MUF-17 is built up from inexpensive precursors and formed in a high yield. Based on commercial prices, we estimate the raw material cost of this material to be less than $30 per kg: 1 kg of H_2aip = 15USD; 1 kg of $Co(OAc)_2.4H_2O$ = 10USD. Therefore, 2 kg of $Co(OAc)_2.4H_2O$ (20USD) requires 736 g of H_2aip (11USD) and produces 1 kg of MUF-17 for approx. USD30.

Single crystal X-ray diffraction revealed that MUF-17 crystallizes in the monoclinic space group *C*2/c (Table 6.2).

Table 6.2 Crystal data and structure refinement for MUF-17.

CCDC deposition number	1907595
Formula	$Co_5(\mu_3\text{-}OH)_2(aip)_4(H_2O)_2.6H_2O$
Empirical formula	$C_{32}H_{38}Co_5N_4O_{26}$
Formula weight	1189.31
Temperature/K	292.15
Crystal system	monoclinic
Space group	*C*2/c
a/Å	35.4961(19)
b/Å	11.1880(5)
c/Å	21.9119(16)
α/°	90
β/°	94.224(11)
γ/°	90
Volume/Å^3	8678.2(9)
Z	8
ρ_{calc}/g cm^{-3}	1.821
μ/mm^{-1}	15.533
F(000)	4808.0
Data range for refinement	8.0 – 1.40 Å
Index ranges	$-25 \leq h \leq 25$, $-7 \leq k \leq 7$, $-15 \leq l \leq 15$
Reflections collected	17789
Independent reflections	1639 [R_{int} = 0.2678, R_{sigma} = 0.1334]
Data/restraints/parameters	1639/0/251
Goodness-of-fit on F^2	1.420
Final R indexes [I>=2σ (I)]	R_1 = 0.1503, wR_2 = 0.3628
Final R indexes [all data]	R_1 = 0.1990, wR_2 = 0.4129
Largest diff. peak/hole / e Å^{-3}	1.33/-0.60

It comprises a pentanuclear cobalt(II) cluster connected by twelve dianionic aip linkers (Figure 6.3a). The five cobalt ions exhibit tetrahedral (Co4), square pyramidal (Co2), or octahedral (Co1, Co3 and Co5) coordination environments. Each of the eight carboxyl groups from the aip ligands bridges two cobalt ions, and two μ_3-OH groups are present within each cluster. Amino groups of four aip ligands and two terminal aquo ligands complete the coordination spheres within each cluster. By considering the cobalt clusters as

12-connected nodes linked by aip ligands (Figure 6.3b), MUF-17 can be depicted as a porous coordination polymer (Figure 6.3c, d). The framework defines narrow zigzag 1-dimensional pores including relatively large cavities with pore aperture size of 4.7 × 4.8 Å (accounting for the van der Waals surface of the framework) that are connected by narrow channels of around 3.1 × 3.5 Å, as highlighted in Figure 6.3e. The pore topology of MUF-17 is suitable for trapping and discriminating small molecules like C_2H_2, C_2H_4 and CO_2.

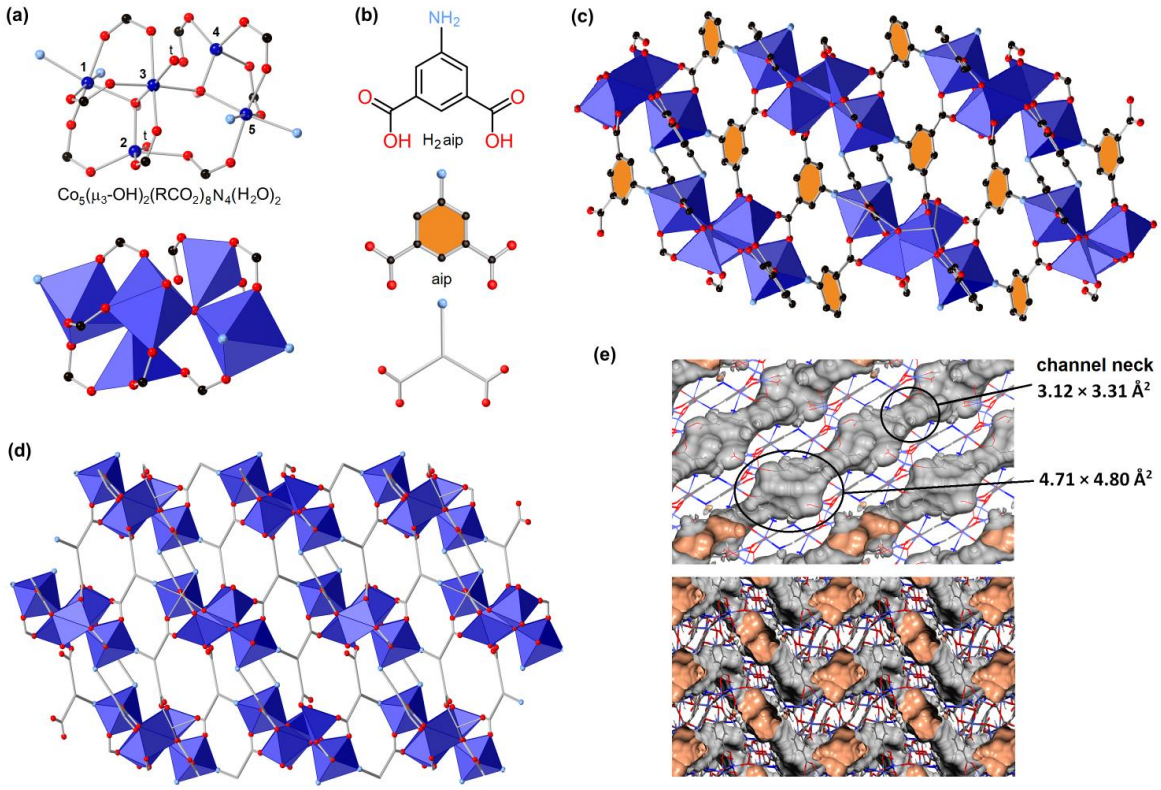

Figure 6.3 (a) The structure of MUF-17, as determined by SCXRD, comprises pentanuclear **cobalt(**II) clusters (cobalt = dark blue; oxygen = red; carbon = black; nitrogen = light blue; hydrogen = pink (most omitted for clarity)). The sites occupied by terminal H_2O ligands are marked with a t. (b) The structure of the aip linker and its stick representation. (c, d) The **cobalt(**II) clusters and aip ligand assemble into network that defines a 3D array of channels. (e) The structure of the pore network in MUF-17 illustrated by the Connolly surface in orange/gray (probe of diameter 1.0 Å).

Guest-free MUF-17 can be readily produced at 130 °C under vacuum, which preserves the coordinated water molecules. These water ligands are lost (as are the crystallinity and porosity) by heating above 200 °C, therefore high temperatures were avoided. The phase purity of the material activated at 130 °C was confirmed by matching its powder X-ray diffraction pattern with that simulated from its SCXRD structure (Figure 6.4), and by

elemental analysis (Anal. calcd. (found) for $[Co_5(OH)_2(aip)_4(H_2O)_2]\cdot 8H_2O$: C, 35.58 (35.32); H, 3.71 (3.70); N, 5.18 (4.79)).

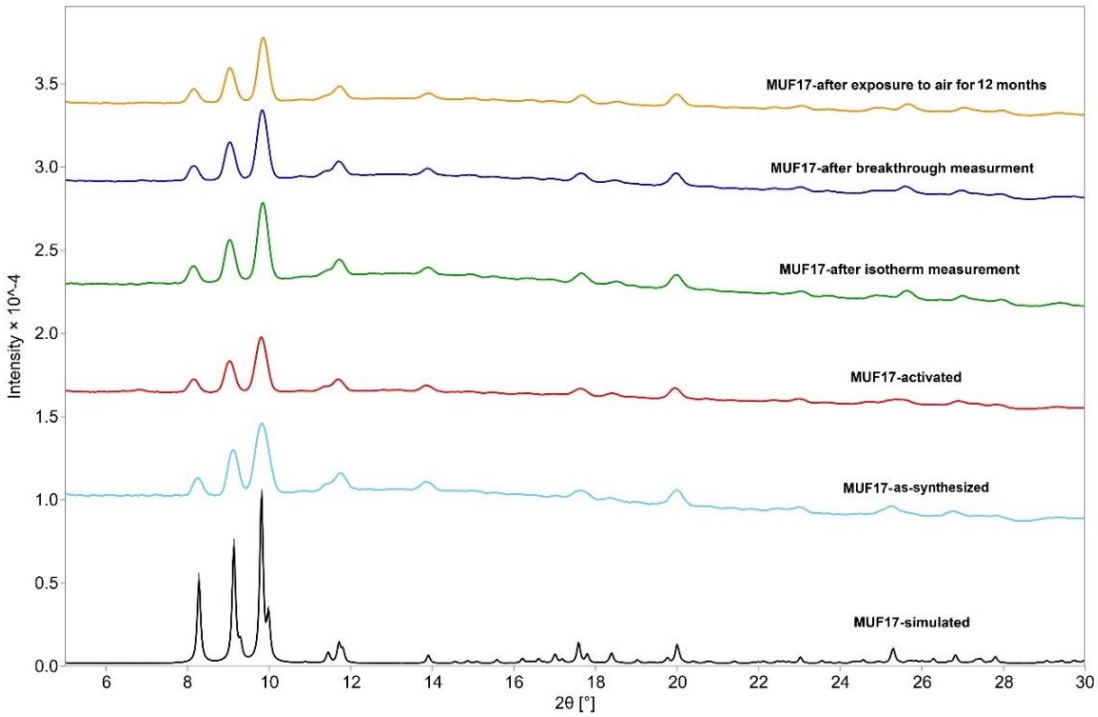

Figure 6.4 PXRD patterns of MUF-17 showing that its structure remains unchanged after activation at 130 °C under vacuum (red), after isotherm measurements (green), after breakthrough experiments (dark blue), and after exposure to air with relative humidity of >80% for at least 12 months (orange).

Thermogravimetric analysis and PXRD demonstrated that MUF-17 decomposes above 300 °C under nitrogen (Figure 6.5), while it is stable when exposed to a laboratory atmosphere (~80% humidity) at ambient temperatures for at least one year (Figure 6.4).

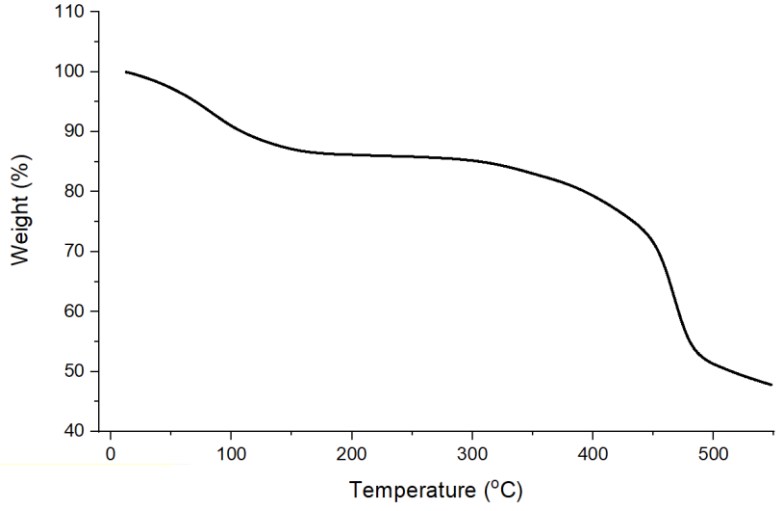

Figure 6.5 TGA curve of MUF-17.

A CO_2 adsorption isotherm at 273 K showed the permanent porosity of MUF-17 and gave a BET surface area of 247 m^2/g and a pore volume of 0.14 cm^3/g (see appendix E for BET calculation). These values are consistent with the geometric surface area of 323 m^2/g and pore volume of 0.20 cm^3/g calculated from the crystallographic coordinates. These data together with pore limiting diameter and largest cavity diameter are presented in Table 6.3

Table 6.3 Some calculated and experimentally determined properties of MUF-17.

Geometric surface area (RASPA2)	323 m^2/g
BET surface area (from experimental CO_2 isotherm/273 K)	247 m^2/g
BET surface area (from experimental N_2 isotherm/77 K)	211 m^2/g
Crystallographic density	1.65 g/cm^3
Pore volume (RASPA2)	0.20 cm^3/g
Pore volume (from experimental CO_2 isotherm/273 K)	0.14 cm^3/g
Largest cavity diameter (Zeo++)	4.63 Å
Pore limiting diameter (Zeo++)	3.15 Å

Based on the high stability, permanent porosity, and suitable pore size and chemistry of MUF-17, we were intrigued by its potential to meet the challenges of separating C_2H_2/C_2H_4 and C_2H_2/CO_2 under ambient conditions. Low pressure C_2H_2, C_2H_4, and CO_2 adsorption isotherms were collected up to 1 bar at different temperatures (Figures 6.6a,b and see appendix E for other temperatures and gases).

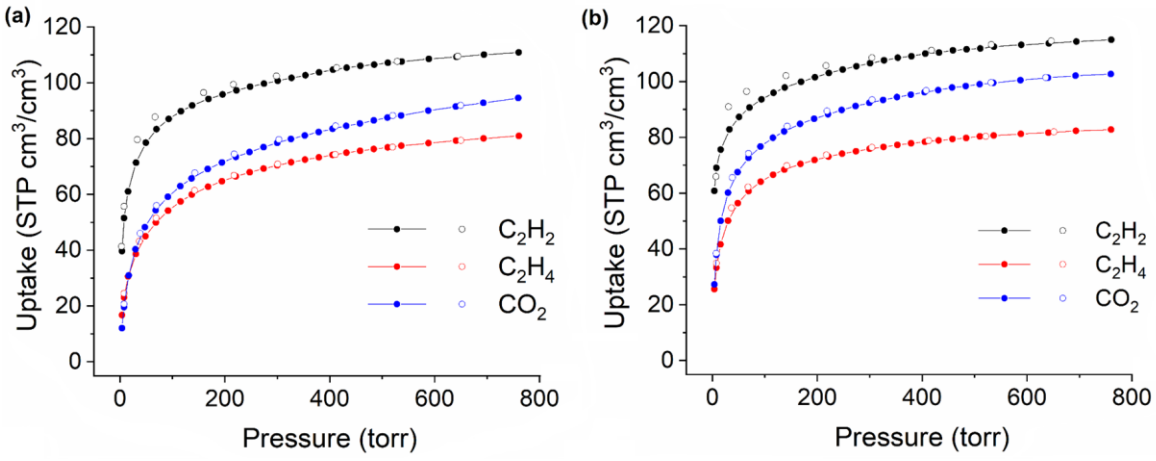

Figure 6.6 Experimental C_2H_2, C_2H_4 and CO_2 adsorption (solid symbols) and desorption (open symbols) isotherms of MUF-17 at (a) 293 K and (b) 273 K.

The adsorption results show that MUF-17 adsorbs considerably more C_2H_2 than C_2H_4 under the same conditions. At 293 K and 1.0 bar, the C_2H_2 uptake of MUF-17 is 111.58 STP

cm^3/cm^3 (3.01 mmol/g, 0.68 C_2H_2 per cobalt, 67.42 STP cm^3/g), while the C_2H_4 uptake is only 79.70 STP cm^3/cm^3 (2.15 mmol/g, 48.16 STP cm^3/g) and the CO_2 uptake is 93.05 cm^3/cm^3 (2.51 mmol/g, 56.22 STP cm^3/g).

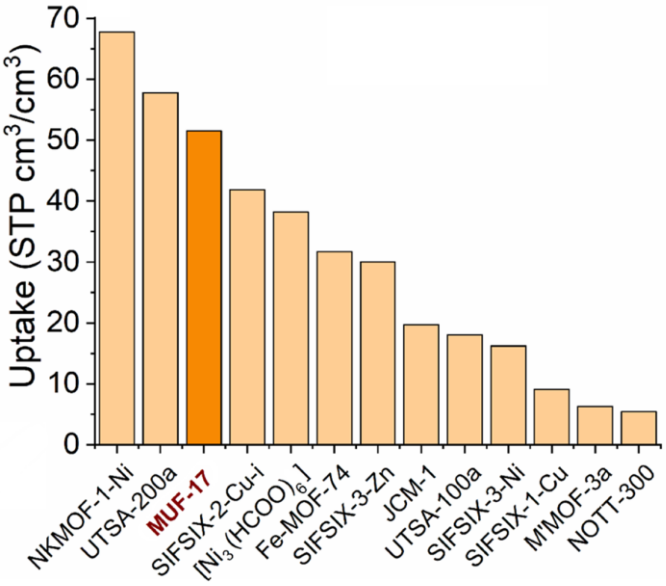

Figure 6.7 C_2H_2 uptake capacity of MUF-17 in comparison with selected reported high-performance materials at 0.01 bar and ambient temperature.

Importantly in the context of gas separations, the C_2H_2 isotherms rise steeply in the low pressure region. For instance, at 293 K and 0.01 bar (7.5 Torr) (which is the indicator of partial pressure of C_2H_2 in industrially encountered C_2H_2/C_2H_4 mixture), the capacity of C_2H_2 reaches 51.53 STP cm^3/cm^3, more than double that of C_2H_4 and CO_2. This exceptional affinity for C_2H_2 at low pressure indicates that MUF-17 has the potential to separate C_2H_2/C_2H_4 and C_2H_2/CO_2 mixtures with high efficiency, including the removal of trace acetylene. At 0.01 bar, MUF-17 adsorbs more C_2H_2 than top-performing materials such as SIFSIX-2-Cu-i[317] (41.9 cm^3/cm^3), Fe-MOF-74[408] (31.7 cm^3/cm^3) SIFSIX-3-Zn[317] (30.0 cm^3/cm^3), UTSA100-a[397] (18.03 cm^3/cm^3) and NOTT-300[401] (5.4 cm^3/cm^3) at ambient temperature and 0.01 bar, and is comparable to that of the benchmark materials UTSA-200a[395] (57.8 cm^3/cm^3) and NKMOF-1-Ni[325] (67.8 cm^3/cm^3) (Figure 6.7). Also, a summary of adsorption metrics of top-performing MOFs in comparison with MUF-17 are presented in Table 6.4.

Table 6.4 The separation parameters of MUF-17 compared with selected MOFs reported in the literature.

MOF	C_2H_2 uptake [a] (cm^3/cm^3)	C_2H_2 uptake at 0.01 bar (cm^3/cm^3)	C_2H_4 uptake [a] (cm^3/cm^3)	CO_2 uptake [a] (cm^3/cm^3)	IAST selectivity [b] (C_2H_2/C_2H_4)	IAST selectivity [b] (C_2H_2/CO_2)	Q_{st} C_2H_2 [c] (kJ/mol)	Q_{st} C_2H_4 [c] (kJ/mol)	Q_{st} CO_2 [c] (kJ/mol)	T (°C)
NOTT-300[401, 409]	162.49	5.39	109.87	138.62	2.4	-	32	16	-	20
SIFSIX-3-Ni[317, 410]	119.01	16.23	63.11	97.73	6.0	-	30.5	30.3	-	25
SIFSIX-1-Cu[317]	164.70	9.10	79.54	98.70	8.3	-	30	23.5	-	25
UTSA-100a[397]	101.58	18.03	39.49	-	19.6	-	22	-	-	23
FeMOF-74[408, 411]	167.98	31.71	153.86	92.31[d]	2.08	-	46	-	-	45
SIFSIX-2-Cu-i[317]	112.01	41.90	61.17	135.47	44.5	-	41.9	30.7	-	25
UTSA-67a[405]	121.46	8.29	66.53	-	4.5	-	32			23
SIFSIX-2-Cu[317]	76.53	3.84	28.73	-	5.0	-	26.3	20.8	-	25
M'MOF-3a[402]	44.73	6.29	9.55	14.91	5.2	8.4	27.1	27.3	40.5	22
JCM-1[321]	101.67	19.68	47.40	50.68	13.2	13.7	36.7	34.2	33.3	25
PCP-33[412]	164.08	6.54	122.47	77.58	2.0	4.6	27.5	24.1	26.2	25
FJU-22a[413]	125.42	38.81	94.13	121.30	-	1.9[f]	23	21.7	19.5	23
UTSA-200a[395]	115.85	57.77	20.00	-	e	e	40	27	-	25
NKMOF-1-Ni[325]	107.51	67.78	81.41	88.42	-	20.0	60	45	41	25
ZJU-196a[324]	108.16	1.46	-	10.23	-	18.0	39	-	-	25
MAF-2[323]	102.21	1.83	-	21.49	-	4.5	33	-	27	25
FJU-90[353]	146.78	6.58	-	88.83	-	4.3	25.1	-	20.7	25
UTSA-74a[322]	144.08	39.32	-	90.05	-	8.0	31.5	-	25.5	25
HOF-3a[320]	20.61	2.12	-	8.96	-	21.0	19.5	-	42	23
$[Ni_3(HCOO)_6]$[352]	164.81	38.20	-	119.18	-	22	41	-	24.8	25
Cu-BTC[305, 319-320]	216.90	24.61	-	124.54	-	5.5	30	-	26.9	25
MFM-188[318]	152.32	8.95	-	79.81	-	3.7	32.5	-	20.8	25
MUF-17	**111.59**	**51.53**	**79.70**	**93.05**	**8.73**	**6.01**	**49.5**	**31.1**	**33.8**	**20**

[a] At a pressure of 1 bar. [b] For an equimolar mixture of C_2H_2/C_2H_4 or CO_2/C_2H_2 and a total pressure of 1 bar. [c] At low loading. [d] At 298 K. [e] Molecular sieving. [f] Determined experimentally.

Motivated by the high uptake and preferential binding of C_2H_2 by MUF-17, the adsorption selectivity towards C_2H_2 in mixtures with C_2H_4 was predicted on the basis of ideal adsorbed solution theory using a range of starting compositions (50/50, 5/95 and 0.1/99.9 C_2H_2/C_2H_4) at 273 and 293 K (Figures 6.8 and see appendix E for the remainder). For 50/50 C_2H_2/C_2H_4 mixtures, the selectivity of MUF-17 at 293 K and 1 bar is 8.73. Although the separation selectivity of MUF-17 is lower than benchmark materials such as SIFSIX-2-Cu-i[317] (41.0) and UTSA-100a[397] (19.6), it is still high and on par with SIFSIX-1-Cu[317] (8.3) and superior to frameworks such as UTSA-67a[405] (4.5), FeMOF-74[408] (2.1), SIFSIX-2-Cu[317] (5.0) and M'MOF-3a[402] (5.2) (Table 6.4). With respect to CO_2, acetylene is found in crude product streams in approximately equimolar ratios with this gas.[414] Therefore, the IAST selectivity was calculated for a 50/50 mixture of C_2H_2/CO_2 and it is also presented in Figure 6.8 (see appendix E for other mixture compositions). This value is 6.01 at 293 K and 1 bar, which is comparable to the previously-reported high-performing MOF UTSA-74a[322] and higher than others such as UTSA-50a,[415] HKUST-1[320] and MFM-188,[318] while it dips below that of NKMOF-1-Ni[325] and $[Ni_3(HCOO)_6]$[352] (Table 6.4). These results imply that MUF-17 can separate C_2H_2 from C_2H_4 and CO_2 under typically-encountered industrial conditions.

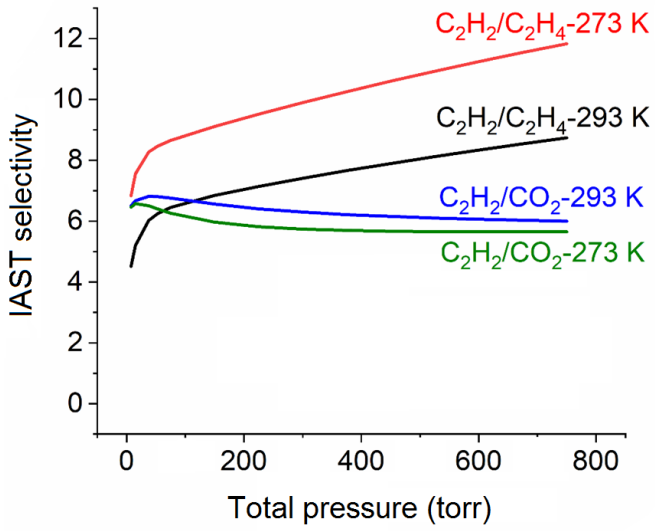

Figure 6.8 Predicted IAST selectivity of MUF-17 for 50/50 C_2H_2/C_2H_4 and C_2H_2/CO_2 mixtures at 293 K and 273 K.

To evaluate the binding strength between MUF-17 and guest molecules, coverage-dependent adsorption enthalpies (Q_{st}) for C_2H_2, C_2H_4 and CO_2 were evaluated from pure component isotherms collected at 273, 288, 293, and 298 K by the implementation of a virial equation (see Appendix E for virial fitting curves). The Q_{st} profiles show values of 49.5, 31.1

and 33.8 kJ/mol for C_2H_2, C_2H_4 and CO_2, respectively, at zero loading. The high Q_{st} of C_2H_2 compared to that of C_2H_4 and CO_2 illustrates that the interaction of MUF-17 with C_2H_2 is energetically more favourable than the other gases. This is only true up to intermediate pressures since the Q_{st} for C_2H_2 decreases with an increase of gas loading. This indicates that MUF-17 presents a range of binding sites with various affinities for C_2H_2. Interestingly, the Q_{st} of C_2H_4 rises at higher pressures, possibly due to interactions between the absorbed gas molecules as the pores fill.

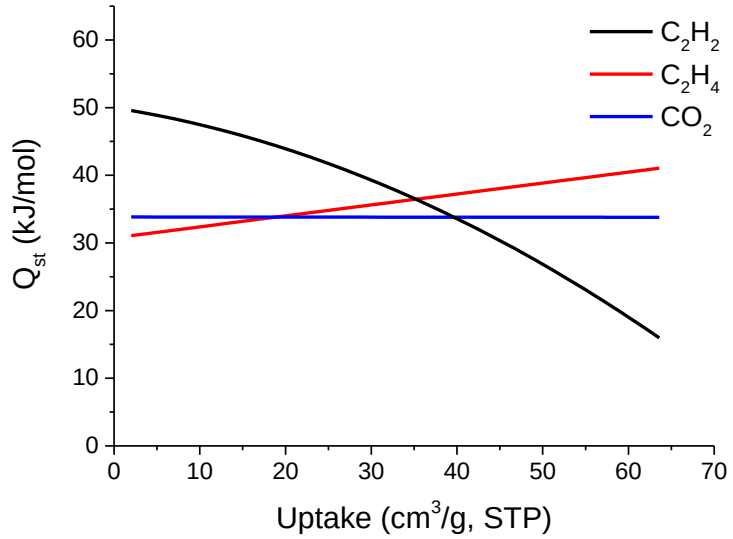

Figure 6.9 Isosteric heat of adsorption plotted as a function of gas uptake for the adsorption of C_2H_2, C_2H_4 and CO_2 by MUF-17.

To gain further insight into the mechanism of adsorption in MUF-17 first-principles dispersion-corrected density functional theory (DFT-D3)[233] calculations were implemented in the software package VASP.[234] The calculated static binding energy for C_2H_2 at its preferred binding site (one guest per unit cell) is around -61.9 kJ/mol, whereas it is −40.4 and -48.6 kJ/mol for C_2H_4 and CO_2, respectively. The stronger host-guest interaction calculated for C_2H_2 are in accord with the earlier Q_{st} values. In the density functional theory optimized host–guest structures, it can be seen that C_2H_2, C_2H_4 and CO_2 are all adsorbed in the narrowest channel neck, but they interact differently with the pore surface. As shown in Figure 6.10a, the C_2H_2 molecules form two strong and three weak electrostatic interactions with MUF-17. Coordinated oxygen atoms of a framework carboxyl group interact with a highly polar hydrogen atom of C_2H_2, through C≡C-H···O hydrogen bonding with a very short distance of 2.34 Å. The carbon atom of the C_2H_2 guest, which carries a partial negative charge, interacts with a hydrogen atom of a coordinated amino group through a C≡C···H-N contact with a separation of 2.46 Å, much shorter than the sum of van der Waals radii of

hydrogen (1.20 Å) and carbon (1.85 Å) atoms. Three other attractive interactions involve the carbon atom of C_2H_2 with hydrogen atoms of the framework. For example, a coordinated amino group forms C≡C···H-N contacts with distances of 4.16 - 4.33 Å (Figure 6.10a).

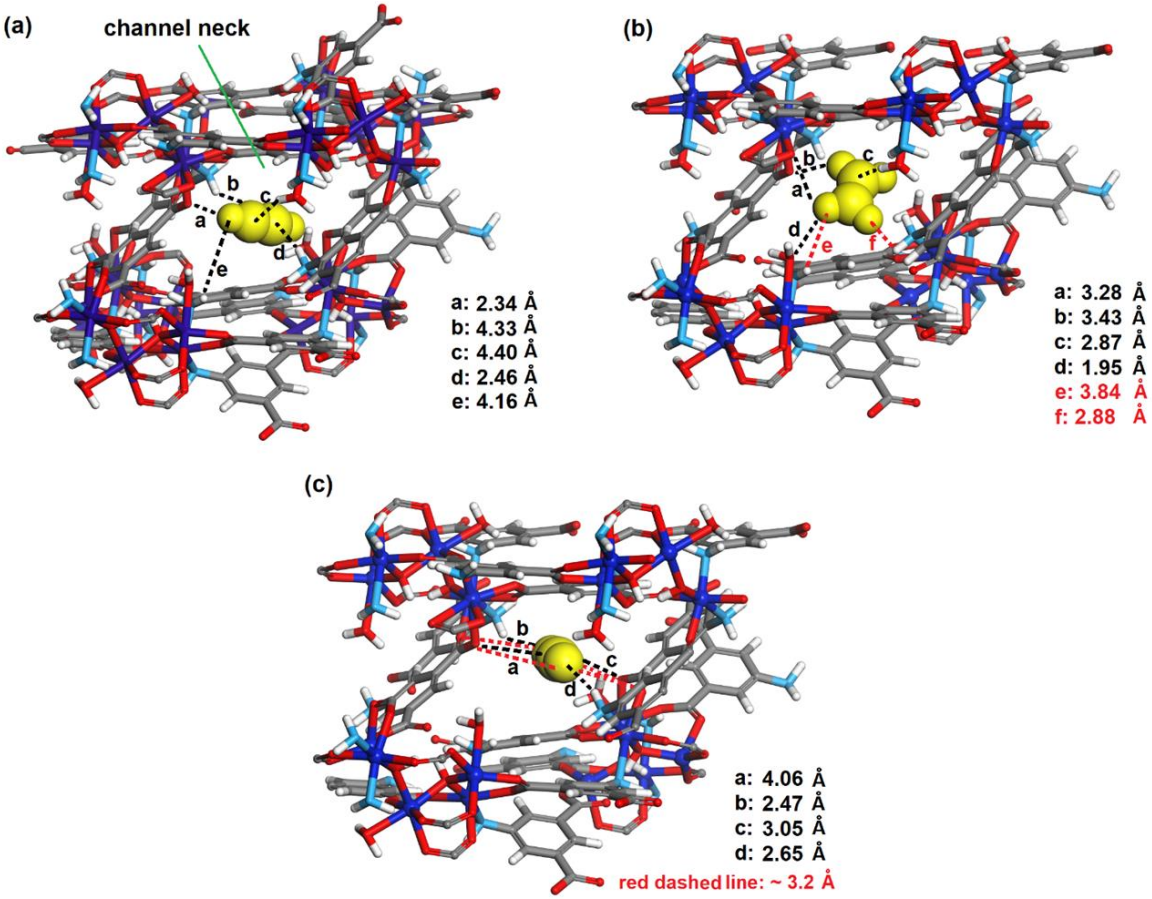

Figure 6.10 Comparison of the preferential (a) C_2H_2, (b) C_2H_4, and (c) CO_2 adsorption sites (Co dark blue, N light blue, O red, C gray, H white) observed by DFT-D3 calculations. Black and red dashed lines indicate attractive and repulsive electrostatic interactions, respectively.

For C_2H_4, the strongest interactions involve a guest CH_2 group and coordinated water at the narrowest channel neck (C=C-H···N) at particularly short distances of 1.95 and 2.87 Å. Weaker interactions involve coordinated oxygen atoms of a carboxyl group (C=C-H···O). These interactions are similar in geometry and type with those observed for C_2H_2. Naturally, the geometry of C_2H_4 prevents its carbon atoms from forming strong C=C···H interactions with the narrow channel neck in the manner of C_2H_2 (Figure 6.10b). Furthermore, there is significant electrostatic repulsion between the partial positive charges of N–H moieties of the two amino groups from the host channel and the hydrogen atoms of the guest C_2H_4 (H···H = 2.85 Å and 3.84 Å). These prevent the guest from assuming a position that would allow further attractive interactions. Evidently, the size and electrostatic characteristics of the pores

play critical roles in distinguishing C_2H_2 and C_2H_4 and underlie the large adsorption enthalpy difference. In the simulated adsorption location of CO_2, the guest carbon atom is located at the centre of the host channel neck in a head-on orientation (Figure 6.10c). Both of its oxygen atoms adopt favourable short contacts with hydrogen atoms of two amino groups (2.47 and 2.67 Å), and its carbon atom interacts on both sides with oxygen atoms of coordinated carboxyl groups (distances of 4.06 and 3.05 Å). Although these host–guest interactions seem relatively strong, they are counteracted by O···O repulsive forces involving the CO_2 oxygen atoms. These atoms are surrounded by four oxygens from two coordinated carboxyl groups at short distances of ~ 3.2 Å.

Based on the promising gas adsorption results, we investigated the feasibility of C_2H_2/C_2H_4 and C_2H_2/CO_2 separations under dynamic conditions. We measured experimental breakthrough curves for 50/50 and 1/99 gas mixtures of C_2H_2/C_2H_4 at 293 K and 1.1 bar. Figure 6.11a shows the relative concentration profile of C_2H_2, C_2H_4 exiting an adsorption bed packed with MUF-17 as a function of time. Complete separation was realized by MUF-17, whereby the C_2H_4 broke through from the column at an early stage because of its low adsorption capacity and affinity for the framework. This occurred after around 10 minutes, which means the uptake of C_2H_4 under these dynamic conditions is 1.10 and 0.55 mmol/g for 1/99 and 50/50 mixtures, respectively. Dynamic capacity of a gas component was obtained by calculating the amount of the gas adsorbed until the breakthrough point and it is usually less than equilibrium capacity because of limited contact time during dynamic breakthrough condition where gas components have lesser time to be adsorbed compared to equilibrium adsorption.

Conversely, the signal of C_2H_2 was not detected for at least 37 and 99 minutes for 50/50 and 1/99 mixtures, respectively. This equates to dynamic uptake capacities of 1.92 and 0.11 mmol/g, respectively. These results indicate that MUF-17 can efficiently trap small quantities of C_2H_2 when it is present in both bulk and trace quantities. Advantageously, the breakthrough trace of C_2H_2 is steep, which arises from the high affinity of MUF-17 for this guest. This indicates the mass transfer zone (the area of the bed in which adsorption is taking place) of C_2H_2 in the adsorption will be narrow, which decreases the unused bed length to maximize the capture efficiency. The C_2H_4 productivity, defined by the amount of this gas with a purity of at least 99.95% that can be produced from an adsorption bed packed with 1 kg of MUF-17 under these conditions, is 192 L.

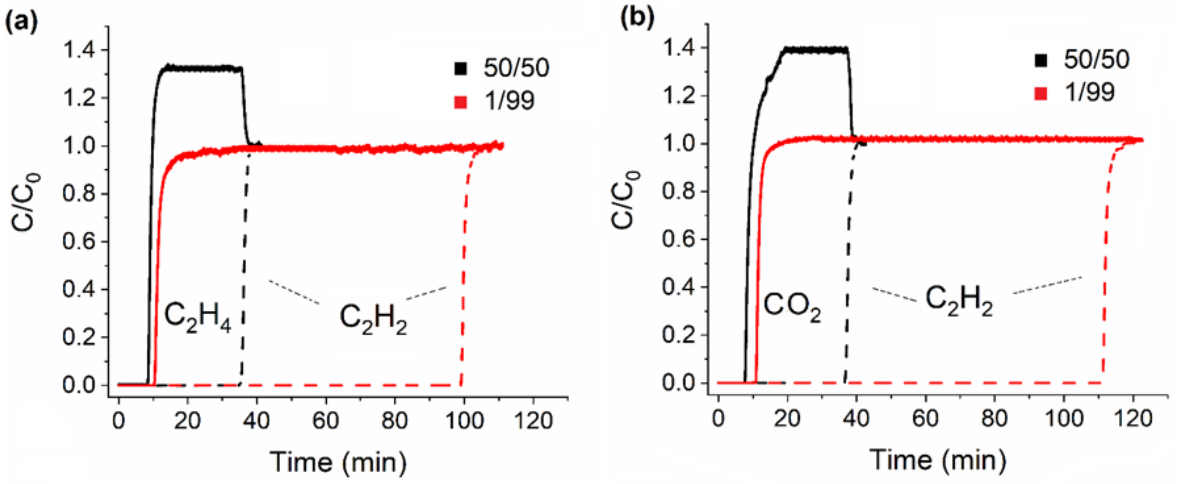

Figure 6.11 (a, b) Experimental breakthrough curves for 50/50 and 1/99 mixtures of C_2H_2/C_2H_4 and C_2H_2/CO_2 at 293 K and 1.1 bar in an adsorption column packed with MUF-17.

Subsequent multiple breakthrough tests revealed that MUF-17 maintains its performance over at least 10 cycles (Figure 6.12a). The full regeneration of MUF-17 was achieved by simply placing it under vacuum or purging with an inert gas. As evident in Figure 6.12b, almost all of the adsorbed C_2H_4 and half of the C_2H_2 can be removed from the bed by purging with helium at 80 °C. The remaining guests can be fully desorbed at 130 °C.

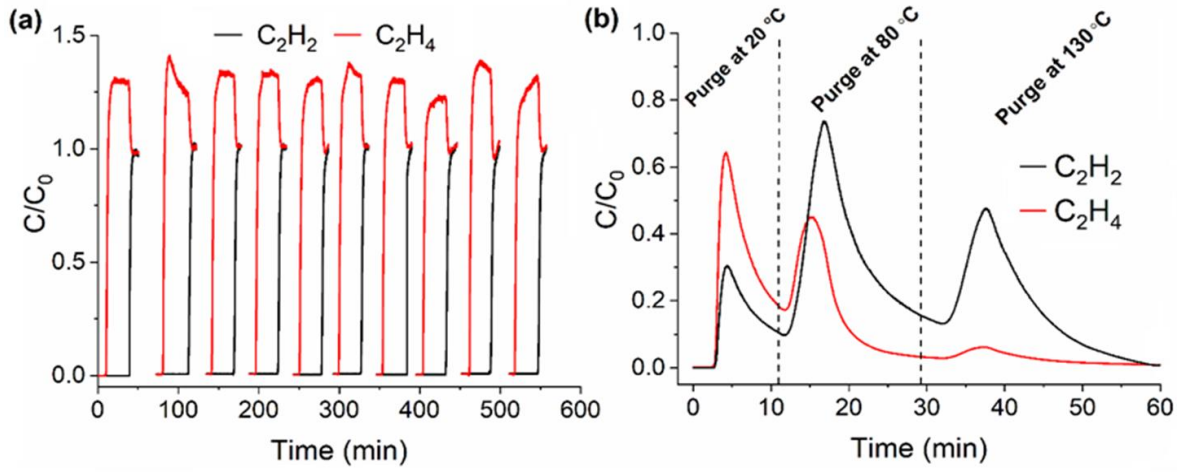

Figure 6.12 (a) C_2H_2/C_2H_4 separation cycles for a 50/50 mixture lasting for 10 cycles. Each separation process was carried out at 293 K and 1.1 bar and MUF-17 was regenerated between cycles in *vacuo* at 60 °C for 40−50 min. (b) Desorption profile of CO_2 and C_2H_2 from a MUF-17 bed upon heating under a helium flow of 5 mL_N/min at 1.1 bar. All of the adsorbates were removed upon heating at various stages up to 130 °C.

The multipurpose capabilities of MUF-17 were experimentally verified by its ability to separate C_2H_2 from an equimolar mixture with CO_2, which mimics typical process conditions (Figure 6.11b).[414] The framework accomplishes this by sequestering the C_2H_2 and

allowing the CO_2 to escape. The long time lag before the acetylene breaks through from the adsorption bed speaks to a high productivity. The dynamic capacity obtained from breakthrough curves were 0.44 and 2.12 mmol/g for CO_2 and C_2H_2, respectively. As expected, the breakthrough performance is further improved when a 1/99 C_2H_2/CO_2 mixture is used as a feed (Figure 6.11b).

The PXRD patterns (Figure 6.4) and C_2H_2 adsorption isotherm of MUF-17 (Figure 6.13) exhibit no notable differences after consecutive adsorption-desorption cycles nor after exposure to air with ~80% humidity for 8 months, in accord with the high stability of MUF-17. Therefore, MUF-17 is relevant to the removal and sequestration of acetylene in practical operating situations.

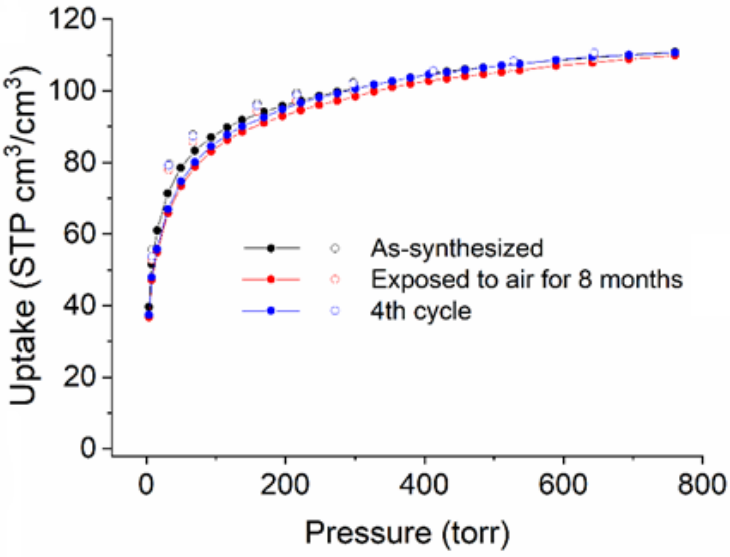

Figure 6.13 C_2H_2 adsorption isotherms (293 K) of MUF-17 after four consecutive adsorption-desorption cycles and after exposing it to air with high humidity for 8 months.

To investigate the elimination of highly dilute quantities of C_2H_2, we simulated breakthrough curves under these conditions. First, the mass transfer coefficient used for the simulated breakthrough curves was empirically tuned to produce a match between the simulated and experimental breakthrough curves. With this realistic mass transfer coefficient in hand, we predicted breakthrough curves using feed compositions comprising 0.1% C_2H_2 in C_2H_4 or CO_2 (Figure 6.14). These calculations revealed MUF-17 eliminates vanishingly small quantities of C_2H_2, as often required in industrial processes.

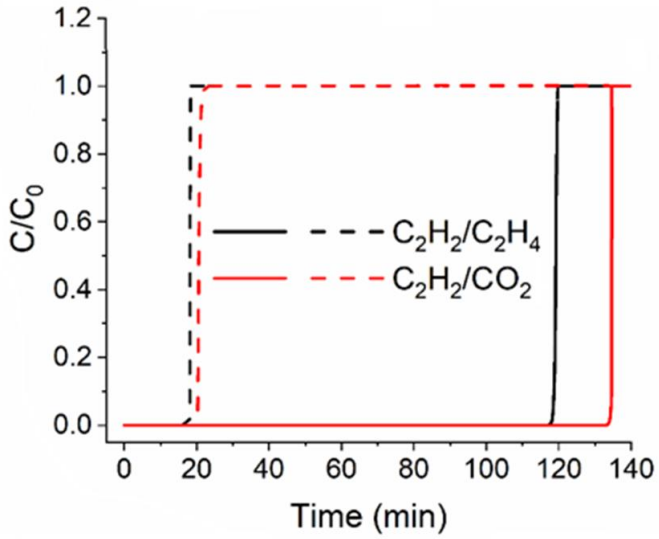

Figure 6.14 Simulated breakthrough curves for 0.1/99.9 mixtures of C_2H_2/C_2H_4 and C_2H_2/CO_2 at 293 K and 1.1 bar.

Taken together, these data reveal MUF-17 to be a highly effective multipurpose acetylene adsorbent. Its capabilities rely on a combination of affinity-based selectivity and uptake capacity. These characteristics arise from its structure, in which relatively large pockets are connected by narrow necks (Figure 6.3). The selectivity for acetylene over the other gases draws from the size and polarity of the neck regions, which provides high levels of discrimination (Figure 6.10). The pockets provide the capacity for significant amounts of acetylene to be sequestered by the framework. These characteristics operate in tandem to underpin the effectiveness of MUF-17.

6.3 Conclusion

MUF-17 efficiently separates C_2H_2 from both C_2H_4 and CO_2. Owing to its unique pore structure and the intimate contact between small guest molecules and the pore necks, MUF-17 exhibits a steep C_2H_2 adsorption isotherm and a high capacity at low pressures. This exceptional affinity arises from ideal structural features: its narrow channel neck is rich with polar residues that are complementary to acetylene in terms of both geometry and electrostatics. The underlying host-guest noncovalent interactions were elucidated by first-principles dispersion-corrected density functional theory calculations. The unique structure of MUF-17 underpins its ability to remove trace acetylene where required, for example in the clean-up of ethylene, or to sequester bulk acetylene in other circumstances, such as the purification of acetylene itself in a typical industrial process. Combining these functional attributes in a single multipurpose material is an attractive step forward, especially when embodied in an inexpensive, robust, stable and recyclable material such as MUF-17.

6.4 Experimental and computational section

6.4.1 General procedures

All starting compounds and solvents were used as received from commercial sources without further purification unless otherwise noted. Elemental analyses were performed by the Campbell Microanalytical Laboratory at the University of Otago, New Zealand. IAST selectivity and heat of adsorption were calculated based on the methods presented in previous sections.

6.4.2 Thermogravimetric Analysis (TGA)

As per Chapter 2. Freshly prepared MOF samples were washed with MeOH, and then activated at 130 °C under vacuum for 18 hours. Samples were exposed to air for few hours and then transferred to an aluminum sample pan, and then measurements were commenced under an N_2 flow with a heating rate of 4 °C /min.

6.4.3 Single crystal X-ray diffraction

As per Chapter 2. All atoms were found in the electron density difference map. Electron density difference maps were carefully analyzed for the possible presence of disordered framework components. All atoms were treated isotropically except metal centres.

6.4.4 Powder X-ray diffraction patterns

As per Chapter 2. The data were obtained from freshly prepared MOF samples that had been washed several times with MeOH..

6.4.5 Gas adsorption measurements

As per Chapter 2.

6.4.6 Physical properties and pore characteristics calculations

The Zeo++[242] code and RASPA2[232] were used to characterize the geometric features of the framework by calculating the pore volume (with the use of a helium probe), surface area (with the use of a H_2 probe), pore limiting diameter and largest cavity diameter. Accelrys Materials Studio 7.0 software package was performed to visualize the MOF structure and pore topology.

6.4.7 BET surface area calculations

The BET surface area was calculated from the both CO_2 adsorption isotherm at 273 K and N2 adsorption isotherms at 77 K according to the procedures presented in Chapter 2. A cross-sectional area of a 21.8 was used for CO_2.

6.4.8 Breakthrough separation experiment

In a typical breakthrough experiment, 1.2 g of activated MUF-17 was placed in an adsorption column (6.4 mm in diameter × 11 cm in length) to form a fixed bed. The adsorbent was activated at 130 °C under high vacuum for 12 hours and then the column was left under vacuum for another 3 hours while being cooled to 20 °C. The column was then purged under a 20 mL_N/min flow of He gas for 1 hr at 1.1 bar prior to the breakthrough experiment. A gas mixture containing either C_2H_2/C_2H_4 or C_2H_2/CO_2 with different compositions along with He as a carrier was introduced to the column at 1.1 bar and 20 °C. A total feed flowrate of 6 mL_N/min was set for the experiments with 50/50 and 1/99 mixtures of gases, and the flowrate of He in the feed was kept constant at 3 mL_N/min for all the experiments. The operating pressure was controlled at 1.1 bar with a back-pressure regulator. The outlet composition was continuously monitored by the mass spectrometer until complete breakthrough was observed. The adsorbent was regenerated under vacuum for 40-50 minutes at 60 °C between each cycle.

Regeneration profile

The desorption behaviour of C_2H_2, CO_2 and C_2H_4 from the adsorption column was also investigated. Once the adsorbent was saturated with an equimolar mixture of C_2H_2/C_2H_4 or C_2H_2/CO_2, the column was purged with a helium flow of 5 mL_N/min for 11 mins at 20 °C at 1 bar, while monitoring the effluent gas. The column was then heated to 80 °C with a ramp of 10 °C/min for 18 mins. Finally, the column was heated to 130 °C with the same ramping rate for 30 min before cooling to 20 °C. A breakthrough measurement was then performed, which showed that the absorbent had been fully regenerated.

6.4.9 Breakthrough curves simulation

Breakthrough curves were simulated based on the procedure presented earlier. Adsorption bed characteristics and other related parameters for simulation are presented in Table 6.5.

Table 6.5 Adsorption column parameters and feed gas metrics used for the simulations for MUF-17.

Adsorption bed	***Feed***
Length: 110 mm Diameter: 6.4 mm Amount of adsorbent in the bed: 1.2 g Bed voidage: 0.85 Adsorbent average radius: 0.05 mm k_{CO2}: 6.12 s^{-1} k_{C2H2}: 5.95 s^{-1} k_{C2H4}: 6.02 s^{-1}	Total flow rate (including He): 6 mL_N/min Temperature: 293 K Pressure: 1.1 bar Carrier gas (He) flow rate: 3 mL_N/min Purge gas: He with a flow rate of 20 mL_N/min

6.4.10 Productivity calculation

The C_2H_4 productivity was defined by the breakthrough amount of ethylene (defined as a volume of gas at STP) from an adsorption bed packed with 1 kg of MOF. The breakthrough amount was calculated by integration of the breakthrough curves (for a mixture of 1/99 C_2H_2/C_2H_4) during a period from t_1 to t_2 during which the C_2H_4 purity is higher than or equal to a threshold value of 99.95%:

$$(C_2H_4)_{\text{Productivity}}: \frac{\int_{t_1}^{t_2} F_{C_2H_4,out}\, dt}{m_{MOF}}$$

Where $F_{C_2H_4,out}$ is the flowrate of effluent ethylene and m_{MOF} is the amount of MOF packed in the bed.

6.4.11 DFT calculations

Static binding energies for guest molecules in the MUF-17 framework were calculated using density functional theory (DFT) as implemented in the software package VASP 5.4.4.[234] It is well-known that standard DFT methods based on generalized gradient approximation do not fully account for the long-range dispersion interactions between the framework and the bound adsorbates. Therefore, to accurately estimate static binding energies for the guest molecules within the MUF-17 framework, we implemented dispersion corrections using DFT-D3 method.[233] Electron exchange and correlation were described using the generalized gradient approximation Perdew, Burke, and Ernzerhof (PBE)[243] form, and the projector-augmented wave potentials were used to treat core and valence electrons. In all cases, we used a plane-wave kinetic energy cutoff of 600 eV and a Gamma-point mesh for sampling the Brillouin zone. The ionic coordinates were relaxed until the Hellman-Feynman ionic forces were less than 0.02 eV/Å. The initial location of the guest molecule (one guest molecule per cell) in MUF-17 was obtained from a classical simulated annealing

technique using classical force fields, as implemented in the sorption module in *Materials Studio.*[244] In the simulated annealing method, the temperature was lowered stepwise, allowing the gas molecule to reach a desirable configuration based on different moves such as rotation, translation and repositioning with preset probabilities of occurrence. This process of heating and cooling the system was repeated over several heating cycles to find the local minima. Forty heating cycles were performed where the maximum temperature and the final temperature were 10^5 K and 100 K, respectively. Static binding energies (ΔE) at 0 K in vacuum were calculated using the following expression

$$\Delta E = E_{MOF+Guest} - E_{MOF} - E_{Guest}$$

Where E_x refers, respectively, to the total energies of the MOF + guest complex, the MOF alone, and the guest molecule.

Chapter 7

Summary and perspectives

7.1 Thesis summary

The study presented in this thesis involves the design, synthesis and evaluation of metal-organic frameworks for gas separation applications with a focus on development of inexpensive and highly stable MOFs. Three families of MOFs were synthesized and characterized followed by a comprehensive evaluation of their performance for a variety of different gas separation applications.

In Chapter 2, a MOF termed MUF-15 was developed showing great potential for producing pure ethane through a single adsorption stage by selectively adsorbing ethane over ethylene. Built from isophthalic acid and cobalt acetate, MUF-15 features three narrow zigzag 1-dimensional channels mainly decorated with phenyl rings. As revealed by DFT calculations and confirmed by gas adsorption studies, an optimal pore dimensions that allowed optimal van der Waals interactions between the guest and the framework surface and the avoidance of built-in regions of high polarity (such as open metal sites) underlie its ethane-selective nature. Owing to these pore characteristics, MUF-15 combines a high uptake capacity and good selectivity, where it exhibits one of the highest productivities amongst materials with reverse selectivity (preference for ethane over ethylene). Additionally, MUF-15 shows a relatively good stability to laboratory atmospheres, is synthesized from inexpensive precursors and maintains its adsorption capacity over multiple adsorption-desorption cycles. Remarkably, heat of adsorption calculations revealed MUF-15 has a moderate heat of adsorption which enables a facile regeneration by purging at moderate temperatures or *in vacuo* over a short period of time. Taken together, these attributes represent a significant addition to the portfolio of known C_2H_6-selective MOFs. Also, a clear illustration of how such selectivity may be achieved using straightforward components are presented which can defines the way forward to design materials for challenging separations.

Suitable pore characteristics and chemistry of MUF-15 motivated us to investigate the effect of different ligand functional groups on its structural properties and gas separation performance. From the crystal structure of MUF-15, the hydrogen atom of the 5-position of the isophthalate phenyl ring is positioned towards the pore aperture. Therefore, substituting

it with different functional groups might drastically change the pore characteristics and adsorption performance of MUF-15. Hence, in Chapter 3, six different groups (fluoro, hydroxy, bromo, nitro, methyl and methoxy) representing a broad range of sizes and functionalities, were substituted into the structure of MUF-15 to produce six isostructural analogues. As anticipated, the introduction of these functionalities greatly changed the stability and gas sorption behaviour of these MOFs. Generally, these groups reduced the surface area and pore volumes, but had a diverse impact in framework stability. Furthermore, selectivity of ethane over ethylene also decreased or reversed upon functionalization, as most of these functionalities enhance the polarity of the surface which favours the adsorption of ethylene.

Surprisingly, MUF-21 (functionalized by a nitro group) and MUF-23 (functionalized by a methoxy group) showed flexibility upon inclusion of guest molecules such as C_2H_2, CO_2, C_2H_4 and C_2H_6 at ambient conditions. We believe this flexibility originates from the rotation of phenyl rings upon the inclusion of guest molecules, thus opening up more space. We also hypothesize that MUF-15 and its isoreticular analogues all have flexible structures varying in their gate opening pressures and temperatures. MUF-21 was further investigated to see the effect of flexibility on its separation performance. A combination of predicted and experimental gas breakthrough measurements proved that gate opening phenomena improves the performance of MUF-23 to efficiently separate CO_2 from N_2.

Additionally, MUF-22 (functionalized by a methyl group) and MUF-23 (functionalized by a methoxy group) indicated extraordinary stability upon exposure to a humid air mostly because of the hydrophobic nature of these groups and shielding of the SBUs from incoming H_2O molecules.

In Chapter 4, we introduced the MUF-16 family. It is a series of isostructural MOFs built up from 5-aminoisophthalic acid and a divalent metal ion: cobalt (MUF-16), manganese (MUF-16(Mn)) or nickel (MUF-16(Ni)). We found that the structures of MUF-16 and MUF-16(Mn) had previously been reported.[303-304] We added the nickel version of MUF-16 to this family and developed a synthesis procedure for MUF-16 to afford a higher yield, shorter reaction time and milder synthesis condition. These frameworks feature narrow one-dimensional channels with a pore windows of about 3.1 × 5.9 $Å^2$ decorated with amino functionalities and non-coordinated carboxylate groups.

The MUF-16 family features a pore size that perfectly matches the size of CO_2 molecules (3.33 × 3.18 × 5.36 $Å^3$). This combines with an optimal distribution of electrostatic forces on the pore surface to enable high levels of CO_2 adsorption. Single-crystal studies of samples loaded with CO_2 was successfully conducted to determine binding location of the CO_2

molecules in MUF-16. This revealed that the adsorbed CO_2 molecules are orientated in a way that perfectly surrounded by favourable adsorption sites both in the corners and middle of the pores. The oxygen atoms of one of the CO_2 guest molecules forms close N-H···O and C-H···O interactions with the phenyl and amino functionalities of the Haip ligand. Similarly, the carbon atom of adsorbed CO_2 molecule forms a C···O interaction with an oxygen atom of uncoordinated carboxylate group.

The electrostatic properties of the pore surface of MUF-16 family as well as its suitable pore dimension motivated us to investigate its performance for separating CO_2 from different gas mixtures in Chapter 5. As revealed by gas adsorption measurements, MUF-16 exhibited appreciable selectivity for CO_2 by taking up significant amount of CO_2, while adsorbing near-zero amounts of C2 hydrocarbons. This material sets a benchmark for MOFs that are selective for CO_2 over C2 hydrocarbons. In the context of CO_2/C2 hydrocarbons separation, the favourable orientation of electrostatic potential in the pore surface has amplifies the small difference between CO_2 and C2 hydrocarbons that have opposite electrostatic distributions, i.e., C2 hydrocarbons have quadrupole moment of different signs to CO_2. This results in an attractive interaction of CO_2 molecules and thus a high adsorption amount. On the other hand, the interaction of C2 hydrocarbons with the framework is repulsive, resulting in negligible adsorption. For the case of CO_2/N_2 and CO_2/CH_4, the same mechanism is applied. The combined effect of the small pore size of MUF-16 and the weaker interaction of N_2 and CH_4 with framework leads to a negligible adsorption of these gases.

The efficiency of MUF-16 for separating CO_2 from C2 hydrocarbon, CH_4+C_2H_6 and N_2 was well demonstrated by breakthrough experiments. Complete separation was achieved by very early breaking through of N_2, CH_4 and C2 hydrocarbons, while CO_2 was adsorbed on the bed at nearly its equilibrium capacity. The ability of MUF-16 to capturing CO_2 directly from air was also investigated via breakthrough experiments. MUF-16 could not completely eliminate the 400 ppm of CO_2 from the air mostly because of co-adsorption of water by the framework.

Pelletization of MUF-16 also was successfully achieved by incorporating a polymeric PVDF binder. In addition, MUF-16 is built up from inexpensive reactants and indicated an easy regeneration and excellent recyclability. Surprisingly, MUF-16 exhibited an extraordinary water stability, where it maintains its adsorption capacity upon exposure to humid environment for a long time and immersion in water. Therefore, MUF-16 shows great potential in the practical separation of CO_2 from different gas streams.

Finally, in Chapter 6, we introduced a MOF termed MUF-17 which efficiently separates C_2H_2 from both C_2H_4 and CO_2. MUF-17 also was synthesized from the same ligand (5-

aminoisophthalic acid) and metal salt (cobalt acetate) that was used for the synthesis of MUF-16 under different synthesis conditions and with different ligand/metal salt ratios. Therefore, the end price of this MOF is also expected to be quite cheap. Single-crystal structure determination revealed that MUF-17 is a porous coordination polymer featuring narrow zigzag 1-dimensional pores including relatively large cavities with pore aperture size of 4.7 × 4.8 Å. Adsorption isotherm measurements followed by selectivity calculations demonstrated that MUF-17 is capable of efficiently adsorbing acetylene over ethane and CO_2 with steep isotherms and high capacities at low pressures of acetylene. The underlying host-guest noncovalent interactions were elucidated by first-principles dispersion-corrected density functional theory calculations, where it was revealed that its narrow channel neck which is rich with polar residues are complementary to acetylene in terms of both geometry and electrostatics. MUF-17 thus adsorbs significant amounts of acetylene especially at low pressures.

The efficiency of MUF-17 for separating acetylene from both CO_2 and ethylene was successfully demonstrated by breakthrough experiments and simulated breakthrough curves. Moreover, MUF-17 is extremely stable when exposed to humid atmosphere and maintains its adsorption capacity upon several adsorption-desorption cycles. Combining these functional attributes in a single multipurpose material is an attractive step forward for designing efficient materials for challenging gas separation applications.

7.2 Perspectives and future directions

7.2.1 Propane/propylene separations with MUF-15 family

In Chapters 2 and 3, the MUF-15 family was presented as efficient set of materials with relatively small pore window apertures and pore surfaces decorated with aromatic or aliphatic moieties (phenyl rings) . Such pore surfaces favour the adsorption of highly polarizable molecules such as ethane over polar gases like ethylene. C_2H_6-selective MOFs are significantly more important than C_2H_4-selective MOFs since high-purity C_2H_4 is afforded directly through a single adsorption step, simplifying the process and resulting in an increase in productivity. Another important olefin/paraffin mixture that is in high demand to be separated is propane/propylene.[95, 126, 205, 416] Pure propylene may be produced by selectively adsorbing propane. The MUF-15 family could be a great choice to do this because of the similar properties of this mixture with ethane/ethylene mixtures. To best of our knowledge, if the MUF-15 family adsorbs propane over propylene it would be the first material in the literature with such an adsorption behaviour.

7.2.2 Investigating the flexibility of other members of MUF-15 family

As was revealed by gas sorption studies followed by PXRD measurements under vacuum, two members of MUF-15 family namely MUF-21 (functionalized by nitro group) and MUF-23 (functionalized by methoxy groups) exhibited flexibility upon inclusion of different gas molecules under ambient conditions (pressure from 0.1 to 1 bar and temperatures from 263 K to 293 K) or under vacuum. Later, a sign of flexibility in MUF-15 was observed by a slight structural change upon exposure to some solvents such as DMF and DEF. The flexible nature of MUF-15 was afterwards confirmed by measuring PXRD patterns under vacuum.

However, we did not see any sign of flexibility for the other members - including the parent MOF - based on their adsorption isotherms. As three members of this family have shown flexible nature, there is some promise that the remainder also might have some extent of flexibility. Hence, as a future work, this family can be comprehensively investigated for their flexibility by measuring isotherms at high pressure, lower temperatures or exposure to different guest molecules or solvents. PXRD measurement at different pressures and neutron diffraction studies are helpful techniques to understand the flexibility, and host-guest interaction of these frameworks.

7.2.3 Synthesis of MUF-15 with other interesting substituents and investigation of their gas separation performance

In Chapter 3, we substituted the hydrogen atoms of phenyl groups with six different functional groups. As these substituents are pointing towards the pore surface of framework, they significantly change the pore dimensions and electrostatics. Hence, further attempts can be made to introduce other interesting functional groups such as amino groups (highly polar) or ethyl groups (relatively large). These functionalities can greatly alter the pore characteristics of these frameworks and thus boost their separation performance in interesting ways.

Four of isophthalate ligands functionalized by ethyl, thiol, iodo and boronic acid groups are presented in Figure 7.2. As these functionalities have different sizes and electrostatic properties, their introduction into the pore structure of MUF-15 can be interesting to improve the separation performance of MUF-15. All of these linkers are also commercially available.

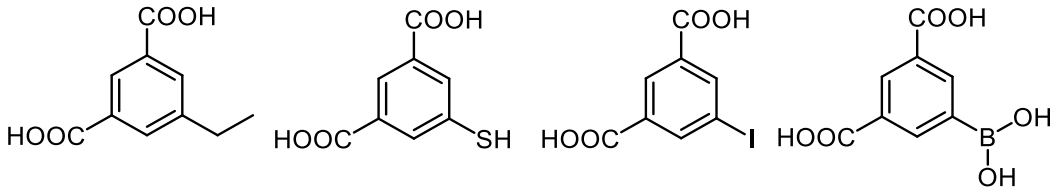

Figure 7.1 Some possible functionalized isophthalate substituents for the synthesis of MUF-15.

Additionally, other linkers with the same linking geometry of isophthalic acid might be able to be substituted in the structure of MUF-15. In this way, a MOF with the same topology as MUF-15 but larger pores with higher surface area and pore volumes can be achieved. Three possible ligands are presented in Figure 7.1.

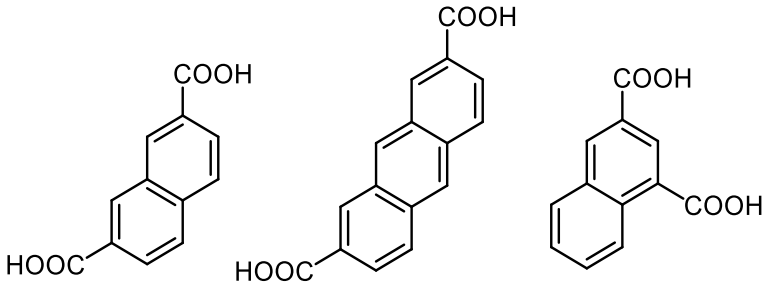

Figure 7.2 Three possible substituents for the synthesis of MUF-15.

As these linkers are consist of phenyl rings (aromatic moieties) they can improve ethane/ethylene selectivity of MUF-15 through stronger interaction of ethane with the framework. It should be noted that incorporation of these linkers might drastically increase the pore dimension of MUF-15 and thus weaken the overall strength of the interaction between guest molecules and the frameworks. These linkers are all commercially available and can be purchased from available providers.

7.2.4 Investigation of MUF-16 family separation performance in presence of water and H_2S

As was demonstrated in Chapter 5, MUF-16 loses its CO_2 adsorption capacity during direct air capture experiments. Here, the ratio of water content (0.01-0.03 mole fraction) to CO_2 content (400 ppmv) in air is extremely high. These water molecules occupy adsorption sites within the framework, thus leading to near-zero adsorption of CO_2. MUF-16 was successfully applied for post-combustion capture processes and natural gas upgrading but this assumed there exists only CO_2, N_2, CH_4 and C_2H_6 and not any other impurities such as

water vapor and H_2S. In the context of CO_2/N_2 separation for post-combustion processes there exists around 10% water vapor and 14% CO_2. Although the ratio of CO_2/water is not comparable with direct air capture processes, it still seems that water vapour greatly influences the adsorption capacity of MUF-16. So as future work, breakthrough curves for CO_2/N_2 separation can be performed in the presence of water to investigate the feasibility of using MUF-16 under simulated process conditions. In the case of CO_2/CH_4 separation for natural gas upgrading, small quantities of H_2S exist in the raw feed that need to be removed. H_2S might have two negative effects: Similar to water, it might occupy adsorption sites and reduce the adsorption of CO_2. Or it may damage the porosity of the framework by collapsing its structure.[417] Thus it is necessary to investigate the effect of H_2S on separation performance of MUF-16 in natural gas processing applications.

7.2.5 Large-scale synthesis of MUF-16 family using less solvents and under milder synthesis conditions

The largest scale we synthesized MUF-16 was one gram in a single batch. To investigate the application of MUF-16 for industrial adsorption processes such as PSA and TSA, a larger amount of material is required. So it is of great importance to synthesize the MOF on large scales. As future work, the feasibility of synthesizing MUF-16 on a kilogram scale or more can be explored. For this, designing synthetic methods with milder synthesis conditions (near room temperature and atmospheric pressures) are critical. Additionally, synthesis methods using less amount of solvents are highly recommended as an environmentally friendly approach. It is notable that solvent free methods for synthesizing MOFs have gained significant attention recently.[58]

7.2.6 A comprehensive comparison of MUF-16 family with current industrial adsorbent for carbon capture processes and natural gas upgrading

Currently, MUF-16 has been compared with current CO_2 selective MOFs for carbon capture processes and natural gas upgrading in terms of their uptake capacity, IAST selectivity, uptake ratio and heat of adsorption, separately. The design of an efficient adsorptive separation units including PSA, TSA and VSA combines the effects of all of those metrics. For example, for an optimal TSA process, besides a high adsorption capacity and selectivity, a MOF should possess a moderate heat of adsorption to enable a facile regeneration. Furthermore, it should have a fast kinetics (a high adsorption rate or mass transfer coefficient) where it minimizes the unused length of the adsorbent bed. This is reflected by steep breakthrough curves. Additionally, all of these metrics together dictate the

energy efficiency and productivities of the unit and they need to be considered together to assess the performance of a porous material. Thus, as future work, reported materials can be compared with MUF-16 through a comprehensive analysis considering the effect of all of these metrics simultaneously.

7.2.7 Exploring separations of C3 hydrocarbons (propane/propylene and propyne/propylene) with MUF-17

As was discussed in Chapter 6, MUF-17 features one-dimensional channels including relatively large cavities that are connected to each other by narrow channels. These narrow channel necks are rich with highly polar residues. Such pore characteristics promise two possible applications of MUF-17 for gas separations. Separating highly polar gases from gases with lower polarity and separating smaller gases from larger gases through molecular sieving of them by channel neck windows. Therefore, this MOF can be a potential material for separating highly polar propylene from propane and/or propyne from propylene to produce polymer grade propylene. Furthermore, these gases can be separated based on the difference in their molecular size which again MUF-17 can be an efficient material because of its narrow channel necks that can act as molecular sieve.

7.2.8 Neutron powder diffraction studies for better understanding of host-guest interactions in MUF-15 and MUF-17 and X-ray diffraction studies of flexible MOFs

The underlying mechanism behind the ethane-selective nature of MUF-15 and acetylene-selective nature of MUF-17 was investigated through DFT calculations. As a future work, these materials can be loaded with these gases and then analyzed by neutron diffraction studies to achieve a better understandings of the guest binding conformation in the frameworks. Such valuable information can be a great help to design efficient materials for gas separation applications. In the context of flexible MOFs, PXRD studies can be performed at different pressures and temperatures to address the breathing behaviour of those MOFs. Neutron powder diffraction analysis as well as SCXRD studies also can be performed to solve the structure of flexible MOFs before and after breathing points. Some preliminary neutron powder diffractions analysis has initiated by our collaborators on MUF-23, however sensible conclusions from these measurements were precluded by crystallographic disorder.

7.2.9 The applicability of high-throughput screening of MOFs for gas separation applications

Apparently, combination of isophthalate ligands and cobalt clusters can results in MOFs with interesting gas adsorption behaviour and gas separation performance. High-throughput screening of MOFs through computational techniques can be an interesting tool to discover new MOFs with the same or close characteristics of MUF-15, MUF-16 or MUF-17. These tools along with deep understanding of adsorption mechanism in mentioned MOFs also can be exploited to explore huge library of known MOFs to find even better materials with enhanced adsorption capability and separation performance.

7.2.10 Incorporation of MUF-15, MUF-16 and MUF-17 in mixed matrix membranes

Membrane technologies are one of the most energy-efficient and operationally easy processes that can be sometimes alternatively used instead of adsorption column separation processes.[129, 418] In the context of MOFs, instead of being packed into an adsorption column, they can be incorporated into or used as membranes in two ways: MOF membranes where MOFs grow into a membrane shapes using a support and mixed matrix membranes where they are incorporated into a polymeric media.[419-420] All of the MUF-15 family, MUF-16 family and MUF-17 can be explored for their applicability as components of polymer-based mixed-matrix MOF membranes in the future.

References

1. Moghadam, P. Z.; Li, A.; Wiggin, S. B.; Tao, A.; Maloney, A. G. P.; Wood, P. A.; Ward, S. C.; Fairen-Jimenez, D., Development of a Cambridge Structural Database Subset: A Collection of Metal–Organic Frameworks for Past, Present, and Future. *Chem. Mater.* **2017,** *29* (7), 2618-2625.
2. Batten, S. R.; Champness, N. R.; Chen, X.-M.; Garcia-Martinez, J.; Kitagawa, S.; Öhrström, L.; O'Keeffe, M.; Suh, M. P.; Reedijk, J., Terminology of metal–organic frameworks and coordination polymers (IUPAC Recommendations 2013). *Pure Appl. Chem.* **2013,** *85* (8), 1715-1724.
3. Li, H.; Eddaoudi, M.; O'Keeffe, M.; Yaghi, O. M., Design and synthesis of an exceptionally stable and highly porous metal-organic framework. *Nature* **1999,** *402* (6759), 276-279.
4. Caskey, S. R.; Wong-Foy, A. G.; Matzger, A. J., Dramatic Tuning of Carbon Dioxide Uptake via Metal Substitution in a Coordination Polymer with Cylindrical Pores. *J. Am. Chem. Soc.* **2008,** *130* (33), 10870-10871.
5. Mason, J. A.; Sumida, K.; Herm, Z. R.; Krishna, R.; Long, J. R., Evaluating metal-organic frameworks for post-combustion carbon dioxide capture via temperature swing adsorption. *Energy Environ. Sci.* **2011,** *4* (8), 3030-3040.
6. McDonald, T. M.; Mason, J. A.; Kong, X.; Bloch, E. D.; Gygi, D.; Dani, A.; Crocella, V.; Giordanino, F.; Odoh, S. O.; Drisdell, W. S.; Vlaisavljevich, B.; Dzubak, A. L.; Poloni, R.; Schnell, S. K.; Planas, N.; Lee, K.; Pascal, T.; Wan, L. F.; Prendergast, D.; Neaton, J. B.; Smit, B.; Kortright, J. B.; Gagliardi, L.; Bordiga, S.; Reimer, J. A.; Long, J. R., Cooperative insertion of CO2 in diamine-appended metal-organic frameworks. *Nature* **2015,** *519* (7543), 303-308.
7. Qazvini, O. T.; Babarao, R.; Shi, Z.-L.; Zhang, Y.-B.; Telfer, S. G., A Robust Ethane-Trapping Metal–Organic Framework with a High Capacity for Ethylene Purification. *J. Am. Chem. Soc.* **2019,** *141* (12), 5014-5020.
8. Férey, G.; Mellot-Draznieks, C.; Serre, C.; Millange, F.; Dutour, J.; Surblé, S.; Margiolaki, I., A Chromium Terephthalate-Based Solid with Unusually Large Pore Volumes and Surface Area. *Science* **2005,** *309* (5743), 2040-2042.
9. Cavka, J. H.; Jakobsen, S.; Olsbye, U.; Guillou, N.; Lamberti, C.; Bordiga, S.; Lillerud, K. P., A New Zirconium Inorganic Building Brick Forming Metal Organic Frameworks with Exceptional Stability. *J. Am. Chem. Soc.* **2008,** *130* (42), 13850-13851.
10. Buser, H. J.; Schwarzenbach, D.; Petter, W.; Ludi, A., The crystal structure of Prussian Blue: Fe4[Fe(CN)6]3.xH2O. *Inorg. Chem.* **1977,** *16* (11), 2704-2710.
11. Hoskins, B. F.; Robson, R., Infinite polymeric frameworks consisting of three dimensionally linked rod-like segments. *J. Am. Chem. Soc.* **1989,** *111* (15), 5962-5964.
12. Hoskins, B. F.; Robson, R., Design and construction of a new class of scaffolding-like materials comprising infinite polymeric frameworks of 3D-linked molecular rods. A reappraisal of the zinc cyanide and cadmium cyanide structures and the synthesis and structure of the diamond-related frameworks [N(CH3)4][CuIZnII(CN)4] and CuI[4,4',4",4"'-tetracyanotetraphenylmethane]BF4.xC6H5NO2. *J. Am. Chem. Soc.* **1990,** *112* (4), 1546-1554.
13. Li, H.; Eddaoudi, M.; O'Keeffe, M.; Yaghi, O. M., Design and synthesis of an exceptionally stable and highly porous metal-organic framework. *nature* **1999,** *402* (6759), 276.
14. Chui, S. S.-Y.; Lo, S. M.-F.; Charmant, J. P.; Orpen, A. G.; Williams, I. D., A chemically functionalizable nanoporous material [Cu3 (TMA) 2 (H2O) 3] n. *Science* **1999,** *283* (5405), 1148-1150.

15. Park, H. J.; Suh, M. P., Mixed‐Ligand Metal–Organic Frameworks with Large Pores: Gas Sorption Properties and Single‐Crystal‐to‐Single‐Crystal Transformation on Guest Exchange. *Chem. Eur. J.* **2008,** *14* (29), 8812-8821.
16. Zhou, H.-C.; Long, J. R.; Yaghi, O. M., Introduction to Metal–Organic Frameworks. *Chem. Rev.* **2012,** *112* (2), 673-674.
17. Farha, O. K.; Eryazici, I.; Jeong, N. C.; Hauser, B. G.; Wilmer, C. E.; Sarjeant, A. A.; Snurr, R. Q.; Nguyen, S. T.; Yazaydın, A. Ö.; Hupp, J. T., Metal–Organic Framework Materials with Ultrahigh Surface Areas: Is the Sky the Limit? *J. Am. Chem. Soc.* **2012,** *134* (36), 15016-15021.
18. Ma, S.; Zhou, H.-C., Gas storage in porous metal–organic frameworks for clean energy applications. *Chem. Commun.* **2010,** *46* (1), 44-53.
19. Ricco, R.; Pfeiffer, C.; Sumida, K.; Sumby, C. J.; Falcaro, P.; Furukawa, S.; Champness, N. R.; Doonan, C. J., Emerging applications of metal–organic frameworks. *CrystEngComm* **2016,** *18* (35), 6532-6542.
20. Yang, R. T.; Yang, R. T., Adsorbents: fundamentals and applications. **2003**.
21. Xu, R.; Pang, W.; Yu, J.; Huo, Q.; Chen, J., *Chemistry of zeolites and related porous materials: synthesis and structure*. John Wiley & Sons: 2009.
22. Bansal, R. C.; Goyal, M., *Activated carbon adsorption*. CRC press: 2005.
23. Ma, S., Gas adsorption applications of porous metal–organic frameworks. *Pure Appl. Chem.* **2009,** *81* (12), 2235-2251.
24. Li, J.-R.; Sculley, J.; Zhou, H.-C., Metal–Organic Frameworks for Separations. *Chem. Rev.* **2012,** *112* (2), 869-932.
25. Roques, N.; Mugnaini, V.; Veciana, J., Magnetic and porous molecule-based materials. In *Functional Metal-Organic Frameworks: Gas Storage, Separation and Catalysis*, Springer: 2009; pp 207-258.
26. Huang, Y.-G.; Jiang, F.-L.; Hong, M.-C., Magnetic lanthanide–transition-metal organic–inorganic hybrid materials: From discrete clusters to extended frameworks. *Coord. Chem. Rev.* **2009,** *253* (23-24), 2814-2834.
27. Allendorf, M.; Bauer, C.; Bhakta, R.; Houk, R., Luminescent metal–organic frameworks. *Chem. Soc. Rev.* **2009,** *38* (5), 1330-1352.
28. Lustig, W. P.; Mukherjee, S.; Rudd, N. D.; Desai, A. V.; Li, J.; Ghosh, S. K., Metal–organic frameworks: functional luminescent and photonic materials for sensing applications. *Chem. Soc. Rev.* **2017,** *46* (11), 3242-3285.
29. Kitagawa, S.; Matsuda, R., Chemistry of coordination space of porous coordination polymers. *Coord. Chem. Rev.* **2007,** *251* (21-24), 2490-2509.
30. Uemura, T.; Yanai, N.; Kitagawa, S., Polymerization reactions in porous coordination polymers. *Chem. Soc. Rev.* **2009,** *38* (5), 1228-1236.
31. Kawamichi, T.; Haneda, T.; Kawano, M.; Fujita, M., X-ray observation of a transient hemiaminal trapped in a porous network. *Nature* **2009,** *461* (7264), 633.
32. Yaghi, O. M.; O'keeffe, M.; Ockwig, N. W.; Chae, H. K.; Eddaoudi, M.; Kim, J., Reticular synthesis and the design of new materials. *Nature* **2003,** *423* (6941), 705.
33. Wang, Z.; Cohen, S. M., Postsynthetic modification of metal–organic frameworks. *Chem. Soc. Rev.* **2009,** *38* (5), 1315-1329.
34. Tanabe, K. K.; Cohen, S. M., Postsynthetic modification of metal–organic frameworks—a progress report. *Chem. Soc. Rev.* **2011,** *40* (2), 498-519.
35. Moreau, F.; Kolokolov, D. I.; Stepanov, A. G.; Easun, T. L.; Dailly, A.; Lewis, W.; Blake, A. J.; Nowell, H.; Lennox, M. J.; Besley, E.; Yang, S.; Schröder, M., Tailoring porosity and rotational dynamics in a series of octacarboxylate metal-organic frameworks. *Proceedings of the National Academy of Sciences* **2017,** *114* (12), 3056-3061.
36. Chen, K.-J.; Madden, D. G.; Pham, T.; Forrest, K. A.; Kumar, A.; Yang, Q.-Y.; Xue, W.; Space, B.; Perry IV, J. J.; Zhang, J.-P.; Chen, X.-M.; Zaworotko, M. J., Tuning

Pore Size in Square-Lattice Coordination Networks for Size-Selective Sieving of CO2. *Angew. Chem.* **2016,** *128* (35), 10424-10428.
37. Lin, R.-B.; Wu, H.; Li, L.; Tang, X.-L.; Li, Z.; Gao, J.; Cui, H.; Zhou, W.; Chen, B., Boosting Ethane/Ethylene Separation within Isoreticular Ultramicroporous Metal–Organic Frameworks. *J. Am. Chem. Soc.* **2018,** *140* (40), 12940-12946.
38. Lin, Y.; Kong, C.; Chen, L., Amine-functionalized metal–organic frameworks: structure, synthesis and applications. *RSC Adv.* **2016,** *6* (39), 32598-32614.
39. Grancha, T.; Mon, M.; Ferrando-Soria, J.; Gascon, J.; Seoane, B.; Ramos-Fernandez, E. V.; Armentano, D.; Pardo, E., Tuning the selectivity of light hydrocarbons in natural gas in a family of isoreticular MOFs. *J. Mater. Chem. A* **2017,** *5* (22), 11032-11039.
40. Nugent, P.; Belmabkhout, Y.; Burd, S. D.; Cairns, A. J.; Luebke, R.; Forrest, K.; Pham, T.; Ma, S.; Space, B.; Wojtas, L.; Eddaoudi, M.; Zaworotko, M. J., Porous materials with optimal adsorption thermodynamics and kinetics for CO2 separation. *Nature* **2013,** *495*, 80.
41. Li, B.; Dong, X.; Wang, H.; Ma, D.; Tan, K.; Shi, Z.; Chabal, Y. J.; Han, Y.; Li, J., Functionalized metal organic frameworks for effective capture of radioactive organic iodides. *Faraday Discuss.* **2017,** *201* (0), 47-61.
42. Ryder, M. R.; Civalleri, B.; Tan, J.-C., Isoreticular zirconium-based metal–organic frameworks: discovering mechanical trends and elastic anomalies controlling chemical structure stability. *Phys. Chem. Chem. Phys.* **2016,** *18* (13), 9079-9087.
43. Li, N.; Xu, J.; Feng, R.; Hu, T.-L.; Bu, X.-H., Governing metal–organic frameworks towards high stability. *Chem. Commun.* **2016,** *52* (55), 8501-8513.
44. Yuan, S.; Feng, L.; Wang, K.; Pang, J.; Bosch, M.; Lollar, C.; Sun, Y.; Qin, J.; Yang, X.; Zhang, P.; Wang, Q.; Zou, L.; Zhang, Y.; Zhang, L.; Fang, Y.; Li, J.; Zhou, H.-C., Stable Metal–Organic Frameworks: Design, Synthesis, and Applications. *Adv. Mater.* **2018,** *30* (37), 1704303.
45. Liu, L.; Telfer, S. G., Systematic Ligand Modulation Enhances the Moisture Stability and Gas Sorption Characteristics of Quaternary Metal–Organic Frameworks. *J. Am. Chem. Soc.* **2015,** *137* (11), 3901-3909.
46. Schneemann, A.; Bon, V.; Schwedler, I.; Senkovska, I.; Kaskel, S.; Fischer, R. A., Flexible metal–organic frameworks. *Chem. Soc. Rev.* **2014,** *43* (16), 6062-6096.
47. Chang, Z.; Yang, D. H.; Xu, J.; Hu, T. L.; Bu, X. H., Flexible metal–organic frameworks: recent advances and potential applications. *Adv. Mater.* **2015,** *27* (36), 5432-5441.
48. Jansen, M.; Schön, J. C., "Design" in chemical synthesis—An illusion? *Angew. Chem. Int. Ed.* **2006,** *45* (21), 3406-3412.
49. Perry Iv, J. J.; Perman, J. A.; Zaworotko, M. J., Design and synthesis of metal–organic frameworks using metal–organic polyhedra as supermolecular building blocks. *Chem. Soc. Rev.* **2009,** *38* (5), 1400-1417.
50. Hoskins, B.; Robson, R., Design and construction of a new class of scaffolding-like materials comprising infinite polymeric frameworks of 3D-linked molecular rods. A reappraisal of the zinc cyanide and cadmium cyanide structures and the synthesis and structure of the diamond-related frameworks [N (CH3) 4][CuIZnII (CN) 4] and CuI [4, 4', 4", 4"'-tetracyanotetraphenylmethane] BF4. xC6H5NO2. *J. Am. Chem. Soc.* **1990,** *112* (4), 1546-1554.
51. Férey, G., Some suggested perspectives for multifunctional hybrid porous solids. *Dalton Trans.* **2009,** (23), 4400-4415.
52. Li, C.-P.; Du, M., Role of solvents in coordination supramolecular systems. *Chem. Commun.* **2011,** *47* (21), 5958-5972.
53. McKinstry, C.; Cussen, E. J.; Fletcher, A. J.; Patwardhan, S. V.; Sefcik, J., Effect of Synthesis Conditions on Formation Pathways of Metal Organic Framework (MOF-5) Crystals. *Cryst. Growth Des.* **2013,** *13* (12), 5481-5486.

54. O'Keeffe, M., Design of MOFs and intellectual content in reticular chemistry: a personal view. *Chem. Soc. Rev.* **2009,** *38* (5), 1215-1217.
55. Zhao, D.; Timmons, D. J.; Yuan, D.; Zhou, H.-C., Tuning the topology and functionality of metal− organic frameworks by ligand design. *Acc. Chem. Res.* **2010,** *44* (2), 123-133.
56. Klinowski, J.; Almeida Paz, F. A.; Silva, P.; Rocha, J., Microwave-Assisted Synthesis of Metal–Organic Frameworks. *Dalton Trans.* **2011,** *40* (2), 321-330.
57. Parnham, E. R.; Morris, R. E., Ionothermal synthesis of zeolites, metal–organic frameworks, and inorganic–organic hybrids. *Acc. Chem. Res.* **2007,** *40* (10), 1005-1013.
58. Garay, A. L.; Pichon, A.; James, S. L., Solvent-free synthesis of metal complexes. *Chem. Soc. Rev.* **2007,** *36* (6), 846-855.
59. Li, J.-R.; Timmons, D. J.; Zhou, H.-C., Interconversion between molecular polyhedra and metal− organic frameworks. *J. Am. Chem. Soc.* **2009,** *131* (18), 6368-6369.
60. Zaworotko, M. J., Metal–organic materials: a reversible step forward. *Nature Chem.* **2009,** *1* (4), 267.
61. Carne, A.; Carbonell, C.; Imaz, I.; Maspoch, D., Nanoscale metal–organic materials. *Chem. Soc. Rev.* **2011,** *40* (1), 291-305.
62. Della Rocca, J.; Liu, D.; Lin, W., Nanoscale metal–organic frameworks for biomedical imaging and drug delivery. *Acc. Chem. Res.* **2011,** *44* (10), 957-968.
63. Farha, O. K.; Hupp, J. T., Rational design, synthesis, purification, and activation of metal− organic framework materials. *Acc. Chem. Res.* **2010,** *43* (8), 1166-1175.
64. Dhakshinamoorthy, A.; Li, Z.; Garcia, H., Catalysis and photocatalysis by metal organic frameworks. *Chem. Soc. Rev.* **2018,** *47* (22), 8134-8172.
65. Zhu, L.; Liu, X.-Q.; Jiang, H.-L.; Sun, L.-B., Metal–organic frameworks for heterogeneous basic catalysis. *Chem. Rev.* **2017,** *117* (12), 8129-8176.
66. Lee, J.; Farha, O. K.; Roberts, J.; Scheidt, K. A.; Nguyen, S. T.; Hupp, J. T., Metal–organic framework materials as catalysts. *Chem. Soc. Rev.* **2009,** *38* (5), 1450-1459.
67. Kurmoo, M., Magnetic metal–organic frameworks. *Chem. Soc. Rev.* **2009,** *38* (5), 1353-1379.
68. Taylor, K. M.; Rieter, W. J.; Lin, W., Manganese-based nanoscale metal− organic frameworks for magnetic resonance imaging. *J. Am. Chem. Soc.* **2008,** *130* (44), 14358-14359.
69. Cui, Y.; Yue, Y.; Qian, G.; Chen, B., Luminescent Functional Metal–Organic Frameworks. *Chem. Rev.* **2012,** *112* (2), 1126-1162.
70. Cornelio, J.; Zhou, T.-Y.; Alkaş, A.; Telfer, S. G., Systematic Tuning of the Luminescence Output of Multicomponent Metal–Organic Frameworks. *J. Am. Chem. Soc.* **2018,** *140* (45), 15470-15476.
71. Kumar, P.; Bansal, V.; Kim, K.-H.; Kwon, E. E., Metal-organic frameworks (MOFs) as futuristic options for wastewater treatment. *J. Ind. Eng. Chem.* **2018,** *62*, 130-145.
72. Xie, Q.; Li, Y.; Lv, Z.; Zhou, H.; Yang, X.; Chen, J.; Guo, H., Effective Adsorption and Removal of Phosphate from Aqueous Solutions and Eutrophic Water by Fe-based MOFs of MIL-101. *Sci. Rep.* **2017,** *7* (1), 3316.
73. Dias, E. M.; Petit, C., Towards the use of metal–organic frameworks for water reuse: a review of the recent advances in the field of organic pollutants removal and degradation and the next steps in the field. *J. Mater. Chem. A* **2015,** *3* (45), 22484-22506.
74. Kreno, L. E.; Leong, K.; Farha, O. K.; Allendorf, M.; Van Duyne, R. P.; Hupp, J. T., Metal–Organic Framework Materials as Chemical Sensors. *Chem. Rev.* **2012,** *112* (2), 1105-1125.
75. Fang, X.; Zong, B.; Mao, S., Metal–Organic Framework-Based Sensors for Environmental Contaminant Sensing. *Nano-Micro Letters* **2018,** *10* (4), 64.

76. Lian, X.; Fang, Y.; Joseph, E.; Wang, Q.; Li, J.; Banerjee, S.; Lollar, C.; Wang, X.; Zhou, H.-C., Enzyme–MOF (metal–organic framework) composites. *Chem. Soc. Rev.* **2017,** *46* (11), 3386-3401.
77. Wang, C.; Zhang, T.; Lin, W., Rational Synthesis of Noncentrosymmetric Metal–Organic Frameworks for Second-Order Nonlinear Optics. *Chem. Rev.* **2012,** *112* (2), 1084-1104.
78. Narayan, T. C.; Miyakai, T.; Seki, S.; Dincă, M., High Charge Mobility in a Tetrathiafulvalene-Based Microporous Metal–Organic Framework. *J. Am. Chem. Soc.* **2012,** *134* (31), 12932-12935.
79. Sheberla, D.; Sun, L.; Blood-Forsythe, M. A.; Er, S.; Wade, C. R.; Brozek, C. K.; Aspuru-Guzik, A.; Dincă, M., High Electrical Conductivity in Ni_3(2,3,6,7,10,11-hexaiminotriphenylene)$_2$, a Semiconducting Metal–Organic Graphene Analogue. *J. Am. Chem. Soc.* **2014,** *136* (25), 8859-8862.
80. Park, S. S.; Hontz, E. R.; Sun, L.; Hendon, C. H.; Walsh, A.; Van Voorhis, T.; Dincă, M., Cation-Dependent Intrinsic Electrical Conductivity in Isostructural Tetrathiafulvalene-Based Microporous Metal–Organic Frameworks. *J. Am. Chem. Soc.* **2015,** *137* (5), 1774-1777.
81. Campbell, M. G.; Sheberla, D.; Liu, S. F.; Swager, T. M.; Dincă, M., Cu3(hexaiminotriphenylene)2: An Electrically Conductive 2D Metal–Organic Framework for Chemiresistive Sensing. *Angew. Chem. Int. Ed.* **2015,** *54* (14), 4349-4352.
82. Sun, L.; Hendon, C. H.; Minier, M. A.; Walsh, A.; Dincă, M., Million-Fold Electrical Conductivity Enhancement in Fe_2(DEBDC) versus Mn_2(DEBDC) (E = S, O). *J. Am. Chem. Soc.* **2015,** *137* (19), 6164-6167.
83. Bureekaew, S.; Horike, S.; Higuchi, M.; Mizuno, M.; Kawamura, T.; Tanaka, D.; Yanai, N.; Kitagawa, S., One-dimensional imidazole aggregate in aluminium porous coordination polymers with high proton conductivity. *Nat Mater* **2009,** *8* (10), 831-836.
84. Sadakiyo, M.; Yamada, T.; Kitagawa, H., Rational Designs for Highly Proton-Conductive Metal−Organic Frameworks. *J. Am. Chem. Soc.* **2009,** *131* (29), 9906-9907.
85. Tominaka, S.; Coudert, F.-X.; Dao, T. D.; Nagao, T.; Cheetham, A. K., Insulator-to-Proton-Conductor Transition in a Dense Metal–Organic Framework. *J. Am. Chem. Soc.* **2015,** *137* (20), 6428-6431.
86. Wu, D.; Guo, Z.; Yin, X.; Pang, Q.; Tu, B.; Zhang, L.; Wang, Y.-G.; Li, Q., Metal–Organic Frameworks as Cathode Materials for Li–O2 Batteries. *Adv. Mater.* **2014,** *26* (20), 3258-3262.
87. Talin, A. A.; Centrone, A.; Ford, A. C.; Foster, M. E.; Stavila, V.; Haney, P.; Kinney, R. A.; Szalai, V.; El Gabaly, F.; Yoon, H. P.; Léonard, F.; Allendorf, M. D., Tunable Electrical Conductivity in Metal-Organic Framework Thin-Film Devices. *Science* **2014,** *343* (6166), 66-69.
88. Deng, H.; Grunder, S.; Cordova, K. E.; Valente, C.; Furukawa, H.; Hmadeh, M.; Gándara, F.; Whalley, A. C.; Liu, Z.; Asahina, S.; Kazumori, H.; O'Keeffe, M.; Terasaki, O.; Stoddart, J. F.; Yaghi, O. M., Large-Pore Apertures in a Series of Metal-Organic Frameworks. *Science* **2012,** *336* (6084), 1018-1023.
89. Lykourinou, V.; Chen, Y.; Wang, X.-S.; Meng, L.; Hoang, T.; Ming, L.-J.; Musselman, R. L.; Ma, S., Immobilization of MP-11 into a Mesoporous Metal–Organic Framework, MP-11@mesoMOF: A New Platform for Enzymatic Catalysis. *J. Am. Chem. Soc.* **2011,** *133* (27), 10382-10385.
90. Horcajada, P.; Serre, C.; Vallet-Regí, M.; Sebban, M.; Taulelle, F.; Férey, G., Metal–Organic Frameworks as Efficient Materials for Drug Delivery. *Angew. Chem. Int. Ed.* **2006,** *45* (36), 5974-5978.

91. McKinlay, A. C.; Morris, R. E.; Horcajada, P.; Férey, G.; Gref, R.; Couvreur, P.; Serre, C., BioMOFs: Metal–Organic Frameworks for Biological and Medical Applications. *Angew. Chem. Int. Ed.* **2010,** *49* (36), 6260-6266.
92. Lu, K.; He, C.; Lin, W., Nanoscale Metal–Organic Framework for Highly Effective Photodynamic Therapy of Resistant Head and Neck Cancer. *J. Am. Chem. Soc.* **2014,** *136* (48), 16712-16715.
93. Walton, K. S.; Snurr, R. Q., Applicability of the BET Method for Determining Surface Areas of Microporous Metal−Organic Frameworks. *J. Am. Chem. Soc.* **2007,** *129* (27), 8552-8556.
94. Itodo, A.; Itodo, H.; Gafar, M., Estimation of specific surface area using langmuir isotherm method. *J. Appl. Sci. Envi. Manag.* **2010,** *14* (4).
95. Li, J.-R.; Sculley, J.; Zhou, H.-C., Metal–organic frameworks for separations. *Chem. Rev.* **2011,** *112* (2), 869-932.
96. Mason, J. A.; Veenstra, M.; Long, J. R., Evaluating metal–organic frameworks for natural gas storage. *Chem. Sci.* **2014,** *5* (1), 32-51.
97. Sumida, K.; Rogow, D. L.; Mason, J. A.; McDonald, T. M.; Bloch, E. D.; Herm, Z. R.; Bae, T.-H.; Long, J. R., Carbon Dioxide Capture in Metal–Organic Frameworks. *Chem. Rev.* **2012,** *112* (2), 724-781.
98. Dinca, M.; Dailly, A.; Liu, Y.; Brown, C. M.; Neumann, D. A.; Long, J. R., Hydrogen storage in a microporous metal− organic framework with exposed Mn2+ coordination sites. *J. Am. Chem. Soc.* **2006,** *128* (51), 16876-16883.
99. Yang, R. T., *Gas separation by adsorption processes*. Butterworth-Heinemann: 2013.
100. Yang, R. T., Adsorbents: Fundamentals and Applications. John Wiley & Sons, Inc: Hoboken, 2003.
101. Bond, R. L., *Porous carbon solids*. Academic Press: 1967.
102. King, C. J., *Separation processes*. Courier Corporation: 2013.
103. Karger, B. L.; Snyder, L. R.; Horvath, C., Introduction to separation science. **1973**.
104. Rouquerol, J.; Rouquerol, F.; Llewellyn, P.; Maurin, G.; Sing, K. S., *Adsorption by powders and porous solids: principles, methodology and applications*. Academic press: 2013.
105. Chaemchuen, S.; Kabir, N. A.; Zhou, K.; Verpoort, F., Metal–organic frameworks for upgrading biogas via CO 2 adsorption to biogas green energy. *Chem. Soc. Rev.* **2013,** *42* (24), 9304-9332.
106. Sircar, S.; Golden, T.; Rao, M., Activated carbon for gas separation and storage. *Carbon* **1996,** *34* (1), 1-12.
107. Ackley, M. W.; Rege, S. U.; Saxena, H., Application of natural zeolites in the purification and separation of gases. *Microporous Mesoporous Mater.* **2003,** *61* (1-3), 25-42.
108. Ebner, A. D.; Ritter, J. A., State-of-the-art adsorption and membrane separation processes for carbon dioxide production from carbon dioxide emitting industries. *Sep. Sci. Technol.* **2009,** *44* (6), 1273-1421.
109. Sircar, S.; Myers, A. L., Gas separation by zeolites. *Handbook of Zeolite Science and Technology* **2003,** *1063*.
110. Li, J.-R.; Kuppler, R. J.; Zhou, H.-C., Selective gas adsorption and separation in metal–organic frameworks. *Chem. Soc. Rev.* **2009,** *38* (5), 1477-1504.
111. Seader, J. D.; Henley, E. J.; Roper, D. K., Separation process principles. **1998**.
112. Do, D. D., *Adsorption analysis: equilibria and kinetics*. Imperial college press London: 1998; Vol. 2.
113. Ruthven, D. M., *Principles of adsorption and adsorption processes*. John Wiley & Sons: 1984.
114. Auerbach, S. M.; Carrado, K. A.; Dutta, P. K., *Handbook of zeolite science and technology*. CRC press: 2003.
115. Breck, D. W., Zeolite Molecular Sieves, John Wiley & Sons, New York. **1974**.

116. W John Thomas, F.; Crittenden, B., *Adsorption technology and design*. Butterworth-Heinemann: 1998.
117. McDonald, T. M.; Mason, J. A.; Kong, X.; Bloch, E. D.; Gygi, D.; Dani, A.; Crocella, V.; Giordanino, F.; Odoh, S. O.; Drisdell, W. S., Cooperative insertion of CO 2 in diamine-appended metal-organic frameworks. *Nature* **2015,** *519* (7543), 303.
118. Myers, A.; Prausnitz, J. M., Thermodynamics of mixed ‐ gas adsorption. *AIChE J.* **1965,** *11* (1), 121-127.
119. Liao, P. Q.; Zhang, W. X.; Zhang, J. P.; Chen, X. M., Efficient purification of ethene by an ethane-trapping metal-organic framework. *Nat. Commun.* **2015,** *6*, 8697.
120. Qazvini, O. T.; Babarao, R.; Shi, Z.-L.; Zhang, Y.-B.; Telfer, S. G., A Robust Ethane-Trapping Metal–Organic Framework with a High Capacity for Ethylene Purification. *J. Am. Chem. Soc.* **2019**.
121. Builes, S.; Sandler, S. I.; Xiong, R., Isosteric Heats of Gas and Liquid Adsorption. *Langmuir* **2013,** *29* (33), 10416-10422.
122. Dincă, M.; Dailly, A.; Liu, Y.; Brown, C. M.; Neumann, D. A.; Long, J. R., Hydrogen Storage in a Microporous Metal−Organic Framework with Exposed Mn2+ Coordination Sites. *J. Am. Chem. Soc.* **2006,** *128* (51), 16876-16883.
123. Sholl, D. S.; Lively, R. P., Seven chemical separations to change the world. *Nature News* **2016,** *532* (7600), 435.
124. Kerry, F. G., *Industrial gas handbook: gas separation and purification*. CRC press: 2007.
125. Mokhatab, S.; Poe, W. A., *Handbook of natural gas transmission and processing*. Gulf professional publishing: 2012.
126. Eldridge, R. B., Olefin/paraffin separation technology: a review. *Ind. Eng. Chem. Res.* **1993,** *32* (10), 2208-2212.
127. Rousseau, R. W., *Handbook of separation process technology*. John Wiley & Sons: 1987.
128. Cavalcante Jr, C., Industrial adsorption separation processes: Fundamentals, modeling and applications. *Lat. Am. Appl. Res.* **2000,** *30* (4), 357-364.
129. Rautenbach, R.; Albrecht, R., Membrane separation processes. **1989**.
130. Kitagawa, S.; Kitaura, R.; Noro, S. i., Functional porous coordination polymers. *Angew. Chem. Int. Ed.* **2004,** *43* (18), 2334-2375.
131. Zhou, H.-C.; Long, J. R.; Yaghi, O. M., Introduction to metal–organic frameworks. ACS Publications: 2012.
132. Furukawa, H.; Cordova, K. E.; O'Keeffe, M.; Yaghi, O. M., The Chemistry and Applications of Metal-Organic Frameworks. *Science* **2013,** *341* (6149), 1230444.
133. Foo, M. L.; Matsuda, R.; Kitagawa, S., Functional hybrid porous coordination polymers. *Chem. Mater.* **2013,** *26* (1), 310-322.
134. Wang, C.; Liu, D.; Lin, W., Metal–Organic Frameworks as A Tunable Platform for Designing Functional Molecular Materials. *J. Am. Chem. Soc.* **2013,** *135* (36), 13222-13234.
135. Eddaoudi, M.; Kim, J.; Rosi, N.; Vodak, D.; Wachter, J.; O'keeffe, M.; Yaghi, O. M., Systematic design of pore size and functionality in isoreticular MOFs and their application in methane storage. *Science* **2002,** *295* (5554), 469-472.
136. Cohen, S. M., Postsynthetic methods for the functionalization of metal–organic frameworks. *Chem. Rev.* **2011,** *112* (2), 970-1000.
137. Chen, B.; Xiang, S.; Qian, G., Metal− organic frameworks with functional pores for recognition of small molecules. *Acc. Chem. Res.* **2010,** *43* (8), 1115-1124.
138. Sumida, K.; Rogow, D. L.; Mason, J. A.; McDonald, T. M.; Bloch, E. D.; Herm, Z. R.; Bae, T.-H.; Long, J. R., Carbon dioxide capture in metal–organic frameworks. *Chem. Rev.* **2011,** *112* (2), 724-781.

139. Bosch, H.; Versteeg, G. F.; Van Swaaij, W. P. M., Gas—liquid mass transfer with parallel reversible reactions—III. Absorption of CO2 into solutions of blends of amines. *Chem. Eng. Sci.* **1989,** *44* (11), 2745-2750.
140. Rochelle, G. T., Amine scrubbing for CO2 capture. *Science* **2009,** *325* (5948), 1652-1654.
141. Ma, X.; Wang, X.; Song, C., "Molecular Basket" Sorbents for Separation of CO2 and H2S from Various Gas Streams. *J. Am. Chem. Soc.* **2009,** *131* (16), 5777-5783.
142. Mason, J. A.; Sumida, K.; Herm, Z. R.; Krishna, R.; Long, J. R., Evaluating metal–organic frameworks for post-combustion carbon dioxide capture via temperature swing adsorption. *Energy Environ. Sci.* **2011,** *4* (8), 3030-3040.
143. McDonald, T. M.; D'Alessandro, D. M.; Krishna, R.; Long, J. R., Enhanced carbon dioxide capture upon incorporation of N, N′ -dimethylethylenediamine in the metal‐organic framework CuBTTri. *Chem. Sci.* **2011,** *2* (10), 2022-2028.
144. McDonald, T. M.; Lee, W. R.; Mason, J. A.; Wiers, B. M.; Hong, C. S.; Long, J. R., Capture of carbon dioxide from air and flue gas in the alkylamine-appended metal–organic framework mmen-Mg2 (dobpdc). *J. Am. Chem. Soc.* **2012,** *134* (16), 7056-7065.
145. Fracaroli, A. M.; Furukawa, H.; Suzuki, M.; Dodd, M.; Okajima, S.; Gándara, F.; Reimer, J. A.; Yaghi, O. M., Metal–organic frameworks with precisely designed interior for carbon dioxide capture in the presence of water. *J. Am. Chem. Soc.* **2014,** *136* (25), 8863-8866.
146. Lee, W. R.; Jo, H.; Yang, L.-M.; Lee, H.; Ryu, D. W.; Lim, K. S.; Song, J. H.; Min, D. Y.; Han, S. S.; Seo, J. G.; Park, Y. K.; Moon, D.; Hong, C. S., Exceptional CO2 working capacity in a heterodiamine-grafted metal–organic framework. *Chem. Sci.* **2015,** *6* (7), 3697-3705.
147. Lee, W. R.; Hwang, S. Y.; Ryu, D. W.; Lim, K. S.; Han, S. S.; Moon, D.; Choi, J.; Hong, C. S., Diamine-functionalized metal–organic framework: exceptionally high CO2 capacities from ambient air and flue gas, ultrafast CO2 uptake rate, and adsorption mechanism. *Energy Environ. Sci.* **2014,** *7* (2), 744-751.
148. Jo, H.; Lee, W. R.; Kim, N. W.; Jung, H.; Lim, K. S.; Kim, J. E.; Kang, D. W.; Lee, H.; Hiremath, V.; Seo, J. G.; Jin, H.; Moon, D.; Han, S. S.; Hong, C. S., Fine-Tuning of the Carbon Dioxide Capture Capability of Diamine-Grafted Metal–Organic Framework Adsorbents Through Amine Functionalization. *ChemSusChem* **2017,** *10* (3), 541-550.
149. Li, H.; Wang, K.; Feng, D.; Chen, Y.-P.; Verdegaal, W.; Zhou, H.-C., Incorporation of Alkylamine into Metal–Organic Frameworks through a Brønsted Acid–Base Reaction for CO2 Capture. *ChemSusChem* **2016,** *9* (19), 2832-2840.
150. Liao, P.-Q.; Chen, X.-W.; Liu, S.-Y.; Li, X.-Y.; Xu, Y.-T.; Tang, M.; Rui, Z.; Ji, H.; Zhang, J.-P.; Chen, X.-M., Putting an ultrahigh concentration of amine groups into a metal–organic framework for CO2 capture at low pressures. *Chem. Sci.* **2016,** *7* (10), 6528-6533.
151. Liao, P.-Q.; Chen, H.; Zhou, D.-D.; Liu, S.-Y.; He, C.-T.; Rui, Z.; Ji, H.; Zhang, J.-P.; Chen, X.-M., Monodentate hydroxide as a super strong yet reversible active site for CO2 capture from high-humidity flue gas. *Energy Environ. Sci.* **2015,** *8* (3), 1011-1016.
152. Shekhah, O.; Belmabkhout, Y.; Chen, Z.; Guillerm, V.; Cairns, A.; Adil, K.; Eddaoudi, M., Made-to-order metal-organic frameworks for trace carbon dioxide removal and air capture. *Nat. Commun.* **2014,** *5*, 4228.
153. Shekhah, O.; Belmabkhout, Y.; Adil, K.; Bhatt, P. M.; Cairns, A. J.; Eddaoudi, M., A facile solvent-free synthesis route for the assembly of a highly CO2 selective and H2S tolerant NiSIFSIX metal–organic framework. *Chem. Commun.* **2015,** *51* (71), 13595-13598.

154. Higman, C., Gasification. In *Combustion Engineering Issues for Solid Fuel Systems*, Elsevier: 2008; pp 423-468.
155. Sircar, S.; Golden, T., Purification of hydrogen by pressure swing adsorption. *Sep. Sci. Technol.* **2000,** *35* (5), 667-687.
156. Gupta, R. B., *Hydrogen fuel: production, transport, and storage*. Crc Press: 2008.
157. Song, C.; Liu, K.; Subramani, V., Introduction to hydrogen and syngas production and purification technologies. *Hydrogen and syngas production and purification technologies. J. Wiley & Sons, Hobocken, NJ* **2010**, 1-13.
158. Plasynski, S.; Litynski, J.; McIlvried, H.; Srivastava, R., Progress and new developments in carbon capture and storage. *Crit. Rev. Plant. Sci.* **2009,** *28* (3), 123-138.
159. Kang, Z.; Peng, Y.; Hu, Z.; Qian, Y.; Chi, C.; Yeo, L. Y.; Tee, L.; Zhao, D., Mixed matrix membranes composed of two-dimensional metal–organic framework nanosheets for pre-combustion CO 2 capture: a relationship study of filler morphology versus membrane performance. *J. Mater. Chem. A* **2015,** *3* (41), 20801-20810.
160. Nandi, S.; De Luna, P.; Daff, T. D.; Rother, J.; Liu, M.; Buchanan, W.; Hawari, A. I.; Woo, T. K.; Vaidhyanathan, R., A single-ligand ultra-microporous MOF for precombustion CO2 capture and hydrogen purification. *Sci. Adv.* **2015,** *1* (11), e1500421.
161. Chung, Y. G.; Gómez-Gualdrón, D. A.; Li, P.; Leperi, K. T.; Deria, P.; Zhang, H.; Vermeulen, N. A.; Stoddart, J. F.; You, F.; Hupp, J. T., In silico discovery of metal-organic frameworks for precombustion CO2 capture using a genetic algorithm. *Sci. Adv.* **2016,** *2* (10), e1600909.
162. Keskin, S.; Sholl, D. S., Assessment of a metal− organic framework membrane for gas separations using atomically detailed calculations: CO2, CH4, N2, H2 mixtures in MOF-5. *Ind. Eng. Chem. Res.* **2008,** *48* (2), 914-922.
163. Guo, H.; Zhu, G.; Hewitt, I. J.; Qiu, S., "Twin copper source" growth of metal− organic framework membrane: Cu3 (BTC) 2 with high permeability and selectivity for recycling H2. *J. Am. Chem. Soc.* **2009,** *131* (5), 1646-1647.
164. Fischer, M.; Hoffmann, F.; Fröba, M., Metal–organic frameworks and related materials for hydrogen purification: Interplay of pore size and pore wall polarity. *RSC Adv.* **2012,** *2* (10), 4382-4396.
165. Nenoff, T. M., MOF membranes put to the test. *Nature Chem.* **2015,** *7*, 377.
166. Zhou, S.; Zou, X.; Sun, F.; Ren, H.; Liu, J.; Zhang, F.; Zhao, N.; Zhu, G., Development of hydrogen-selective CAU-1 MOF membranes for hydrogen purification by 'dual-metal-source' approach. *Int. J. Hydrogen Energy* **2013,** *38* (13), 5338-5347.
167. Peng, Y.; Li, Y.; Ban, Y.; Jin, H.; Jiao, W.; Liu, X.; Yang, W., Metal-organic framework nanosheets as building blocks for molecular sieving membranes. *Science* **2014,** *346* (6215), 1356-1359.
168. Bloch, E. D.; Murray, L. J.; Queen, W. L.; Chavan, S.; Maximoff, S. N.; Bigi, J. P.; Krishna, R.; Peterson, V. K.; Grandjean, F.; Long, G. J.; Smit, B.; Bordiga, S.; Brown, C. M.; Long, J. R., Selective Binding of O2 over N2 in a Redox–Active Metal–Organic Framework with Open Iron(II) Coordination Sites. *J. Am. Chem. Soc.* **2011,** *133* (37), 14814-14822.
169. Murray, L. J.; Dinca, M.; Yano, J.; Chavan, S.; Bordiga, S.; Brown, C. M.; Long, J. R., Highly-Selective and Reversible O2 Binding in Cr3(1,3,5-benzenetricarboxylate)2. *J. Am. Chem. Soc.* **2010,** *132* (23), 7856-7857.
170. Bloch, E. D.; Queen, W. L.; Hudson, M. R.; Mason, J. A.; Xiao, D. J.; Murray, L. J.; Flacau, R.; Brown, C. M.; Long, J. R., Hydrogen Storage and Selective, Reversible O2 Adsorption in a Metal–Organic Framework with Open Chromium(II) Sites. *Angew. Chem. Int. Ed.* **2016,** *55* (30), 8605-8609.

171. Murray, L. J.; Dinca, M.; Yano, J.; Chavan, S.; Bordiga, S.; Brown, C. M.; Long, J. R., Highly-selective and reversible O2 binding in Cr3 (1, 3, 5-benzenetricarboxylate) 2. *J. Am. Chem. Soc.* **2010,** *132* (23), 7856-7857.
172. Xiao, D. J.; Gonzalez, M. I.; Darago, L. E.; Vogiatzis, K. D.; Haldoupis, E.; Gagliardi, L.; Long, J. R., Selective, tunable O2 binding in cobalt (II)–triazolate/pyrazolate metal–organic frameworks. *J. Am. Chem. Soc.* **2016,** *138* (22), 7161-7170.
173. Sanz-Perez, E. S.; Murdock, C. R.; Didas, S. A.; Jones, C. W., Direct capture of CO2 from ambient air. *Chem. Rev.* **2016,** *116* (19), 11840-11876.
174. Madden, D. G.; Scott, H. S.; Kumar, A.; Chen, K.-J.; Sanii, R.; Bajpai, A.; Lusi, M.; Curtin, T.; Perry, J. J.; Zaworotko, M. J., Flue-gas and direct-air capture of CO2 by porous metal–organic materials. *Philos. Trans. Royal Soc. A* **2017,** *375* (2084), 20160025.
175. Lu, W.; Sculley, J. P.; Yuan, D.; Krishna, R.; Zhou, H.-C., Carbon dioxide capture from air using amine-grafted porous polymer networks. *J. Phys. Chem. C* **2013,** *117* (8), 4057-4061.
176. Bhatt, P. M.; Belmabkhout, Y.; Cadiau, A.; Adil, K.; Shekhah, O.; Shkurenko, A.; Barbour, L. J.; Eddaoudi, M., A Fine-Tuned Fluorinated MOF Addresses the Needs for Trace CO2 Removal and Air Capture Using Physisorption. *J. Am. Chem. Soc.* **2016,** *138* (29), 9301-9307.
177. Lee, W. R.; Hwang, S. Y.; Ryu, D. W.; Lim, K. S.; Han, S. S.; Moon, D.; Choi, J.; Hong, C. S., Diamine-functionalized metal–organic framework: exceptionally high CO 2 capacities from ambient air and flue gas, ultrafast CO 2 uptake rate, and adsorption mechanism. *Energy Environ. Sci.* **2014,** *7* (2), 744-751.
178. Darunte, L. A.; Oetomo, A. D.; Walton, K. S.; Sholl, D. S.; Jones, C. W., Direct Air Capture of CO2 Using Amine Functionalized MIL-101(Cr). *ACS Sustainable Chem. Eng.* **2016,** *4* (10), 5761-5768.
179. Liu, J.; Wei, Y.; Zhao, Y., Trace Carbon Dioxide Capture by Metal–Organic Frameworks. *ACS Sustainable Chem. Eng.* **2019,** *7* (1), 82-93.
180. Grunker, R.; Bon, V.; Muller, P.; Stoeck, U.; Krause, S.; Mueller, U.; Senkovska, I.; Kaskel, S., A new metal-organic framework with ultra-high surface area. *Chem. Commun.* **2014,** *50* (26), 3450-3452.
181. Liu, L.; Konstas, K.; Hill, M. R.; Telfer, S. G., Programmed Pore Architectures in Modular Quaternary Metal–Organic Frameworks. *J. Am. Chem. Soc.* **2013,** *135* (47), 17731-17734.
182. Simon, C. M.; Smit, B.; Haranczyk, M., pyIAST: Ideal adsorbed solution theory (IAST) Python package. *Comput. Phys. Commun.* **2016,** *200*, 364-380.
183. Qazvini, O. T.; Fatemi, S., Modeling and simulation pressure–temperature swing adsorption process to remove mercaptan from humid natural gas; a commercial case study. *Sep. Purif. Technol.* **2015,** *139*, 88-103.
184. Mehdipour, M.; Fatemi, S., Modeling of a PSA-TSA Process for Separation of CH4from C2Products of OCM Reaction. *Sep. Sci. Technol.* **2012,** *47* (8), 1199-1212.
185. Chahbani, M. H.; Tondeur, D., Mass transfer kinetics in pressure swing adsorption. *Sep. Purif. Technol.* **2000,** *20* (2), 185-196.
186. Bird, R. B., Transport phenomena. *Appl. Mech. Rev* **2002,** *55* (1), R1-R4.
187. Perry, R.; Green, D.; Maloney, J., *Chemical engineers handbook*. 8th edition ed.; The McGraw Hill Companies, Inc: 2008.
188. Farooq, S.; Ruthven, D. M., A comparison of linear driving force and pore diffusion models for a pressure swing adsorption bulk separation process. *Chem. Eng. Sci.* **1990,** *45* (1), 107-115.
189. Kiusalaas, J., *Numerical methods in engineering with Python 3*. Cambridge university press: 2013.
190. Matar, S.; Hatch, L. F., *Chemistry of petrochemical processes*. Elsevier: 2001.

191. Liao, P. Q.; Zhu, A. X.; Zhang, W. X.; Zhang, J. P.; Chen, X. M., Self-catalysed aerobic oxidization of organic linker in porous crystal for on-demand regulation of sorption behaviours. *Nat. Commun.* **2015,** *6*, 6350.
192. Horike, S.; Kishida, K.; Watanabe, Y.; Inubushi, Y.; Umeyama, D.; Sugimoto, M.; Fukushima, T.; Inukai, M.; Kitagawa, S., Dense coordination network capable of selective CO2 capture from C1 and C2 hydrocarbons. *J. Am. Chem. Soc.* **2012,** *134* (24), 9852-5.
193. Bux, H.; Chmelik, C.; Krishna, R.; Caro, J., Ethene/ethane separation by the MOF membrane ZIF-8: Molecular correlation of permeation, adsorption, diffusion. *J. Membr. Sci.* **2011,** *369* (1-2), 284-289.
194. Van Miltenburg, A.; Zhu, W.; Kapteijn, F.; Moulijn, J. A., Adsorptive Separation of Light Olefin/Paraffin Mixtures. *Chem. Eng. Res. Des.* **2006,** *84* (5), 350-354.
195. Pires, J.; Fernandes, J.; Fernandes, A. C.; Pinto, M., Reverse selectivity of zeolites and metal-organic frameworks in the ethane/ethylene separation by adsorption. *Sep. Sci. Technol.* **2017,** *52* (1), 51-57.
196. Bereciartua, P. J.; Cantín, Á.; Corma, A.; Jordá, J. L.; Palomino, M.; Rey, F.; Valencia, S.; Corcoran, E. W.; Kortunov, P.; Ravikovitch, P. I.; Burton, A.; Yoon, C.; Wang, Y.; Paur, C.; Guzman, J.; Bishop, A. R.; Casty, G. L., Control of zeolite framework flexibility and pore topology for separation of ethane and ethylene. *Science* **2017,** *358* (6366), 1068-1071.
197. Sholl, D. S.; Lively, R. P., Seven chemical separations: to change the world: purifying mixtures without using heat would lower global energy use, emissions and pollution--and open up new routes to resources. *Nature* **2016,** *532* (7600), 435-438.
198. Li, H.; Wang, K.; Sun, Y.; Lollar, C. T.; Li, J.; Zhou, H.-C., Recent advances in gas storage and separation using metal–organic frameworks. *Mater. Today* **2018,** *21* (2), 108-121.
199. Li, J. R.; Sculley, J.; Zhou, H. C., Metal-organic frameworks for separations. *Chem. Rev.* **2012,** *112* (2), 869-932.
200. Kim, J.; Lin, L. C.; Martin, R. L.; Swisher, J. A.; Haranczyk, M.; Smit, B., Large-scale computational screening of zeolites for ethane/ethene separation. *Langmuir* **2012,** *28* (32), 11914-9.
201. Narin, G.; Martins, V. F. D.; Campo, M.; Ribeiro, A. M.; Ferreira, A.; Santos, J. C.; Schumann, K.; Rodrigues, A. E., Light olefins/paraffins separation with 13X zeolite binderless beads. *Sep. Purif. Technol.* **2014,** *133*, 452-475.
202. Choi, B.-U.; Choi, D.-K.; Lee, Y.-W.; Lee, B.-K.; Kim, S.-H., Adsorption Equilibria of Methane, Ethane, Ethylene, Nitrogen, and Hydrogen onto Activated Carbon. *J. Chem. Eng. Data* **2003,** *48* (3), 603-607.
203. Kitagawa, S.; Kitaura, R.; Noro, S.-i., Functional Porous Coordination Polymers. *Angew. Chem. Int. Ed.* **2004,** *43* (18), 2334-2375.
204. Zhang, Y.; Li, B.; Krishna, R.; Wu, Z.; Ma, D.; Shi, Z.; Pham, T.; Forrest, K.; Space, B.; Ma, S., Highly selective adsorption of ethylene over ethane in a MOF featuring the combination of open metal site and pi-complexation. *Chem. Commun.* **2015,** *51* (13), 2714-7.
205. Li, J. R.; Kuppler, R. J.; Zhou, H. C., Selective gas adsorption and separation in metal-organic frameworks. *Chem. Soc. Rev.* **2009,** *38* (5), 1477-504.
206. Yang, Y.; Burke, N.; Ali, S.; Huang, S.; Lim, S.; Zhu, Y., Experimental studies of hydrocarbon separation on zeolites, activated carbons and MOFs for applications in natural gas processing. *RSC Adv.* **2017,** *7* (21), 12629-12638.
207. Lin, R.-B.; Xiang, S.; Xing, H.; Zhou, W.; Chen, B., Exploration of porous metal–organic frameworks for gas separation and purification. *Coord. Chem. Rev.* **2019,** *378*, 87-103.

208. Pires, J.; Fernandes, J.; Fernandes, A. C.; Pinto, M., Reverse selectivity of zeolites and metal-organic frameworks in the ethane/ethylene separation by adsorption. *Sep. Sci. Technol.* **2016,** *52* (1), 51-57.
209. Maghsoudi, H., Comparative study of adsorbents performance in ethylene/ethane separation. *Adsorption* **2016,** *22* (7), 985-992.
210. Luna-Triguero, A.; Vicent-Luna, J. M.; Gómez-Álvarez, P.; Calero, S., Olefin/Paraffin Separation in Open Metal Site Cu-BTC Metal–Organic Framework. *J. Phys. Chem. C* **2017,** *121* (5), 3126-3132.
211. Bloch, E. D.; W. L. Queen; R. Krishna; J. M. Zadrozny; C. M. Brown; J. R. Long, Hydrocarbon Separations in a Metal-Organic Framework with Open Iron(II) Coordination Sites. *Science* **2012,** *335* (6076), 1606-1610.
212. Martins, V. F. D.; Ribeiro, A. M.; Ferreira, A.; Lee, U. H.; Hwang, Y. K.; Chang, J.-S.; Loureiro, J. M.; Rodrigues, A. E., Ethane/ethylene separation on a copper benzene-1,3,5-tricarboxylate MOF. *Sep. Purif. Technol.* **2015,** *149*, 445-456.
213. Kulkarni, A. R.; Sholl, D. S., Screening of Copper Open Metal Site MOFs for Olefin/Paraffin Separations Using DFT-Derived Force Fields. *J. Phys. Chem. C* **2016,** *120* (40), 23044-23054.
214. Wang, Y.; Hu, Z.; Cheng, Y.; Zhao, D., Silver-Decorated Hafnium Metal–Organic Framework for Ethylene/Ethane Separation. *Ind. Eng. Chem. Res.* **2017,** *56* (15), 4508-4516.
215. He, Y.; Krishna, R.; Chen, B., Metal–organic frameworks with potential for energy-efficient adsorptive separation of light hydrocarbons. *Energy Environ. Sci.* **2012,** *5* (10), 9107.
216. Pillai, R. S.; Pinto, M. L.; Pires, J.; Jorge, M.; Gomes, J. R., Understanding Gas adsorption selectivity in IRMOF-8 using molecular simulation. *ACS Appl. Mater. Interfaces* **2015,** *7* (1), 624-37.
217. Mersmann, A.; Fill, B.; Hartmann, R.; Maurer, S., The Potential of Energy Saving by Gas-Phase Adsorption Processes. *Chem. Eng. Technol.* **2000,** *23* (11), 937-944.
218. Ren, T.; Patel, M.; Blok, K., Olefins from conventional and heavy feedstocks: Energy use in steam cracking and alternative processes. *Energy* **2006,** *31* (4), 425-451.
219. Chen, Y.; Wu, H.; Lv, D.; Shi, R.; Chen, Y.; Xia, Q.; Li, Z., Highly Adsorptive Separation of Ethane/Ethylene by An Ethane-Selective MOF MIL-142A. *Ind. Eng. Chem. Res.* **2018,** *57* (11), 4063-4069.
220. Lv, D.; Shi, R.; Chen, Y.; Wu, Y.; Wu, H.; Xi, H.; Xia, Q.; Li, Z., Selective Adsorption of Ethane over Ethylene in PCN-245: Impacts of Interpenetrated Adsorbent. *ACS Appl. Mater. Interfaces* **2018,** *10* (9), 8366-8373.
221. Pires, J.; Pinto, M. L.; Saini, V. K., Ethane selective IRMOF-8 and its significance in ethane-ethylene separation by adsorption. *ACS Appl. Mater. Interfaces* **2014,** *6* (15), 12093-9.
222. Chen, Y.; Qiao, Z.; Wu, H.; Lv, D.; Shi, R.; Xia, Q.; Zhou, J.; Li, Z., An ethane-trapping MOF PCN-250 for highly selective adsorption of ethane over ethylene. *Chem. Eng. Sci.* **2018,** *175*, 110-117.
223. Böhme, U.; Barth, B.; Paula, C.; Kuhnt, A.; Schwieger, W.; Mundstock, A.; Caro, J.; Hartmann, M., Ethene/Ethane and Propene/Propane Separation via the Olefin and Paraffin Selective Metal–Organic Framework Adsorbents CPO-27 and ZIF-8. *Langmuir* **2013,** *29* (27), 8592-8600.
224. Liang, W.; Xu, F.; Zhou, X.; Xiao, J.; Xia, Q.; Li, Y.; Li, Z., Ethane selective adsorbent Ni(bdc)(ted)0.5 with high uptake and its significance in adsorption separation of ethane and ethylene. *Chem. Eng. Sci.* **2016,** *148*, 275-281.
225. Gücüyener, C.; van den Bergh, J.; Gascon, J.; Kapteijn, F., Ethane/Ethene Separation Turned on Its Head: Selective Ethane Adsorption on the Metal−Organic Framework ZIF-7 through a Gate-Opening Mechanism. *J. Am. Chem. Soc.* **2010,** *132* (50), 17704-17706.

226. Hartmann, M.; Böhme, U.; Hovestadt, M.; Paula, C., Adsorptive Separation of Olefin/Paraffin Mixtures with ZIF-4. *Langmuir* **2015,** *31* (45), 12382-12389.
227. Lin, R.-B.; Wu, H.; Li, L.; Tang, X.-L.; Li, Z.; Gao, J.; Cui, H.; Zhou, W.; Chen, B., Boosting Ethane/Ethylene Separation within Isoreticular Ultramicroporous Metal-Organic Frameworks. *J. Am. Chem. Soc.* **2018,** *140* (40), 12940-12946.
228. Krishna, R., Screening metal–organic frameworks for mixture separations in fixed-bed adsorbers using a combined selectivity/capacity metric. *RSC Adv.* **2017,** *7* (57), 35724-35737.
229. Li, L.; Lin, R.-B.; Krishna, R.; Li, H.; Xiang, S.; Wu, H.; Li, J.; Zhou, W.; Chen, B., Ethane/ethylene separation in a metal-organic framework with iron-peroxo sites. *Science* **2018,** *362* (6413), 443-446.
230. Wang, H.-N.; Liu, F.-H.; Zhu, Y.-F.; Wang, X.-L.; Chen, Z.-H.; Su, Z.-M., Synthesis and property investigation of two hexa-cobalt cluster based porous coordination polymers. *CrystEngComm* **2013,** *15* (37), 7402.
231. First, E. L.; Floudas, C. A., MOFomics: Computational pore characterization of metal–organic frameworks. *Microporous Mesoporous Mater.* **2013,** *165*, 32-39.
232. Dubbeldam, D.; Calero, S.; Ellis, D. E.; Snurr, R. Q., RASPA: molecular simulation software for adsorption and diffusion in flexible nanoporous materials. *Mol. Simul.* **2016,** *42* (2), 81-101.
233. Grimme, S.; Ehrlich, S.; Goerigk, L., Effect of the damping function in dispersion corrected density functional theory. *J. Comput. Chem.* **2011,** *32* (7), 1456-1465.
234. Kresse, G.; Hafner, J., Ab initio molecular dynamics for open-shell transition metals. *Physical Review B* **1993,** *48* (17), 13115-13118.
235. Eguchi, R.; Uchida, S.; Mizuno, N., Inverse and High CO2/C2H2 Sorption Selectivity in Flexible Organic–Inorganic Ionic Crystals. *Angew. Chem. Int. Ed.* **2012,** *51* (7), 1635-1639.
236. Reid, C. R.; Thomas, K. M., Adsorption Kinetics and Size Exclusion Properties of Probe Molecules for the Selective Porosity in a Carbon Molecular Sieve Used for Air Separation. *J. Phys. Chem. B* **2001,** *105* (43), 10619-10629.
237. Li, Y.; Yi, H.; Tang, X.; Li, F.; Yuan, Q., Adsorption separation of CO2/CH4 gas mixture on the commercial zeolites at atmospheric pressure. *Chem. Eng. J.* **2013,** *229*, 50-56.
238. Park, K. S.; Ni, Z.; Côté, A. P.; Choi, J. Y.; Huang, R.; Uribe-Romo, F. J.; Chae, H. K.; O'Keeffe, M.; Yaghi, O. M., Exceptional chemical and thermal stability of zeolitic imidazolate frameworks. *Proc. Natl. Acad. Sci.* **2006,** *103* (27), 10186-10191.
239. Rigaku; Rigaku Corporation: Tokyo, J. 1996.
240. Sheldrick, G. M., A short history of SHELX. *Acta Crystallogr A* **2008,** *64* (Pt 1), 112-22.
241. Dolomanov, O. V.; Bourhis, L. J.; Gildea, R. J.; Howard, J. A. K.; Puschmann, H., OLEX2: a complete structure solution, refinement and analysis program. *J. Appl. Crystallogr.* **2009,** *42* (2), 339-341.
242. Willems, T. F.; Rycroft, C. H.; Kazi, M.; Meza, J. C.; Haranczyk, M., Algorithms and tools for high-throughput geometry-based analysis of crystalline porous materials. *Microporous Mesoporous Mater.* **2012,** *149* (1), 134-141.
243. Perdew, J. P.; Burke, K.; Ernzerhof, M., Generalized Gradient Approximation Made Simple. *Phys. Rev. Lett.* **1996,** *77* (18), 3865-3868.
244. *Material studio*. 8th ed.; Accelrys, San Diego, 2015.
245. Xue, M.; Liu, Y.; Schaffino, R. M.; Xiang, S.; Zhao, X.; Zhu, G.-S.; Qiu, S.-L.; Chen, B., New Prototype Isoreticular Metal−Organic Framework Zn4O(FMA)3 for Gas Storage. *Inorg. Chem.* **2009,** *48* (11), 4649-4651.
246. Spanopoulos, I.; Tsangarakis, C.; Klontzas, E.; Tylianakis, E.; Froudakis, G.; Adil, K.; Belmabkhout, Y.; Eddaoudi, M.; Trikalitis, P. N., Reticular Synthesis of HKUST-like tbo-MOFs with Enhanced CH4 Storage. *J. Am. Chem. Soc.* **2016,** *138* (5), 1568-1574.

247. Alezi, D.; Belmabkhout, Y.; Suyetin, M.; Bhatt, P. M.; Weseliński, Ł. J.; Solovyeva, V.; Adil, K.; Spanopoulos, I.; Trikalitis, P. N.; Emwas, A.-H.; Eddaoudi, M., MOF Crystal Chemistry Paving the Way to Gas Storage Needs: Aluminum-Based soc-MOF for CH4, O2, and CO2 Storage. *J. Am. Chem. Soc.* **2015,** *137* (41), 13308-13318.
248. Schukraft, G. E. M.; Ayala, S.; Dick, B. L.; Cohen, S. M., Isoreticular expansion of polyMOFs achieves high surface area materials. *Chem. Commun.* **2017,** *53* (77), 10684-10687.
249. Ma, L.; Falkowski, J. M.; Abney, C.; Lin, W., A series of isoreticular chiral metal–organic frameworks as a tunable platform for asymmetric catalysis. *Nature Chem.* **2010,** *2*, 838.
250. Song, F.; Wang, C.; Falkowski, J. M.; Ma, L.; Lin, W., Isoreticular Chiral Metal−Organic Frameworks for Asymmetric Alkene Epoxidation: Tuning Catalytic Activity by Controlling Framework Catenation and Varying Open Channel Sizes. *J. Am. Chem. Soc.* **2010,** *132* (43), 15390-15398.
251. Yao, Q.; Bermejo Gómez, A.; Su, J.; Pascanu, V.; Yun, Y.; Zheng, H.; Chen, H.; Liu, L.; Abdelhamid, H. N.; Martín-Matute, B.; Zou, X., Series of Highly Stable Isoreticular Lanthanide Metal–Organic Frameworks with Expanding Pore Size and Tunable Luminescent Properties. *Chem. Mater.* **2015,** *27* (15), 5332-5339.
252. Liu, J.-Q.; Wu, J.; Jia, Z.-B.; Chen, H.-L.; Li, Q.-L.; Sakiyama, H.; Soares, T.; Ren, F.; Daiguebonne, C.; Guillou, O.; Ng, S. W., Two isoreticular metal–organic frameworks with CdSO4-like topology: selective gas sorption and drug delivery. *Dalton Trans.* **2014,** *43* (46), 17265-17273.
253. Chen, W.; Wu, C., Synthesis, functionalization, and applications of metal–organic frameworks in biomedicine. *Dalton Trans.* **2018,** *47* (7), 2114-2133.
254. Kotzabasaki, M.; Tylianakis, E.; Klontzas, E.; Froudakis, G. E., OH-functionalization strategy in Metal-Organic Frameworks for drug delivery. *Chem. Phys. Lett.* **2017,** *685*, 114-118.
255. Tchalala, M. R.; Bhatt, P. M.; Chappanda, K. N.; Tavares, S. R.; Adil, K.; Belmabkhout, Y.; Shkurenko, A.; Cadiau, A.; Heymans, N.; De Weireld, G.; Maurin, G.; Salama, K. N.; Eddaoudi, M., Fluorinated MOF platform for selective removal and sensing of SO2 from flue gas and air. *Nat. Commun.* **2019,** *10* (1), 1328.
256. Hu, X.-L.; Liu, F.-H.; Wang, H.-N.; Qin, C.; Sun, C.-Y.; Su, Z.-M.; Liu, F.-C., Controllable synthesis of isoreticular pillared-layer MOFs: gas adsorption, iodine sorption and sensing small molecules. *J. Mater. Chem. A* **2014,** *2* (36), 14827-14834.
257. Lu, W.; Wei, Z.; Gu, Z.-Y.; Liu, T.-F.; Park, J.; Park, J.; Tian, J.; Zhang, M.; Zhang, Q.; Gentle Iii, T.; Bosch, M.; Zhou, H.-C., Tuning the structure and function of metal–organic frameworks via linker design. *Chem. Soc. Rev.* **2014,** *43* (16), 5561-5593.
258. Cohen, S. M., Postsynthetic Methods for the Functionalization of Metal–Organic Frameworks. *Chem. Rev.* **2012,** *112* (2), 970-1000.
259. Wang, H.; Peng, J.; Li, J., Ligand Functionalization in Metal–Organic Frameworks for Enhanced Carbon Dioxide Adsorption. *The Chemical Record* **2016,** *16* (3), 1298-1310.
260. Lyu, J.; Zhang, X.; Otake, K.-i.; Wang, X.; Li, P.; Li, Z.; Chen, Z.; Zhang, Y.; Wasson, M. C.; Yang, Y.; Bai, P.; Guo, X.; Islamoglu, T.; Farha, O. K., Topology and porosity control of metal–organic frameworks through linker functionalization. *Chem. Sci.* **2019,** *10* (4), 1186-1192.
261. Qiao, Z.; Wang, N.; Jiang, J.; Zhou, J., Design of amine-functionalized metal–organic frameworks for CO2 separation: the more amine, the better? *Chem. Commun.* **2016,** *52* (5), 974-977.
262. Huang, X. C.; Lin, Y. Y.; Zhang, J. P.; Chen, X. M., Ligand‐directed strategy for zeolite‐type metal‐organic frameworks: zinc (II) imidazolates with unusual zeolitic topologies. *Angew. Chem. Int. Ed.* **2006,** *45* (10), 1557-1559.

263. Zhao, Y.; Wu, H.; Emge, T. J.; Gong, Q.; Nijem, N.; Chabal, Y. J.; Kong, L.; Langreth, D. C.; Liu, H.; Zeng, H., Enhancing gas adsorption and separation capacity through ligand functionalization of microporous metal–organic framework structures. *Chem. Eur. J.* **2011,** *17* (18), 5101-5109.
264. Yuan, D.; Zhao, D.; Sun, D.; Zhou, H. C., An Isoreticular Series of Metal–Organic Frameworks with Dendritic Hexacarboxylate Ligands and Exceptionally High Gas‐Uptake Capacity. *Angew. Chem. Int. Ed.* **2010,** *49* (31), 5357-5361.
265. Jasuja, H.; Huang, Y.-g.; Walton, K. S., Adjusting the stability of metal–organic frameworks under humid conditions by ligand functionalization. *Langmuir* **2012,** *28* (49), 16874-16880.
266. Xu, X.; Yang, F.; Chen, S.-L.; He, J.; Xu, Y.; Wei, W., Dynamic behaviours of a rationally prepared flexible MOF by postsynthetic modification of ligand struts. *Chem. Commun.* **2017,** *53* (22), 3220-3223.
267. Lin, Z.-J.; Lü, J.; Hong, M.; Cao, R., Metal–organic frameworks based on flexible ligands (FL-MOFs): structures and applications. *Chem. Soc. Rev.* **2014,** *43* (16), 5867-5895.
268. Zhang, J.-P.; Zhou, H.-L.; Zhou, D.-D.; Liao, P.-Q.; Chen, X.-M., Controlling flexibility of metal–organic frameworks. *Natl. Sci. Rev.* **2017,** *5* (6), 907-919.
269. Chang, Z.; Yang, D.-H.; Xu, J.; Hu, T.-L.; Bu, X.-H., Flexible Metal–Organic Frameworks: Recent Advances and Potential Applications. *Adv. Mater.* **2015,** *27* (36), 5432-5441.
270. Noro, S.-i.; Nakamura, T., Fluorine-functionalized metal–organic frameworks and porous coordination polymers. *NPG Asia Mater.* **2017,** *9*, e433.
271. Kanoo, P.; Reddy, S. K.; Kumari, G.; Haldar, R.; Narayana, C.; Balasubramanian, S.; Maji, T. K., Unusual room temperature CO 2 uptake in a fluoro-functionalized MOF: insight from Raman spectroscopy and theoretical studies. *Chem. Commun.* **2012,** *48* (68), 8487-8489.
272. Pachfule, P.; Chen, Y.; Jiang, J.; Banerjee, R., Fluorinated metal–organic frameworks: advantageous for higher H2 and CO2 adsorption or not? *Chem. Eur. J.* **2012,** *18* (2), 688-694.
273. Pal, T. K.; De, D.; Senthilkumar, S.; Neogi, S.; Bharadwaj, P. K., A Partially Fluorinated, Water-Stable Cu (II)–MOF Derived via Transmetalation: Significant Gas Adsorption with High CO2 Selectivity and Catalysis of Biginelli Reactions. *Inorg. Chem.* **2016,** *55* (16), 7835-7842.
274. Fairen-Jimenez, D.; Moggach, S. A.; Wharmby, M. T.; Wright, P. A.; Parsons, S.; Düren, T., Opening the Gate: Framework Flexibility in ZIF-8 Explored by Experiments and Simulations. *J. Am. Chem. Soc.* **2011,** *133* (23), 8900-8902.
275. Hahm, H.; Yoo, K.; Ha, H.; Kim, M., Aromatic Substituent Effects on the Flexibility of Metal–Organic Frameworks. *Inorg. Chem.* **2016,** *55* (15), 7576-7581.
276. Henke, S.; Schneemann, A.; Wütscher, A.; Fischer, R. A., Directing the Breathing Behaviour of Pillared-Layered Metal–Organic Frameworks via a Systematic Library of Functionalized Linkers Bearing Flexible Substituents. *J. Am. Chem. Soc.* **2012,** *134* (22), 9464-9474.
277. Devic, T.; Horcajada, P.; Serre, C.; Salles, F.; Maurin, G.; Moulin, B.; Heurtaux, D.; Clet, G.; Vimont, A.; Grenèche, J.-M.; Ouay, B. L.; Moreau, F.; Magnier, E.; Filinchuk, Y.; Marrot, J.; Lavalley, J.-C.; Daturi, M.; Férey, G., Functionalization in Flexible Porous Solids: Effects on the Pore Opening and the Host−Guest Interactions. *J. Am. Chem. Soc.* **2010,** *132* (3), 1127-1136.
278. Nakagawa, K.; Tanaka, D.; Horike, S.; Shimomura, S.; Higuchi, M.; Kitagawa, S., Enhanced selectivity of CO2 from a ternary gas mixture in an interdigitated porous framework. *Chem. Commun.* **2010,** *46* (24), 4258-4260.

279. Chen, X. Y.; Vinh-Thang, H.; Rodrigue, D.; Kaliaguine, S., Amine-Functionalized MIL-53 Metal–Organic Framework in Polyimide Mixed Matrix Membranes for CO2/CH4 Separation. *Ind. Eng. Chem. Res.* **2012,** *51* (19), 6895-6906.
280. Nijem, N.; Wu, H.; Canepa, P.; Marti, A.; Balkus, K. J.; Thonhauser, T.; Li, J.; Chabal, Y. J., Tuning the Gate Opening Pressure of Metal–Organic Frameworks (MOFs) for the Selective Separation of Hydrocarbons. *J. Am. Chem. Soc.* **2012,** *134* (37), 15201-15204.
281. Lin, R.-B.; Li, L.; Wu, H.; Arman, H.; Li, B.; Lin, R.-G.; Zhou, W.; Chen, B., Optimized Separation of Acetylene from Carbon Dioxide and Ethylene in a Microporous Material. *J. Am. Chem. Soc.* **2017,** *139* (23), 8022-8028.
282. Casper, J. K., *Greenhouse gases: worldwide impacts*. Infobase Publishing: 2010.
283. Monastersky, R., Global carbon dioxide levels near worrisome milestone. *Nature* **2013,** *497* (7447), 13.
284. Mokhatab, S.; Poe, W. A.; Mak, J. Y., *Handbook of natural gas transmission and processing: principles and practices*. Gulf professional publishing: 2018.
285. Chen, B.; Xiang, S.; Qian, G., Metal−Organic Frameworks with Functional Pores for Recognition of Small Molecules. *Acc. Chem. Res.* **2010,** *43* (8), 1115-1124.
286. Lin, Y.; Kong, C.; Zhang, Q.; Chen, L., Metal-Organic Frameworks for Carbon Dioxide Capture and Methane Storage. *Adv. Energy Mater.* **2017,** *7* (4), 1601296.
287. Madden David, G.; Scott Hayley, S.; Kumar, A.; Chen, K.-J.; Sanii, R.; Bajpai, A.; Lusi, M.; Curtin, T.; Perry John, J.; Zaworotko Michael, J., Flue-gas and direct-air capture of CO2 by porous metal–organic materials. *Philos. Trans. Royal Soc. A* **2017,** *375* (2084), 20160025.
288. Li, J.-R.; Ma, Y.; McCarthy, M. C.; Sculley, J.; Yu, J.; Jeong, H.-K.; Balbuena, P. B.; Zhou, H.-C., Carbon dioxide capture-related gas adsorption and separation in metal-organic frameworks. *Coord. Chem. Rev.* **2011,** *255* (15), 1791-1823.
289. Trickett, C. A.; Helal, A.; Al-Maythalony, B. A.; Yamani, Z. H.; Cordova, K. E.; Yaghi, O. M., The chemistry of metal–organic frameworks for CO2 capture, regeneration and conversion. *Nat. Rev. Mater.* **2017,** *2*, 17045.
290. Li, B.; Wen, H.-M.; Cui, Y.; Zhou, W.; Qian, G.; Chen, B., Emerging Multifunctional Metal–Organic Framework Materials. *Adv. Mater.* **2016,** *28* (40), 8819-8860.
291. Chen, K.-J.; Madden, D. G.; Pham, T.; Forrest, K. A.; Kumar, A.; Yang, Q.-Y.; Xue, W.; Space, B.; Perry IV, J. J.; Zhang, J.-P.; Chen, X.-M.; Zaworotko, M. J., Tuning Pore Size in Square-Lattice Coordination Networks for Size-Selective Sieving of CO2. *Angew. Chem. Int. Ed.* **2016,** *55* (35), 10268-10272.
292. Karra, J. R.; Walton, K. S., Effect of Open Metal Sites on Adsorption of Polar and Nonpolar Molecules in Metal−Organic Framework Cu-BTC. *Langmuir* **2008,** *24* (16), 8620-8626.
293. Couck, S.; Denayer, J. F. M.; Baron, G. V.; Rémy, T.; Gascon, J.; Kapteijn, F., An Amine-Functionalized MIL-53 Metal−Organic Framework with Large Separation Power for CO2 and CH4. *J. Am. Chem. Soc.* **2009,** *131* (18), 6326-6327.
294. Zhang, Z.; Yao, Z.-Z.; Xiang, S.; Chen, B., Perspective of microporous metal–organic frameworks for CO2 capture and separation. *Energy Environ. Sci.* **2014,** *7* (9), 2868-2899.
295. Stylianou, K. C.; Warren, J. E.; Chong, S. Y.; Rabone, J.; Bacsa, J.; Bradshaw, D.; Rosseinsky, M. J., CO2 selectivity of a 1D microporous adenine-based metal–organic framework synthesised in water. *Chem. Commun.* **2011,** *47* (12), 3389-3391.
296. Phan, A.; Doonan, C. J.; Uribe-Romo, F. J.; Knobler, C. B.; O'Keeffe, M.; Yaghi, O. M., Synthesis, Structure, and Carbon Dioxide Capture Properties of Zeolitic Imidazolate Frameworks. *Acc. Chem. Res.* **2010,** *43* (1), 58-67.
297. Hamon, L.; Jolimaître, E.; Pirngruber, G. D., CO2 and CH4 separation by adsorption using Cu-BTC metal− organic framework. *Ind. Eng. Chem. Res.* **2010,** *49* (16), 7497-7503.

298. Llewellyn, P. L.; Bourrelly, S.; Serre, C.; Vimont, A.; Daturi, M.; Hamon, L.; De Weireld, G.; Chang, J.-S.; Hong, D.-Y.; Kyu Hwang, Y.; Hwa Jhung, S.; Férey, G., High Uptakes of CO2 and CH4 in Mesoporous Metal—Organic Frameworks MIL-100 and MIL-101. *Langmuir* **2008,** *24* (14), 7245-7250.
299. Yang, Q.; Wiersum, A. D.; Llewellyn, P. L.; Guillerm, V.; Serre, C.; Maurin, G., Functionalizing porous zirconium terephthalate UiO-66(Zr) for natural gas upgrading: a computational exploration. *Chem. Commun.* **2011,** *47* (34), 9603-9605.
300. Kizzie, A. C.; Wong-Foy, A. G.; Matzger, A. J., Effect of Humidity on the Performance of Microporous Coordination Polymers as Adsorbents for CO2 Capture. *Langmuir* **2011,** *27* (10), 6368-6373.
301. Yu, J.; Balbuena, P. B., Water Effects on Postcombustion CO2 Capture in Mg-MOF-74. *J. Phys. Chem. C* **2013,** *117* (7), 3383-3388.
302. Demessence, A.; D'Alessandro, D. M.; Foo, M. L.; Long, J. R., Strong CO2 Binding in a Water-Stable, Triazolate-Bridged Metal−Organic Framework Functionalized with Ethylenediamine. *J. Am. Chem. Soc.* **2009,** *131* (25), 8784-8786.
303. Tang, E.; Dai, Y.-M.; Zhang, J.; Li, Z.-J.; Yao, Y.-G.; Zhang, J.; Huang, X.-D., Two Cobalt(II) 5-Aminoisophthalate Complexes and Their Stable Supramolecular Microporous Frameworks. *Inorg. Chem.* **2006,** *45* (16), 6276-6281.
304. Tian, C.-B.; He, C.; Han, Y.-H.; Wei, Q.; Li, Q.-P.; Lin, P.; Du, S.-W., Four New MnII Inorganic–Organic Hybrid Frameworks with Diverse Inorganic Magnetic Chain's Sequences: Syntheses, Structures, Magnetic, NLO, and Dielectric Properties. *Inorg. Chem.* **2015,** *54* (6), 2560-2571.
305. Xiang, S.; He, Y.; Zhang, Z.; Wu, H.; Zhou, W.; Krishna, R.; Chen, B., Microporous metal-organic framework with potential for carbon dioxide capture at ambient conditions. *Nat. Commun.* **2012,** *3*, 954.
306. Rufford, T. E.; Smart, S.; Watson, G. C. Y.; Graham, B. F.; Boxall, J.; Diniz da Costa, J. C.; May, E. F., The removal of CO2 and N2 from natural gas: A review of conventional and emerging process technologies. *J. Pet. Sci. Eng.* **2012,** *94-95*, 123-154.
307. Yeo, Z. Y.; Chew, T. L.; Zhu, P. W.; Mohamed, A. R.; Chai, S.-P., Conventional processes and membrane technology for carbon dioxide removal from natural gas: A review. *J. Nat. Gas Chem.* **2012,** *21* (3), 282-298.
308. Granada, A.; Karra, S. B.; Senkan, S. M., Conversion of methane into acetylene and ethylene by the chlorine-catalyzed oxidative-pyrolysis (CCOP) process. 1. Oxidative pyrolysis of chloromethane. *Ind. Eng. Chem. Res.* **1987,** *26* (9), 1901-1905.
309. Li, X.-Y.; Li, Y.-Z.; Yang, Y.; Hou, L.; Wang, Y.-Y.; Zhu, Z., Efficient light hydrocarbon separation and CO2 capture and conversion in a stable MOF with oxalamide-decorated polar tubes. *Chem. Commun.* **2017,** *53* (96), 12970-12973.
310. Yang, H.; Xu, Z.; Fan, M.; Gupta, R.; Slimane, R. B.; Bland, A. E.; Wright, I., Progress in carbon dioxide separation and capture: A review. *J. Environ. Sci.* **2008,** *20* (1), 14-27.
311. Haszeldine, R. S., Carbon Capture and Storage: How Green Can Black Be? *Science* **2009,** *325* (5948), 1647-1652.
312. Wang, M.; Lawal, A.; Stephenson, P.; Sidders, J.; Ramshaw, C., Post-combustion CO2 capture with chemical absorption: a state-of-the-art review. *Chem. Eng. Res. Des.* **2011,** *89* (9), 1609-1624.
313. Zhou, H.-C. J.; Kitagawa, S., Metal–Organic Frameworks (MOFs). *Chem. Soc. Rev.* **2014,** *43* (16), 5415-5418.
314. Matsuda, R.; Kitaura, R.; Kitagawa, S.; Kubota, Y.; Belosludov, R. V.; Kobayashi, T. C.; Sakamoto, H.; Chiba, T.; Takata, M.; Kawazoe, Y.; Mita, Y., Highly controlled acetylene accommodation in a metal–organic microporous material. *Nature* **2005,** *436*, 238.

315. Zhao, X.; Wang, Y.; Li, D.-S.; Bu, X.; Feng, P., Metal–Organic Frameworks for Separation. *Adv. Mater.* **2018,** *30* (37), 1705189.
316. Lin, R.-B.; Li, L.; Zhou, H.-L.; Wu, H.; He, C.; Li, S.; Krishna, R.; Li, J.; Zhou, W.; Chen, B., Molecular sieving of ethylene from ethane using a rigid metal–organic framework. *Nat. Mater.* **2018,** *17* (12), 1128-1133.
317. Cui, X.; Chen, K.; Xing, H.; Yang, Q.; Krishna, R.; Bao, Z.; Wu, H.; Zhou, W.; Dong, X.; Han, Y.; Li, B.; Ren, Q.; Zaworotko, M. J.; Chen, B., Pore chemistry and size control in hybrid porous materials for acetylene capture from ethylene. *Science* **2016,** *353* (6295), 141-144.
318. Moreau, F.; da Silva, I.; Al Smail, N. H.; Easun, T. L.; Savage, M.; Godfrey, H. G. W.; Parker, S. F.; Manuel, P.; Yang, S.; Schröder, M., Unravelling exceptional acetylene and carbon dioxide adsorption within a tetra-amide functionalized metal-organic framework. *Nat. Commun.* **2017,** *8*, 14085.
319. Xiang, S.; Zhou, W.; Gallegos, J. M.; Liu, Y.; Chen, B., Exceptionally High Acetylene Uptake in a Microporous Metal−Organic Framework with Open Metal Sites. *J. Am. Chem. Soc.* **2009,** *131* (34), 12415-12419.
320. Li, P.; He, Y.; Zhao, Y.; Weng, L.; Wang, H.; Krishna, R.; Wu, H.; Zhou, W.; O'Keeffe, M.; Han, Y.; Chen, B., A Rod-Packing Microporous Hydrogen-Bonded Organic Framework for Highly Selective Separation of C2H2/CO2 at Room Temperature. *Angew. Chem. Int. Ed.* **2015,** *54* (2), 574-577.
321. Lee, J.; Chuah, C. Y.; Kim, J.; Kim, Y.; Ko, N.; Seo, Y.; Kim, K.; Bae, T. H.; Lee, E., Separation of Acetylene from Carbon Dioxide and Ethylene by a Water-Stable Microporous Metal–Organic Framework with Aligned Imidazolium Groups inside the Channels. *angew. chem. int. ed.* **2018,** *57* (26), 7869-7873.
322. Luo, F.; Yan, C.; Dang, L.; Krishna, R.; Zhou, W.; Wu, H.; Dong, X.; Han, Y.; Hu, T.-L.; O'Keeffe, M.; Wang, L.; Luo, M.; Lin, R.-B.; Chen, B., UTSA-74: A MOF-74 Isomer with Two Accessible Binding Sites per Metal Center for Highly Selective Gas Separation. *J. Am. Chem. Soc.* **2016,** *138* (17), 5678-5684.
323. Zhang, J.-P.; Chen, X.-M., Optimized Acetylene/Carbon Dioxide Sorption in a Dynamic Porous Crystal. *J. Am. Chem. Soc.* **2009,** *131* (15), 5516-5521.
324. Zhang, L.; Jiang, K.; Li, L.; Xia, Y.-P.; Hu, T.-L.; Yang, Y.; Cui, Y.; Li, B.; Chen, B.; Qian, G., Efficient separation of C2H2 from C2H2/CO2 mixtures in an acid–base resistant metal–organic framework. *Chem. Commun.* **2018,** *54* (38), 4846-4849.
325. Peng, Y.-L.; Pham, T.; Li, P.; Wang, T.; Chen, Y.; Chen, K.-J.; Forrest, K. A.; Space, B.; Cheng, P.; Zaworotko, M. J.; Zhang, Z., Robust Ultramicroporous Metal–Organic Frameworks with Benchmark Affinity for Acetylene. *Angew. Chem. Int. Ed.* **2018,** *57* (34), 10971-10975.
326. Scott, H. S.; Shivanna, M.; Bajpai, A.; Madden, D. G.; Chen, K.-J.; Pham, T.; Forrest, K. A.; Hogan, A.; Space, B.; Perry Iv, J. J.; Zaworotko, M. J., Highly Selective Separation of C2H2 from CO2 by a New Dichromate-Based Hybrid Ultramicroporous Material. *ACS Appl. Mater. Interfaces* **2017,** *9* (39), 33395-33400.
327. Chen, K.-J.; Scott, Hayley S.; Madden, David G.; Pham, T.; Kumar, A.; Bajpai, A.; Lusi, M.; Forrest, Katherine A.; Space, B.; Perry, John J.; Zaworotko, Michael J., Benchmark C2H2/CO2 and CO2/C2H2 Separation by Two Closely Related Hybrid Ultramicroporous Materials. *Chem* **2016,** *1* (5), 753-765.
328. Duan, X.; Wang, H.; Ji, Z.; Cui, Y.; Yang, Y.; Qian, G., A novel metal-organic framework for high storage and separation of acetylene at room temperature. *J. Solid State Chem.* **2016,** *241*, 152-156.
329. Duan, X.; Zhang, Q.; Cai, J.; Yang, Y.; Cui, Y.; He, Y.; Wu, C.; Krishna, R.; Chen, B.; Qian, G., A new metal–organic framework with potential for adsorptive separation of methane from carbon dioxide, acetylene, ethylene, and ethane established by simulated breakthrough experiments. *J. Mater. Chem. A* **2014,** *2* (8), 2628-2633.

330. Yang, W.; Davies, A. J.; Lin, X.; Suyetin, M.; Matsuda, R.; Blake, A. J.; Wilson, C.; Lewis, W.; Parker, J. E.; Tang, C. C.; George, M. W.; Hubberstey, P.; Kitagawa, S.; Sakamoto, H.; Bichoutskaia, E.; Champness, N. R.; Yang, S.; Schröder, M., Selective CO2 uptake and inverse CO2/C2H2 selectivity in a dynamic bifunctional metal–organic framework. *Chem. Sci.* **2012,** *3* (10), 2993-2999.
331. Noro, S.-i.; Tanaka, D.; Sakamoto, H.; Shimomura, S.; Kitagawa, S.; Takeda, S.; Uemura, K.; Kita, H.; Akutagawa, T.; Nakamura, T., Selective Gas Adsorption in One-Dimensional, Flexible CuII Coordination Polymers with Polar Units. *Chem. Mater.* **2009,** *21* (14), 3346-3355.
332. Yanai, N.; Kitayama, K.; Hijikata, Y.; Sato, H.; Matsuda, R.; Kubota, Y.; Takata, M.; Mizuno, M.; Uemura, T.; Kitagawa, S., Gas detection by structural variations of fluorescent guest molecules in a flexible porous coordination polymer. *Nat. Mater.* **2011,** *10*, 787.
333. Foo, M. L.; Matsuda, R.; Hijikata, Y.; Krishna, R.; Sato, H.; Horike, S.; Hori, A.; Duan, J.; Sato, Y.; Kubota, Y.; Takata, M.; Kitagawa, S., An Adsorbate Discriminatory Gate Effect in a Flexible Porous Coordination Polymer for Selective Adsorption of CO2 over C2H2. *J. Am. Chem. Soc.* **2016,** *138* (9), 3022-3030.
334. Duan, J.; Higuchi, M.; Foo, M. L.; Horike, S.; Rao, K. P.; Kitagawa, S., A Family of Rare Earth Porous Coordination Polymers with Different Flexibility for CO2/C2H4 and CO2/C2H6 Separation. *Inorg. Chem.* **2013,** *52* (14), 8244-8249.
335. Horike, S.; Kishida, K.; Watanabe, Y.; Inubushi, Y.; Umeyama, D.; Sugimoto, M.; Fukushima, T.; Inukai, M.; Kitagawa, S., Dense Coordination Network Capable of Selective CO2 Capture from C1 and C2 Hydrocarbons. *J. Am. Chem. Soc.* **2012,** *134* (24), 9852-9855.
336. Li, L.; Wang, J.; Zhang, Z.; Yang, Q.; Yang, Y.; Su, B.; Bao, Z.; Ren, Q., Inverse Adsorption Separation of CO2/C2H2 Mixture in Cyclodextrin-Based Metal–Organic Frameworks. *ACS Appl. Mater. Interfaces* **2019,** *11* (2), 2543-2550.
337. Krishna, R., Methodologies for evaluation of metal–organic frameworks in separation applications. *RSC Adv.* **2015,** *5* (64), 52269-52295.
338. Silva, F. A. D.; Rodrigues, A. E., Propylene/propane separation by vacuum swing adsorption using 13X zeolite. *AIChE J.* **2001,** *47* (2), 341-357.
339. Cavenati, S.; Grande, C. A.; Rodrigues, A. E., Adsorption Equilibrium of Methane, Carbon Dioxide, and Nitrogen on Zeolite 13X at High Pressures. *J. Chem. Eng. Data* **2004,** *49* (4), 1095-1101.
340. McEwen, J.; Hayman, J.-D.; Ozgur Yazaydin, A., A comparative study of CO2, CH4 and N2 adsorption in ZIF-8, Zeolite-13X and BPL activated carbon. *Chem. Phys.* **2013,** *412*, 72-76.
341. Delgado, J. A.; Águeda, V. I.; Uguina, M. A.; Sotelo, J. L.; Brea, P.; Grande, C. A., Adsorption and Diffusion of H2, CO, CH4, and CO2 in BPL Activated Carbon and 13X Zeolite: Evaluation of Performance in Pressure Swing Adsorption Hydrogen Purification by Simulation. *Ind. Eng. Chem. Res.* **2014,** *53* (40), 15414-15426.
342. Herm, Z. R.; Swisher, J. A.; Smit, B.; Krishna, R.; Long, J. R., Metal−Organic Frameworks as Adsorbents for Hydrogen Purification and Precombustion Carbon Dioxide Capture. *J. Am. Chem. Soc.* **2011,** *133* (15), 5664-5667.
343. McDonald, T. M.; Lee, W. R.; Mason, J. A.; Wiers, B. M.; Hong, C. S.; Long, J. R., Capture of Carbon Dioxide from Air and Flue Gas in the Alkylamine-Appended Metal–Organic Framework mmen-Mg2(dobpdc). *J. Am. Chem. Soc.* **2012,** *134* (16), 7056-7065.
344. McDonald, T. M.; D'Alessandro, D. M.; Krishna, R.; Long, J. R., Enhanced carbon dioxide capture upon incorporation of N,N′-dimethylethylenediamine in the metal‐organic framework CuBTTri. *Chem. Sci.* **2011,** *2* (10), 2022.

345. An, J.; Geib, S. J.; Rosi, N. L., High and Selective CO2 Uptake in a Cobalt Adeninate Metal−Organic Framework Exhibiting Pyrimidine- and Amino-Decorated Pores. *J. Am. Chem. Soc.* **2010,** *132* (1), 38-39.
346. Burd, S. D.; Ma, S.; Perman, J. A.; Sikora, B. J.; Snurr, R. Q.; Thallapally, P. K.; Tian, J.; Wojtas, L.; Zaworotko, M. J., Highly Selective Carbon Dioxide Uptake by [Cu(bpy-n)2(SiF6)] (bpy-1 = 4,4′ -Bipyridine; bpy-2 = 1,2-Bis(4-pyridyl)ethene). *J. Am. Chem. Soc.* **2012,** *134* (8), 3663-3666.
347. Nugent, P.; Rhodus, V.; Pham, T.; Tudor, B.; Forrest, K.; Wojtas, L.; Space, B.; Zaworotko, M., Enhancement of CO2 selectivity in a pillared pcu MOM platform through pillar substitution. *Chem. Commun.* **2013,** *49* (16), 1606-1608.
348. Jiang, M.; Li, B.; Cui, X.; Yang, Q.; Bao, Z.; Yang, Y.; Wu, H.; Zhou, W.; Chen, B.; Xing, H., Controlling Pore Shape and Size of Interpenetrated Anion-Pillared Ultramicroporous Materials Enables Molecular Sieving of CO2 Combined with Ultrahigh Uptake Capacity. *ACS Appl. Mater. Interfaces* **2018,** *10* (19), 16628-16635.
349. Scott, H. S.; Ogiwara, N.; Chen, K.-J.; Madden, D. G.; Pham, T.; Forrest, K.; Space, B.; Horike, S.; Perry Iv, J. J.; Kitagawa, S.; Zaworotko, M. J., Crystal engineering of a family of hybrid ultramicroporous materials based upon interpenetration and dichromate linkers. *Chemical Science* **2016,** *7* (8), 5470-5476.
350. Mohamed, M. H.; Elsaidi, S. K.; Wojtas, L.; Pham, T.; Forrest, K. A.; Tudor, B.; Space, B.; Zaworotko, M. J., Highly Selective CO2 Uptake in Uninodal 6-Connected "mmo" Nets Based upon MO42– (M = Cr, Mo) Pillars. *J. Am. Chem. Soc.* **2012,** *134* (48), 19556-19559.
351. Du, M.; Li, C.-P.; Chen, M.; Ge, Z.-W.; Wang, X.; Wang, L.; Liu, C.-S., Divergent Kinetic and Thermodynamic Hydration of a Porous Cu(II) Coordination Polymer with Exclusive CO2 Sorption Selectivity. *J. Am. Chem. Soc.* **2014,** *136* (31), 10906-10909.
352. Zhang, L.; Jiang, K.; Zhang, J.; Pei, J.; Shao, K.; Cui, Y.; Yang, Y.; Li, B.; Chen, B.; Qian, G., Low-Cost and High-Performance Microporous Metal–Organic Framework for Separation of Acetylene from Carbon Dioxide. *ACS Sustainable Chem. Eng.* **2019,** *7* (1), 1667-1672.
353. Ye, Y.; Ma, Z.; Lin, R.-B.; Krishna, R.; Zhou, W.; Lin, Q.; Zhang, Z.; Xiang, S.; Chen, B., Pore Space Partition within a Metal–Organic Framework for Highly Efficient C2H2/CO2 Separation. *J. Am. Chem. Soc.* **2019,** *141* (9), 4130-4136.
354. Tlili, N.; Grévillot, G.; Vallières, C., Carbon dioxide capture and recovery by means of TSA and/or VSA. *International Journal of Greenhouse Gas Control* **2009,** *3* (5), 519-527.
355. Liang, Z.; Marshall, M.; Chaffee, A. L., CO2 Adsorption-Based Separation by Metal Organic Framework (Cu-BTC) versus Zeolite (13X). *Energy Fuels* **2009,** *23* (5), 2785-2789.
356. Kidnay, A. J.; Parrish, W. R.; McCartney, D. G., *Fundamentals of natural gas processing*. CRC press: 2011.
357. Hudson, M. R.; Queen, W. L.; Mason, J. A.; Fickel, D. W.; Lobo, R. F.; Brown, C. M., Unconventional, Highly Selective CO2 Adsorption in Zeolite SSZ-13. *J. Am. Chem. Soc.* **2012,** *134* (4), 1970-1973.
358. Saha, D.; Bao, Z.; Jia, F.; Deng, S., Adsorption of CO2, CH4, N2O, and N2 on MOF-5, MOF-177, and Zeolite 5A. *Environ. Sci. Technol.* **2010,** *44* (5), 1820-1826.
359. Nam, G.-M.; Jeong, B.-M.; Kang, S.-H.; Lee, B.-K.; Choi, D.-K., Equilibrium Isotherms of CH4, C2H6, C2H4, N2, and H2 on Zeolite 5A Using a Static Volumetric Method. *J. Chem. Eng. Data* **2005,** *50* (1), 72-76.
360. Shao, W.; Zhang, L.; Li, L.; Lee, R. L., Adsorption of CO2 and N2 on synthesized NaY zeolite at high temperatures. *Adsorption* **2009,** *15* (5), 497.
361. Ahmed, M. J.; Theydan, S. K., Equilibrium isotherms studies for light hydrocarbons adsorption on 4A molecular sieve zeolite. *J. Pet. Sci. Eng.* **2013,** *108*, 316-320.

362. Liu, B.; Smit, B., Comparative Molecular Simulation Study of CO2/N2 and CH4/N2 Separation in Zeolites and Metal−Organic Frameworks. *Langmuir* **2009,** *25* (10), 5918-5926.
363. Si, X.; Jiao, C.; Li, F.; Zhang, J.; Wang, S.; Liu, S.; Li, Z.; Sun, L.; Xu, F.; Gabelica, Z.; Schick, C., High and selective CO2 uptake, H2storage and methanol sensing on the amine-decorated 12-connected MOF CAU-1. *Energy Environ. Sci.* **2011,** *4* (11), 4522-4527.
364. Li, J.-R.; Yu, J.; Lu, W.; Sun, L.-B.; Sculley, J.; Balbuena, P. B.; Zhou, H.-C., Porous materials with pre-designed single-molecule traps for CO2 selective adsorption. *Nat. Commun.* **2013,** *4*, 1538.
365. Banerjee, R.; Furukawa, H.; Britt, D.; Knobler, C.; O'Keeffe, M.; Yaghi, O. M., Control of Pore Size and Functionality in Isoreticular Zeolitic Imidazolate Frameworks and their Carbon Dioxide Selective Capture Properties. *J. Am. Chem. Soc.* **2009,** *131* (11), 3875-3877.
366. Zhang, Y.; Su, W.; Sun, Y.; Liu, J.; Liu, X.; Wang, X., Adsorption Equilibrium of N2, CH4, and CO2 on MIL-101. *J. Chem. Eng. Data* **2015,** *60* (10), 2951-2957.
367. Zeeshan, M.; Keskin, S.; Uzun, A., Enhancing CO2/CH4 and CO2/N2 separation performances of ZIF-8 by post-synthesis modification with [BMIM][SCN]. *Polyhedron* **2018,** *155*, 485-492.
368. Russell, B. A.; Migone, A. D., Low temperature adsorption study of CO2 in ZIF-8. *Microporous Mesoporous Mater.* **2017,** *246*, 178-185.
369. Madden, D. G.; O'Nolan, D.; Chen, K.-J.; Hua, C.; Kumar, A.; Pham, T.; Forrest, K. A.; Space, B.; Perry, J. J.; Khraisheh, M., Highly selective CO 2 removal for one-step liquefied natural gas processing by physisorbents. *Chem. Commun.* **2019,** *55* (22), 3219-3222.
370. Wen, H.-M.; Liao, C.; Li, L.; Alsalme, A.; Alothman, Z.; Krishna, R.; Wu, H.; Zhou, W.; Hu, J.; Chen, B., A metal–organic framework with suitable pore size and dual functionalities for highly efficient post-combustion CO2 capture. *J. Mater. Chem. A* **2019**.
371. Mohamed, M. H.; Elsaidi, S. K.; Pham, T.; Forrest, K. A.; Tudor, B.; Wojtas, L.; Space, B.; Zaworotko, M. J., Pillar substitution modulates CO2 affinity in "mmo" topology networks. *Chem. Commun.* **2013,** *49* (84), 9809-9811.
372. Hou, L.; Shi, W.-J.; Wang, Y.-Y.; Guo, Y.; Jin, C.; Shi, Q.-Z., A rod packing microporous metal–organic framework: unprecedented ukv topology, high sorption selectivity and affinity for CO2. *Chem. Commun.* **2011,** *47* (19), 5464-5466.
373. Bloch, W. M.; Babarao, R.; Hill, M. R.; Doonan, C. J.; Sumby, C. J., Post-synthetic Structural Processing in a Metal–Organic Framework Material as a Mechanism for Exceptional CO2/N2 Selectivity. *J. Am. Chem. Soc.* **2013,** *135* (28), 10441-10448.
374. Masala, A.; Vitillo, J. G.; Mondino, G.; Grande, C. A.; Blom, R.; Manzoli, M.; Marshall, M.; Bordiga, S., CO2 Capture in Dry and Wet Conditions in UTSA-16 Metal–Organic Framework. *ACS Appl. Mater. Interfaces* **2017,** *9* (1), 455-463.
375. Pal, A.; Chand, S.; Elahi, S. M.; Das, M. C., A microporous MOF with a polar pore surface exhibiting excellent selective adsorption of CO2 from CO2–N2 and CO2–CH4 gas mixtures with high CO2 loading. *Dalton Trans.* **2017,** *46* (44), 15280-15286.
376. Li, B.; Zhang, Z.; Li, Y.; Yao, K.; Zhu, Y.; Deng, Z.; Yang, F.; Zhou, X.; Li, G.; Wu, H.; Nijem, N.; Chabal, Y. J.; Lai, Z.; Han, Y.; Shi, Z.; Feng, S.; Li, J., Enhanced Binding Affinity, Remarkable Selectivity, and High Capacity of CO2 by Dual Functionalization of a rht-Type Metal–Organic Framework. *Angew. Chem. Int. Ed.* **2012,** *51* (6), 1412-1415.
377. Lu, W.; Sculley, J. P.; Yuan, D.; Krishna, R.; Wei, Z.; Zhou, H.-C., Polyamine-Tethered Porous Polymer Networks for Carbon Dioxide Capture from Flue Gas. *Angew. Chem. Int. Ed.* **2012,** *51* (30), 7480-7484.

378. Nandi, S.; Collins, S.; Chakraborty, D.; Banerjee, D.; Thallapally, P. K.; Woo, T. K.; Vaidhyanathan, R., Ultralow parasitic energy for postcombustion CO2 capture realized in a nickel isonicotinate metal–organic framework with excellent moisture stability. *J. Am. Chem. Soc.* **2017,** *139* (5), 1734-1737.
379. Vaidhyanathan, R.; Iremonger, S. S.; Shimizu, G. K. H.; Boyd, P. G.; Alavi, S.; Woo, T. K., Direct Observation and Quantification of CO2 Binding Within an Amine-Functionalized Nanoporous Solid. *Science* **2010,** *330*, 650-653.
380. Datta, S. J.; Khumnoon, C.; Lee, Z. H.; Moon, W. K.; Docao, S.; Nguyen, T. H.; Hwang, I. C.; Moon, D.; Oleynikov, P.; Terasaki, O.; Yoon, K. B., CO₂ capture from humid flue gases and humid atmosphere using a microporous coppersilicate. *Science* **2015,** *350* (6258), 302-306.
381. Jones, C. W., CO2 capture from dilute gases as a component of modern global carbon management. *Annual review of chemical and biomolecular engineering* **2011,** *2*, 31-52.
382. Goeppert, A.; Czaun, M.; Prakash, G. S.; Olah, G. A., Air as the renewable carbon source of the future: an overview of CO 2 capture from the atmosphere. *Energy Environ. Sci.* **2012,** *5* (7), 7833-7853.
383. Tans, P.; Keeling, R., Trends in atmospheric carbon dioxide. *National Oceanic and Atmospheric Administration. Global Greenhouse Gas Reference Network. http://www. esrl. noaa. gov/gmd/ccgg/trends/(Page consultée le 20 janvier 2014)* **2014**.
384. Torres-Knoop, A.; Krishna, R.; Dubbeldam, D., Separating Xylene Isomers by Commensurate Stacking of p-Xylene within Channels of MAF-X8. *Angew. Chem. Int. Ed.* **2014,** *53* (30), 7774-7778.
385. Hofmann, H.; Gerhartz, W., *Ullmann's encyclopedia of industrial chemistry*. Sl: 1990.
386. Hort, E. V.; Taylor, P., Acetylene‐Derived Chemicals. *Kirk‐Othmer Encyclopedia of Chemical Technology* **2000**.
387. Pereira, C. J., New avenues in ethylene synthesis. *Science* **1999,** *285* (5428), 670-671.
388. Huang, W.; McCormick, J. R.; Lobo, R. F.; Chen, J. G., Selective hydrogenation of acetylene in the presence of ethylene on zeolite-supported bimetallic catalysts. *J. Catal.* **2007,** *246* (1), 40-51.
389. Matsuda, R.; Kitaura, R.; Kitagawa, S.; Kubota, Y.; Belosludov, R. V.; Kobayashi, T. C.; Sakamoto, H.; Chiba, T.; Takata, M.; Kawazoe, Y., Highly controlled acetylene accommodation in a metal–organic microporous material. *Nature* **2005,** *436* (7048), 238.
390. Acetylene. In *Kirk‐Othmer Encyclopedia of Chemical Technology*.
391. Pässler, P.; Hefner, W.; Buckl, K.; Meinass, H.; Meiswinkel, A.; Wernicke, H. J.; Ebersberg, G.; Müller, R.; Bässler, J.; Behringer, H., Acetylene. *Ullmann's Encyclopedia of Industrial Chemistry* **2008**.
392. Zhao, X.; Yang, Q.; Xu, D.; Bao, Z.; Zhang, Y.; Su, B.; Ren, Q.; Xing, H., Design and screening of ionic liquids for C2H2/C2H4 separation by COSMO-RS and experiments. *AIChE J.* **2015,** *61* (6), 2016-2027.
393. Xu, G.; Liang, F.; Yang, Y.; Hu, Y.; Zhang, K.; Liu, W., An Improved CO2 Separation and Purification System Based on Cryogenic Separation and Distillation Theory. *Energies* **2014,** *7* (5), 3484.
394. Studt, F.; Abild-Pedersen, F.; Bligaard, T.; Sørensen, R. Z.; Christensen, C. H.; Nørskov, J. K., Identification of non-precious metal alloy catalysts for selective hydrogenation of acetylene. *Science* **2008,** *320* (5881), 1320-1322.
395. Li, B.; Cui, X.; O'Nolan, D.; Wen, H.-M.; Jiang, M.; Krishna, R.; Wu, H.; Lin, R.-B.; Chen, Y.-S.; Yuan, D.; Xing, H.; Zhou, W.; Ren, Q.; Qian, G.; Zaworotko, M. J.; Chen, B., An Ideal Molecular Sieve for Acetylene Removal from Ethylene with Record Selectivity and Productivity. *Adv. Mater.* **2017,** *29* (47), 1704210.
396. Fan, C. B.; Le Gong, L.; Huang, L.; Luo, F.; Krishna, R.; Yi, X. F.; Zheng, A. M.; Zhang, L.; Pu, S. Z.; Feng, X. F.; Luo, M. B.; Guo, G. C., Significant Enhancement

of C2H2/C2H4 Separation by a Photochromic Diarylethene Unit: A Temperature- and Light-Responsive Separation Switch. *Angew. Chem. Int. Ed.* **2017,** *56* (27), 7900-7906.

397. Hu, T.-L.; Wang, H.; Li, B.; Krishna, R.; Wu, H.; Zhou, W.; Zhao, Y.; Han, Y.; Wang, X.; Zhu, W.; Yao, Z.; Xiang, S.; Chen, B., Microporous metal–organic framework with dual functionalities for highly efficient removal of acetylene from ethylene/acetylene mixtures. *Nat. Commun.* **2015,** *6*, 7328.
398. Xu, H.; Cai, J.; Xiang, S.; Zhang, Z.; Wu, C.; Rao, X.; Cui, Y.; Yang, Y.; Krishna, R.; Chen, B.; Qian, G., A cationic microporous metal–organic framework for highly selective separation of small hydrocarbons at room temperature. *J. Mater. Chem. A* **2013,** *1* (34), 9916-9921.
399. Hong, X.-J.; Wei, Q.; Cai, Y.-P.; Wu, B.-b.; Feng, H.-X.; Yu, Y.; Dong, R.-F., Pillar-Layered Metal–Organic Framework with Sieving Effect and Pore Space Partition for Effective Separation of Mixed Gas C2H2/C2H4. *ACS Appl. Mater. Interfaces* **2017,** *9* (34), 29374-29379.
400. O'Nolan, D.; Madden, D. G.; Kumar, A.; Chen, K.-J.; Pham, T.; Forrest, K. A.; Patyk-Kazmierczak, E.; Yang, Q.-Y.; Murray, C. A.; Tang, C. C.; Space, B.; Zaworotko, M. J., Impact of partial interpenetration in a hybrid ultramicroporous material on C2H2/C2H4 separation performance. *Chem. Commun.* **2018,** *54* (28), 3488-3491.
401. Yang, S.; Ramirez-Cuesta, A. J.; Newby, R.; Garcia-Sakai, V.; Manuel, P.; Callear, S. K.; Campbell, S. I.; Tang, C. C.; Schröder, M., Supramolecular binding and separation of hydrocarbons within a functionalized porous metal–organic framework. *Nature Chem.* **2014,** *7*, 121.
402. Xiang, S.-C.; Zhang, Z.; Zhao, C.-G.; Hong, K.; Zhao, X.; Ding, D.-R.; Xie, M.-H.; Wu, C.-D.; Das, M. C.; Gill, R.; Thomas, K. M.; Chen, B., Rationally tuned micropores within enantiopure metal-organic frameworks for highly selective separation of acetylene and ethylene. *Nat. Commun.* **2011,** *2*, 204.
403. Lee, J.; Chuah, C. Y.; Kim, J.; Kim, Y.; Ko, N.; Seo, Y.; Kim, K.; Bae, T. H.; Lee, E., Separation of Acetylene from Carbon Dioxide and Ethylene by a Water-Stable Microporous Metal–Organic Framework with Aligned Imidazolium Groups inside the Channels. *Angew. Chem. Int. Ed.* **2018,** *57* (26), 7869-7873.
404. Jiang, M.; Cui, X.; Yang, L.; Yang, Q.; Zhang, Z.; Yang, Y.; Xing, H., A thermostable anion-pillared metal-organic framework for C2H2/C2H4 and C2H2/CO2 separations. *Chem. Eng. J.* **2018,** *352*, 803-810.
405. Wen, H.-M.; Li, B.; Wang, H.; Krishna, R.; Chen, B., High acetylene/ethylene separation in a microporous zinc(ii) metal–organic framework with low binding energy. *Chem. Commun.* **2016,** *52* (6), 1166-1169.
406. Li, L.; Lin, R.-B.; Krishna, R.; Wang, X.; Li, B.; Wu, H.; Li, J.; Zhou, W.; Chen, B., Efficient separation of ethylene from acetylene/ethylene mixtures by a flexible-robust metal–organic framework. *J. Mater. Chem. A* **2017,** *5* (36), 18984-18988.
407. Li, L.; Guo, L.; Pu, S.; Wang, J.; Yang, Q.; Zhang, Z.; Yang, Y.; Ren, Q.; Alnemrat, S.; Bao, Z., A calcium-based microporous metal-organic framework for efficient adsorption separation of light hydrocarbons. *Chem. Eng. J. (Lausanne)* **2019,** *358*, 446-455.
408. Bloch, E. D.; Queen, W. L.; Krishna, R.; Zadrozny, J. M.; Brown, C. M.; Long, J. R., Hydrocarbon Separations in a Metal-Organic Framework with Open Iron(II) Coordination Sites. *Science* **2012,** *335* (6076), 1606-1610.
409. Yang, S.; Sun, J.; Ramirez-Cuesta, A. J.; Callear, S. K.; David, W. I. F.; Anderson, D. P.; Newby, R.; Blake, A. J.; Parker, J. E.; Tang, C. C.; Schröder, M., Selectivity and direct visualization of carbon dioxide and sulfur dioxide in a decorated porous host. *Nature Chem.* **2012,** *4*, 887.

410. Kumar, A.; Madden, D. G.; Lusi, M.; Chen, K.-J.; Daniels, E. A.; Curtin, T.; Perry IV, J. J.; Zaworotko, M. J., Direct Air Capture of CO2 by Physisorbent Materials. *Angew. Chem. Int. Ed.* **2015,** *54* (48), 14372-14377.
411. Lou, W.; Yang, J.; Li, L.; Li, J., Adsorption and separation of CO2 on Fe(II)-MOF-74: Effect of the open metal coordination site. *J. Solid State Chem.* **2014,** *213*, 224-228.
412. Duan, J.; Jin, W.; Krishna, R., Natural Gas Purification Using a Porous Coordination Polymer with Water and Chemical Stability. *Inorg. Chem.* **2015,** *54* (9), 4279-4284.
413. Yao, Z.; Zhang, Z.; Liu, L.; Li, Z.; Zhou, W.; Zhao, Y.; Han, Y.; Chen, B.; Krishna, R.; Xiang, S., Extraordinary Separation of Acetylene-Containing Mixtures with Microporous Metal–Organic Frameworks with Open O Donor Sites and Tunable Robustness through Control of the Helical Chain Secondary Building Units. *Chem. Eur. J.* **2016,** *22* (16), 5676-5683.
414. Gannon, R. E., Manyik, R. M., Dietz, C. M., Sargent, H. B., Thribolet, R. O. and Schaffer, R. P., Acetylene. In *Kirk‐Othmer Encyclopedia of Chemical Technology*.
415. Xu, H.; He, Y.; Zhang, Z.; Xiang, S.; Cai, J.; Cui, Y.; Yang, Y.; Qian, G.; Chen, B., A microporous metal–organic framework with both open metal and Lewis basic pyridyl sites for highly selective C2H2/CH4 and C2H2/CO2 gas separation at room temperature. *J. Mater. Chem. A* **2013,** *1* (1), 77-81.
416. Cadiau, A.; Adil, K.; Bhatt, P. M.; Belmabkhout, Y.; Eddaoudi, M., A metal-organic framework–based splitter for separating propylene from propane. *Science* **2016,** *353* (6295), 137-140.
417. Belmabkhout, Y.; Bhatt, P. M.; Adil, K.; Pillai, R. S.; Cadiau, A.; Shkurenko, A.; Maurin, G.; Liu, G.; Koros, W. J.; Eddaoudi, M., Natural gas upgrading using a fluorinated MOF with tuned H 2 S and CO 2 adsorption selectivity. *Nat. Energy* **2018,** *3* (12), 1059.
418. Baker, R. W.; Cussler, E. L.; Eykamp, W.; Koros, W. J.; Riley, R.; Strathman, R., Membrane separation systems. **1991**.
419. Denny Jr, M. S.; Moreton, J. C.; Benz, L.; Cohen, S. M., Metal–organic frameworks for membrane-based separations. *Nat. Rev. Mater.* **2016,** *1*, 16078.
420. Aroon, M.; Ismail, A.; Matsuura, T.; Montazer-Rahmati, M., Performance studies of mixed matrix membranes for gas separation: a review. *Sep. Purif. Technol.* **2010,** *75* (3), 229-242.

Metal-Organic Frameworks for Selective Gas Separation

Electronic Appendices

Contents

Appendix A for Chapter 2

1. ^{1}H NMR spectroscopy analysis of digested MOF samples

For ^{1}H NMR spectroscopy, guest-free crystals were digested using the following protocol: 150 µL of a 35% DCl solution in D_2O was mixed with 500 µL of DMSO-d_6 to give a DCl/DMSO-d_6 stock solution. Around 5 mg of OMOF-2 was digested in 150 µL of this stock solution together with 450 µL of DMSO-d_6. 5 mg of MUF-15 was also digested in 5 mL of NaOD/D_2O. Spectra were acquired immediately following dissolution. The resulting spectra are presented below.

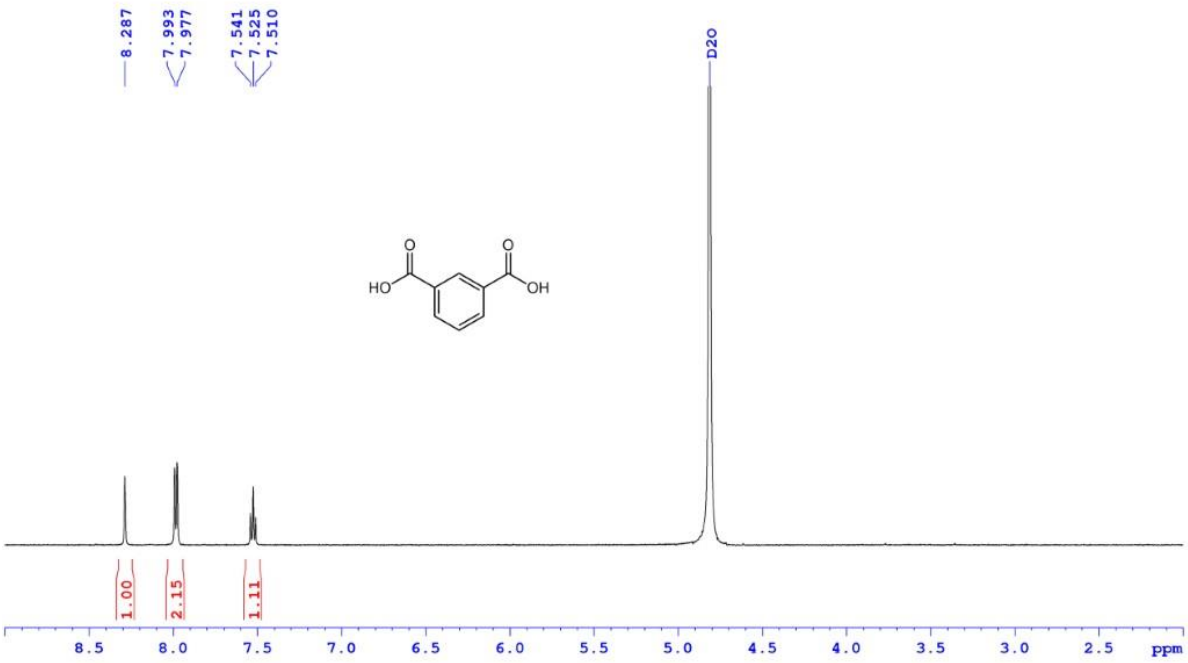

Figure A1 ^{1}H NMR spectrum of MUF-15 digested in D_2O/NaOD.

2. BET surface area calculations

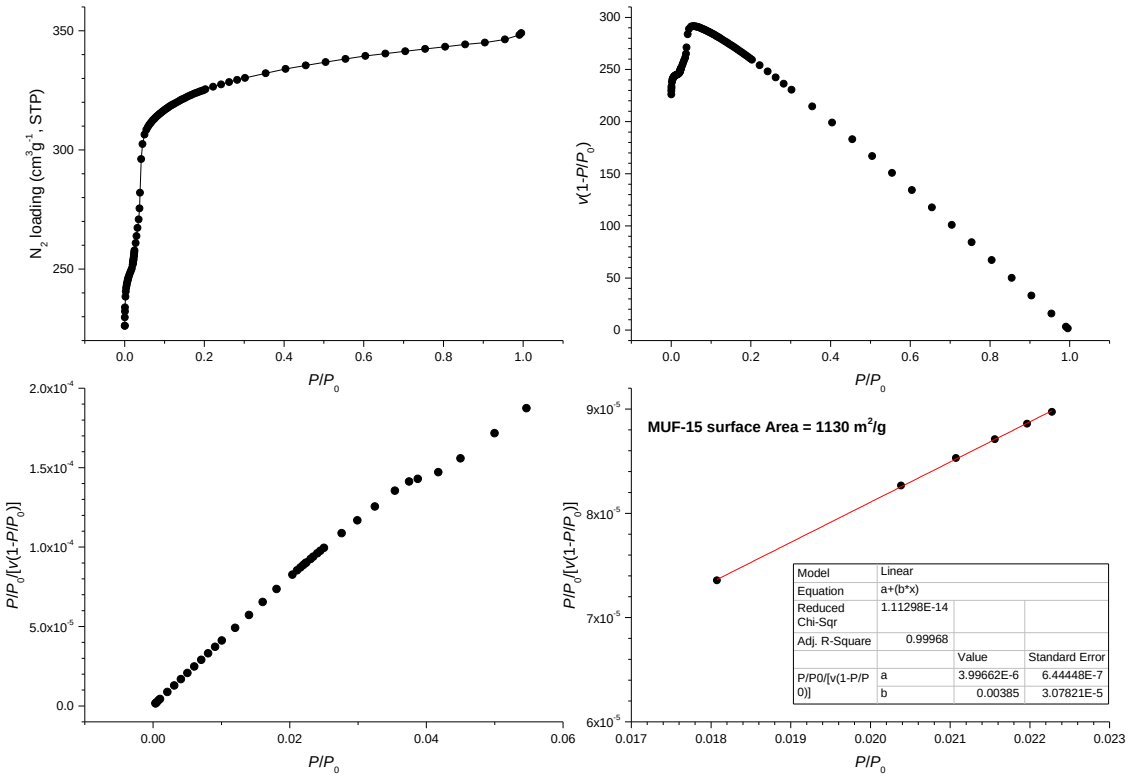

Figure A2 N_2 adsorption isotherm at 77 K and BET surface area plots for MUF-15.

3. Single gas adsorption isotherms

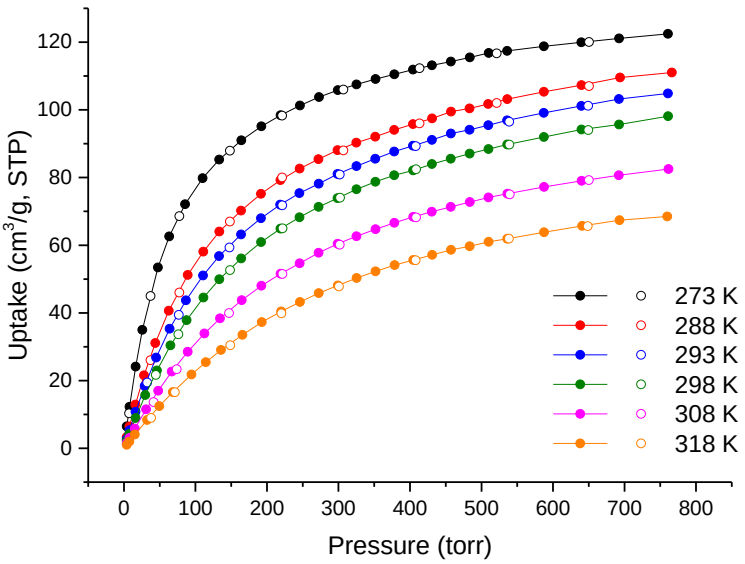

Figure A3 Volumetric C_2H_6 adsorption (filled circles) and desorption (open circles) isotherms measured at different temperatures for MUF-15.

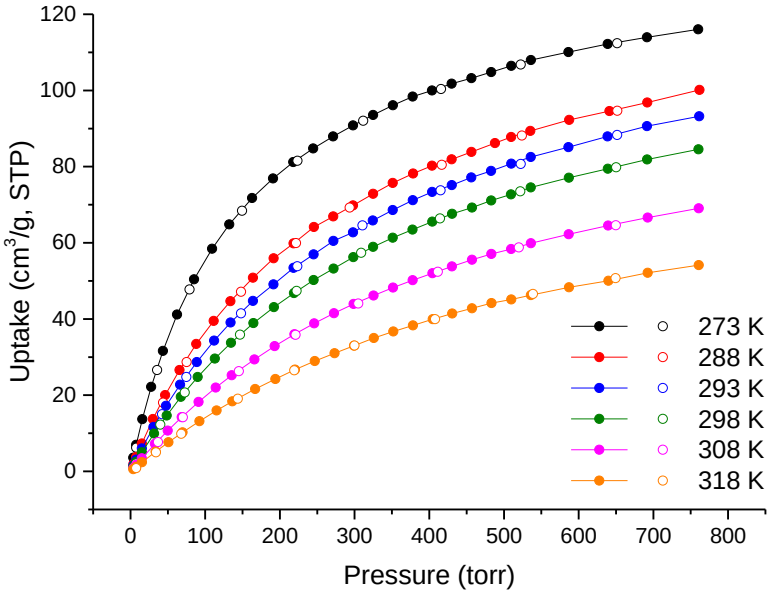

Figure A4 Volumetric C_2H_4 adsorption (filled circles) and desorption (open circles) isotherms measured at different temperatures for MUF-15.

3. IAST calculations

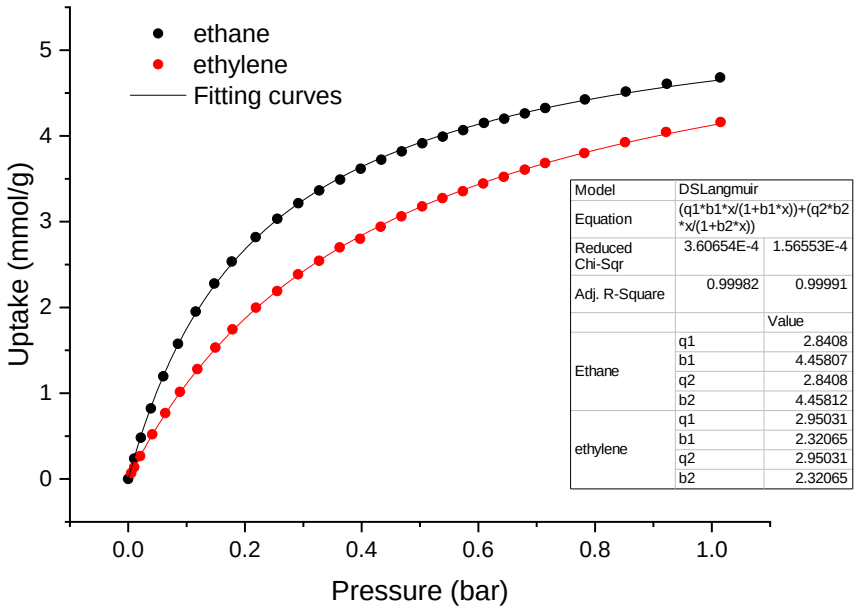

Figure A5 Dual-site Langmuir fits of the MUF-15 isotherms at 293 K.

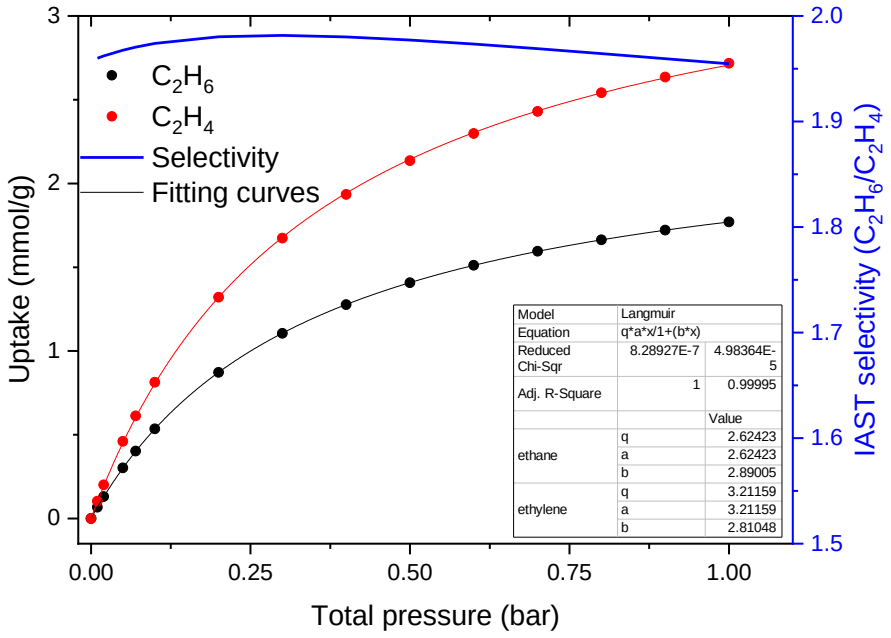

Figure A6 Mixed-gas isotherms and selectivity of MUF-15 predicted by IAST for a mixture of 25/75 C_2H_6/C_2H_4 at 293 K.

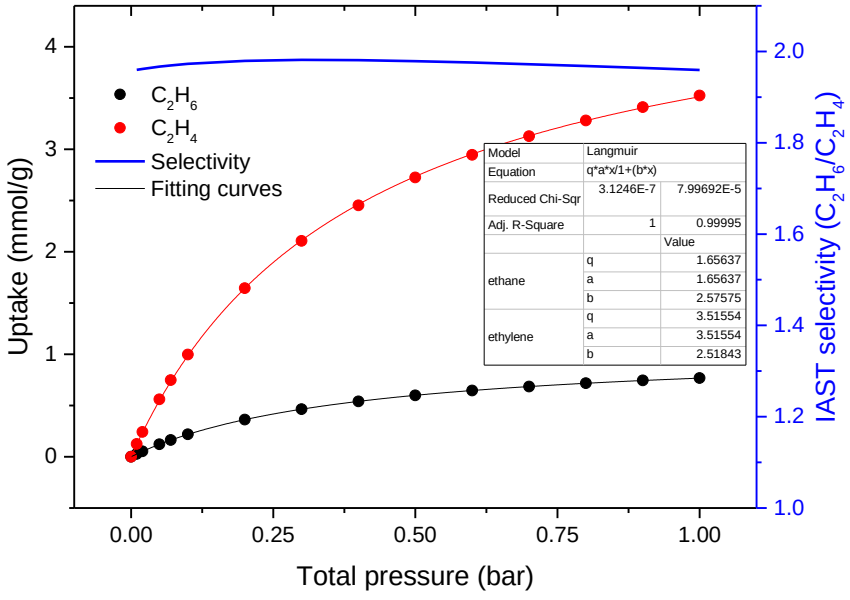

Figure A7 Mixed-gas isotherms and selectivity of MUF-15 predicted by IAST for a mixture of 10/90 C_2H_6/C_2H_4 at 293 K.

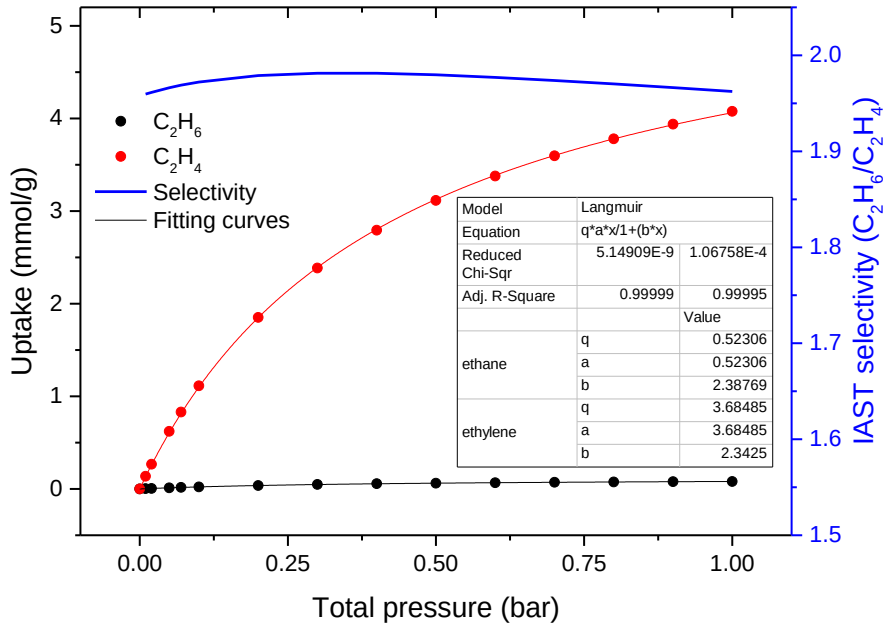

Figure A8 Mixed-gas isotherms and selectivity of MUF-15 predicted by IAST for a mixture of 1/99 C_2H_6/C_2H_4 at 293 K.

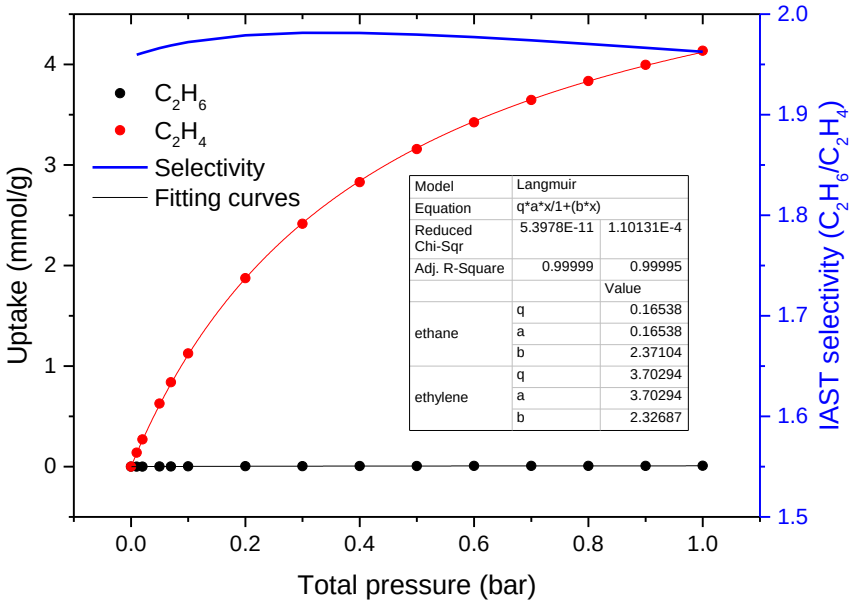

Figure A9 Mixed isotherms and selectivity of MUF-15 predicted by IAST for a mixture of 0.1/99.9 C_2H_6/C_2H_4 at 293 K.

4. Experimental breakthrough curves

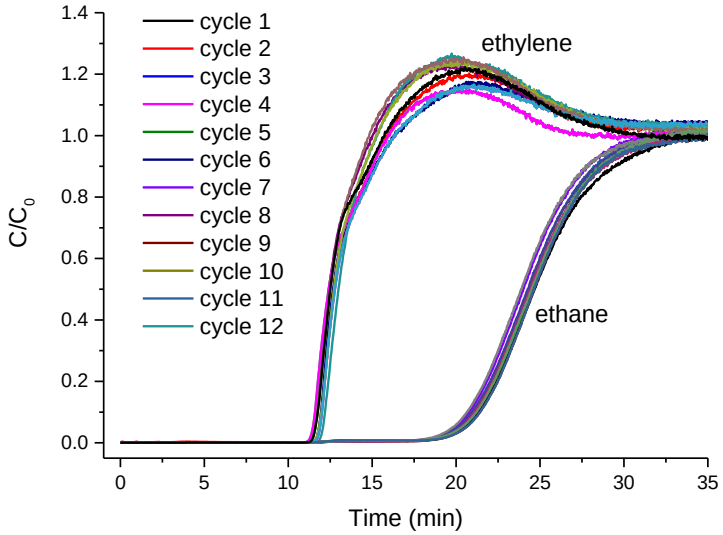

Figure A10 Overlay of experimental breakthrough curves for a mixture of 25/75 ethane/ethylene at 1.1 bar and 293 K for 12 cycles. The helium curve has been removed from the figure.

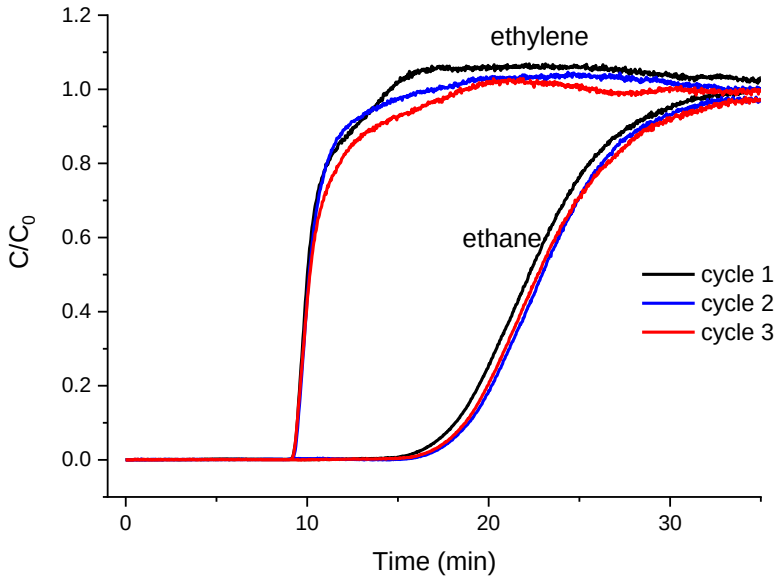

Figure A11 Overlay of experimental breakthrough curves of a mixture of 10:90 ethane/ethylene at 1.1 bar and 293 K for 12 cycles. The helium curve has been removed from the figure.

5. Simulated breakthrough curves

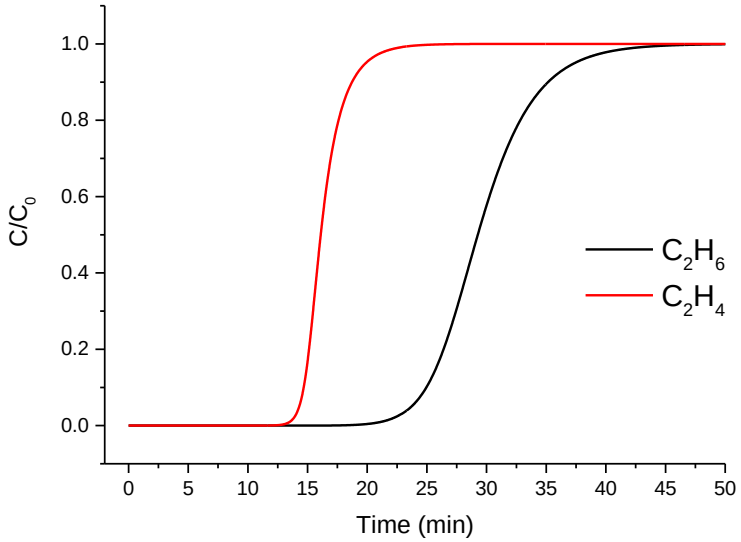

Figure A12 Predicted breakthrough curves for a mixture of 0.1/99.90 of C_2H_6 (black) and C_2H_4 (red) at 293 K and 1.1 bar using a mass transfer coefficient of k_{ethane}: 0.009 1/s and $k_{ethylene}$: 0.013 1/s.

6. Productivity calculations

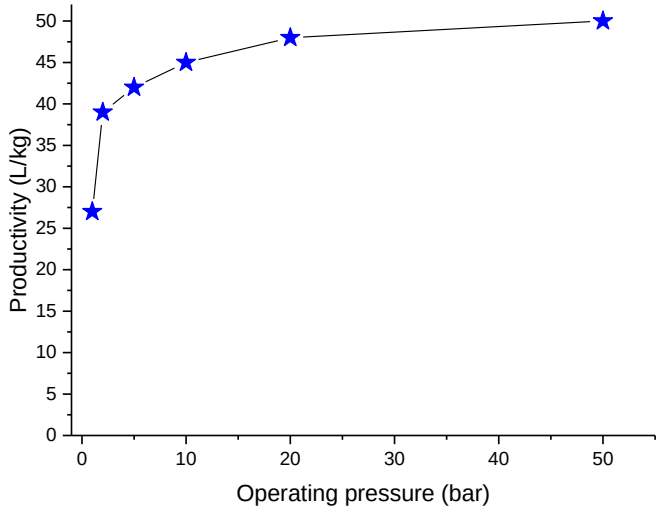

Figure A13 Productivity of ethylene at different operating pressures for a 25/75 mixture of C_2H_6/C_2H_4 at 293 K.

Appendix B for Chapter 3

1. PXRD patterns after exposure to air

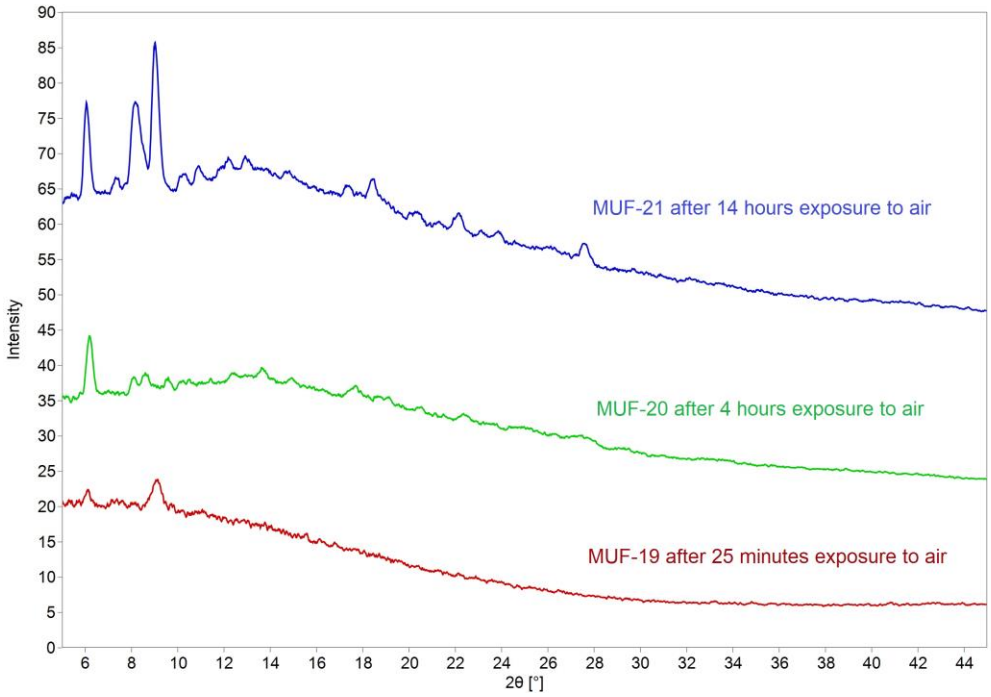

Figure B14. PXRD patterns of MUF-19, MUF-20 and MUF-21 after exposure to air.

Appendix C for Chapter 4

1. BET surface area calculations

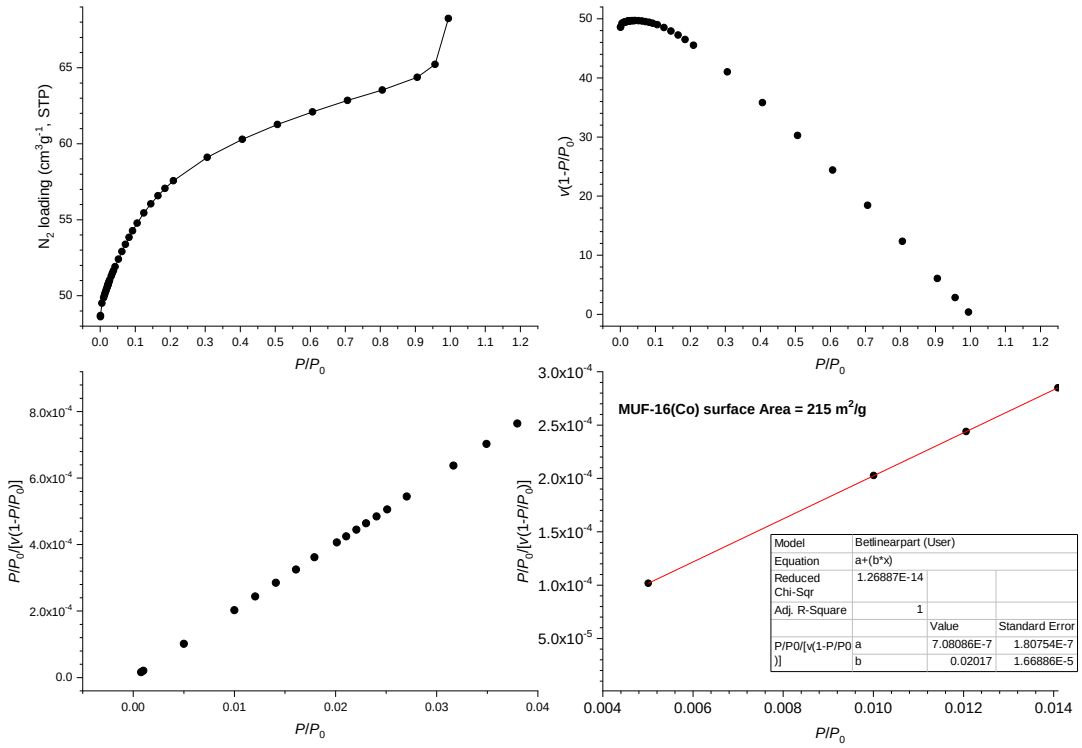

Figure C15 N_2 adsorption isotherm at 77 K and BET surface area plots for MUF-16.

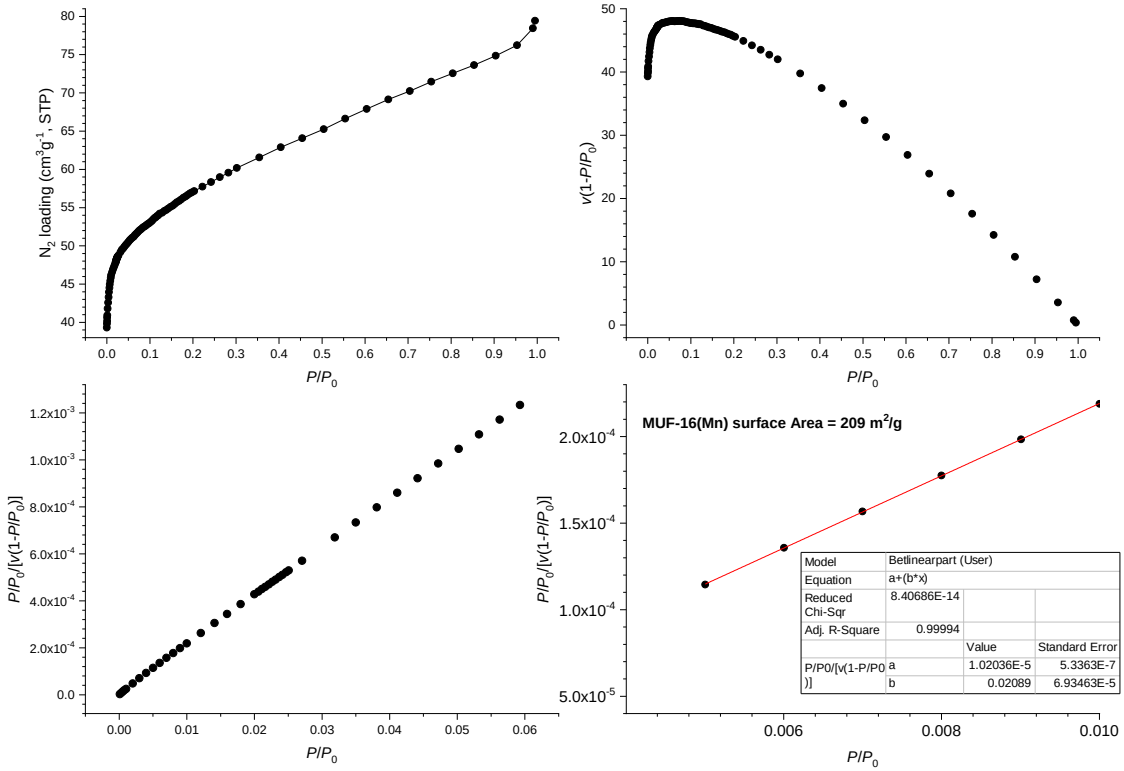

Figure C16 N_2 adsorption isotherm at 77 K and BET surface area plots for MUF-16(Mn).

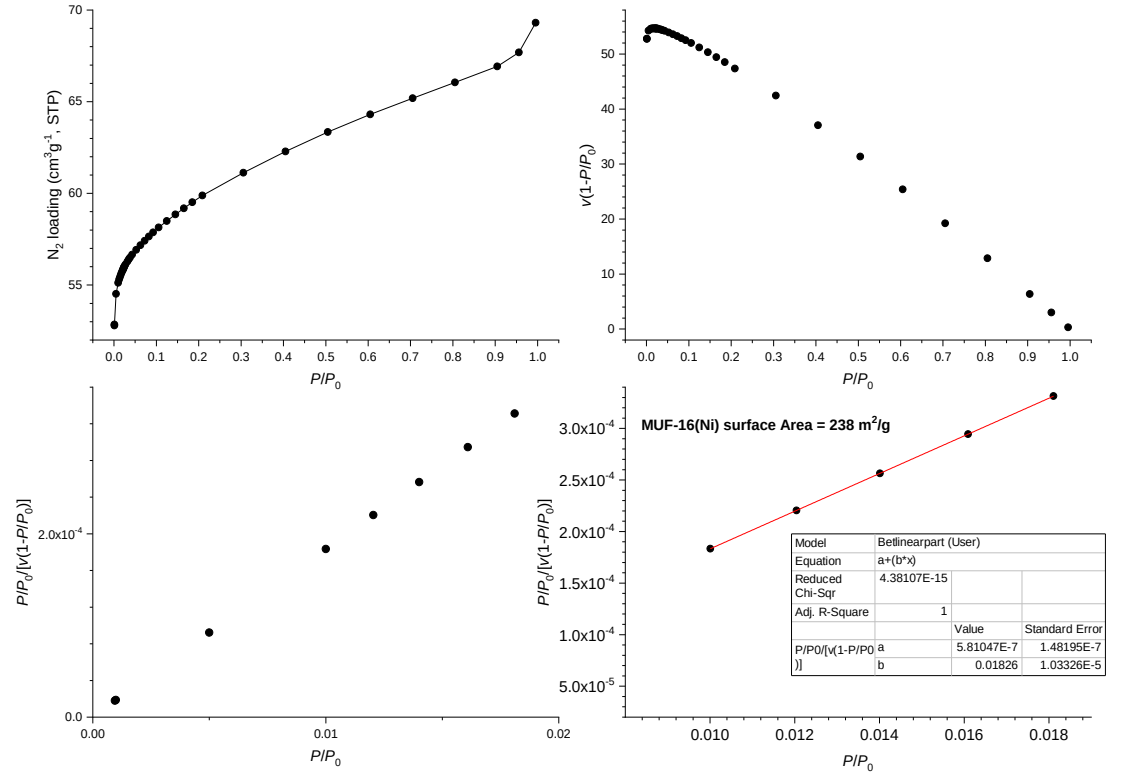

Figure C17 N_2 adsorption isotherm at 77 K and BET surface area plots for MUF-16(Ni).

Appendix D for Chapter 5

1. IAST calculations

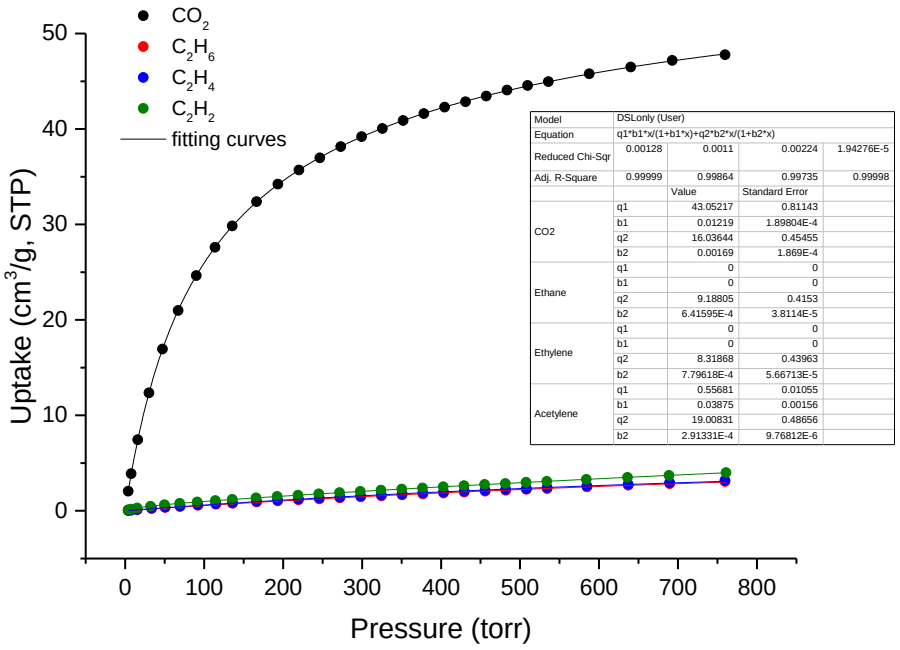

Model	DSLonly (User)			
Equation	q1*b1*x/(1+b1*x)+q2*b2*x/(1+b2*x)			
Reduced Chi-Sqr	0.00128	0.0011	0.00224	1.94276E-5
Adj. R-Square	0.99999	0.99864	0.99735	0.99998
		Value	Standard Error	
CO2	q1	43.05217	0.81143	
	b1	0.01219	1.89804E-4	
	q2	16.03644	0.45455	
	b2	0.00169	1.869E-4	
Ethane	q1	0	0	
	b1	0	0	
	q2	9.18805	0.4153	
	b2	6.41595E-4	3.8114E-5	
Ethylene	q1	0	0	
	b1	0	0	
	q2	8.31868	0.43963	
	b2	7.79618E-4	5.66713E-5	
Acetylene	q1	0.55681	0.01055	
	b1	0.03875	0.00156	
	q2	19.00831	0.48656	
	b2	2.91331E-4	9.76812E-6	

Figure D18 Dual-site Langmuir fits of the MUF-16 isotherms at 293 K.

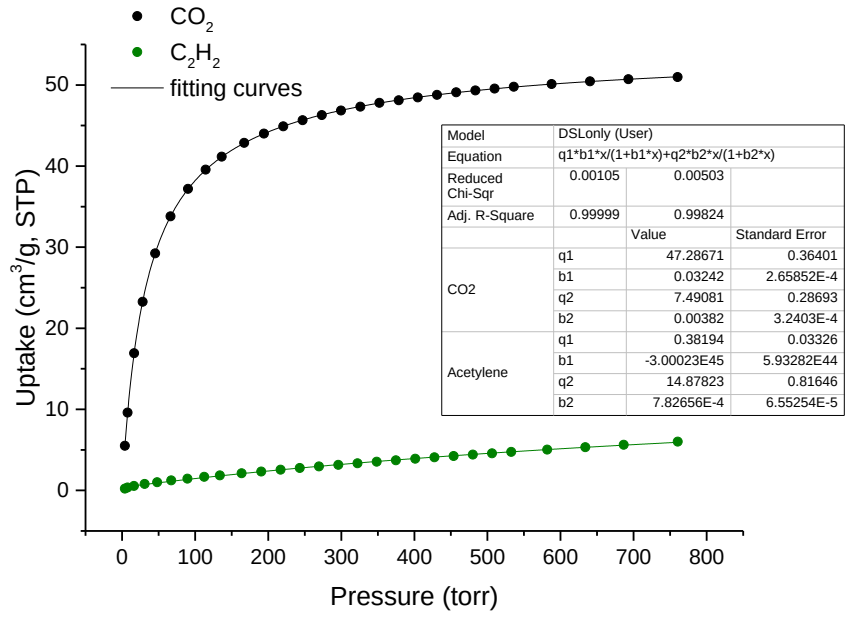

Model	DSLonly (User)		
Equation	q1*b1*x/(1+b1*x)+q2*b2*x/(1+b2*x)		
Reduced Chi-Sqr	0.00105	0.00503	
Adj. R-Square	0.99999	0.99824	
		Value	Standard Error
CO2	q1	47.28671	0.36401
	b1	0.03242	2.65852E-4
	q2	7.49081	0.28693
	b2	0.00382	3.2403E-4
Acetylene	q1	0.38194	0.03326
	b1	-3.00023E45	5.93282E44
	q2	14.87823	0.81646
	b2	7.82656E-4	6.55254E-5

Figure D19 Dual-site Langmuir fits of the MUF-16 isotherms at 273 K.

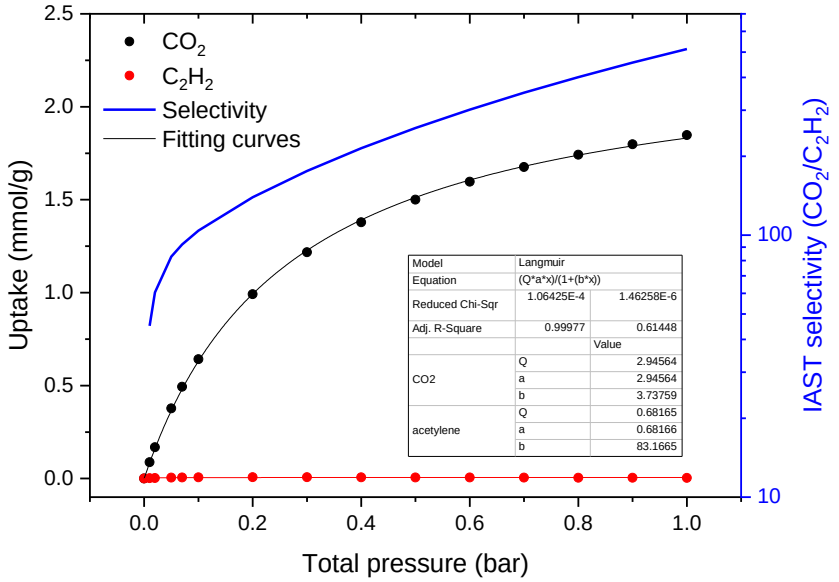

Figure D20 Mixed-gas isotherms and selectivity of MUF-16 predicted by IAST for a mixture of 50/50 CO_2/C_2H_2 at 293 K.

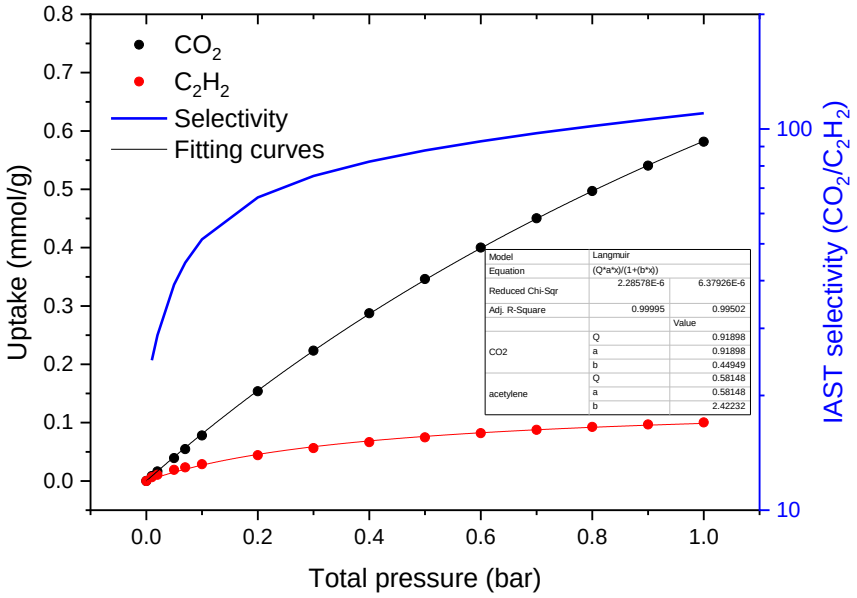

Figure D21 Mixed isotherms and selectivity of MUF-16 predicted by IAST for a mixture of 5/95 CO_2/C_2H_2 at 293 K.

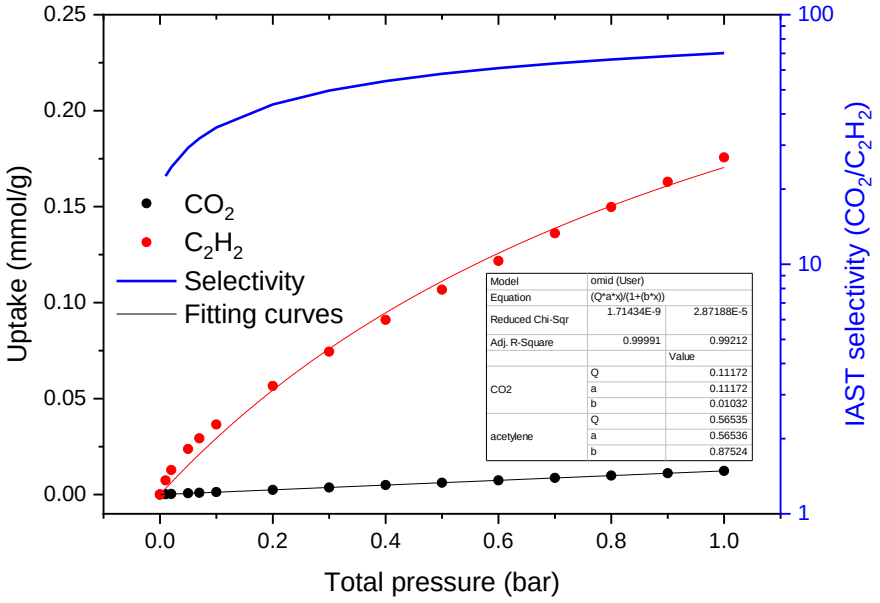

Figure D22 Mixed isotherms and selectivity of MUF-16 predicted by IAST for a mixture of 0.1/99.9 CO_2/C_2H_2 at 293 K.

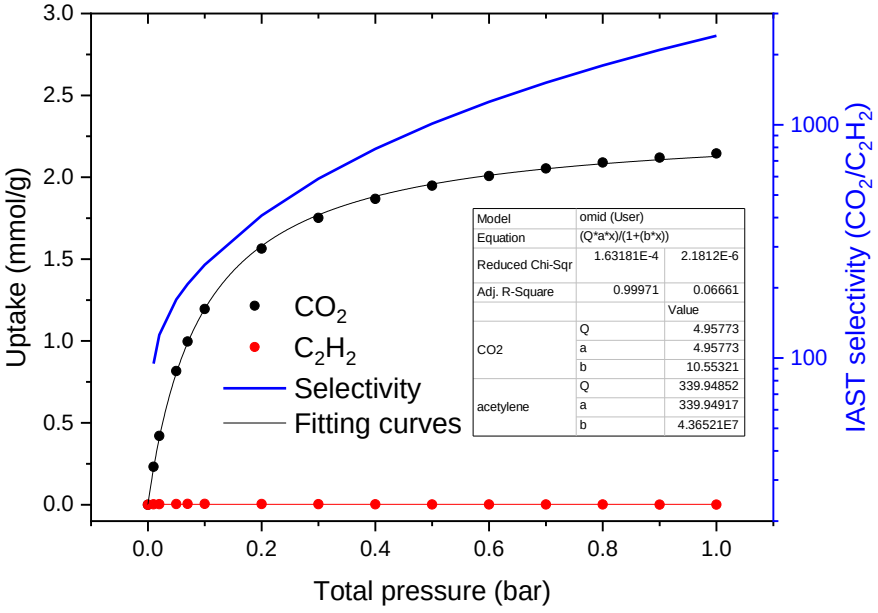

Figure D23 Mixed isotherms and selectivity of MUF-16 predicted by IAST for a mixture of 50/50 CO_2/C_2H_2 at 273 K.

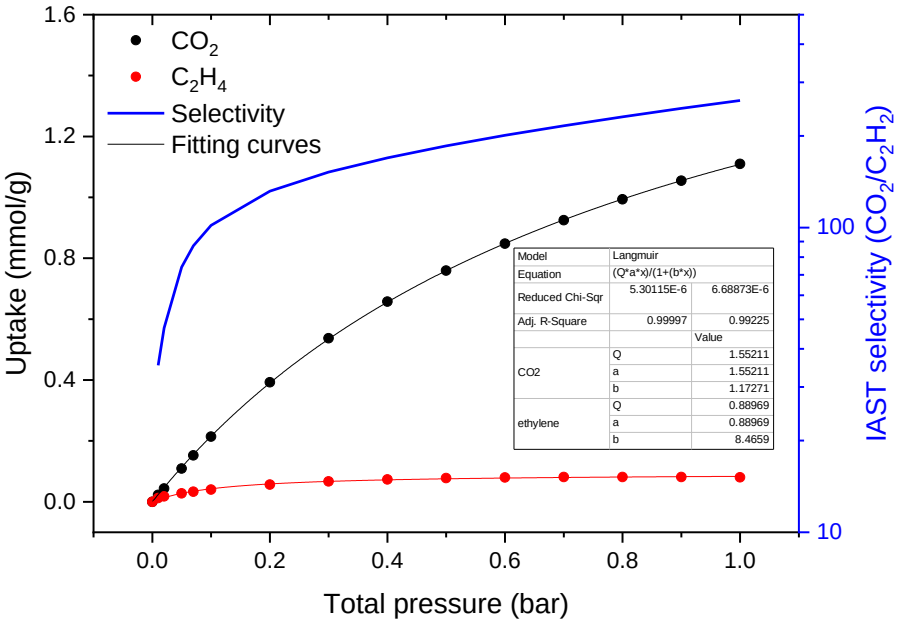

Figure D24 Mixed isotherms and selectivity of MUF-16 predicted by IAST for a mixture of 5/95 CO_2/C_2H_4 at 273 K.

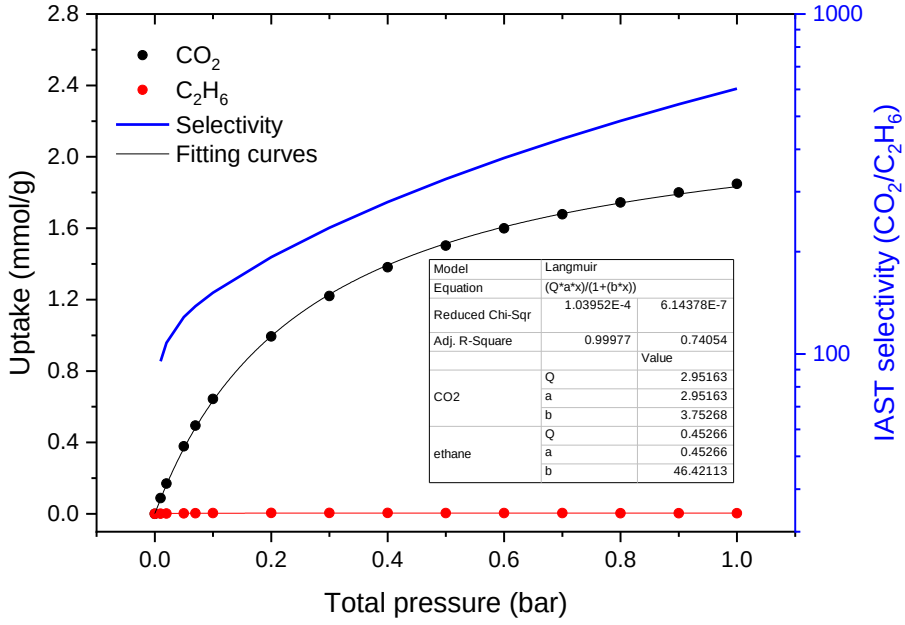

Figure D25 Mixed isotherms and selectivity of MUF-16 predicted by IAST for a mixture of 50/50 CO_2/C_2H_6 at 293 K.

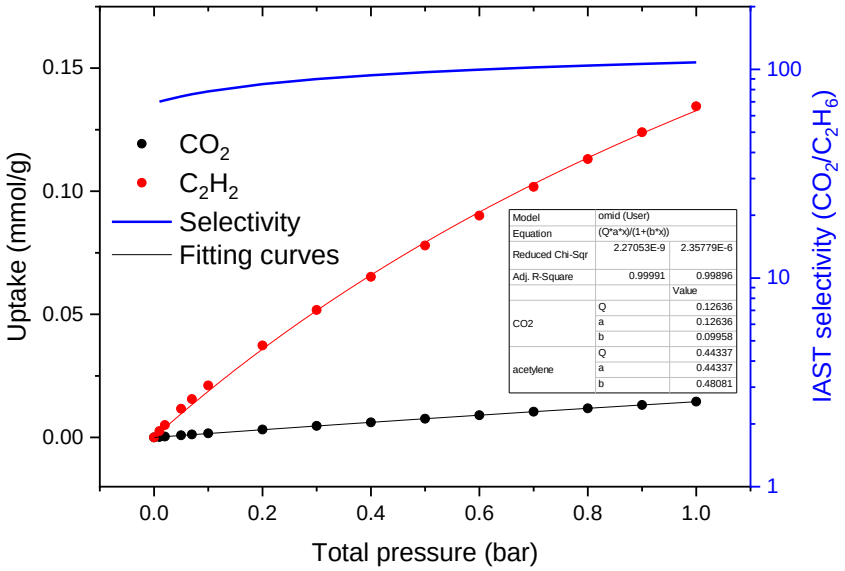

Figure D26 Mixed isotherms and selectivity of MUF-16 predicted by IAST for a mixture of 0.1/99.9 CO_2/C_2H_6 at 293 K.

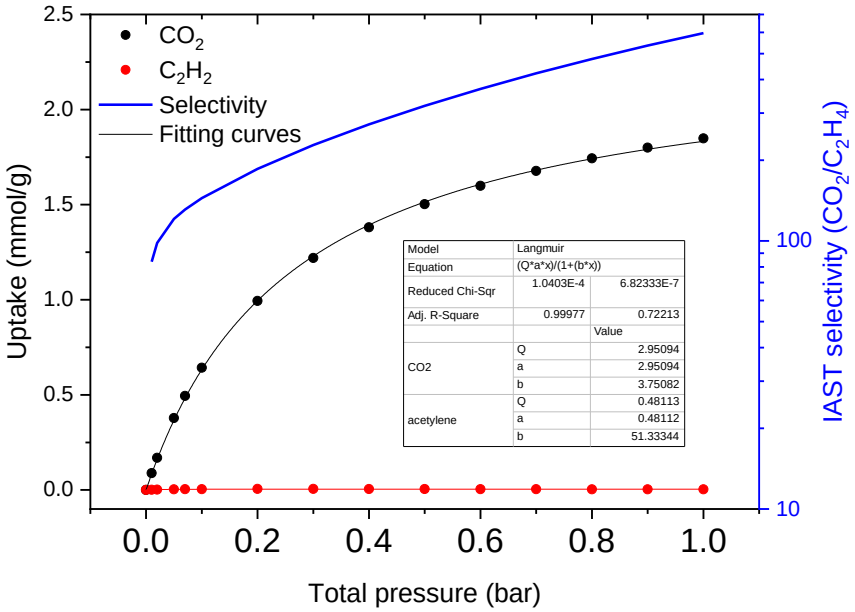

Figure D27 Mixed isotherms and selectivity of MUF-16 predicted by IAST for a mixture of 50/50 CO_2/C_2H_4 at 293 K.

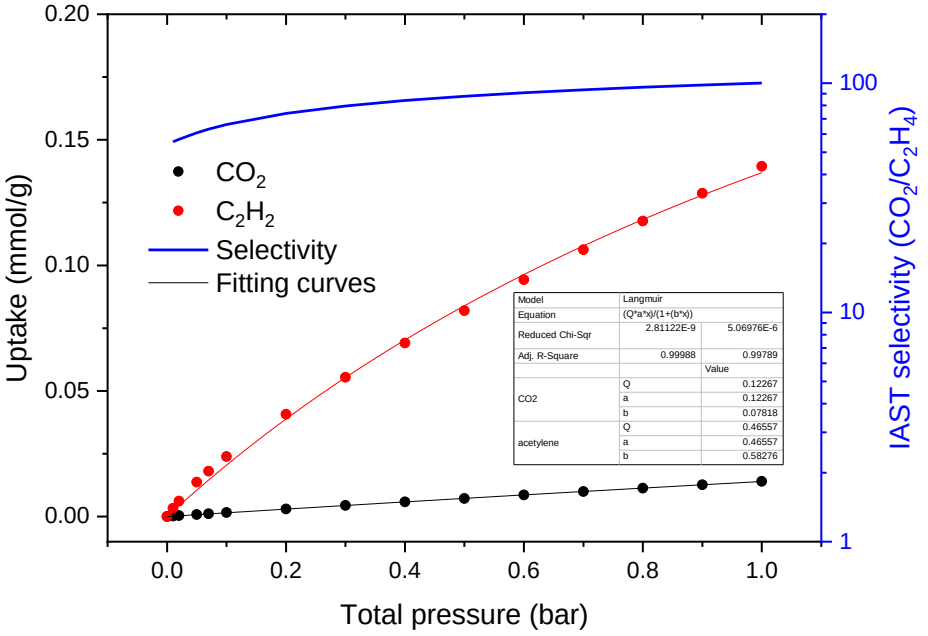

Figure D28 Mixed isotherms and selectivity of MUF-16 predicted by IAST for a mixture of 0.1/99.9 CO_2/C_2H_4 at 293 K.

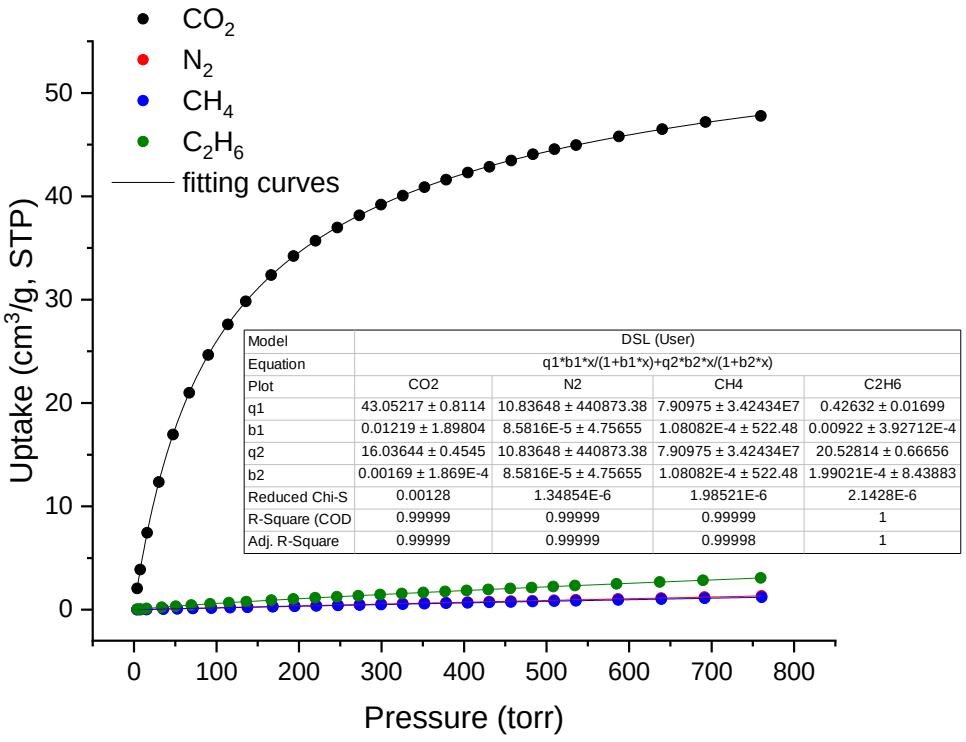

Figure D29 Dual-site Langmuir fits of the MUF-16 isotherms at 293 K.

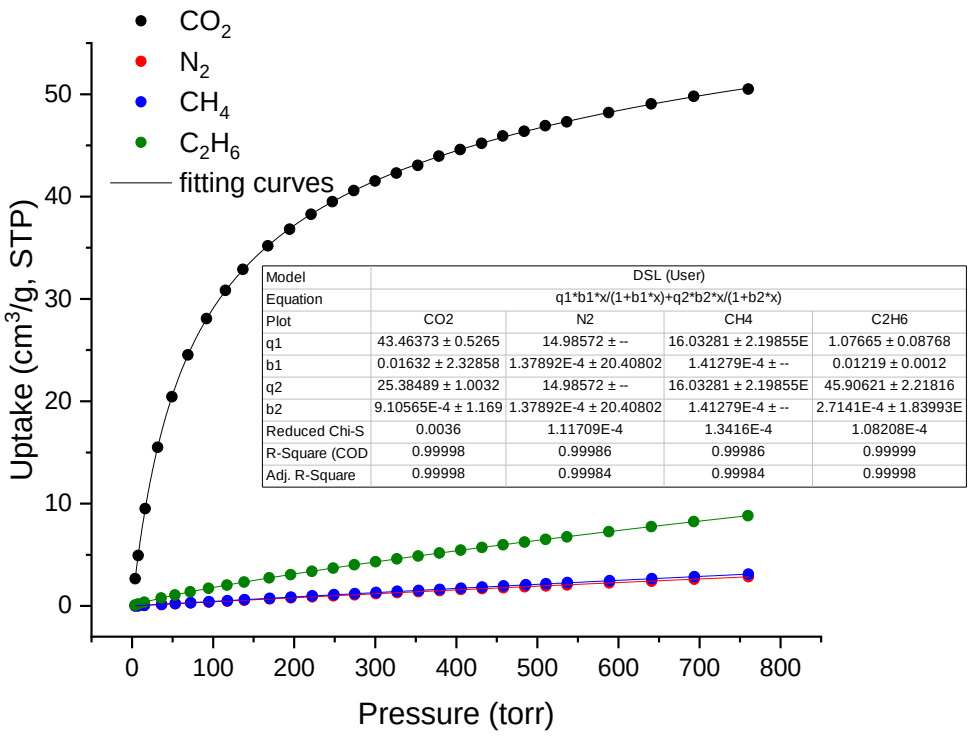

Model	DSL (User)			
Equation	q1*b1*x/(1+b1*x)+q2*b2*x/(1+b2*x)			
Plot	CO2	N2	CH4	C2H6
q1	43.46373 ± 0.5265	14.98572 ± --	16.03281 ± 2.19855E	1.07665 ± 0.08768
b1	0.01632 ± 2.32858	1.37892E-4 ± 20.40802	1.41279E-4 ± --	0.01219 ± 0.0012
q2	25.38489 ± 1.0032	14.98572 ± --	16.03281 ± 2.19855E	45.90621 ± 2.21816
b2	9.10565E-4 ± 1.169	1.37892E-4 ± 20.40802	1.41279E-4 ± --	2.7141E-4 ± 1.83993E
Reduced Chi-S	0.0036	1.11709E-4	1.3416E-4	1.08208E-4
R-Square (COD	0.99998	0.99986	0.99986	0.99999
Adj. R-Square	0.99998	0.99984	0.99984	0.99998

Figure S30. Dual-site Langmuir fits of the MUF-16(Mn) isotherms at 293 K.

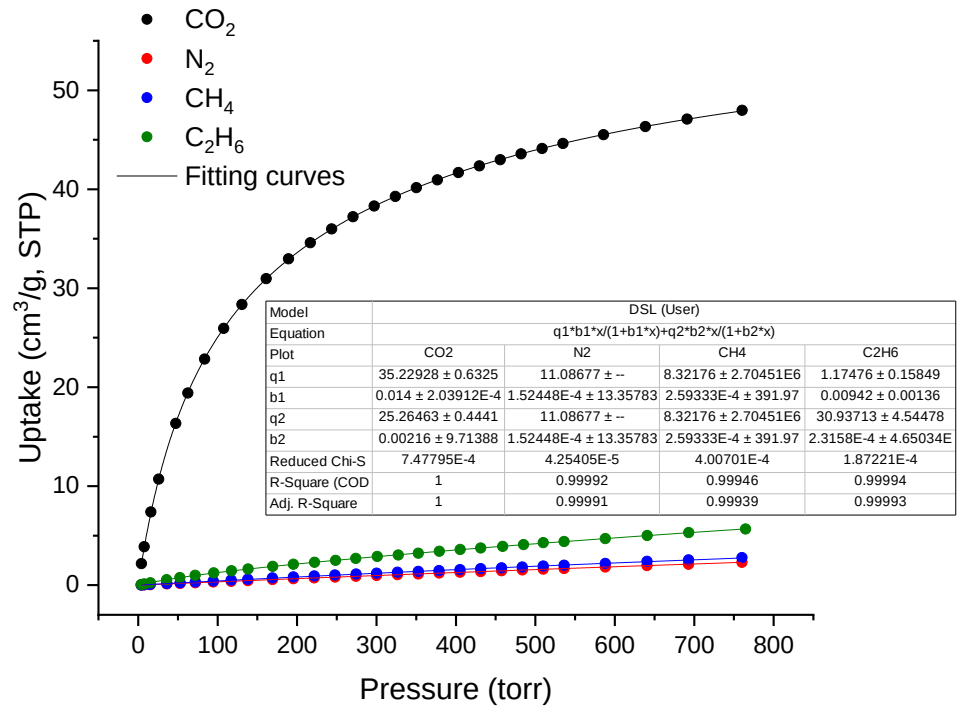

Model	DSL (User)			
Equation	q1*b1*x/(1+b1*x)+q2*b2*x/(1+b2*x)			
Plot	CO2	N2	CH4	C2H6
q1	35.22928 ± 0.6325	11.08677 ± --	8.32176 ± 2.70451E6	1.17476 ± 0.15849
b1	0.014 ± 2.03912E-4	1.52448E-4 ± 13.35783	2.59333E-4 ± 391.97	0.00942 ± 0.00136
q2	25.26463 ± 0.4441	11.08677 ± --	8.32176 ± 2.70451E6	30.93713 ± 4.54478
b2	0.00216 ± 9.71388	1.52448E-4 ± 13.35783	2.59333E-4 ± 391.97	2.3158E-4 ± 4.65034E
Reduced Chi-S	7.47795E-4	4.25405E-5	4.00701E-4	1.87221E-4
R-Square (COD	1	0.99992	0.99946	0.99994
Adj. R-Square	1	0.99991	0.99939	0.99993

Figure D31 Dual-site Langmuir fits of the MUF-16(Ni) isotherms at 293 K.

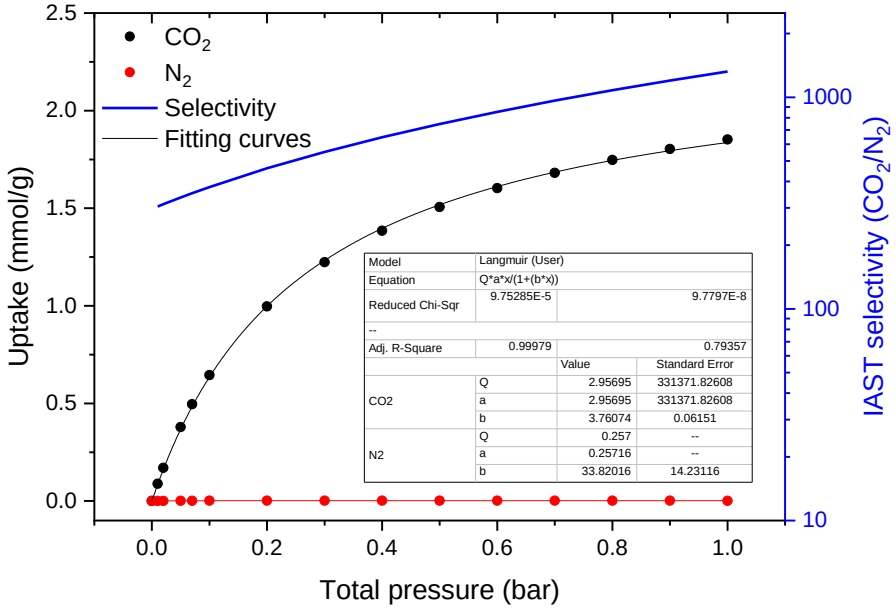

Figure D32 Mixed-gas isotherms and selectivity of MUF-16 predicted by IAST for a mixture of 50/50 CO_2/N_2 at 293 K.

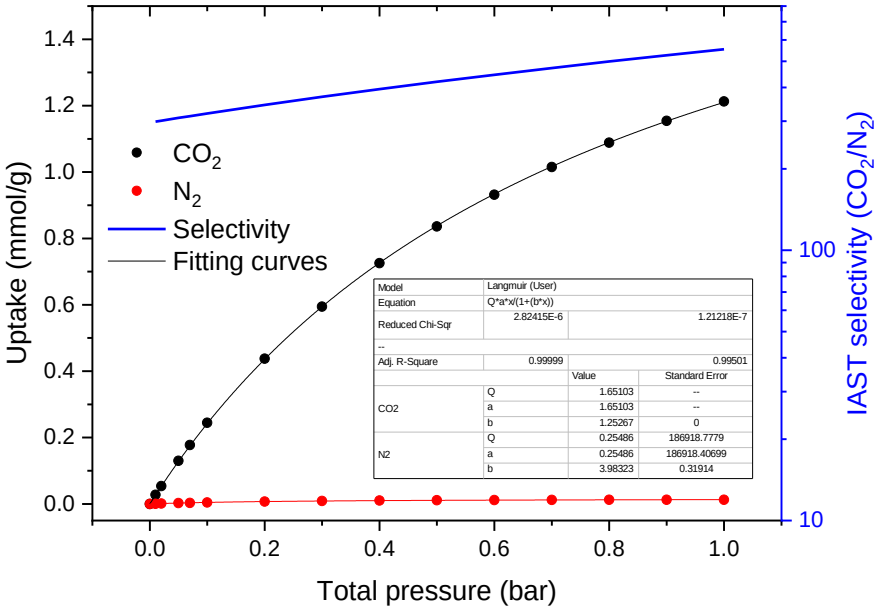

Figure D33 Mixed-gas isotherms and selectivity of MUF-16 predicted by IAST for a mixture of 15/85 CO_2/N_2 at 293 K.

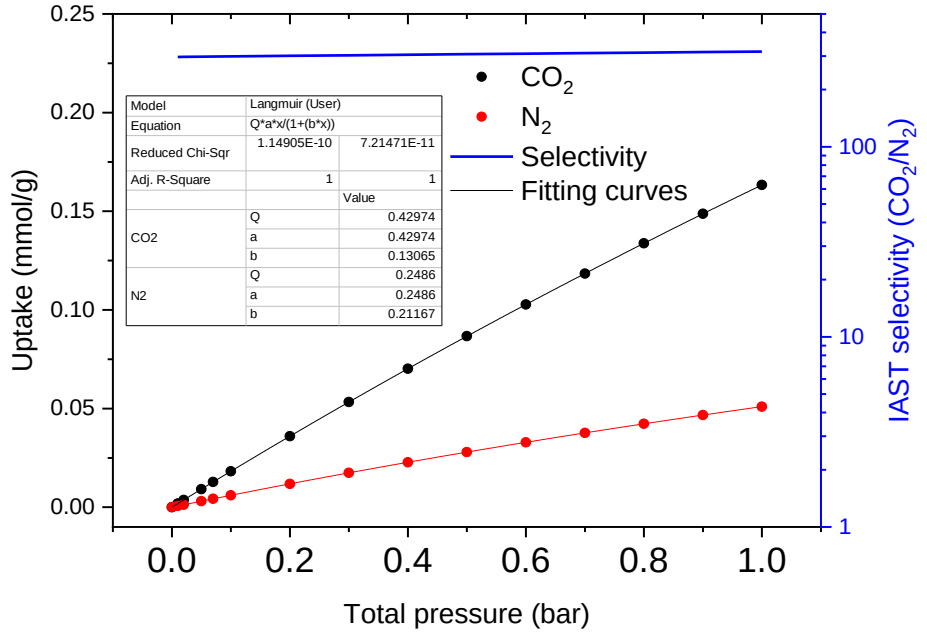

Figure D34 Mixed-gas isotherms and selectivity of MUF-16 predicted by IAST for a mixture of 1/99 CO_2/N_2 at 293 K.

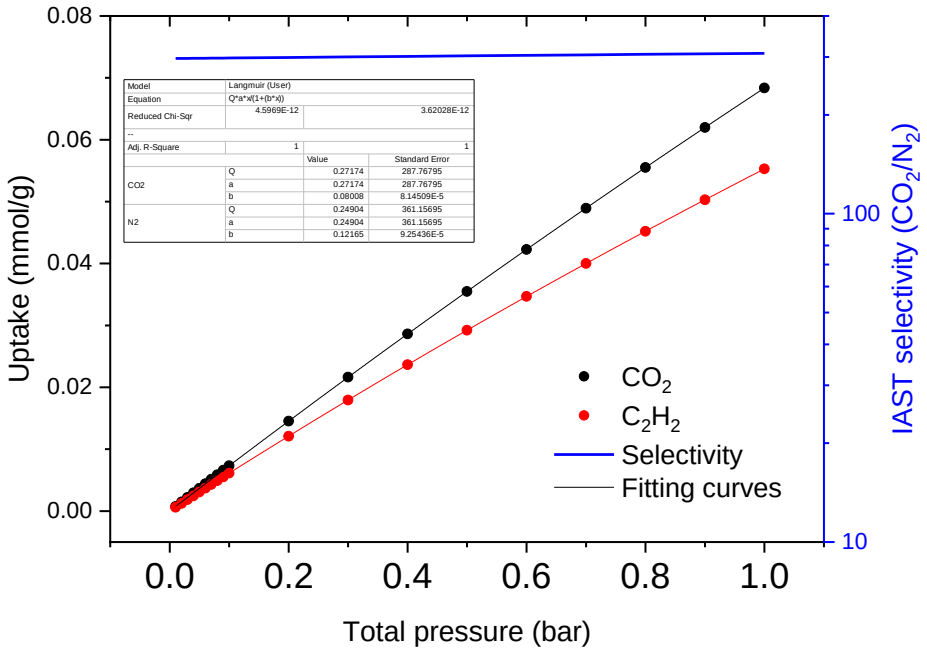

Figure D35 Mixed-gas isotherms and selectivity of MUF-16 predicted by IAST for a mixture of 0.4/99.6 CO_2/N_2 at 293 K.

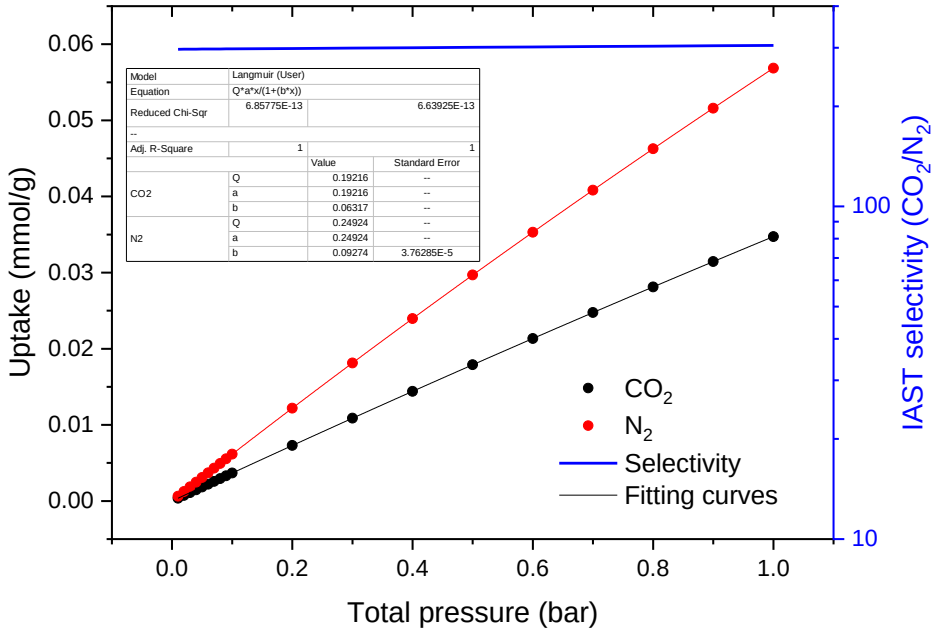

Figure D36 Mixed-gas isotherms and selectivity of MUF-16 predicted by IAST for a mixture of 0.2/99.8 CO_2/N_2 at 293 K.

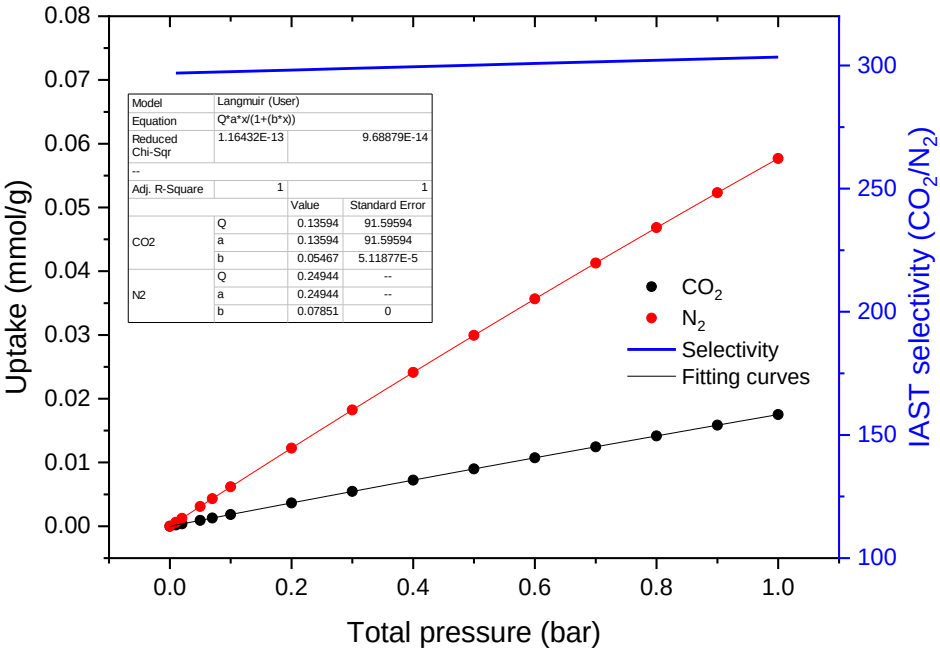

Figure D37 Mixed-gas isotherms and selectivity of MUF-16 predicted by IAST for a mixture of 0.1/99.9 CO2/N2 at 293 K.

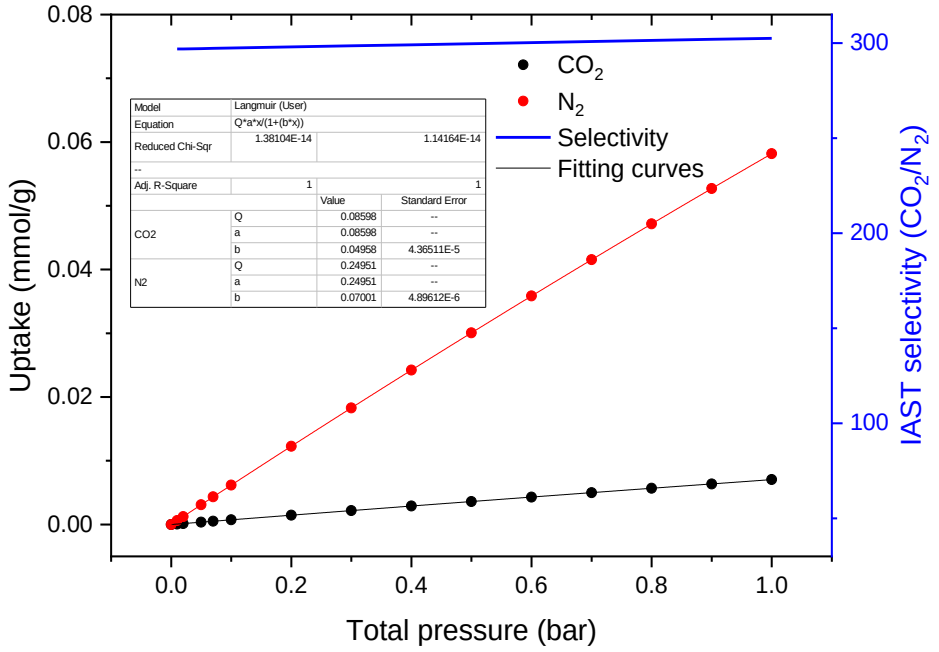

Figure D38 Mixed-gas isotherms and selectivity of MUF-16 predicted by IAST for a mixture of 0.04/99.96 CO_2/N_2 at 293 K.

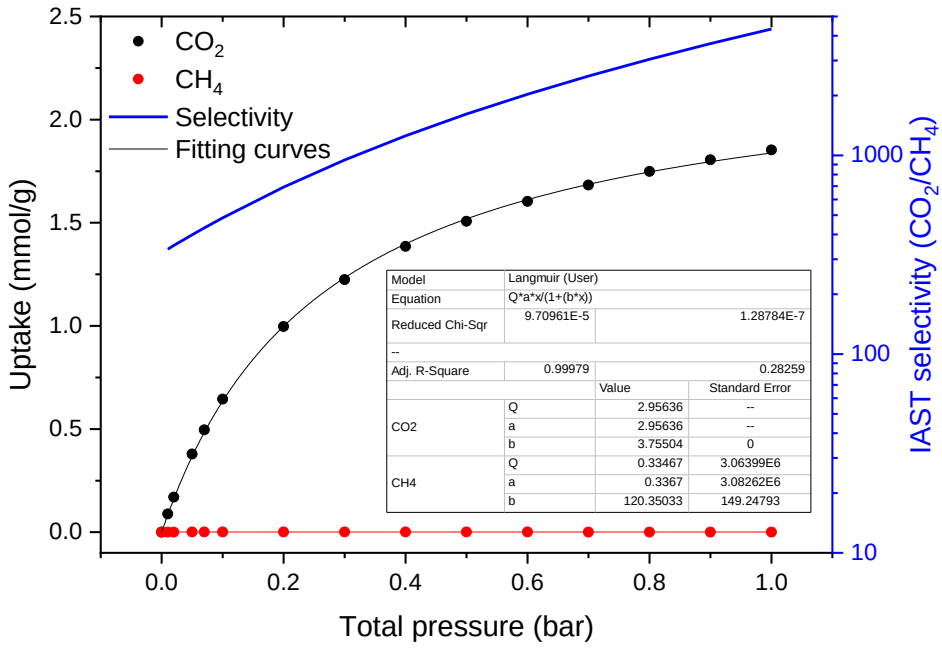

Figure D39 Mixed-gas isotherms and selectivity of MUF-16 predicted by IAST for a mixture of 50/50 CO_2/CH_4 at 293 K.

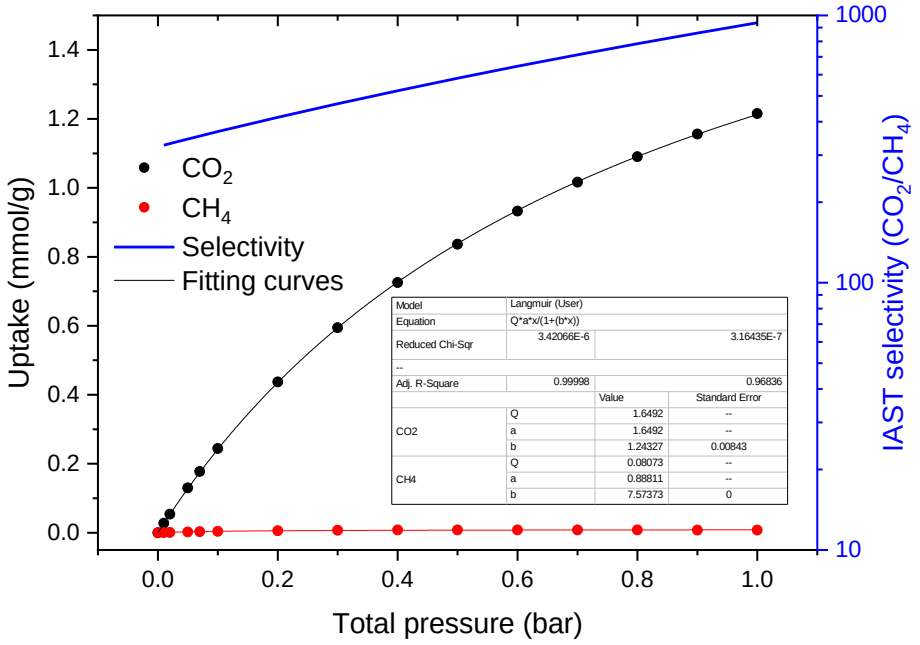

Figure D40 Mixed-gas isotherms and selectivity of MUF-16 predicted by IAST for a mixture of 15/85 CO_2/CH_4 at 293 K.

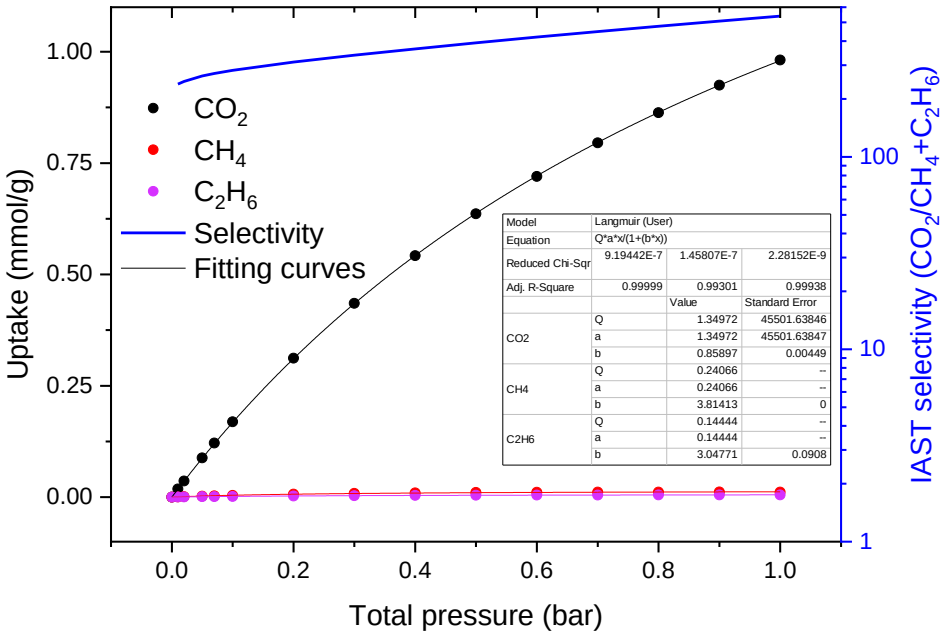

Figure D41 Mixed-gas isotherms and selectivity of MUF-16 predicted by IAST for a mixture of 10/80/10 $CO_2/CH_4/C_2H_6$ at 293 K.

2. Experimental breakthrough curves

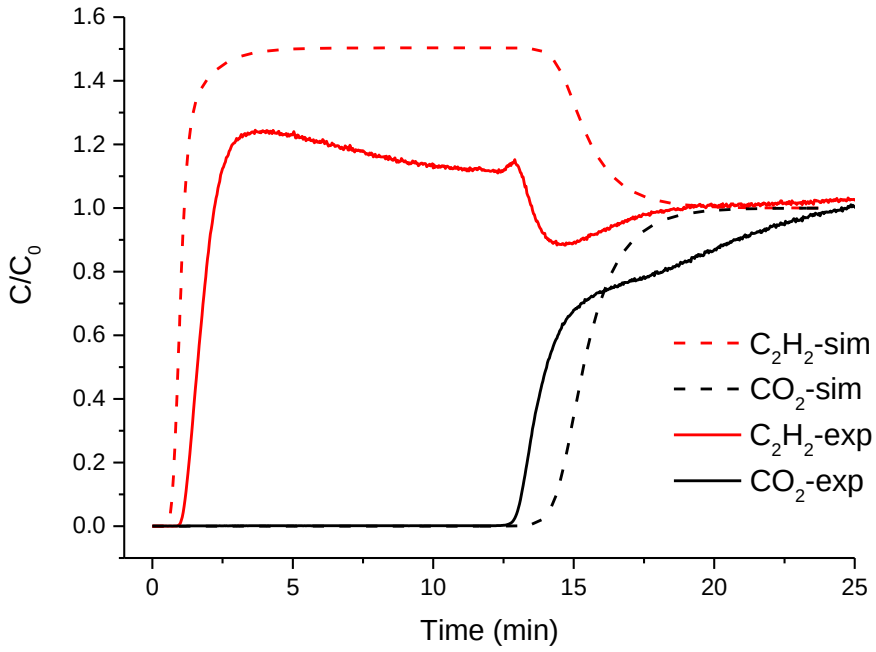

Figure D42. Predicted breakthrough curves for a mixture of 50/50 of CO_2 (black) and C_2H_2 (red) at 293 K and 1.1 bar compared with experimental breakthrough curves after tuning of the mass transfer coefficients (k_{CO2}: 0.021 s^{-1}, k_{C2H2}: 0.024 s^{-1}).

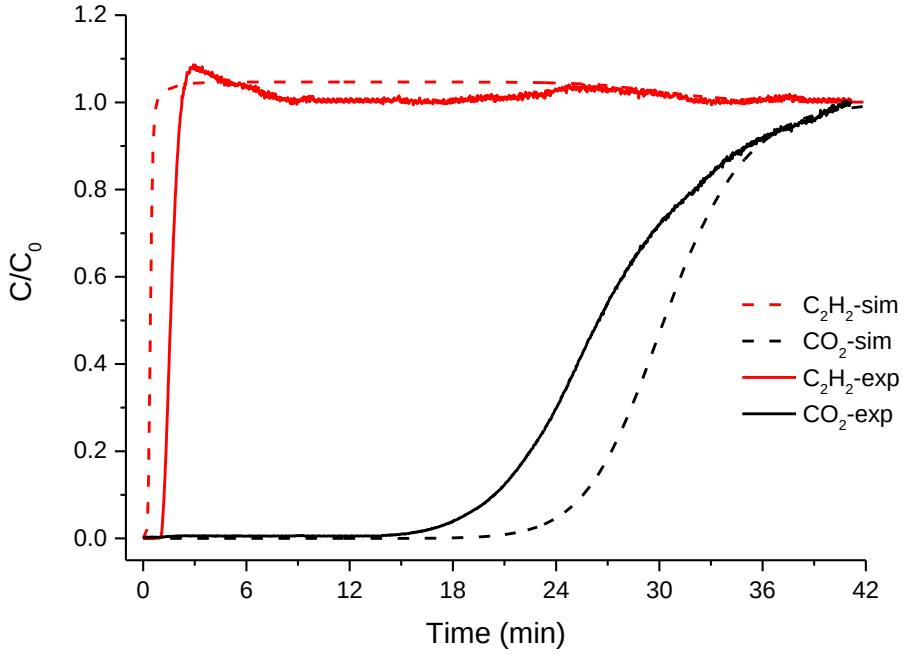

Figure D43. Predicted breakthrough curves for a mixture of 5/95 of CO_2 (black) and C_2H_2 (red) at 293 K and 1.1 bar compared with experimental breakthrough curves after tuning of the mass transfer coefficients (k_{CO2}: 0.021 s^{-1}, k_{C2H2}: 0.024 s^{-1}).

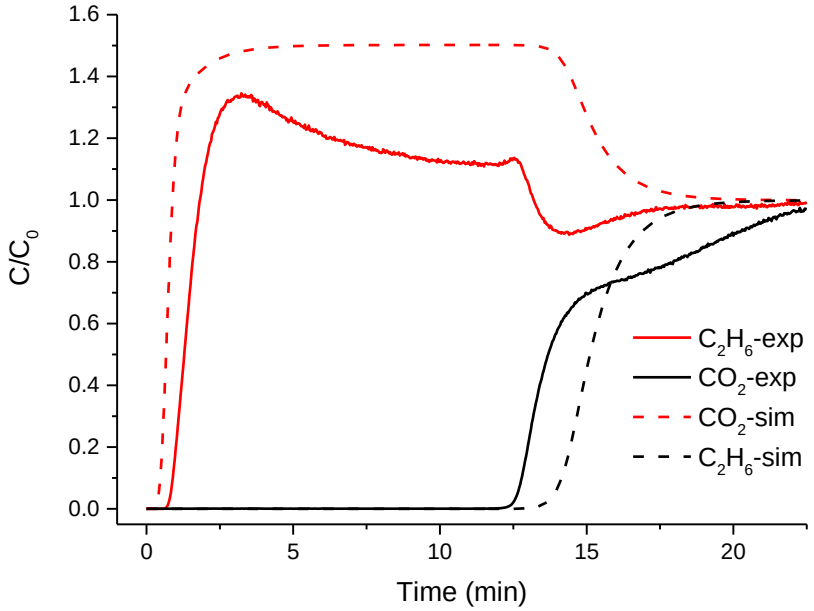

Figure D44. Predicted breakthrough curves for a mixture of 50/50 of CO_2 (black) and C_2H_6 (red) at 293 K and 1.1 bar compared with experimental breakthrough curves after tuning of the mass transfer coefficients (k_{CO2}: 0.021 s^{-1}, k_{C2H6}: 0.018 s^{-1}).

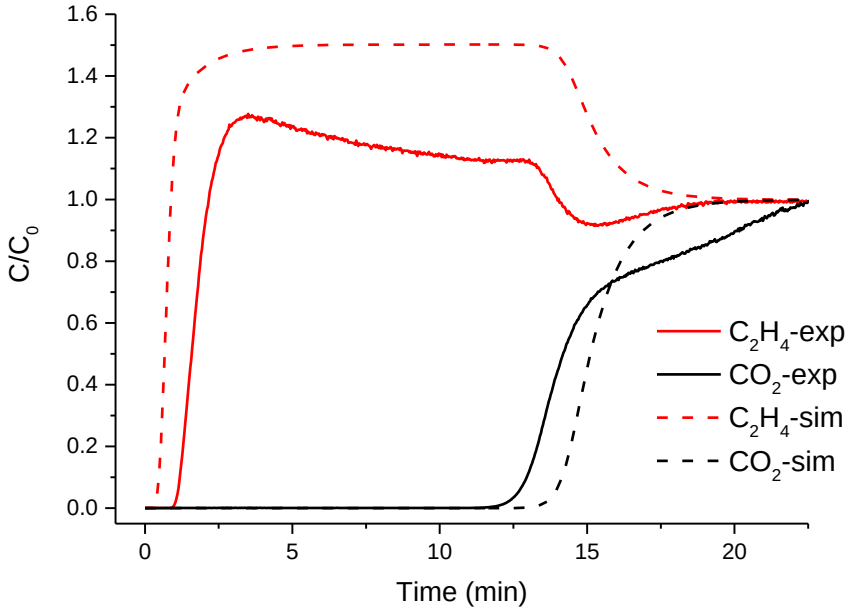

Figure D45. Predicted breakthrough curves for a mixture of 50/50 of CO_2 (black) and C_2H_4 (red) at 293 K and 1.1 bar compared with experimental breakthrough curves after tuning of the mass transfer coefficients (k_{CO2}: 0.021 s^{-1}, k_{C2H4}: 0.017 s^{-1}).

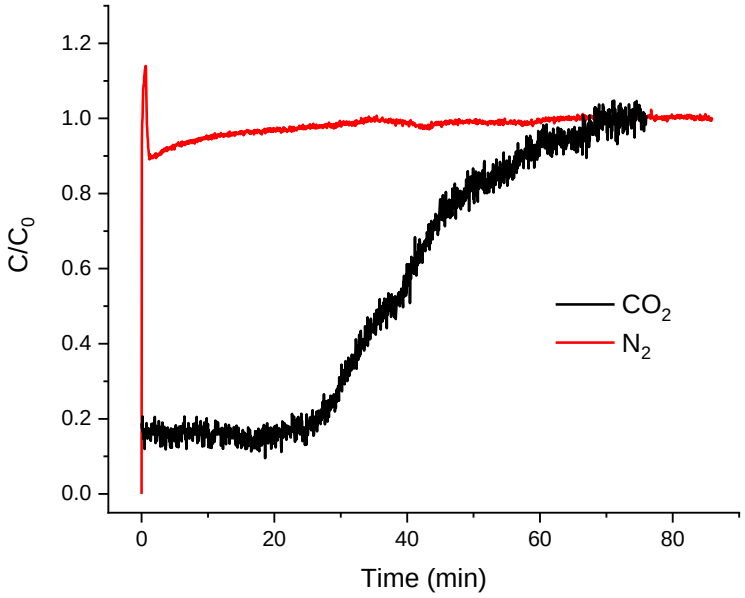

Figure D46 Experimental breakthrough curves for a mixture of 0.2/99.8 CO_2/N_2 at 1.1 bar and 293 K in an adsorption column packed with MUF-16.

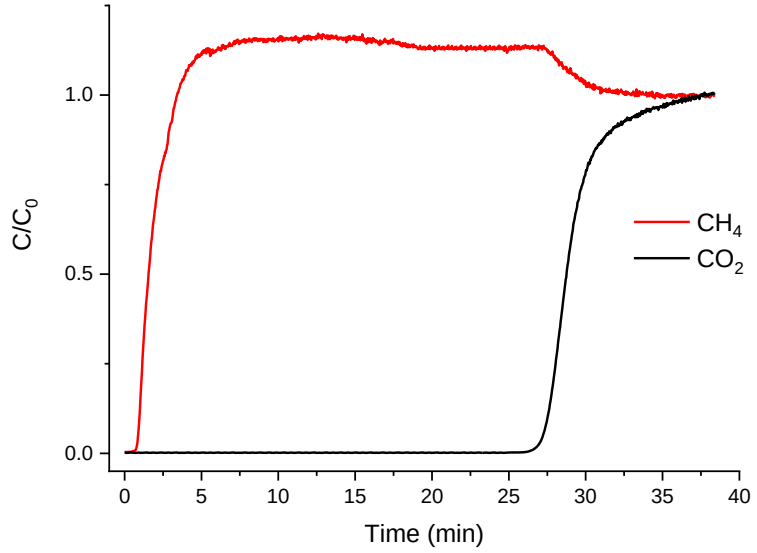

Figure D47 Experimental breakthrough curves for a mixture of 15/85 CO_2/CH_4 at 1.1 bar and 293 K in an adsorption column packed with MUF-16.

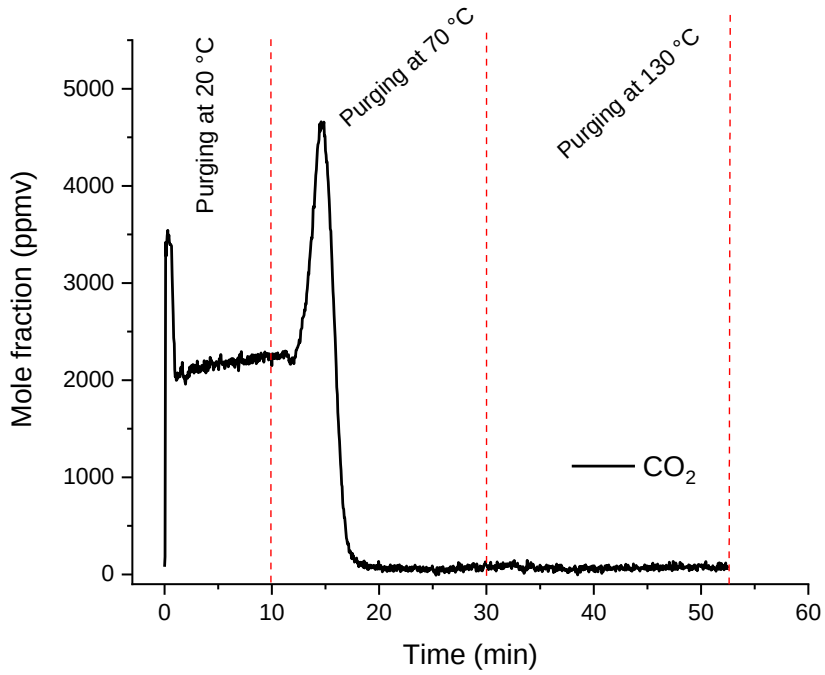

Figure D48 Desorption behaviour of CO_2 from a MUF-16 bed saturated with a 0.4/99.6 CO_2/N_2 mixture by heating the column at 1 bar under a helium flow of 20 mL_N/min. CO_2 is completely desorbed from the column upon heating to 80 °C. No CO_2 remains to be removed upon further heating to 130 °C.

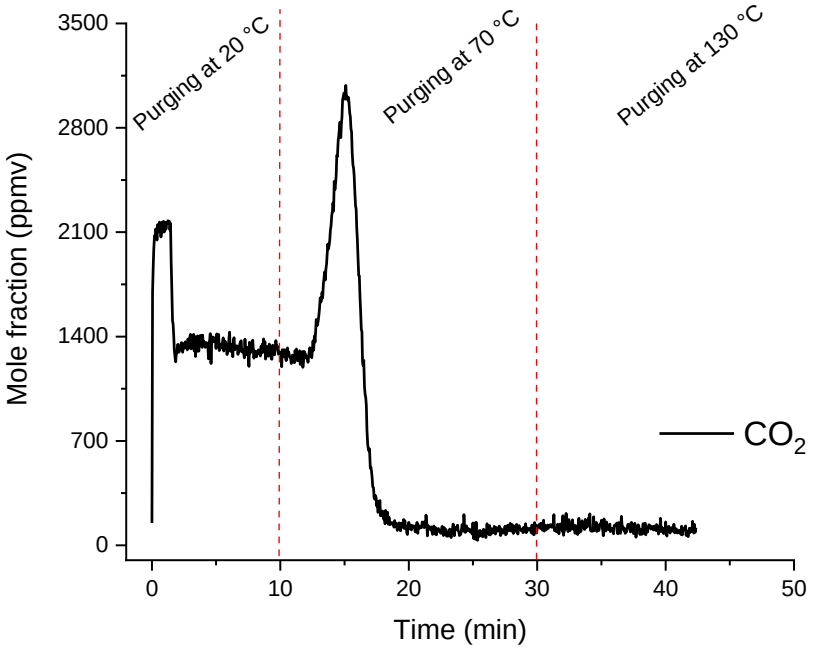

Figure D49 Desorption behaviour of CO_2 from a MUF-16 bed saturated with a 0.2/99.8 CO_2/N_2 mixture by heating the column at 1 bar under a helium flow of 20 mL_N/min. CO_2 is completely desorbed from the column upon heating to 70 °C. No CO_2 remains to be removed upon further heating to 130 °C.

3. Heat of adsorption

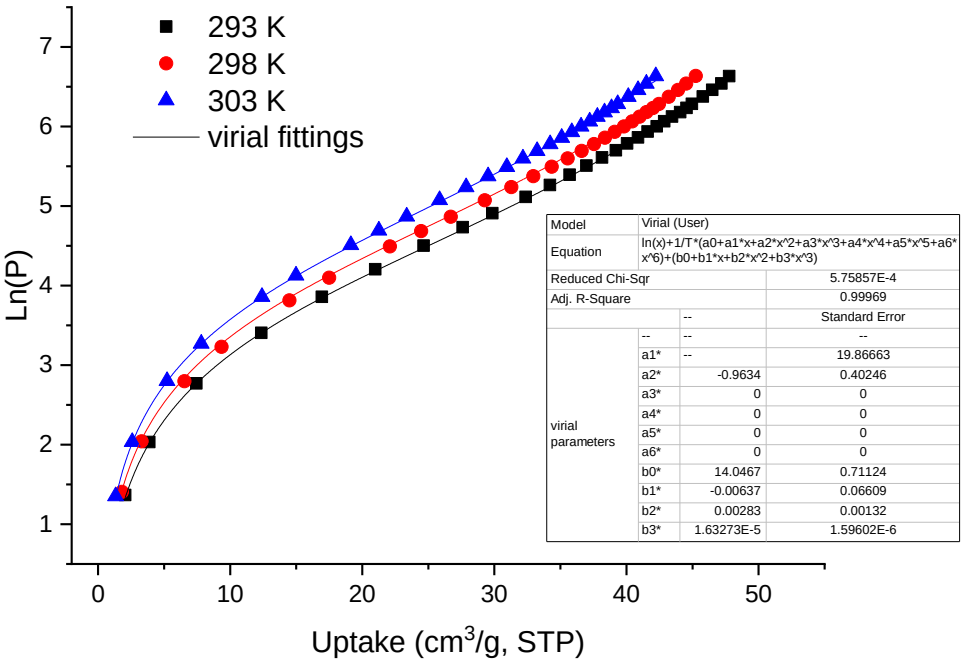

Figure D50 Virial equation fits for CO_2 adsorption isotherms of MUF-16.

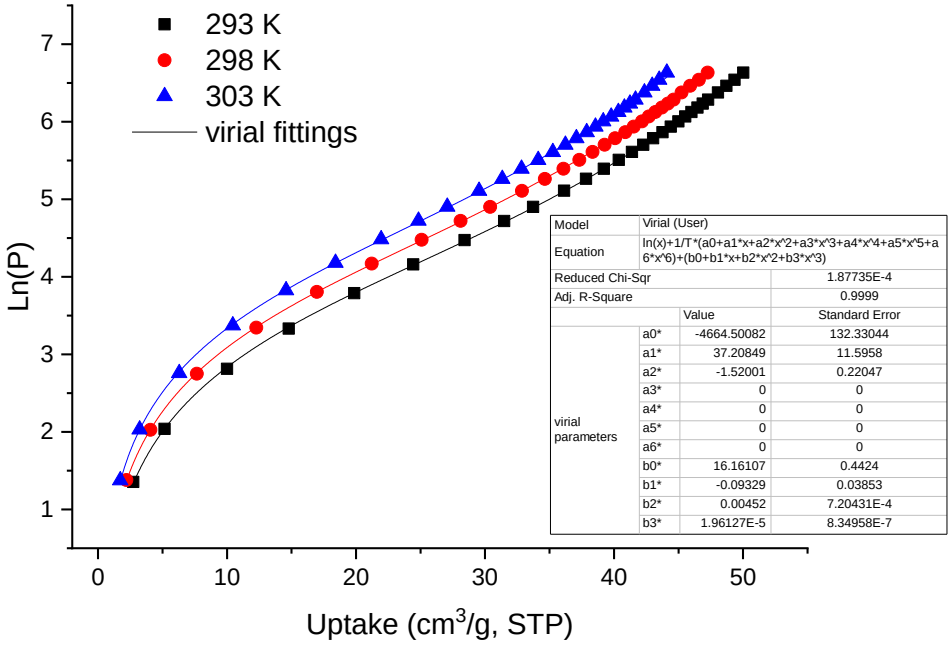

Figure D51 Virial equation fits for CO_2 adsorption isotherms of MUF-16(Mn).

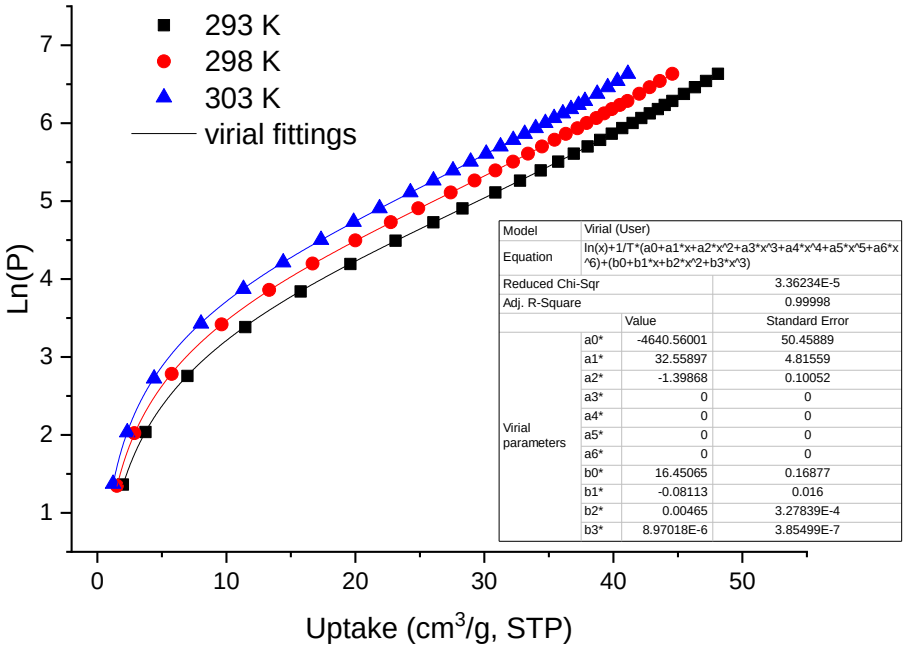

Model	Virial (User)		
Equation	ln(x)+1/T*(a0+a1*x+a2*x^2+a3*x^3+a4*x^4+a5*x^5+a6*x^6)+(b0+b1*x+b2*x^2+b3*x^3)		
Reduced Chi-Sqr			3.36234E-5
Adj. R-Square			0.99998
		Value	Standard Error
Virial parameters	a0*	-4640.56001	50.45889
	a1*	32.55897	4.81559
	a2*	-1.39868	0.10052
	a3*	0	0
	a4*	0	0
	a5*	0	0
	a6*	0	0
	b0*	16.45065	0.16877
	b1*	-0.08113	0.016
	b2*	0.00465	3.27839E-4
	b3*	8.97018E-6	3.85499E-7

Figure D52 Virial equation fits for CO_2 adsorption isotherms of MUF-16(Ni).

Appendix E for Chapter 6

1. Single gas isotherm measurements

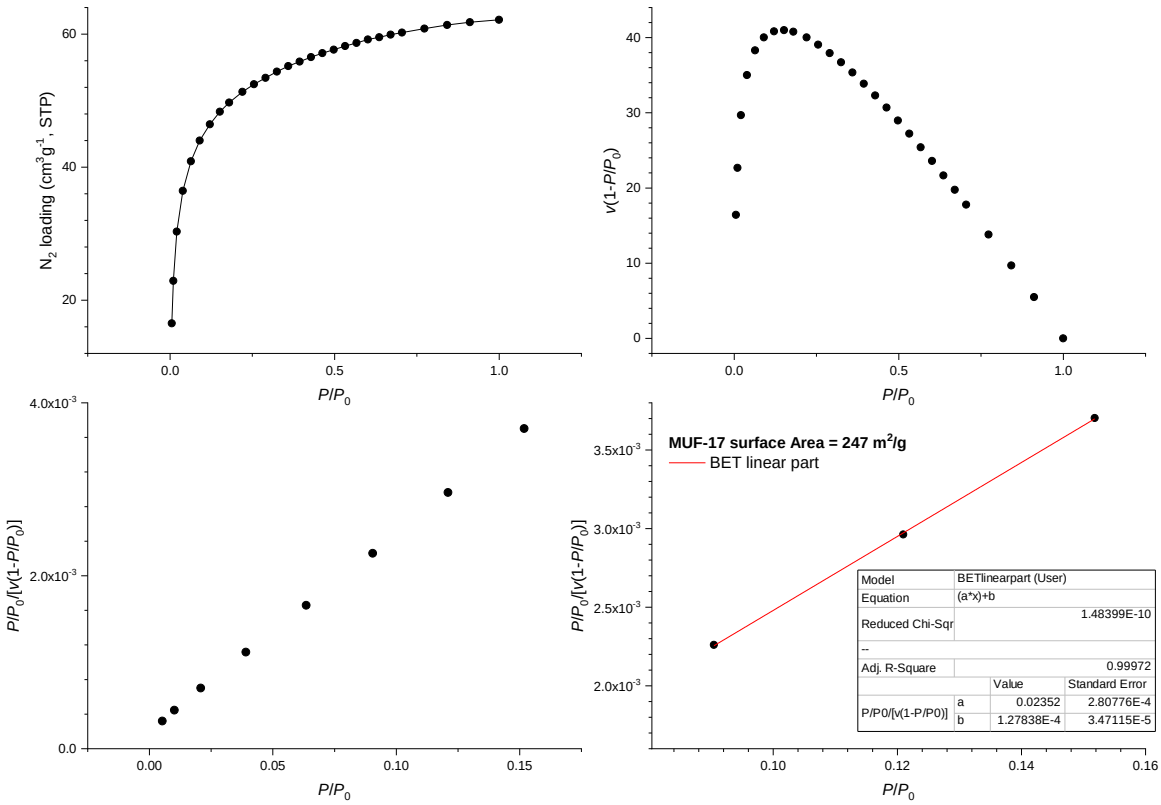

Figure E53 CO_2 adsorption isotherm at 273 K and BET surface area plots for MUF-17.

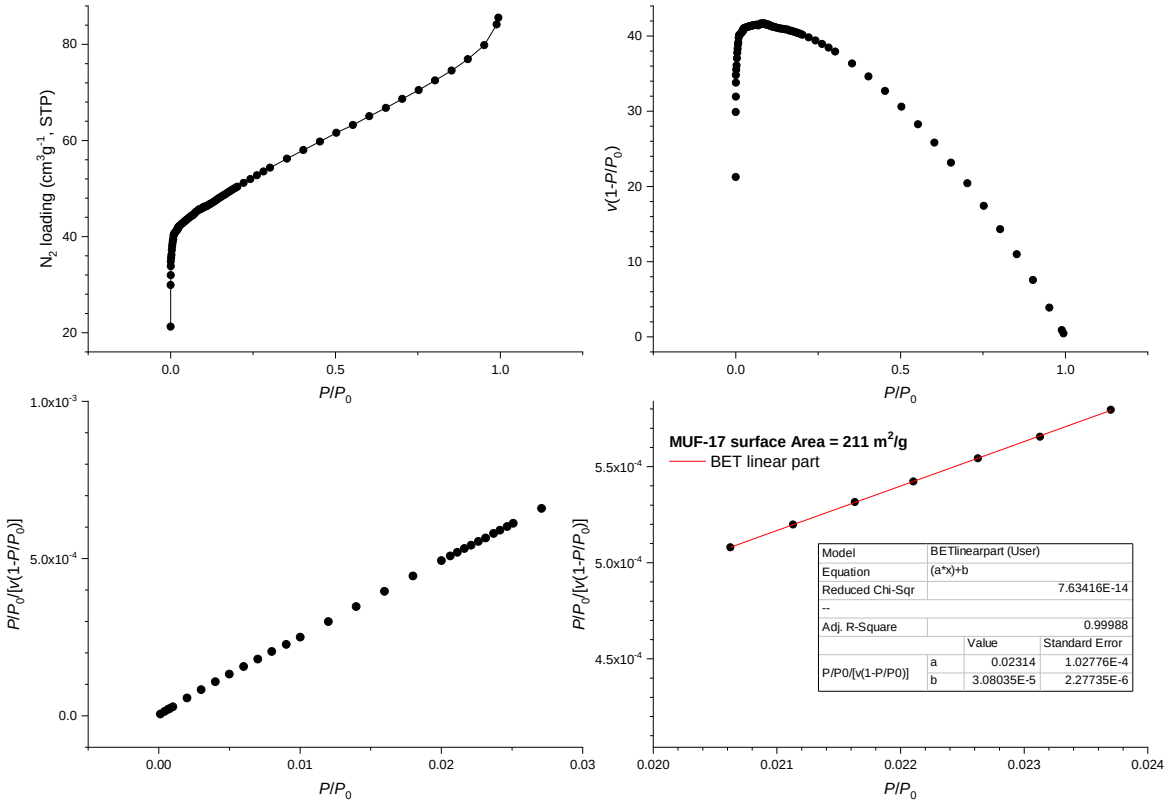

Figure E54 N_2 adsorption isotherm at 77 K and BET surface area plots for MUF-17.

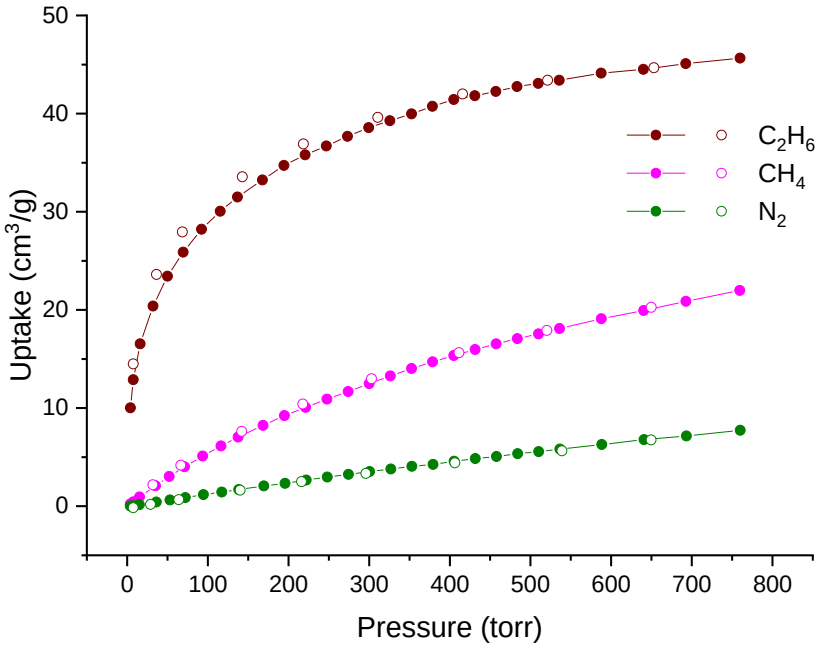

Figure E55 Volumetric adsorption (filled circles) and desorption (open circles) isotherms of C_2H_6 (black), CH_4 (pink) and N_2 (green) measured at 293 K for MUF-17.

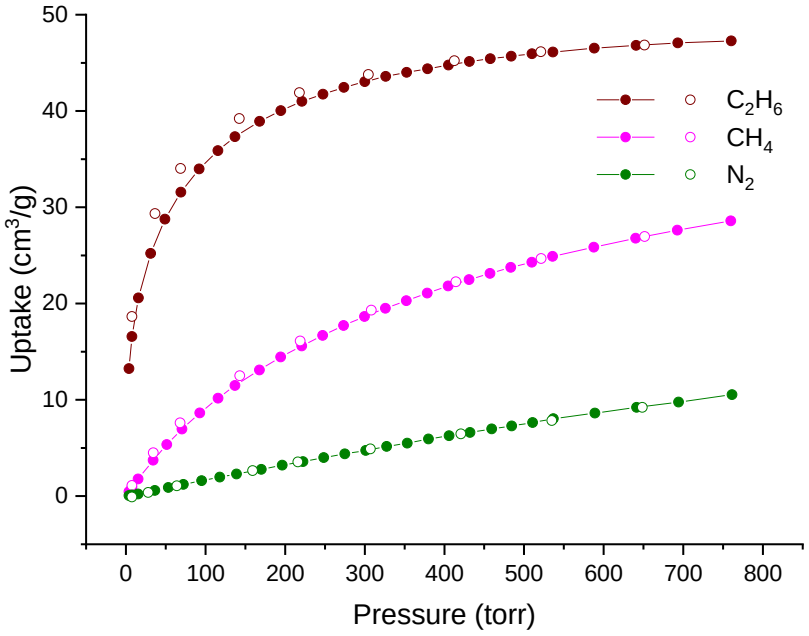

Figure E56 Volumetric adsorption (filled circles) and desorption (open circles) isotherms of C_2H_6 (black), CH_4 (pink) and N_2 (green) measured at 273 K for MUF-17.

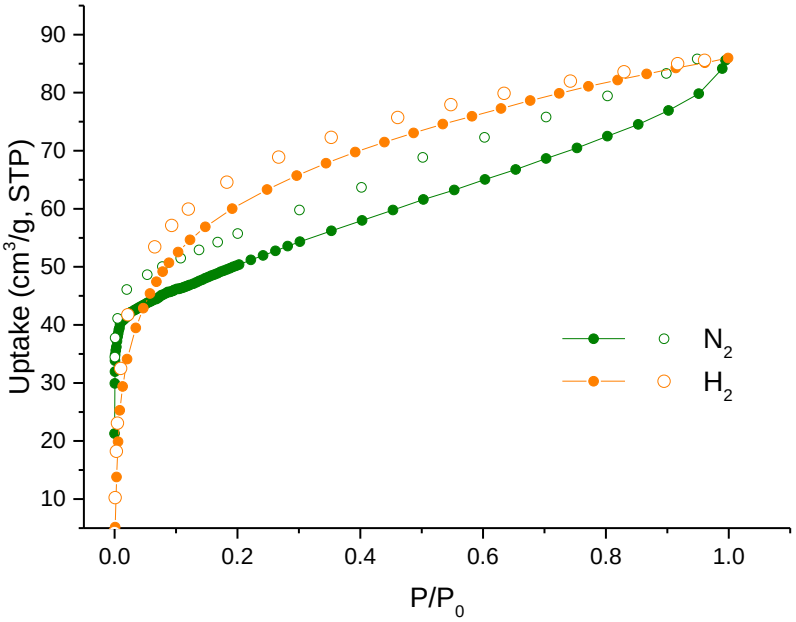

Figure E57 Volumetric adsorption (filled circles) and desorption (open circles) isotherms of N_2 and H_2 measured at 77 K for MUF-17.

2. IAST calculations

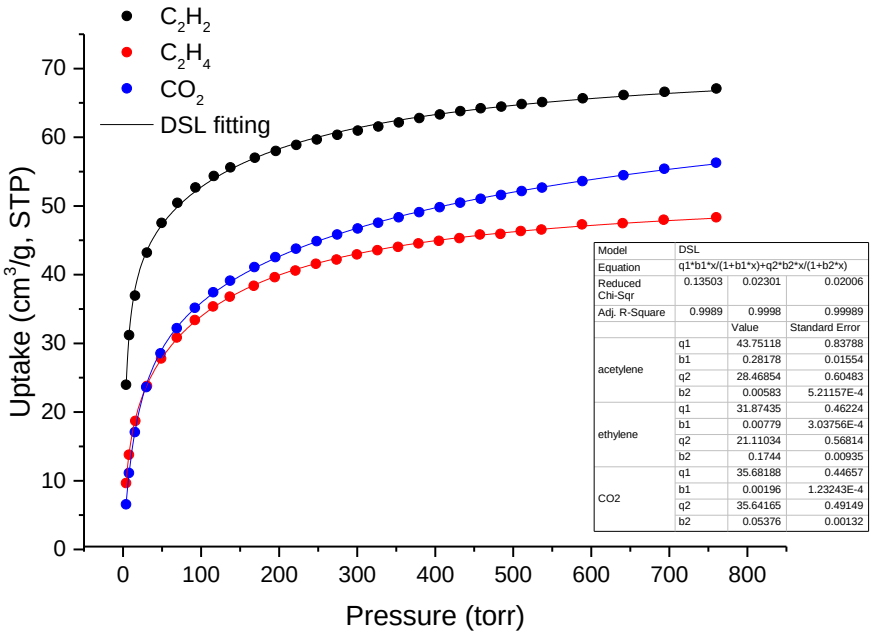

Model	DSL		
Equation	q1*b1*x/(1+b1*x)+q2*b2*x/(1+b2*x)		
Reduced Chi-Sqr	0.13503	0.02301	0.02006
Adj. R-Square	0.9989	0.9998	0.99989
		Value	Standard Error
acetylene	q1	43.75118	0.83788
	b1	0.28178	0.01554
	q2	28.46854	0.60483
	b2	0.00583	5.21157E-4
ethylene	q1	31.87435	0.46224
	b1	0.00779	3.03756E-4
	q2	21.11034	0.56814
	b2	0.1744	0.00935
CO2	q1	35.68188	0.44657
	b1	0.00196	1.23243E-4
	q2	35.64165	0.49149
	b2	0.05376	0.00132

Figure E58. Dual-site Langmuir fits of the MUF-17 isotherms at 293 K.

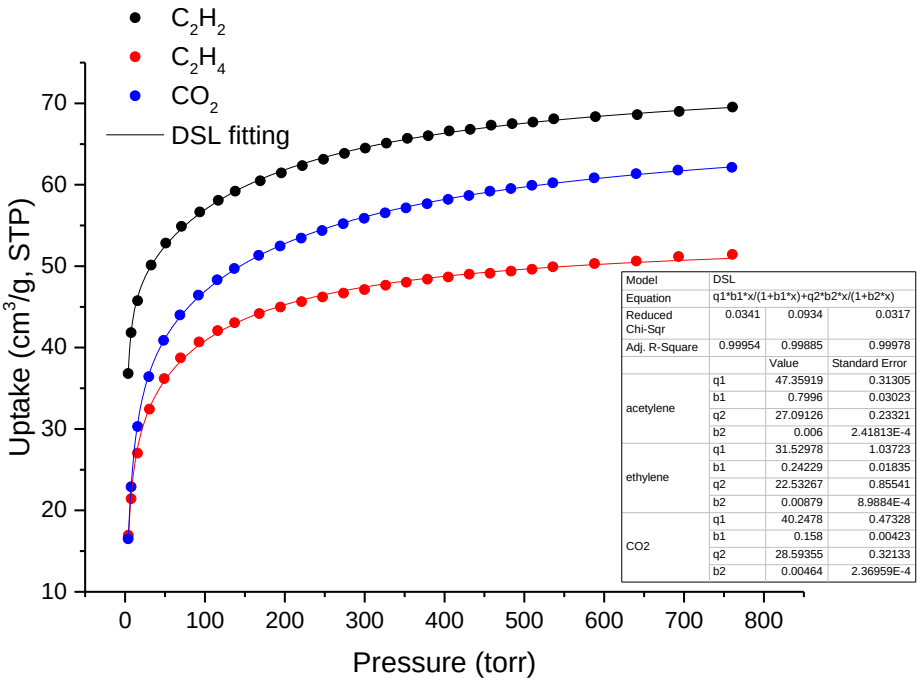

Model	DSL		
Equation	q1*b1*x/(1+b1*x)+q2*b2*x/(1+b2*x)		
Reduced Chi-Sqr	0.0341	0.0934	0.0317
Adj. R-Square	0.99954	0.99885	0.99978
		Value	Standard Error
acetylene	q1	47.35919	0.31305
	b1	0.7996	0.03023
	q2	27.09126	0.23321
	b2	0.006	2.41813E-4
ethylene	q1	31.52978	1.03723
	b1	0.24229	0.01835
	q2	22.53267	0.85541
	b2	0.00879	8.9884E-4
CO2	q1	40.2478	0.47328
	b1	0.158	0.00423
	q2	28.59355	0.32133
	b2	0.00464	2.36959E-4

Figure E59. Dual-site Langmuir fits of the MUF-17 isotherms at 273 K.

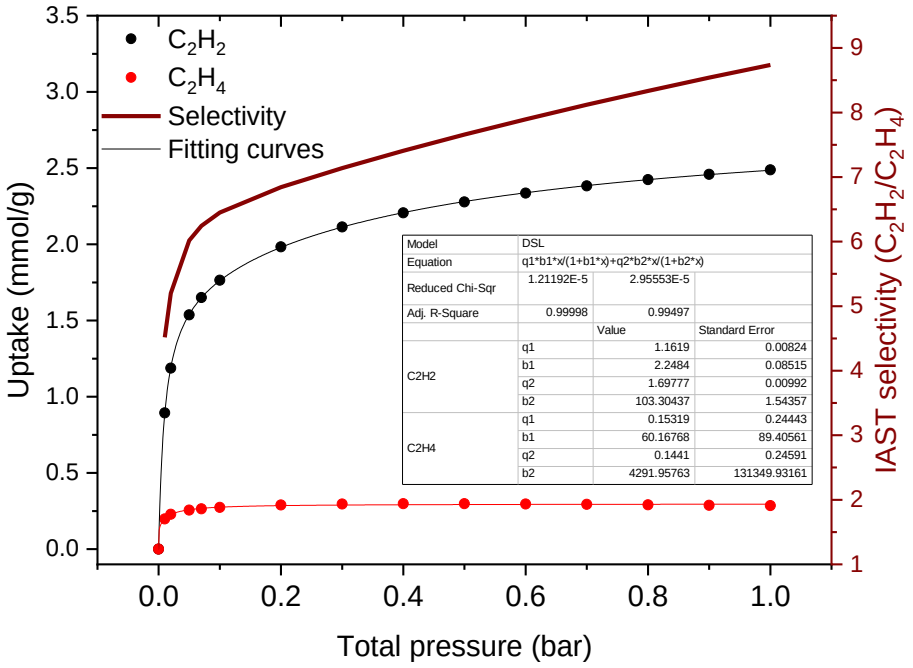

Figure E60. Mixed-gas isotherms and selectivity of MUF-17 predicted by IAST for a 50/50 mixture of C_2H_2/C_2H_4 at 293 K.

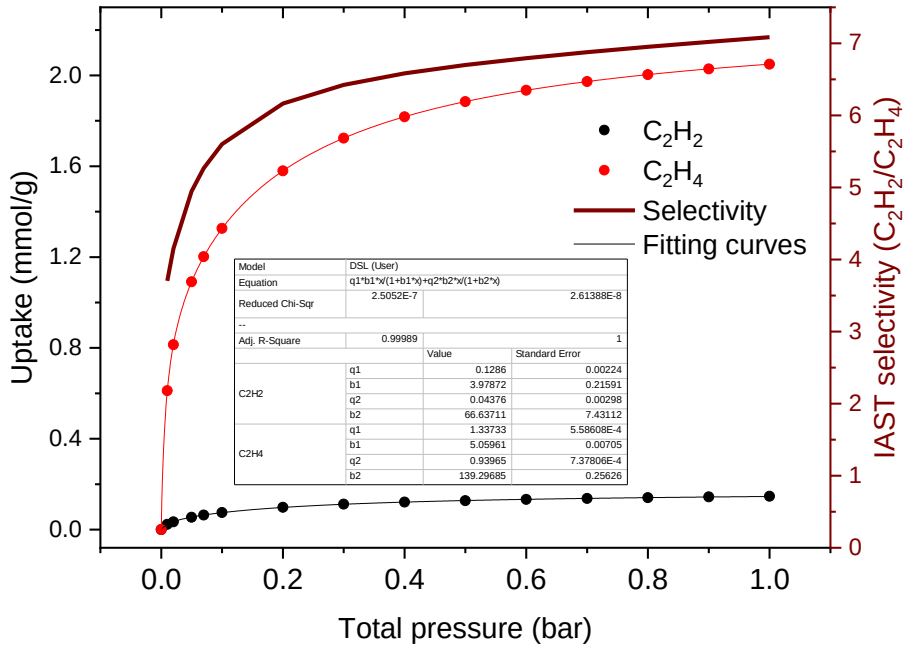

Figure E61. Mixed-gas isotherms and selectivity of MUF-17 predicted by IAST for a 1/99 mixture of C_2H_2/C_2H_4 at 293 K.

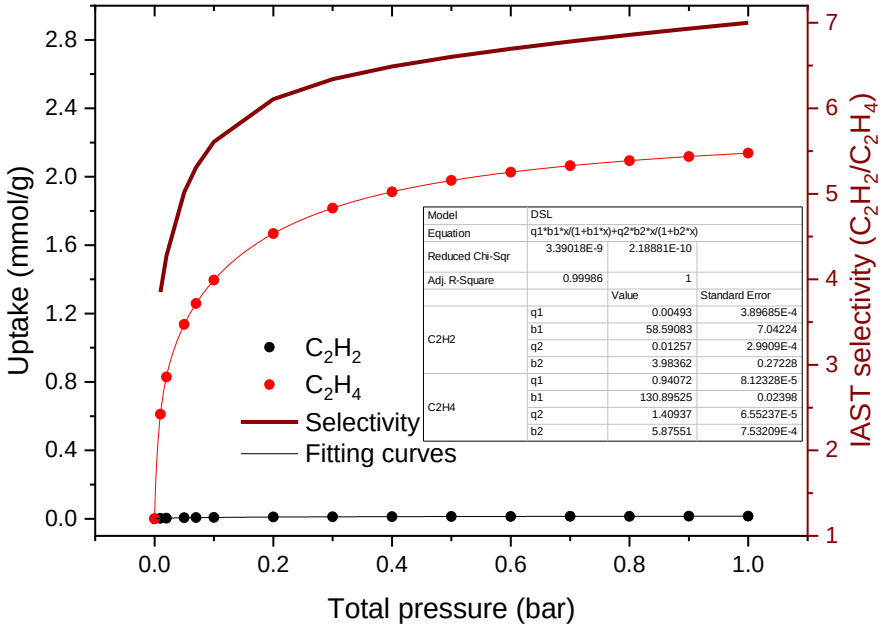

Figure E62. Mixed-gas isotherms and selectivity of MUF-17 predicted by IAST for a 0.1/99.9 mixture of C_2H_2/C_2H_4 at 293 K.

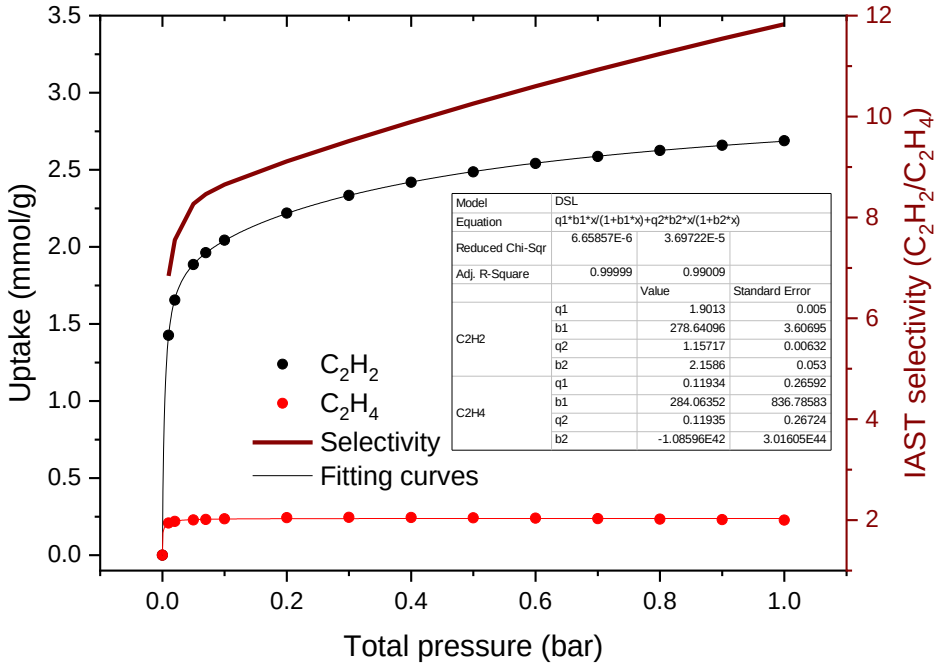

Figure E63. Mixed-gas isotherms and selectivity of MUF-17 predicted by IAST for a 50/50 mixture of C_2H_2/C_2H_4 at 273 K.

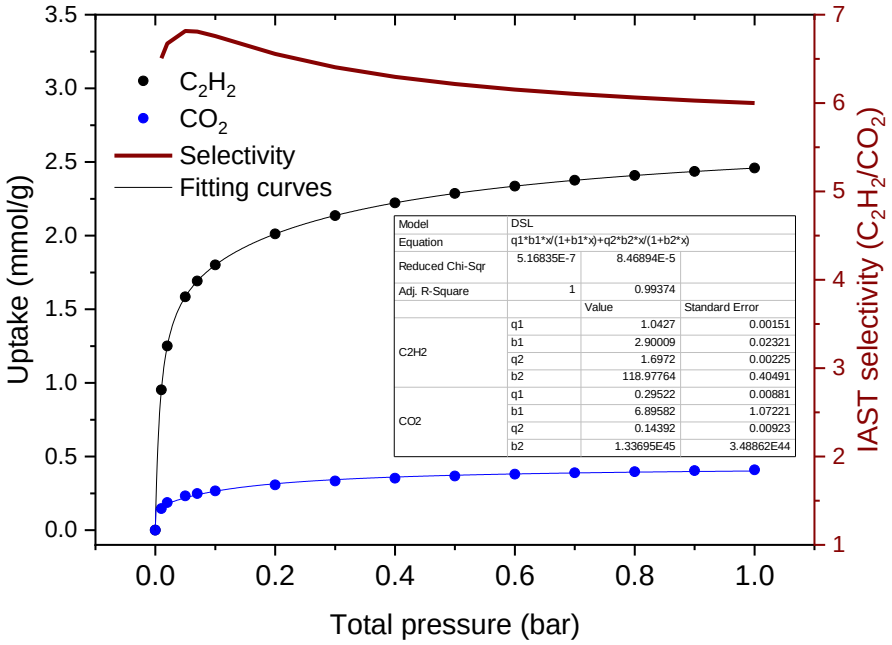

Figure E64. Mixed-gas isotherms and selectivity of MUF-17 predicted by IAST for a 50/50 mixture of C_2H_2/CO_2 at 293 K.

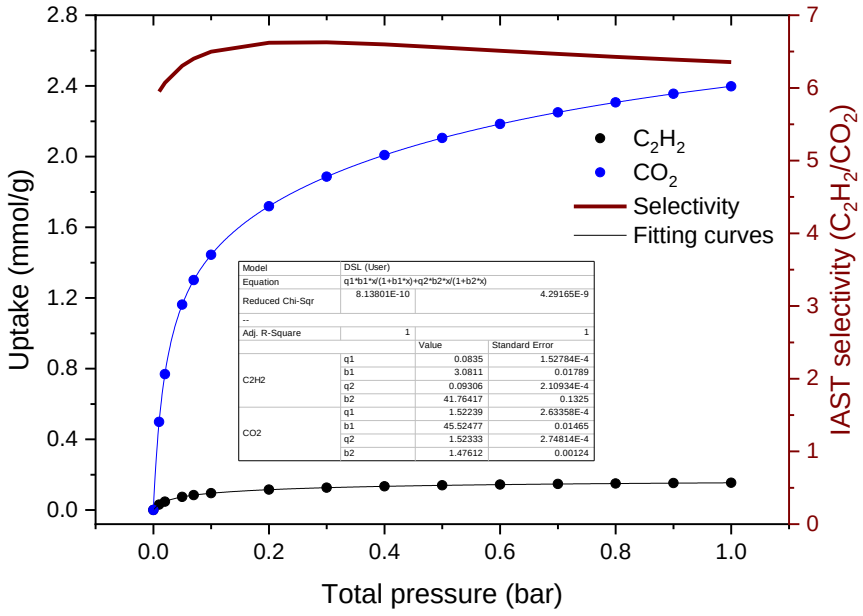

Figure E65. Mixed-gas isotherms and selectivity of MUF-17 predicted by IAST for a 1/99 mixture of C_2H_2/CO_2 at 293 K.

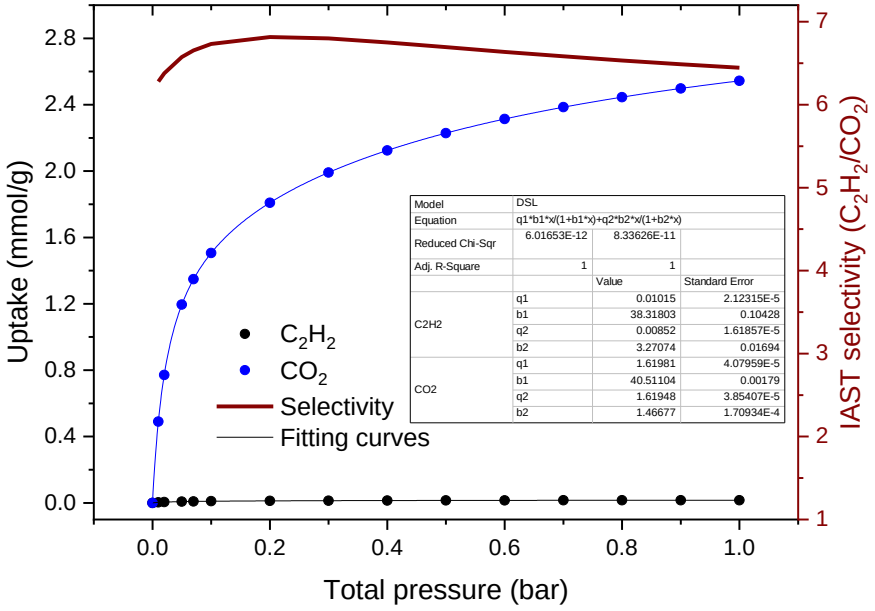

Figure E66. Mixed-gas isotherms and selectivity of MUF-17 predicted by IAST for a 0.1/99.9 mixture of C_2H_2/CO_2 at 293 K.

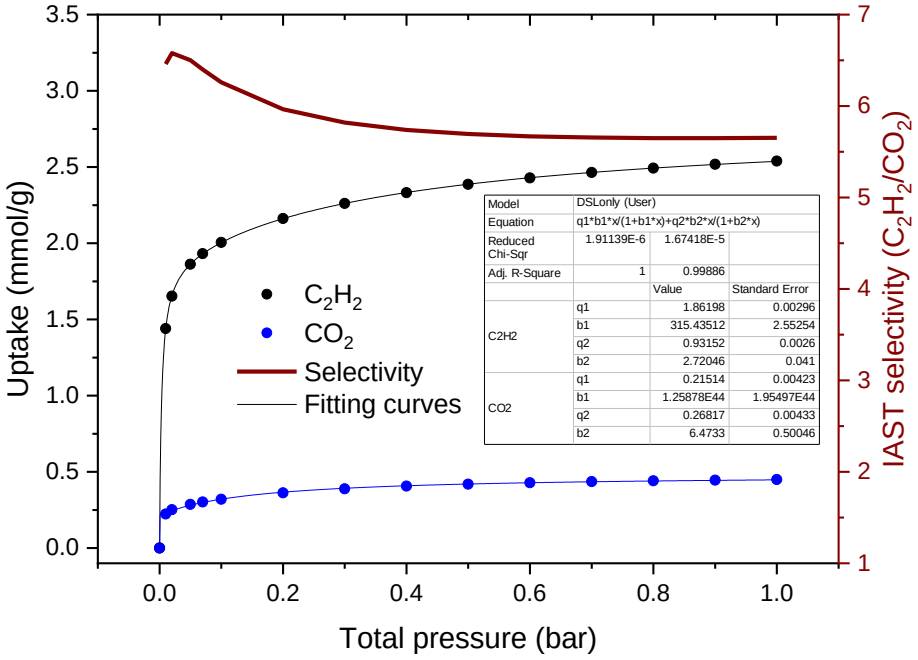

Figure E67 Mixed-gas isotherms and selectivity of MUF-17 predicted by IAST for a mixture of 50/50 C_2H_2/CO_2 at 273 K.

3. Heat of adsorption

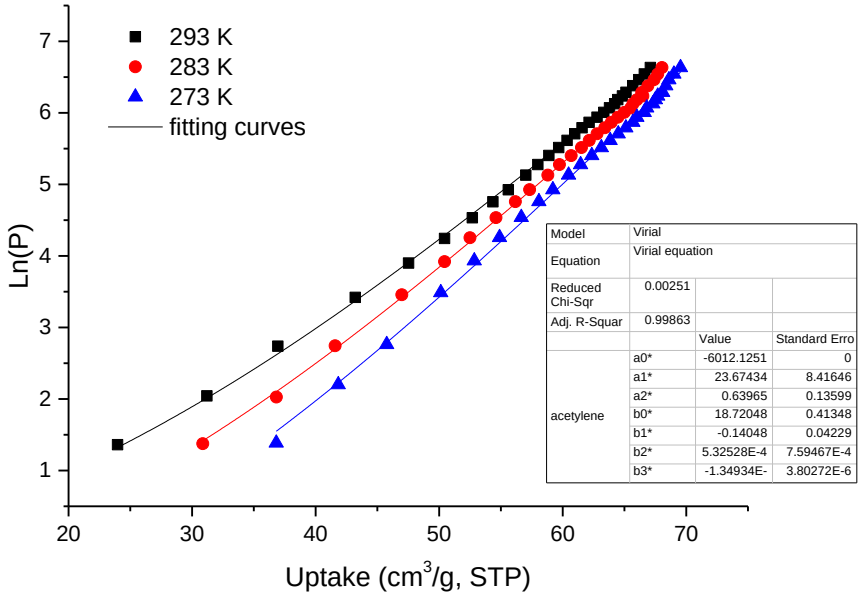

Figure E68 Virial equation fits for C_2H_2 adsorption isotherms of MUF-17.

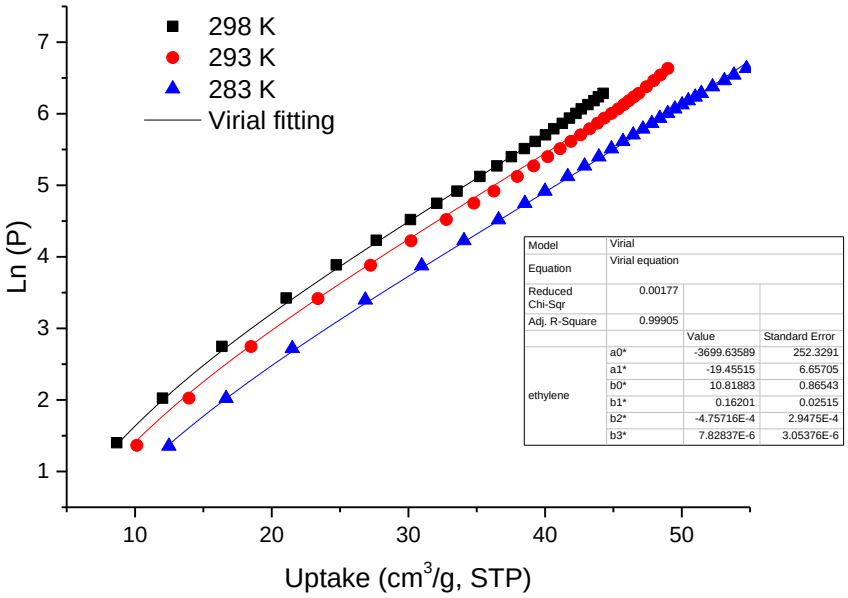

Figure E69 Virial equation fits for C_2H_4 adsorption isotherms of MUF-17.

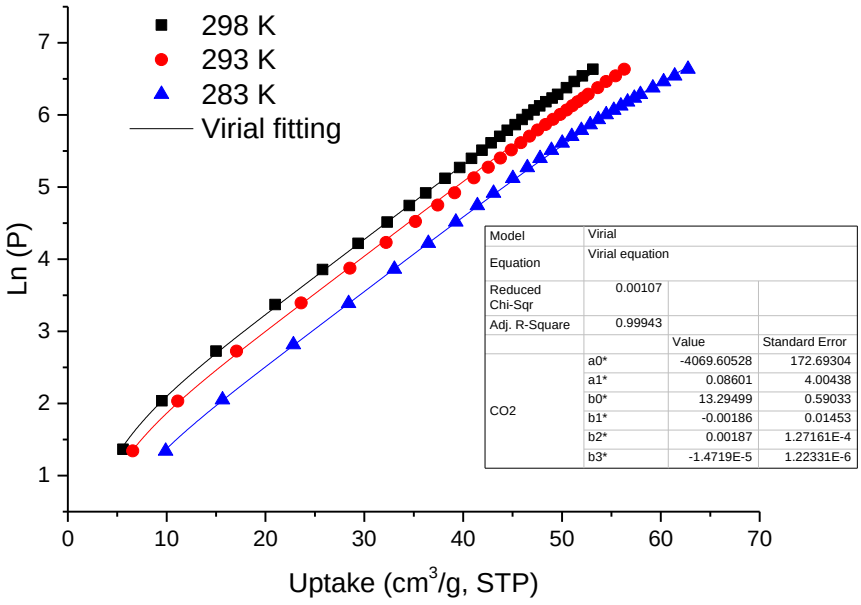

Figure E70 Virial equation fits for CO_2 adsorption isotherms of MUF-17.